

# Engineering of PEM-PEC photocathodes for solar-driven hydrogen production

Présentée le 10 juin 2022

Faculté des sciences de base  
Laboratoire d'ingénierie moléculaire des nanomatériaux optoélectroniques  
Programme doctoral en chimie et génie chimique

pour l'obtention du grade de Docteur ès Sciences

par

**Marina Caroline Michèle CARETTI**

Acceptée sur proposition du jury

Prof. S. Gerber, présidente du jury  
Prof. K. Sivula, directeur de thèse  
Dr L. Steier, rapporteuse  
Dr M. Tsampas, rapporteur  
Prof. R. Buonsanti, rapporteuse

---

A ma sœur, Camille, cette artiste,  
pour sa bienveillance, sa finesse d'esprit,  
et son incroyable sens de l'humour.

A mes parents,  
Pour leur gentillesse, et leur authenticité  
Pour leur soutien, et pour leur amour

---



---

<< Il y a des minutes et des secondes qui contiennent tout un monde. Nous avons roulé de progrès en progrès. Ils ont toujours tout changé de notre façon de sentir, de penser et de vivre. Ils n'ont jamais rien changé à notre humaine condition. Mourir ne me dérange pas. Je suis juste ennuyé par la perspective de ne plus pouvoir savoir ce qui va se passer. On peut tout dire de l'amour. Tout ce qu'on en dit est vrai, et le contraire aussi. Voilà ce que je suis, un miracle. À des milliards et des milliards d'exemplaires. Il y a quelque chose de plus fort que la mort, c'est la présence des absents dans la mémoire des vivants. C'est quand il y a quelque chose au-dessus de la vie que la vie devient belle.

Avec son passé qui n'est plus, son avenir qui n'est pas encore et son éternel présent toujours en train de s'évanouir entre souvenir et projet, le temps est la plus prodigieuse de toutes les machineries. Aucun phénomène de la nature, aucune invention humaine, aucune combinaison de l'esprit, aucune intrigue de roman, de cinéma, de théâtre ou d'opéra, si compliquée qu'elle puisse être, ne lui parvient à la cheville.

La vie n'est pas une fête perpétuelle. Merci pour les roses, merci aussi pour les épines.

Personne ne sait jamais ce qu'on gagne avec une naissance. On n'y gagne que des espérances, des illusions et des rêves. Il faut attendre la mort pour savoir enfin ce qu'on perd. Tâchons de dépasser ce qui nous oppose et de multiplier ce qui nous unit. La vie est belle parce qu'elle a une fin. >>

Jean d'Ormesson

---

---

# Acknowledgements

A Motz, le 10.03.2022,

Professor Kevin Sivula, thank you for giving me the opportunity to join EPFL, first as a master student and then as a PhD student. Thanks for all your wise advice, especially when the frustration level was too high. It was a long journey, so thank you for trusting me. I have learnt a lot, on the professional side but also on the personal side. So, in this sense it was an extremely rich experience.

I would like to thank Dr. Steier, Pr. Buonsanti and Dr. Tsampas for kindly accepting to read and examine my research work, and Pr. Gerber for accepting the role of jury president.

Thanks to all the partners of the Sun-to-X project, it was motivating to work with all of you. Hannah thanks for your kindness and for your support. Jingxian, it was nice to work with you in the lab at EPFL. Marek, thanks for all the great discussions, your cheerfulness, and all the “by the way”.

Dr. Yum Junho, thank you for your help during this PhD, I hope one day I will run as fast as you and maybe we could run the half-marathon of Lausanne together. Dr. Liang Yao, Dr. Hanhee Cho, thank you both for your help and kindness. You were always willing to help and share your knowledge, which I have really appreciated. Thanks to all the LIMNO members for these years, Nukorn for listening all my stories and drama and for your positive mood, Arvin, Colin et Luc pour votre gentillesse incroyable, Benjamin pour ces quelques mois de passage de flambeaux, Connor, and Simon for the memorable mountains trip in Saint-Gervais. Yong-peng and Meng, thanks for choosing me as your wedding witness; I look forward to the celebration. Grazie mille Dr Annalisa Polo per questi sei mesi insieme at EPFL, sei diventata un mia grande amica, è come se ti avessi sempre conosciuto! Merci Dr. Emeline Rideau pour la dernière année de doctorat. Cela a été un plaisir d’avoir partagé le bureau avec toi. Merci pour tes conseils scientifiques, j’ai beaucoup appris à tes côtés et merci pour toutes ces discussions sur tout et rien qui font du bien. Merci Dr. Florian Le Formal d’être resté un très bon ami en dehors du LIMNO, pour ces sorties ski, ce weekend en Provence avec Wiktor (merci à vous deux), et tous les autres moments qui m’ont permis de relativiser et de voir les choses sous un autre angle.

Thanks to all the people outside of LIMNO. Stefania, thanks for all the shrink session and I hope we will do another Jacquie Guillon night in the future. Thanks to Chris, Luca, Jack, Benjamin, Lorenz for all the good moments, that really helped at the beginning of my PhD. Merci Nina pour tous ces lunchs entre le CH et le BCH, qui m’ont permis de m’évader le temps d’un instant. On s’est retrouvé deux fois par le passé, peut-être qu’il y aura une troisième.

Many thanks to the master students that I have supervised. Without them, this thesis would not be the same. Linda, merci de ton investissement et du travail de qualité que tu as fourni. Loï, merci d’avoir partagé le début des semiconducteurs organiques avec moi et pour les jolies figures. Raluca, the last but not the least, thanks for kindness, your work, your ideas, you will do great in your professional life, I have no doubt.

J’ai une pensée pour les apprentis chimistes de Montpellier, pour qui j’ai une attache toute particulière, merci ma Dja-ia (j’espère voir ton joli sourire plus souvent maintenant), merci Lyna, Mathilde, les Camille, Audrey, Pauline, Elisa, Claire, Chris, Baptiste, Florian, Pierre, Alexis.

---

Je tiens à remercier aussi mes superviseurs passés, Dr. Aurélien Vivet au sein de Baikowski, et Dr. Gilles Humbert au sein de Ferroglobe. Merci pour votre gentillesse et merci d'avoir participé grandement à mon parcours scientifique. J'ai une pensée aussi pour tous mes anciens collègues de Ferroglobe, Sabine, Agnès, Michel, Laurent, Lilian.

Rebekah, thanks for being an amazing support and friend since the beginning of my EPFL journey. So many memories that I do not know which one to mention... the Christmas time with my family, the famous "fridge" story will be classic, as well as the destroyed T-shirt for Clément's birthday. Alors, Rebekah, juste merci d'avoir embelli cette expérience, merci pour ta gentillesse et ton altruisme. J'espère qu'on se retrouvera en France ou ailleurs. Adélie, merci pour toutes ces rigolades, la sortie en vélo ou j'ai perdu mes poumons, les remontages de bretelles, ta bonne humeur et ta gentillesse. Nestor, thanks for all the time spent in the lab and outside! Apart from your huge scientific knowledge, I will always remember the weekend in Annecy and the famous lost sunglasses. Thanks for your support, even by text, out the blue, listening all my stories and giving me the best advice. Barbara, my dear, so many good memories (la Girafe...maybe not, le Salon de l'Auto à Genève, the famous sound in the metro station, the diners in St-Sulpice, the long walk with my sister along the lack...), thanks for your kindness. I hope that we will do this trip to Italy one day! Dr Elizabeth Mensi, thanks for being a real mentor at a key moment during the PhD. Your scientific skills and knowledge were a real inspiration for me! I have also met a real friend. I will always remember our lovely lunch/coffee breaks in Coppet with Mounir and Léa. Merci à tous les trois pour votre bienveillance.

Merci à la famille Chomat pour leur bienveillance. Merci à mes grands-parents, à mes oncles et tantes, et à toute ma famille en France et en Italie. Merci aux Nonni pour m'avoir transmis des valeurs humaines importantes, Armando et Michelina, mi mancate. Merci Gabrielle, d'avoir été présente pendant toutes ces années en Suisse. Merci à mon beau-frère Tristan, pour tes créations en tous genres, et surtout Bon Dimanche. Caroline, merci de m'avoir accompagné dans cet énième challenge, dans les bons comme mauvais moments, merci pour Prague, pour la Suisse et toutes nos aventures. Merci pépé Lucien, merci d'avoir été une source d'inspiration, merci de m'avoir toujours soutenu et fait sentir que j'en valais la peine. Merci Clément d'avoir partagé un bout de ce doctorat avec moi. Tu as su trouver les mots, tu as su me faire rire, tu m'as emmené en montagne pour relativiser et comme à chaque fois tu as été mon pilier. J'ai hâte de vivre cette nouvelle étape de notre vie. Papa, Maman merci pour vos encouragements, merci pour votre authenticité, c'est aussi grâce à vous tout ça. Papa, merci pour tous tes efforts, je suis fière de toi. Maman merci d'avoir toujours cru en moi et de m'avoir insufflé l'envie de donner le meilleur de moi-même. Et enfin, merci à ma merveille, ma sœur, mon soutien sans faille depuis 26 ans, sans qui rien de cela n'aurait de sens.

# Abstract

Earth has always been in perpetual evolution, but today we must face its rapid change due to human activity. The intensification of industrial activities and transportation to support our modern lifestyles are the main causes of climate change and the adverse effects on the fauna and flora. In spite of this, the planet has shown resilience and should be able, if the conditions allow, to maintain its balance. Our energy system is at the heart of the transformation we must undertake. To lessen our impact on the environment, we must consider the end of fossil fuels, the main source of greenhouse gas emissions. The immense amount of solar energy which reaches the Earth's surface would be more than enough to meet the world's energy needs, provided that we master its capture and overcome its intermittency. The storage of this energy in solar fuel such as hydrogen is a solution to meet the challenge of intermittent light. Hydrogen can be produced by splitting water molecules into hydrogen and oxygen under the effect of an electric current. Various methods such as proton exchange membrane (PEM) electrolysis can be coupled with solar energy conversion systems to produce carbon-free hydrogen. These technologies are still in their infancy; therefore, their evaluation is a key issue for future energy challenges.

The research work presented in this thesis deals with the engineering of a proton exchange membrane photoelectrochemical cell (PEM-PEC) to produce hydrogen from moist air and solar energy. A new porous electrode support combining transparency and electrical conduction has been created. The use of this novel transparent, porous, conductive support (TPCS) for photoelectrode was demonstrated by depositing an n-type semiconductor (hematite,  $\alpha\text{-Fe}_2\text{O}_3$ ) to produce oxygen by solar-assisted water splitting. The hematite-TPCS electrode exhibited a photocurrent of  $1.6 \text{ mA}\cdot\text{cm}^{-2}$  at  $1.6 \text{ V}$  vs. RHE (reversible hydrogen electrode). For the photocathode portion different p-type semiconductor layers were studied; first on flat conductive glass and later on the TPCS. Tungsten diselenide ( $\text{WSe}_2$ ) nanoflakes produced by liquid phase exfoliation were coated by electrophoretic deposition. Furthermore, an *in-situ* electro-conversion to form copper oxide ( $\text{Cu}_2\text{O}$ ) was identified, allowing for production of thin and transparent layers. Subsequently, p-type semiconductor layers ( $\text{WSe}_2$ ,  $\text{Cu}_2\text{O}$ , organic semiconductors) were deposited on the TPCSs and their photoactivity in liquid media was evaluated. The organic semiconductor was selected based on the ease of implementation and the promising results obtained for the photoreduction of europium in liquid phase, ca.  $-4.5 \text{ mA}\cdot\text{cm}^{-2}$  at  $0 \text{ V}$  vs. RHE. After Pt catalyst coating, the organic semiconductor based TPCS was tested for hydrogen production in liquid media, exhibiting a photocurrent ca.  $-1 \text{ mA}\cdot\text{cm}^{-2}$  at  $0 \text{ V}$  vs. RHE. After the implementation in a half PEM-PEC cell for hydrogen production in the gas phase, a photocurrent of  $-120 \text{ }\mu\text{A}\cdot\text{cm}^{-2}$  at  $0 \text{ V}$  vs. RHE was sustained (i.e.,  $1 \text{ }\mu\text{mol}\cdot\text{h}^{-1}$  of  $\text{H}_2$ ) for 1 hour.

## **Keywords**

Proton-exchange membrane, photoelectrochemical, hydrogen production, transparent porous conductive substrate, hematite, tungsten diselenide, cuprous oxide, organic semiconductor.

# Résumé

La planète Terre a toujours été en perpétuelle évolution, mais aujourd'hui nous devons faire face à son changement rapide du fait de l'activité de l'Homme. L'intensification des activités industrielles et des transports, nos modes de vie modernes sont en partie responsable du dérèglement climatique et des effets néfastes sur la faune et la flore. Malgré tout, la planète Terre a su montrer beaucoup de résilience et pourra être apte, si les conditions le permettent, à assurer le maintien de son équilibre. Notre système d'énergie est au cœur de la transformation que nous devons engager. Outre notre impact sur l'environnement, nous devons aussi avoir la perspective de la fin des ressources fossiles, principales sources d'émissions des gaz à effet de serre. L'immensité de l'énergie solaire suffirait amplement à répondre aux besoins énergétiques mondiaux, à condition de maîtriser sa capture et de pallier son intermittence. Le stockage de cette énergie en combustible solaire tel que l'hydrogène est une solution pour répondre à l'intermittence de l'énergie solaire. L'hydrogène peut être produit par électrolyse, en scindant des molécules d'eau en hydrogène et oxygène sous l'effet d'un courant électrique. Diverses méthodes comme l'électrolyse à membrane échangeuse de protons (PEM) peuvent être couplées à des systèmes de conversion d'énergie solaire afin de produire de l'hydrogène décarboné. Ces technologies en sont encore à leur balbutiement, c'est pourquoi leur évaluation est une question clé pour les enjeux énergétiques du futur.

Le travail de recherche présenté dans cette thèse concerne le développement d'une cellule photoélectrochimique à membrane échangeuse de protons (PEM-PEC) dans le but de produire de l'hydrogène à partir d'air humide et d'énergie solaire. Un nouveau support poreux d'électrode alliant transparence et conduction électrique a été développé. L'utilisation de ce nouveau support transparent poreux conducteur (TPCS) pour photoélectrode a été démontré en déposant un semi-conducteur de type n (hématite,  $\alpha\text{-Fe}_2\text{O}_3$ ) pour produire de l'oxygène par photolyse de l'eau. L'électrode TPCS-hématite a abouti à un photocurrent maximum de  $1.6 \text{ mA.cm}^{-2}$  à  $1.6 \text{ V vs. RHE}$  (réversible hydrogène électrode). Au préalable de l'utilisation de différentes couches semi-conductrices de type p sur les TPCS, leur déposition a été étudiée sur des verres conducteurs plats. Des nanoflocons diséléniure de tungstène ( $\text{WSe}_2$ ) produits par exfoliation ont été appliqués par dépôt électrophorétique. De plus, une conversion électrochimique *in-situ* d'oxyde de cuivre ( $\text{Cu}_2\text{O}$ ) a été identifiée, permettant de produire des couches fines et transparentes. Par la suite, les couches de semi-conducteurs de type p ( $\text{WSe}_2$ ,  $\text{Cu}_2\text{O}$ , semi-conducteurs organiques) ont été déposées sur les TPCSs et leur photoactivité en milieu aqueux a été évaluée. Le choix s'est porté sur le semi-conducteur organique due à la facilité de le mettre en œuvre et aux résultats prometteurs obtenus pour la photoréduction de l'euporium en phase liquide (ca.  $-4.5 \text{ mA.cm}^{-2}$  at  $0 \text{ V vs. RHE}$ ). Enfin, après déposition d'un catalyseur de platine, la photoélectrode à base de semi-conducteur organique a été testée pour la production d'hydrogène en phase liquide, démontrant un photocourant de ca.  $-1 \text{ mA.cm}^{-2}$  at  $0 \text{ V vs. RHE}$ . Après intégration dans une cellule PEM-PEC pour la production d'hydrogène en phase gazeuse, un courant de  $-120 \text{ }\mu\text{A.cm}^{-2}$  at  $0 \text{ V vs. RHE}$  a pu être mesuré (correspondant à une production d'hydrogène de  $1 \text{ }\mu\text{mol.h}^{-1}$ ) durant une heure.

## **Mots-clés**

Membrane à échangeuse de protons, photoélectrochimique, production d'hydrogène, support transparent poreux conducteur, hématite, diséléniure de tungstène, oxyde de cuivre, semi-conducteur organique.

# Contents

<b>Acknowledgements.....</b>	<b>v</b>
<b>Abstract .....</b>	<b>vii</b>
<b>Résumé.....</b>	<b>viii</b>
<b>Contents .....</b>	<b>ix</b>
<b>List of Figures and Tables.....</b>	<b>xiii</b>
<b>List of abbreviations and symbols.....</b>	<b>xvii</b>
<b>Chapter 1      The Energy challenge .....</b>	<b>1</b>
1.1    Hydrogen, a promising energy carrier .....	2
1.2    Electrolysis technologies .....	5
1.2.1 Alkaline electrolyzers (AE) .....	5
1.2.2 Proton-exchange membranes (PEM) electrolyzers.....	6
1.2.3 Anion-exchange membrane (AEM) electrolyzers.....	7
1.2.4 Solid oxide electrolyzers (SOEC) .....	8
1.3    Solar-assisted hydrogen production .....	9
1.3.1 Photovoltaic-electrolyzer (PV-EC).....	11
1.3.2 Photoelectrochemistry (PEC) systems.....	11
1.3.3 Photocatalyst (PC) systems.....	14
1.3.4 Photocatalytic materials .....	15
1.4    PEM-PEC systems: motivation and objectives .....	18
1.4.1 PEM-PEC cells early research.....	18
1.4.2 The PEM-PEC cell: general motivation .....	19
1.4.3 PEM-PEC photocathode engineering .....	21
<b>Chapter 2      A novel Transparent Porous Conductive Substrate for photoelectrode application .....</b>	<b>23</b>
2.1    State of the art .....	24
2.2    TPCS as a new photoelectrode template.....	25
2.2.1 TPCS fabrication.....	25
2.2.2 Thickness effect .....	27
2.2.3 Annealing temperature effect .....	28
2.2.4 FTO deposition study.....	29

2.3	Comparison between conductive substrates .....	31
2.4	TPCS as photoelectrode support: hematite model.....	31
2.5	Conclusion .....	35
2.6	Experimental part.....	35
2.6.1	Chemicals .....	35
2.6.2	TPS preparation .....	35
2.6.3	FTO deposition.....	36
2.6.4	Hematite model.....	36
2.6.5	Characterizations .....	36
<b>Chapter 3</b>	<b>Transparency and morphology control of Cu<sub>2</sub>O photocathodes via an <i>in-situ</i> electro-conversion.....</b>	<b>38</b>
3.1	Cu <sub>2</sub> O photocathode progress and challenges.....	39
3.2	Potential drop identification .....	39
3.3	Parameters identification .....	43
3.4	Electro-conversion study.....	45
3.5	Photoelectrochemical test .....	47
3.6	Conclusion .....	48
3.7	Experimental methods.....	49
3.7.1	Chemicals.....	49
3.7.2	CuSCN deposition .....	49
3.7.3	Cu <sub>2</sub> O deposition .....	49
3.7.4	Material characterization .....	50
3.7.5	Photoelectrochemical characterization .....	50
<b>Chapter 4</b>	<b>WSe<sub>2</sub> processing conditions evaluation for nanostructured photocathode</b>	<b>51</b>
4.1	WSe <sub>2</sub> , a promising semiconductor photocathode .....	52
4.2	Effort to implement WSe <sub>2</sub> nanoflakes photocathodes.....	53
4.3	Nanoflake suspension characterizations .....	56
4.3.1	Solvent degradation during exfoliation .....	56
4.3.2	Exfoliation media investigation .....	57
4.4	Electrophoretic deposition for WSe <sub>2</sub> photocathode fabrication.....	59
4.5	Conclusion .....	62



4.6	Experimental methods.....	62
4.6.1	WSe <sub>2</sub> electrode fabrication.....	62
4.6.2	WSe <sub>2</sub> nanomaterial characterizations .....	63
<b>Chapter 5</b>	<b>Developing photocathode coatings on TPCS .....</b>	<b>66</b>
5.1	Semiconductor coatings for photoelectrodes application .....	67
5.2	WSe <sub>2</sub> -coated TPCS.....	68
5.3	Cu <sub>2</sub> O-coated TPCS .....	71
5.4	Bulk heterojunction-coated TPCS .....	74
5.4.1	CuSCN : Hole transporting layer .....	74
5.4.2	BHJ Performance optimization .....	79
5.4.3	Stability and further investigations .....	82
5.5	Conclusion .....	84
5.6	Experimental method .....	86
5.6.1	WSe <sub>2</sub> .....	86
5.6.2	Cu <sub>2</sub> O .....	87
5.6.3	Bulk heterojunction .....	88
<b>Chapter 6</b>	<b>Engineering bulk heterojunction photocathode for gas phase water splitting</b>	<b>90</b>
6.1	BHJ photoelectrode for water reduction in the gas phase.....	91
6.2	Photocathode for HER in liquid phase .....	91
6.3	Development of the half PEM-PEC cell .....	95
6.4	Photocathode for PEM-PEC operation.....	97
6.5	Conclusion .....	99
6.6	Experimental part.....	100
6.6.1	Electrode fabrication .....	100
6.6.2	PEC characterizations .....	101
6.6.3	PEM-PEC electrolysis .....	101
6.6.4	Material characterizations.....	102
<b>Chapter 7</b>	<b>Conclusion and outlook.....</b>	<b>103</b>
7.1	Transparent Porous Conductive Substrate .....	103
7.2	Material coating onto the TPCS for PEC application.....	104

7.3 BHJ-photocathode for PEM-PEC application .....	105
<b>Appendix 2.....</b>	<b>107</b>
<b>Appendix 3.....</b>	<b>115</b>
<b>Appendix 4.....</b>	<b>121</b>
<b>Appendix 5.....</b>	<b>128</b>
<b>Appendix 6.....</b>	<b>136</b>
<b>References .....</b>	<b>140</b>
<b>Curriculum vitae.....</b>	<b>158</b>

# List of Figures and Tables

<b>Figure 1.1.</b> Global fossil CO <sub>2</sub> emission extracted from The Global Carbon Project <sup>2</sup> 2021. ....	2
<b>Figure 1.2.</b> (a) Evolution of energy use by source (b) Evolution of CO <sub>2</sub> emissions by source extracted from The Global Carbon project <sup>2</sup> 2021.....	3
<b>Figure 1.3.</b> Global proved fossil fuel resources for (a) Coal, (b) Gas, (c) Oil, reserves-to-production ratio. Extracted from ref <sup>3</sup> . ....	3
<b>Figure 1.4.</b> Comparison of electrolysis technologies (a) Schematic of PEM, AEM, A, SO electrolyzers (b) Areas of current densities and cell potential for each technologies, modified and adapted from ref <sup>13</sup> . 5	5
<b>Figure 1.5.</b> Schematic of a PEM electrolyzer, extracted from ref <sup>11</sup> .....	6
<b>Figure 1.6.</b> (a) 2009 estimate of finite and renewable planetary energy reserves (Terawatt-years). Total recoverable reserves are shown for the finite resources. Yearly potential is shown for renewable. Extracted from ref <sup>23,24</sup> (b) Semiconductor band diagram (E <sub>g</sub> stands for band gap) (c) AM1.5 solar spectrum with distinct dips due to molecular absorption in Earth's atmosphere (E <sub>g</sub> , dashed black line corresponds to the band gap of Si). Extracted from ref <sup>25</sup> . ....	9
<b>Figure 1.7.</b> Solar energy conversion technologies a-c, (a) Schematic of particulate photocatalysis (b) photoelectrochemical water splitting, (c) PV-electrolysis (d) Technological map showing various photon-driven water splitting approaches for solar energy conversion and specific experimental demonstrations. (a-c) extracted from ref <sup>31</sup> (d) extracted from ref <sup>24</sup> .....	10
<b>Figure 1.8.</b> Schematic of PEC cells configuration (a) single light absorber (b) dual light absorber side by side (c) dual light absorber-stacked. Extracted from Ref <sup>24</sup> . ....	12
<b>Figure 1.9.</b> (a) Schematic of a PEC tandem cell and different processes ref <sup>33</sup> . ....	13
<b>Figure 1.10.</b> (a-b) Single photoelectrode case (a) schematic of a three-electrode setup used for single photoelectrode testing (b) Typical LSV curves obtained for Cu <sub>2</sub> O photocathodes under chopped illumination (c-f) tandem cell case (c) schematic of a tandem cell setup (d) schematic of an actual BiVO <sub>4</sub> /Cu <sub>2</sub> O tandem cell (e) Typical characteristic of a tandem cell (f) characteristic of a BiVO <sub>4</sub> /Cu <sub>2</sub> O tandem cell. The figures (a,c), (e), and (b,d,f) are extracted from ref <sup>33</sup> , ref <sup>24</sup> , and ref <sup>47</sup> , respectively... 14	14
<b>Figure 1.11.</b> (a) Schematic of the phenomena occurring during PC (b) band diagram for photocatalyst overall water splitting, extracted from ref <sup>48</sup> . ....	14
<b>Figure 1.12.</b> (a) PEM-PEC experimental configuration used for evaluating the photoanodes with a standard hydrogen reference electrode with the capability to operate under a humidified air (b) SEM features of W:BiVO <sub>4</sub> deposited on the Ti-felt (c) Schematic of MEA with BiVO <sub>4</sub> photoanodes, PEM and Pt/C cathode (d) LSV curves of functionalized W:BiVO <sub>4</sub> under chopped light illumination at various RH. Extracted from ref <sup>105</sup> . ....	19
<b>Figure 1.13.</b> Envisioned tandem device for photoelectrochemical water splitting (FTO: Fluorine-doped tin oxide and HTL: Hole Transporting Layer).....	20
<b>Figure 2.1.</b> Illustration of TPCS process (a) schematic of the TPCS procedure (b-e) SEM image of a TPCS, (b-d) top view, (e) cross-sectional image and zoom on a fiber cross section. ....	26
<b>Figure 2.2.</b> TPS thickness tuning from 15 mg, 30 mg and 50 mg (a) Thickness variation (b) Transmittance measured over a range 300 - 800 nm for TPS and TPCS (dashed line) (c) Reflectance measured over a range 300 - 800 nm for TPS. ....	28

<b>Figure 2.3.</b> Comparison annealing temperature (a) sheet resistance average (b) stress-strain curve from bi-axial flexure test, showing the failure point (red circle) (c-d) SEM images top view and cross sectional for TPCS 1350 °C (e-f) SEM images top view and cross sectional for TPCS 1250 °C. ....	29
<b>Figure 2.4</b> (a) Photograph of samples, flat borosilicate glass, commercial FTO glass reference, flat glass substrate, and TPCS deposited with different amount of TFA in the mixture water/FTA (v/v), (0, 1/10, 1/2) (b) XRD diffractograms of deposition on flat glass substrate and FTO glass commercial reference (c) Direct transmittance measurement for flat substrate (d) Direct transmittance measurement for TPCS. ....	30
<b>Figure 2.5.</b> Figure Conductive support comparison between commercial FTO glass, TPS (4 mg.cm <sup>-2</sup> ), TPCS (4 mg.cm <sup>-2</sup> ) and Ti felt (a) photograph (b) Transmittance and total reflectance measurement (c) stress-strain curve from bi-axial flexure test.....	31
<b>Figure 2.6.</b> (a) photograph of hematite samples on TPCS and FTO glass (b) SEM image of hematite-coated TPCS (c) Raman spectra of the hematite film (d) LSV curves obtained in NaOH pH 13.6 under 1 sun illumination. ....	33
<b>Figure 2.7.</b> (a-b) SEM image of hematite-coated TPCS (thin version) (c) Raman spectra of the thin hematite film (d) LSV curves obtained in NaOH pH 13.6 under 1 sun illumination and photograph of the thin hematite-coated TPCS. ....	34
<b>Figure 3.1.</b> SEM images (top view, left, and cross-section, right) of CuSCN films deposited at -0.3V vs. Ag/AgCl for various times (a) 2 min (b) 5 min (c) 10 min. ....	40
<b>Figure 3.2.</b> Photograph (left, substrate width 12 mm) and XRD pattern of 5 min-electrodeposited CuSCN film. ....	41
<b>Figure 3.3.</b> (a) Potential evolution during Cu <sub>2</sub> O electrodeposition by chronopotentiometry at -0.1 mA cm <sup>-2</sup> on bare FTO, and FTO/CuSCN substrates with different thicknesses of CuSCN. SEM images (top-view and cross section) are shown in the insets for the FTO/CuSCN (570 nm) substrate at various times during the electrodeposition (0, 42, and 100 min) and the corresponding points on the chronopotentiometry curve are indicated. (b) XRD patterns of 570 nm CuSCN film during in-situ electro-conversion at time = 0 min, 42 min and 100 min.....	41
<b>Figure 3.4.</b> XPS spectra of Cu <sub>2</sub> O thin film prepared from converting a CuSCN film (deposited with a charge of 120 mC cm <sup>-2</sup> ) “Cu <sub>2</sub> O_C” compared to the original CuSCN substrate (a) for S2p spectra (b), N 1s spectra (c), Cu 2p spectra (d) Cu Auger LMM.....	43
<b>Figure 3.5.</b> (a) Schematic of the possible routes to make Cu <sub>2</sub> O by direct Cu <sub>2</sub> O electrodeposition (Cu <sub>2</sub> O-D) and by CuSCN electrodeposition followed by in-situ electro-conversion to Cu <sub>2</sub> O (Cu <sub>2</sub> O-C), (b-g) SEM images of (b-d) Cu <sub>2</sub> O_D direct deposition (e-g) Cu <sub>2</sub> O_C converted film. ....	46
<b>Figure 3.6.</b> Characterization of thick Cu <sub>2</sub> O films obtained by direct deposition (Cu <sub>2</sub> O_D) and by the in-situ electro-conversion (Cu <sub>2</sub> O_C): (a) Raman spectra (inset) photograph of the electrodes (b) XRD spectra (c) UV-visible total absorptance and direct transmittance spectra.....	47
<b>Figure 3.7.</b> (a) Linear scanning voltammetry of Cu <sub>2</sub> O-based photocathodes for H <sub>2</sub> production under intermittent simulated solar illumination (1 sun) LSV at pH 5 for HER. (b) IPCE spectra of the Cu <sub>2</sub> O photocathodes at 0V vs. RHE at pH 5 are shown next to the standard solar spectrum (green) and the simulator solar spectrum produced by the light source used during the LSV tests (blue).....	47
<b>Figure 4.1.</b> Crystallographic structure of 2H phase TMDs extracted from ref <sup>151</sup> . ....	52
<b>Figure 4.2.</b> Electronic structure of various TMDs to be compared with the water splitting potential required, extracted from ref <sup>153</sup> .....	53

<b>Figure 4.3</b> WSe <sub>2</sub> film characterizations (a) photograph (b) cross sectional SEM image (c) TEM image (d) UV-visible spectrum, comparison between two sample having different PEC performances (e) LSV curves under intermittent illumination (1 Sun) in sacrificial chloranil saturated solution in acetonitrile (MeCN).....	55
<b>Figure 4.4.</b> (a) Photograph of NMP without WSe <sub>2</sub> , bare, after 2h sonication, after 4 hours sonication (b) WSe <sub>2</sub> suspension after 12 hours exfoliation, flakes aggregated together (c) WSe <sub>2</sub> suspension after 12 hours exfoliation, flake separation succeeded (d) PL measurement of pristine NMP, NMP solvent sonicated for 4 hours, yellow supernatant from sample a, brown supernatant from sample b, with $\lambda_{\text{excitation}} = 325 \text{ nm}$ .....	57
<b>Figure 4.5.</b> Picture (a) NMP supernatant for different sonication media with O <sub>2</sub> bubbling, in air, with Ar bubbling and addition of 1%v/v of H <sub>2</sub> O, with Ar bubbling (b) LSV curves under intermittent illumination (1 Sun) in sacrificial chloranil saturated solution in MeCN (C) SEM image of a LLISA deposited film after 2 hours exfoliation. ....	58
<b>Figure 4.6.</b> Schematic of the EPD set-up. ....	60
<b>Figure 4.7.</b> (a) Photograph of EDP-deposited WSe <sub>2</sub> photocathode under operation (b) LSV curve under intermittent light (1 Sun) in H <sub>2</sub> SO <sub>4</sub> adjusted at pH 1 (c-d) SEM pictures. ....	61
<b>Figure 4.8.</b> (a) SEM cross sectional of EPD-WSe <sub>2</sub> film, highlight on the nanoflakes detachment (b) LSV curve under intermittent light (1 sun) in H <sub>2</sub> SO <sub>4</sub> adjusted at pH 1 after 4 scans. ....	61
<b>Figure 5.1</b> (a) Schematic of EPD set-up (b) LSV curve of WSe <sub>2</sub> -Pt coated TPCS at pH 1 under 1 sun illumination (c) SEM picture of WSe <sub>2</sub> -Pt coated TPCS, the red square shows the fully covered fibers and the blue square shows the uncoated fibers. ....	70
<b>Figure 5.2.</b> (a,b) SEM images and photograph of a CuSCN-coated TPCS (10min deposition) (c) SEM image of bare TPCS showing FTO grains (d) SEM image of CuSCN(10min)-coated TPCS showing CuSCN nanorods. ....	71
<b>Figure 5.3.</b> SEM images of CuSCN-coated TPCSs (3 cm <sup>2</sup> ) for different electrodeposition time (a,d) 2 min, (b,e) 5 min, (c,f) 10 min.....	72
<b>Figure 5.4.</b> SEM pictures of Cu <sub>2</sub> O-coated (50 min at -0.2 mA.cm <sup>-2</sup> ) TPCSs on (a-c) bare TPCS (d-f) 5 min CuSCN-coated TPCS. ....	73
<b>Figure 5.5.</b> LSV curves of Cu <sub>2</sub> O-coated TPCS in liquid electrolyte at pH 5 under chopped (1 Sun) illumination and photograph of the sample after LSV testing (a) for TPCS, pre-deposited CuSCN (5 min), Cu <sub>2</sub> O (50 min at -0.2mA.cm <sup>-2</sup> ) and Ga <sub>2</sub> O <sub>3</sub> /TiO <sub>2</sub> (ALD) (b) for TPCS-bare, Cu <sub>2</sub> O (50 min at -0.2mA.cm <sup>-2</sup> ) and Ga <sub>2</sub> O <sub>3</sub> /TiO <sub>2</sub> (ALD).....	74
<b>Figure 5.6.</b> Band diagram for the BHJ systems studied.....	75
<b>Figure 5.7.</b> Characterizations of flat FTO-CuSCN(30 s)-PTB7-BHJ (a) polymers and small molecule chemical structure (b) LSV curves tested in Eu <sup>3+</sup> (1 M) at pH 2 under chopped (1 Sun) (c) illumination UV-visible absorbance spectra.....	76
<b>Figure 5.8.</b> (a) photograph of a TPCS samples coated with CuSCN-600mC and BHJ (PTB7-Th:PCBM, 1:1) 4mg.mL <sup>-1</sup> in chloroform (b) SEM images (c) LSV curve in Eu <sup>3+</sup> 1.2M under (1 sun) intermittent illumination. ....	77
<b>Figure 5.9.</b> (a) Bright light microscope image of a TPCS-CuSCN-BHJ immersed confocal microscope image of (b) TPCS-CuSCN-BHJ immersed and (c) TPCS-CuSCN-BHJ drop-casted (for PL images, laser excitation: 640 nm and emission: from 800nm).....	77
<b>Figure 5.10.</b> SEM pictures of CuSCN-coated TPCS (a,b) with stirring (c,d) without stirring coated with BHJ (e,f) with stirring coated with BHJ (g,h) without stirring coated with BHJ. ....	78

<b>Figure 5.11.</b> SEM pictures of TPCS-CuSCN-BHJ processed (a,c) with Toluene (b,d) with chlorobenzene, (e,f) PEC performance in sacrificial electrolyte $\text{Eu}^{3+}$ 1.2M. ....	80
<b>Figure 5.12.</b> PEC performance in sacrificial electrolyte $\text{Eu}^{3+}$ 1.2M for electrode made with different BHJ concentration (a) $2 \text{ mg.mL}^{-1}$ (b) $10 \text{ mg.mL}^{-1}$ (c) $16 \text{ mg.mL}^{-1}$ .....	81
<b>Figure 5.13.</b> (a) absorption spectra of solutions (PTB7:PCBM, 1:1.5) for different concentration (b) resulting calibration curve (c) photograph of the solution resulting from the BHJ dissolution on TPCSs (d) Absorption spectra of the solution. ....	81
<b>Figure 5.14.</b> Characterization of a device TPCS-CuSCN-BHJ (a) Photograph of the device (b) Top view and cross sectional SEM features (c) LSV curve in sacrificial $\text{Eu}^{3+}$ at pH 2 under (1 Sun) chopped illumination (d) CA at 0 V vs. RHE in sacrificial $\text{Eu}^{3+}$ at pH 2 under (1 Sun) illumination.....	83
<b>Figure 5.15.</b> LSV curve a TPCS-CuSCN-PBDTTTPD:PNDI(2HD)T sample in $\text{Eu}^{3+}$ 1.2M under chopped (1 sun) light illumination. ....	84
<b>Figure 6.1.</b> (a) Schematic of a TPCS-BHJ photocathode (b) Chemical structure of the donor polymer and small molecule acceptor (c) The energy levels of the photocathode components including FTO, CuSCN, PTB7-Th, and PCBM are shown versus vacuum energy or volts vs. the reversible hydrogen electrode (V RHE). ....	92
<b>Figure 6.2.</b> TPSC-CuSCN-BHJ-Pt(photoelectrodeposited) characterizations (a-b) SEM images of the electrode after Pt photoelectrodeposition (c-d) LSV curves in $\text{H}_2\text{SO}_4$ at pH 1 under (1 Sun) chopped illumination for (e) back side (f) front side. ....	93
<b>Figure 6.3.</b> (a-d) SEM features of a TPCS-CuSCN-BHJ-Pt after HER test, (e-f) LSV curves in $\text{H}_2\text{SO}_4$ at pH 1 under (1 Sun) chopped illumination for (e) front side (f) back side. ....	94
<b>Figure 6.4.</b> TPCS-CuSCN-BHJ-Pt long term stability characterizations (a) Photograph of the device during operation (b-c) CA at 0V vs. RHE in curves in $\text{H}_2\text{SO}_4$ at pH 1 under (1 Sun) illumination. ....	95
<b>Figure 6.5.</b> Schematic of the half gas cell. ....	95
<b>Figure 6.6.</b> (a) SEM feature of a fiber from a platinized TPCS (b-d) characterizations of the platinized TPCS cathode in liquid (pH 1) and gas phase with humidified Argon ( $20 \text{ mL.min}^{-1}$ ) (b) LSV curves (c) Photograph during the liquid phase testing (d) chronopotentiometry (CP) at $-1 \text{ mA.cm}^{-2}$ . ....	96
<b>Figure 6.7.</b> Illustration of the half PEM-PEC cell and photocathode composition.....	97
<b>Figure 6.8.</b> TPCS-CuSCN-BHJ-Pt characterizations (a) LSV curve in $\text{H}_2\text{SO}_4$ at pH 1 under (1 Sun) chopped illumination (b) Successive LSV curves in the gas phase at $20 \text{ mL.min}^{-1}$ humidified argon under (1 Sun) chopped illumination (c) CA at 0 V vs. RHE in the gas phase following the successive LSVs. ....	98
<b>Figure 6.9.</b> CA at 0 V vs. RHE and $\text{H}_2$ production rate extracted from GC measurement for an electrode TPCS-CuSCN-BHJ-Pt tested in the half gas cell.....	98

## List of tables

<b>Table 1.</b> PEM components, major functions and materials, adapted from ref <sup>10</sup> . ....	7
<b>Table 2.</b> Comparison of the main characteristics of low-temperature electrolysis technologies (AL, PEM, AEM) adapted from ref <sup>14</sup> . ....	8
<b>Table 3.</b> Characteristics of typical commercial porous conductive substrates. ....	21

## List of abbreviations and symbols

NO <sub>x</sub>	Nitrogen oxide
SO <sub>x</sub>	Sulphur oxide
HER	Hydrogen evolution reaction
OER	Oxygen evolution reaction
GDL	Gas Diffusion Layer
MEA	Membrane electrode assembly
PEM	Proton-Exchange membrane
AEM	Anion-Exchange membrane
SOEC	Solid oxide electrolysis
AE	Alkaline electrolysis
PEC	Photoelectrochemical
PC	Photocatalysis
PV-EC	Photovoltaic-electrolyzer
GHG	Green-house gas
RHE	Reversible hydrogen electrode
NHE	Normal hydrogen electrode
E <sub>g</sub>	Band gap
E <sub>vb</sub>	Valence band maxima
J <sub>ph</sub>	Photocurrent
NMP	N-Methyl-2-pyrrolidone
FTO	Fluorine-doped tin oxide
SEM	Scanning electron microscopy
HTL	Hole transporting layer
BHJ	Bulk heterojunction
TPS	Transparent porous substrate
TPCS	Transparent porous conductive substrate
APCVD	Atmospheric pressure chemical vapour deposition
MBTC	Monobutyltin trichloride
TFA	Trifluoroacetic acid
XRD	X-ray diffraction
BET	Brunauer-Emmett-Teller
CBD	Chemical bath deposition
ETA	Extremely thin absorber
ALD	Atomic layer deposition
AA-CVD	Aerosol assisted chemical vapor deposition
LSV	Linear scan voltammetry
IPCE	Incident photon-to-current efficiency
ETL	Electron transport layer
XPS	X-ray photoelectron spectroscopy
EDX	Energy-dispersive X-ray
IPA	Isopropanol
DI	Deionized
EPD	Electrophoretic deposition
TMD	Transition metal dichalcogenide

AFM	Atomic force microscopy
LLISA	Liquid-liquid self-assembly
PL	Photoluminescence
POM	Polyoxometalate
DLS	Dynamic light scattering
TEM	Transmission electron microscopy
OS	Organic semiconductor
GC	Gas chromatography
FE	Faradic efficiency
CA	Chronoamperometry
CP	Chronopotentiometry



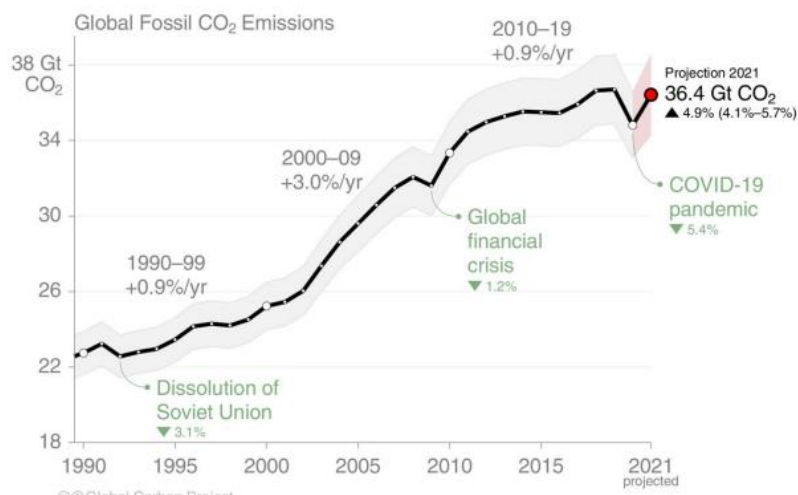
# Chapter 1     The Energy challenge

The Energy challenge is undoubtedly one of the top world priorities. Indeed, our energy system needs to be redesigned to mitigate the impact of the intensive use of fossil fuels on the climate as well as dealing with resources depletion. Global warming will need to be controlled, one way to do that could be using a source of energy with a minimum of greenhouses gas (GHG) emission. Among all the possibilities, solar energy is a promising solution. A total of 173,000 terawatts (trillions of watts) of solar energy strikes the Earth continuously, thus more than 10 000 times the world annual consumption<sup>1</sup>. Nevertheless, the intermittency remains a bottleneck for solar energy usage. Hydrogen appears to be a perfect energy carrier as its production through water electrolysis can be coupled with solar energy conversion. Several electrolysis technologies powered by electricity exist such as alkaline electrolysis (AE), proton-exchange membrane electrolysis (PEM), anion-exchange membrane electrolysis (AEM) and solid oxide electrolysis (SOEC). Solar energy can be utilized to produce hydrogen in a photovoltaic-electrolyzer system (PV-EC). Other technologies are under investigation such as photoelectrochemical (PEC) water splitting or photocatalyst system. Recently, the idea to combine an existing PEM electrolyzer system and a PEC cell has emerged with the goal to produce hydrogen using humid air and solar energy.

## 1.1 Hydrogen, a promising energy carrier

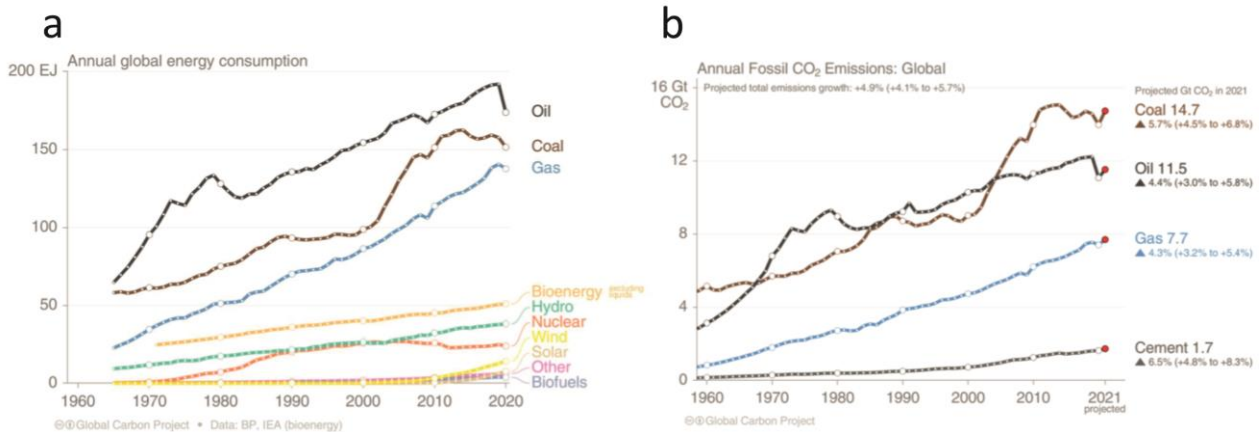
For a decade, dealing with climate change has not been an option but a real obligation if we want to ensure the prosperity of our planet, as well as the next generation. Indeed, according to the last report<sup>2</sup> of the Intergovernmental Panel on Climate Change (IPCC), the emissions of greenhouse gases (GHG) from human activities are responsible for approximately +1.1°C of warming since 1850. The report finds that the global temperature is expected to reach or exceed +1.5°C, due to intensive industrialization and agriculture. To respect the Paris agreement (COP 21) signed by 196 parties in 2015, global warming must be limited to +2.0°C above pre-industrial levels and ideally, efforts must be pursued to limit the temperature increase to +1.5°C.

For more than 100 years, innovation never ceased to develop in every field from medicine to transportation and communication. However, innovation and economic development come with its own set of hurdles. Looking closely at the energy sector, it is obvious that the non-renewable energy resources have participated in the development of a myriad of sectors. Chemistry, medicine, agriculture, transportation, construction, and telecommunication are part of a non-exhaustive list of the areas of application depending on energy. Our current energy system relies on fossil fuels, participating in global warming due to GHG emissions. According to The Global Carbon Project, an international research consortium dedicated to tracking the world's GHG emissions, CO<sub>2</sub> emissions cuts of 1.4 billion tones are needed each year on average to reach net zero emissions by 2050<sup>3</sup>. After a drop in 2020, due to the pandemic situation, global CO<sub>2</sub> emissions are set to rebound to their 2019 levels with a projected growth of 4.9% (i.e., 36.4 Gt of CO<sub>2</sub> as seen in **Figure 1.1**). Therefore, replacing fossil fuels by renewable energy resources is critical to limit climate change.



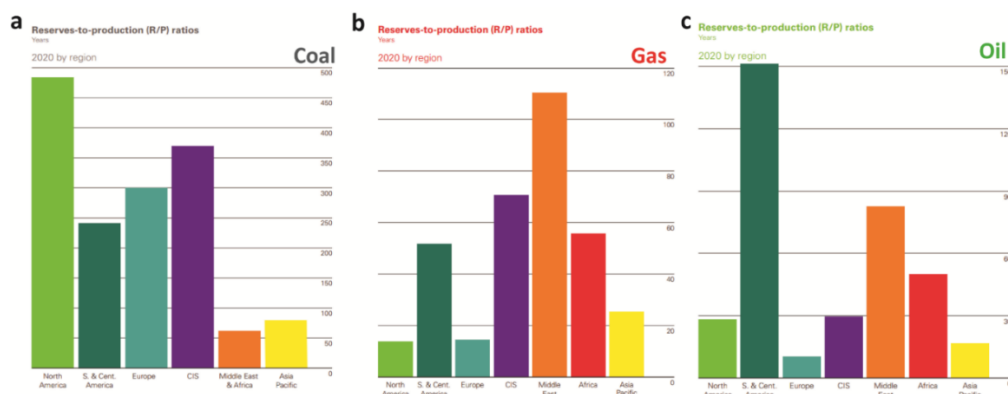
**Figure 1.1.** Global fossil CO<sub>2</sub> emission extracted from The Global Carbon Project<sup>3</sup> 2021.

For decades, the energy demand grew rapidly and unfortunately the energy resources came essentially from fossil fuels (**Figure 1.2a**). Fossil fuels are mostly responsible for global CO<sub>2</sub> emissions, representing 40% for coal, 32% for oil and 21% for gas (**Figure 1.2b**). However, after a rising period of more than 100 years, humanity will have to face the issues related to the use of fossil fuels.



**Figure 1.2.** (a) Evolution of energy use by source (b) Evolution of CO<sub>2</sub> emissions by source extracted from The Global Carbon project<sup>3</sup> 2021.

To begin with, fossil fuels require geological processes of millions of years to be produced. That is the reason why they are not infinite. The global reserves-to-production ratio for 2020, thus the length of time that those remaining reserves would last if the production would continue at that rate, represents 50 years for oil, 48.8 years for natural gas, and 139 years for coal (**Figure 1.3**). These values do not consider the world energy consumption increase and the variability of resources discovery. We must realize that our societies are more and more energy consuming, due to population growth and to our modern lifestyle. The second concern is about the consequences resulting from the intensive use of fossil fuels. Using combustion of fossil fuels induces GHG emissions in the atmosphere. The GHG such as CO<sub>2</sub>, nitrogen oxides (NO<sub>x</sub>), methane (CH<sub>4</sub>), ozone (O<sub>3</sub>) induce the so-called greenhouse effect. Therefore, the climate will be drastically modified, causing multiples issues for the flora, the fauna, and the entire humanity. Scientists consider that the increase of the global warming should be maintained to +2.0 °C by 2050 to avoid massive extinction and large climate disorder. For doing so, companies, governments and individuals need to work together.



**Figure 1.3.** Global proved fossil fuel resources for (a) Coal, (b) Gas, (c) Oil, reserves-to-production ratio. Extracted from ref<sup>4</sup>.

This major issue will not be resolved by a unique method but rather by combining multimodal efforts on the long-term. Even though the renewable energy sector continues to grow (**Figure 1.2a**), its rate

needs to increase faster in order to replace fossil fuel, limit climate change and its inherent consequences. Wind and solar energy could provide enough energy to answer the world demand. However, we might need to redesign our energy system due to the intermittency of these resources. One way to address this issue is to convert the energy harvested to chemical fuel.

Since a few years, hydrogen has been identified as a net-zero carbon energy carrier for answering the worldwide energy demand while decreasing our impact on the environment.<sup>5</sup> At standard conditions (0 °C, 1013 kPa), hydrogen is a colorless and odorless gas. It is the lightest element on Earth, thereby 1 L of hydrogen weighs 90 mg at normal temperature and pressure conditions.<sup>6</sup> Hydrogen is also the most abundant element representing 90% of all atoms in the universe.<sup>7</sup> For instance, our sun is composed of 73% of hydrogen atoms, and  $627.10^6$  kg of  $H_2/s$  undergo a fusion reaction, producing helium and an enormous amount of energy.<sup>8</sup> We can also find hydrogen in the gaseous planets of our solar system (Jupiter, Saturn, Uranus and Neptune). Unfortunately, these resources remain unreachable for us. On Earth, hydrogen is barely present in our atmosphere (0.00005%) due to the low Earth gravitational field.<sup>9</sup> However, it is combined with other elements and is found in all organic molecules such water and hydrocarbons.

In 1766, Henry Cavendish, a British physicist, discovered the formation of inflammable gas while mixing metals and strong acids.<sup>6</sup> Later, in 1783, the French chemist Lavoisier named this gas hydrogen from Greek *hydro* and *genes* meaning “water-former”. In 1838, the German chemist Schönbein discovered the fuel cell effect and was able to produce electricity and water from hydrogen and oxygen.<sup>6</sup> Sir William Grove then built the first fuel cell prototype a few years after.<sup>6</sup> Finally, in 1898, Dewar successfully liquefied hydrogen by cooling it down to -252.87 °C and George Claude improved the liquefaction process.<sup>6</sup>

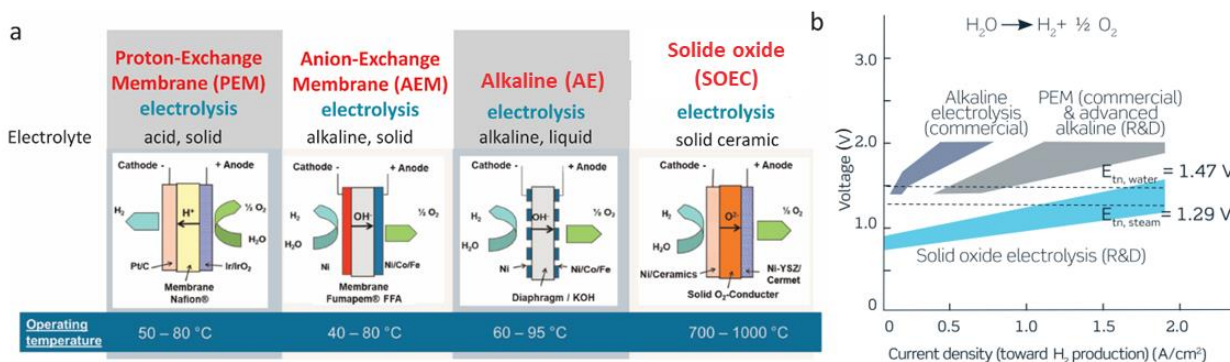
Hydrogen has a large gravimetric energy density and its combustion can liberate  $286 \text{ kJ.mol}^{-1}$ , which make it an ideal candidate for storing and transporting energy.<sup>10</sup> 3 kg of  $H_2$  correspond to 100 kWh of chemical energy, whereas a 450 kg lithium ion battery is needed to produce the same quantity of electrical energy. Thus,  $H_2$  is a powerful energy carrier containing  $39.4 \text{ kWh.kg}^{-1}$  at its upper heating value, corresponding to hydrogen combustion. Hydrogen can also power fuel cells to produce electricity with water as the only by-product. Moreover, the storage of energy into chemical bonds, such as  $H_2$ , a key chemical commodity, opens a new paradigm for the industrial sector, in particular pharmaceuticals or fertilizers. Except from the mobility point of view, hydrogen could also be a key input into a range of industrial applications such as ammonia and chemicals production, glass manufacturing, metal processing, synthetic fuel production and food industry. Hydrogen could be the energy of the future if we tackle major challenges such as production based on low emission electricity power and fuel cell performance (hydrogen-to-electricity). The hydrogen method of production must rely on renewable energy resources to ensure minimum GHG emissions. In addition, in order to be economical viable, the performance of fuel cells needs to be improved, the conversion bottleneck<sup>11</sup> remains at  $\approx 60\%$ .

## 1.2 Electrolysis technologies

Nowadays, hydrogen is produced through steam reforming due to its low production cost (1.3-1.5 \$/kg)<sup>12</sup>. This process however emits a large amount of CO<sub>2</sub>. Each year 110 Mt of hydrogen are produced: 95% from fossil fuel reforming and only 4% from electrolysis<sup>12</sup>. Fossil fuel reforming does not have any advantages compared to utilizing fossil fuel directly except if it is associated with a CO<sub>2</sub> capture system. Hydrogen can also be produced through water splitting using electrolysis, by applying an electric potential to break water molecules into hydrogen and oxygen. In general, water splitting process is described as follow:



The Gibbs free energy of water dissociation (237.1 kJ.mol<sup>-1</sup>) corresponds to a potential of 1.23 V per electron at standard conditions according to the Nernst equation<sup>13</sup>. The availability of water and the low value of the Gibbs free energy render electrolysis a high-potential solution for hydrogen production. Different types of electrolysis technologies exist such as Proton-Exchange Membrane (PEM), Anion-Exchange Membrane (AEM), Alkaline (AE), Solid Oxide (SOEC) electrolyzers bringing their advantage in each case (**Figure 1.4**).



**Figure 1.4.** Comparison of electrolysis technologies (a) Schematic of PEM, AEM, A, SO electrolyzers (b) Areas of current densities and cell potential for each technologies, modified and adapted from ref<sup>14</sup> and ref<sup>15</sup>.

### 1.2.1 Alkaline electrolyzers (AE)

Alkaline electrolysis was introduced in the market in the 1900s<sup>14</sup>, making it the most mature and widespread electrolysis technology. The anode and cathode are separated by a gas-tight diaphragm and in contact with a basic electrolyte solution (20-30 wt% KOH). Water is reduced to hydrogen at the cathode and the hydroxyl ions migrate through the diaphragm to be oxidized at the anode:



The electrodes are made of low cost materials such as steel or nickel alloy-plated steel materials<sup>16</sup>. Alkaline electrolysis is limited in diverse ways despite its cost-efficiency, long lifetime, and absence

of rare and expensive materials. The main drawback is the low pressure and current operation that make ultra-pure pressurized hydrogen production difficult. The low current density ( $0.2\text{--}0.4\text{ A}\cdot\text{cm}^{-2}$ )<sup>13</sup> results from the ohmic losses across the electrolyte and the diaphragm. Moreover, some safety concerns are raised by the presence of corrosive potassium hydroxide electrolyte as well as hydrogen cross over through the diaphragm which should remain below the explosion limit (i.e.,  $> 4\text{ mol\% H}_2$ )<sup>16</sup>.

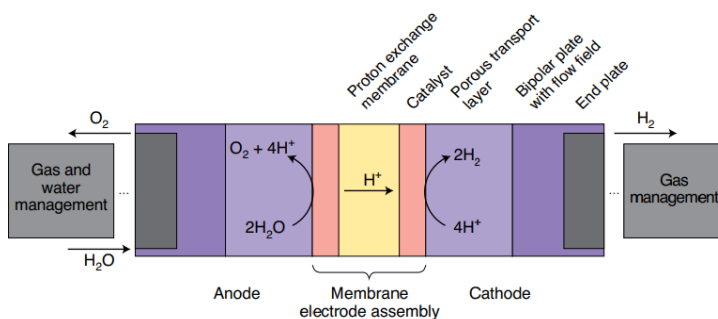
### 1.2.2 Proton-exchange membranes (PEM) electrolyzers

Nowadays, PEM electrolyzer is the most popular technology due to its highly dynamic and fast response operation. To overcome the drawbacks of A electrolysis, a solid sulfonated polystyrene membrane is used as an electrolyte, ensuring high proton conductivity, low gas crossover, compact system design and high pressure operation<sup>17</sup>.

A typical PEM electrolyzer comprises a membrane electrode assembly (MEA), two bipolar plates (BP) and two end plates (**Figure 1.5, Table 1**). The BPs serve for current collection, heat dissipation, reactant distribution and water management<sup>11</sup>. The BPs are often machined with flow channels to ensure a uniform flow of water over the gas diffusion layer (GDL) and easy removal of gases<sup>18</sup>. The membrane electrode assembly is composed of two electrodes separated by a PEM (20–300  $\mu\text{m}$  thick). The electrodes are usually composed of catalyst coated onto a porous transport layer (PTL) also called the GDL. The GDL is a conductive, high surface and porous substrate, which has a major role in reactant distribution and current collection. Ti felts are mostly used as GDL due to their good electrical conductivity, mechanical stability and corrosion resistant under acidic medium<sup>19</sup>. However, the cost of Ti components is a critical point as it represents 48% of the total stack<sup>17</sup>. Carbon-based or stainless steel GDL are also used. Pt-based and Ir-based catalyst are the benchmarks material for hydrogen evolution reaction (HER) and oxygen evolution reaction (OER) respectively. Water circulates and is oxidized at the anode; the protons are transported through the proton conductive membrane to be reduced to hydrogen at the cathode.

Reaction at the anode  $2\text{ H}_2\text{O} \rightarrow \text{O}_2 + 4\text{ H}^+ + 4\text{ e}^-$

Reaction at the cathode  $4\text{ H}^+ + 4\text{ e}^- \rightarrow 2\text{ H}_2$



**Figure 1.5.** Schematic of a PEM electrolyzer, extracted from ref<sup>12</sup>.

**Table 1.** PEM components, major functions and materials, adapted from ref<sup>11</sup>.

Components	Major functions	Components
Bipolar plate (BP)	current collection heat dissipation reactant distribution water management	carbon stainless-steel metal
Gas diffusion layer (GDL)	reactant distribution electrical contact	Ti felt, carbon cloth, stainless-steel
Proton Exchange Membrane (PEM)	proton conduction electron barrier reactant separator	Nafion, Fumapem, Aquivion®
Catalyst	electrochemical reaction site	Pt-based (HER), Ir-based (OER)

PEM electrolyzer operates at high current density ( $2 \text{ A.cm}^{-2}$ ) at 2.1 V, with high stack efficiency, thereby producing high-purity hydrogen at high pressure for future usage. The low oxygen permeability of the PEM membrane is a key advantage allowing the production of ultra-pure hydrogen. The downside of this technology is the need for rare and expensive metal catalyst such as Pt for HER or Ir for OER. Moreover, the acidic conditions imposed during operation creates corrosion issues that requires the use of corrosion-resistant components (bipolar plate, electrode supports, electrocatalyst). Notwithstanding this, it remains the preferred option for coupling with renewable due to its fast start-stop mode. Indeed, in 2021, Air Liquide launched the world largest PEM electrolyzer in Canada, powered by hydroelectricity and able to generate 20 MW in total (i.e., 8.2 metric tons of low-carbon hydrogen per day).

In the view of replacing catalyst by noble metal-free component due to the high cost and scarcity of catalyst, King *et al.*<sup>20</sup> successfully demonstrated that cobalt phosphide (CoP) can act as an active and stable HER catalyst, operating at  $1.86 \text{ A.cm}^{-2}$  for >1700 h of continuous hydrogen production. In order to decrease the final cost, Stiber *et al.*<sup>21</sup> developed a high-performance, durable and low-cost PEM cell with coated stainless steel BPs and PLTs. Although PEM is a mature technology, some aspects are still in progress such as (i) reduction of metal loading and/or substitution of noble catalysts, (ii) development of low cost and corrosion resistant current collectors and separator plates (iii) improvement of long term stability/durability of all components and (iv) improvement of overall membrane characteristics<sup>17</sup>.

### 1.2.3 Anion-exchange membrane (AEM) electrolyzers

The electrochemical reaction taking place in anion-exchange membrane (AEM) electrolyzers are the same than in an alkaline electrolyzer. AEM electrolyzers are at the early stage of their development, but have shown to be a promising solution<sup>22</sup>, allowing to reduce the cost of  $\text{H}_2$  production by using only low-cost catalysts. Moreover, AEM has several advantages compared to AE electrolysis such as lower ohmic losses thanks to the thin AEM and no need for concentrated KOH solution. The main difference with A is that the membrane can transport anion such as  $\text{OH}^-$ , overcoming the need of

highly concentrated KOH electrolyte. Indeed, usually the electrolyte in AEM contained a dilute KOH solution or a  $\text{HCO}_3^-/\text{CO}_3^{2-}$  solution. In addition, in comparison to PEM, the membrane and the materials required are cheaper. The AEM electrolysis unites the advantages of A (cheap and abundant materials) and PEM (pure water feed and membrane), see **Table 2**. Nevertheless, efforts must be made to increase the current density and lifetime of AEM to render the system cost competitive.

**Table 2.** Comparison of the main characteristics of low-temperature electrolysis technologies (AL, PEM, AEM) adapted from ref<sup>16</sup>.

Electrolysis	AE	PEM	AEM
Electrolyte	Aqueous KOH (20-40%wt)	Proton exchange ionomer (Nafion, Aquivion, Fumapem)	Anion exchange ionomer (Sustainion, Aemion, Tokuyama A-201)
Cathode	Ni, Ni-Mo alloys	Pt, Pt-Pd	Ni, Ni alloys
Anode	Ni, Ni-Mo alloys	$\text{RuO}_2$ , $\text{IrO}_2$	Ni, Fe, Co oxides
Half-cell separation	Diaphragm (Zirfon)	Nafion 117	AEM
Current density ( $\text{A.cm}^{-2}$ )	0.2-0.4	0.6 - 2.0	0.2-1.0
Voltage (V)	1.8-2.4	1.8-2.2	1.8-2.2
Cell area ( $\text{m}^{-2}$ )	<4	<3	Lab scale
Operating temperature ( $^{\circ}\text{C}$ )	60-80	50-80	50-60
Operating pressure (bar)	1-30	30-76	1-30
Production rate ( $\text{Nm}^{-3}.\text{h}^{-1}$ )	<760	<40	<1
Gas purity	>99.5	>99.9999	>99.99
System response	Seconds	Milliseconds	NA
Stack lifetime (h)	60k to 100k	20k to 60k	NA
Technology status	Mature	Commercial	R&D

#### 1.2.4 Solid oxide electrolyzers (SOEC)

AEM, PEM and AE electrolysis are based on low-temperature processes. Another type of electrolysis called Solid oxide electrolyzer (SOEC) operates at high temperature. It is composed of three main components<sup>15</sup>: two porous electrodes and a dense ceramic electrolyte able to transport oxide ions  $\text{O}^{2-}$  (**Figure 1.4**). SOEC is a method of choice to reach high conversion efficiency up to 82% due to favorable thermodynamics and fast kinetics at high temperature (600-850  $^{\circ}\text{C}$ )<sup>14</sup>. It relies on scalable method of production and requires mostly earth-abundant elements such as nickel, zirconia and steel<sup>15</sup>. The current density remains low, despite the efforts made over the last 15 years. The major weak point of this technology is the impossibility to operate in a start-stop mode due to the long activation time. However, it could be used in stationary applications, to benefit from the extra-heat of industrial plants for example.

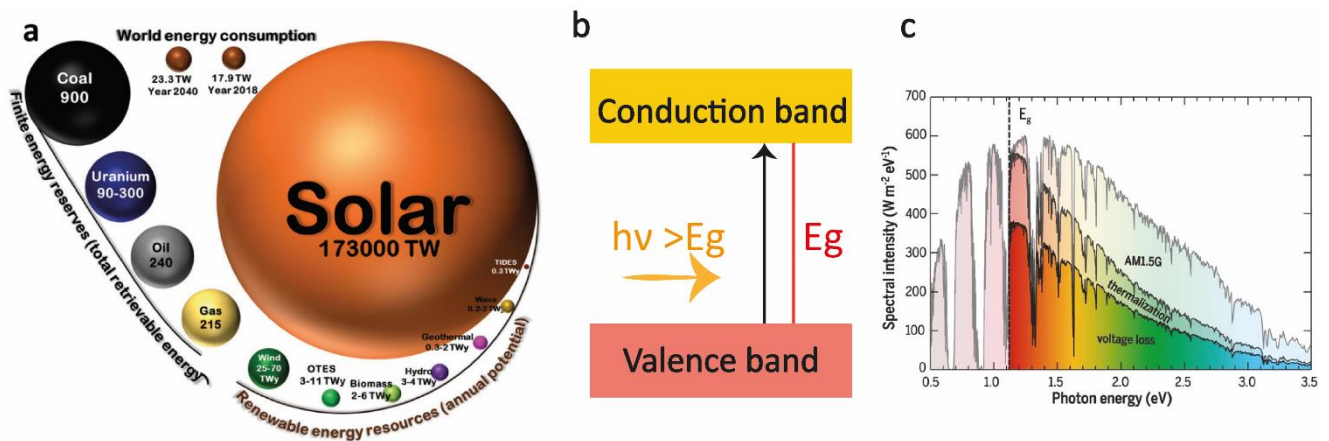
Electrolysis undoubtedly is a promising solution for renewable hydrogen production provided that the energy input comes from renewable energy. The materials used are cheap and earth-abundant,



the water management is respectful, and the cell efficiency allows accelerating market share. A proton-conducting solid oxide electrolysis cell<sup>23</sup> (H-SOEC) is also a promising device that could lower the operating temperature, allow a direct gas separation

### 1.3 Solar-assisted hydrogen production

One of the major challenges for decarbonizing our economy is to harvest renewable energy and store it into a chemical fuel to overcome the issue of intermittency. Diverse electrolysis technologies have been developed in the last decades (see section 1.2) to produce hydrogen as an energy carrier. Nonetheless, electrolyzer installations need electricity to operate. Hence, to guarantee carbon-neutrality, they must be powered by renewable energies such as solar, wind, hydro, or biomass. Taking a closer look to estimate finite and renewable energy resources on earth (**Figure 1.6**), the immensity of solar energy is striking: if we were able to harvest the entirety of solar energy reaching earth, it would represent 173000 TW/year<sup>24</sup>, that is 9800 times larger than the total world consumption (17.65 TW in 2020)<sup>4</sup>.



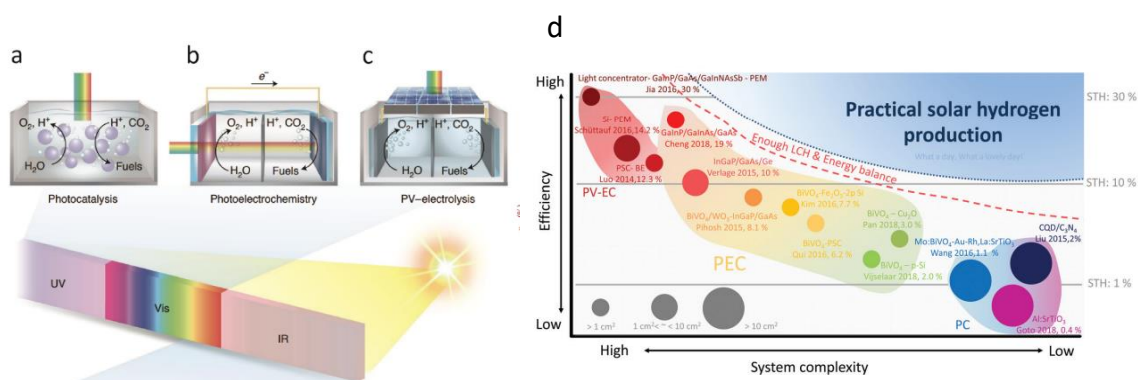
**Figure 1.6.** (a) 2009 estimate of finite and renewable planetary energy reserves (Terawatt-years). Total recoverable reserves are shown for the finite resources. Yearly potential is shown for renewable. Extracted from ref<sup>24,25</sup> (b) Semiconductor band diagram ( $E_g$  stands for band gap) (c) AM1.5 solar spectrum with distinct dips due to molecular absorption in Earth's atmosphere ( $E_g$ , dashed black line corresponds to the band gap of Si). Extracted from ref<sup>26</sup>.

Since solar energy is clean and non-hazardous, photovoltaic is a promising solution to the energy challenge by converting solar energy to electricity. Semiconductors (the main component of a photovoltaic cell) are a type of materials in which electrons are grouped into valence and conduction band, separated by a forbidden energy gap ( $E_g$ ) or band gap<sup>27</sup>. The absorption of photons with an energy greater than the  $E_g$  leads to the excitation of electrons from the valence band to the conduction band (**Figure 1.6b**). The electrons can flow through the material as an electrical current: the solar energy is converted into electrical power. The photons with an energy greater than the semiconductor  $E_g$  are absorbed, accompanied by energy losses, through thermalization of charge carrier. While if  $E < E_g$ , the photons are not absorbed (**Figure 1.6c**). The Shockley-Queisser model<sup>26</sup> estimates that the maximum performance for a single junction solar cell ( $E_g = 1.34$  eV) under one sun illumination (e.g. Air Mass 1.5 global, AM 1.5 G) is limited to 33.7%.

Different types of photovoltaic materials have been developed in the last 50 years (**Figure 1.6b**), Si-based solar cells still dominate the current market (90% share)<sup>28</sup> because of their high efficiency<sup>28</sup> (26.7% with single crystalline Si) and long life span. Other materials also perform decently without increasing the cost<sup>29</sup>, such as thin film single-crystalline GaAs cells (28.8%), CIGS cells (23.4%) or perovskite cells (25.5%)<sup>30</sup>. In 2020, National renewable energy laboratory (NREL) scientists reached a solar conversion value of 47.1% under concentrated light (143 suns) with a six-junctions III-V solar cell<sup>31</sup>. Although photovoltaic technologies are a promising solution, it remains limited due to intermittency of sunlight. The energy harvested by solar cells can be used through the grid, but how to store this energy and deal with irradiation variability and unpredictability?

The concept of converting solar energy into chemical fuels such as hydrogen or carbon-based molecules (methane, methanol, formic acid) is not new. Many reviews<sup>13,25,32–39</sup> summarized the progress made and the ongoing work on sunlight-driven water splitting regarding material or system development before the rise of hydrogen. Techno-economical studies<sup>40–42</sup> have also been carried out to highlight potential, limitations and mandatory progress for solar-assisted hydrogen production. Consistently, coupling solar energy conversion device and electrolyzer would allow producing hydrogen in a sustainable way, decreasing drastically the CO<sub>2</sub> emission inherent to the process.

There are three main roads to convert solar energy into hydrogen, namely photocatalysis (PC), photoelectrochemistry (PEC) and photovoltaic-electrolysis (PV-EC) (**Figure 1.7a-c** respectively). Similarly, to dark electrolysis, sunlight-driven water splitting requires a standard free energy change ( $\Delta G^\circ$ ) of 237.2 kJ.mol<sup>-1</sup>, corresponding to a potential of 1.23 V/electron.



**Figure 1.7.** Solar energy conversion technologies a-c, (a) Schematic of particulate photocatalysis (b) photoelectrochemical water splitting, (c) PV-electrolysis (d) Technological map showing various photon-driven water splitting approaches for solar energy conversion and specific experimental demonstrations. (a-c) extracted from ref<sup>32</sup> (d) extracted from ref<sup>25</sup>.

Performances can be evaluated by different figures of merits such as (i) gas chromatography H<sub>2</sub> evolution analysis for PC (ii) Photocurrent and operating points (open-circuit potential  $V_{oc}$ ,

photovoltage  $V_{ph}$ , photocurrent  $J_{ph}$  or  $J_{sc}$ ) for PEC (iii) J-V curves of the PV cells and electrocatalyst for PV-EC.

However, the most common value assessed to characterize the cell performance is the Solar-To-Hydrogen ( $\eta_{STH}$ ) conversion efficiency under one sun condition (AMG 1.5)  $\eta_{STH}$  efficiency can be calculated as follow:

$$\eta_{STH}(\%) = \frac{(mmol\ H_2/s) \times \Delta G}{P_{total} (mW/cm^2) \times Area (cm^2)} = \frac{J_{sc} (mA/cm^2) \times 1.23V \times \eta_f}{P_{total} (mW/cm^2)}$$

where  $\Delta G=237kJ/mol$ ,  $J_{sc}$  is the operating photocurrent,  $\eta_f$  is the Faradaic efficiency (i.e., the conversion efficiency of free electrons to chemical product through the electrochemical reactions) and  $P_{total}$  is the total incident irradiance.

At the moment the trend<sup>25</sup> shows that PV-EC exhibits the highest  $\eta_{STH}$  (30% with concentrated solar)<sup>43</sup>, followed by PEC (19%)<sup>44</sup> and PC (2%)<sup>45</sup>, as it can be seen in **Figure 1.7d**.

### 1.3.1 Photovoltaic-electrolyzer (PV-EC)

In PV-EC, a photovoltaic (PV) device converts solar energy into electricity and the voltage/current generated can be used to power an electrolyzer (EC), composed of electrocatalyst able to perform water reduction and oxidation<sup>43,46</sup>.

The PV device is made of semiconductor materials able to absorb light and convert it to charge carrier. Since 1954, the discovery of the first practical solar cell in the Bell Laboratories, following the observation of the photovoltaic effect by Becquerel in 1839, lead to intensive research to increase the solar conversion efficiency of PV devices.

Hydrogen can be produced by combining photovoltaic devices and electrolyzers<sup>43,46</sup>. The PV cell supplies the 1.8 V necessary (due to kinetic overpotential) to operate the electrolyzer and reach efficiency  $\eta_{STH} > 10\%$ . The performance is determined mainly by the open-circuit voltage ( $V_{oc}$ ) of the PV cell and by the catalyst overpotential towards HER and OER. In 2016, Jia *et al.*<sup>43</sup> reported the highest  $\eta_{STH}$  efficiency for any water splitting technology consisting of two PEM electrolyzers in series with one InGaP/GaAs/GaInNAsSb triple-junction solar cell. The system achieves a 48 h average  $\eta_{STH}$  efficiency of 30%. PV-EV suffers from the poor matching of current voltage characteristic of the multi-junction PV and those of water electrolyzer. However, in such device, the PV solar cell is completely free of electrolyte, which represents an enormous advantage in term of stability. PV-EC is complex regarding system design and engineering, but the technology is already mature to commercialization.

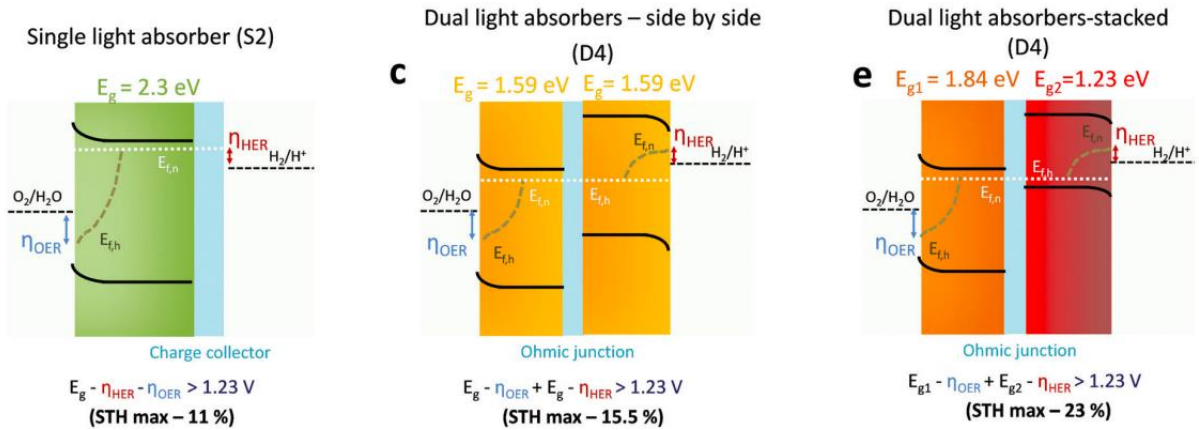
### 1.3.2 Photoelectrochemistry (PEC) systems

While silicon-based photovoltaic cells flood the market, PEC cells draw attention for the possibility of directly storing solar energy into high-value chemicals ( $H_2$ ,  $CH_4$ ,  $CH_3OH$ , etc.) when using  $H_2O$  or  $CO_2$  as feedstock. This technology could play a pivotal role in storing and transporting clean energy.

Hydrogen production via PEC water splitting represents a viable alternative to the conventional methods for hydrogen production and solar energy conversion. Indeed, this type of technology is easy to implement as it requires few components, which cuts down significantly the manufacturing costs if inexpensive materials are utilized, while in parallel reduces the energy losses since less modules (one PEC device vs. PV + electrolyzer) are combined in the complete device.

Upon illumination, the semiconductor absorbs light, promoting the generation of an electron-hole pair in the valence band. The electron-hole pair is separated by the space-charge field, leading to the presence of free charge carriers in the valence band (holes) and in the conduction band (electron). By selecting the appropriate semiconducting material (e.g., a band gap energy large enough to split water: a valence band more positive than the water oxidation potential and a conduction band more negative than the water reduction potential), photogenerated holes and electrons could oxidize and reduce water, respectively.

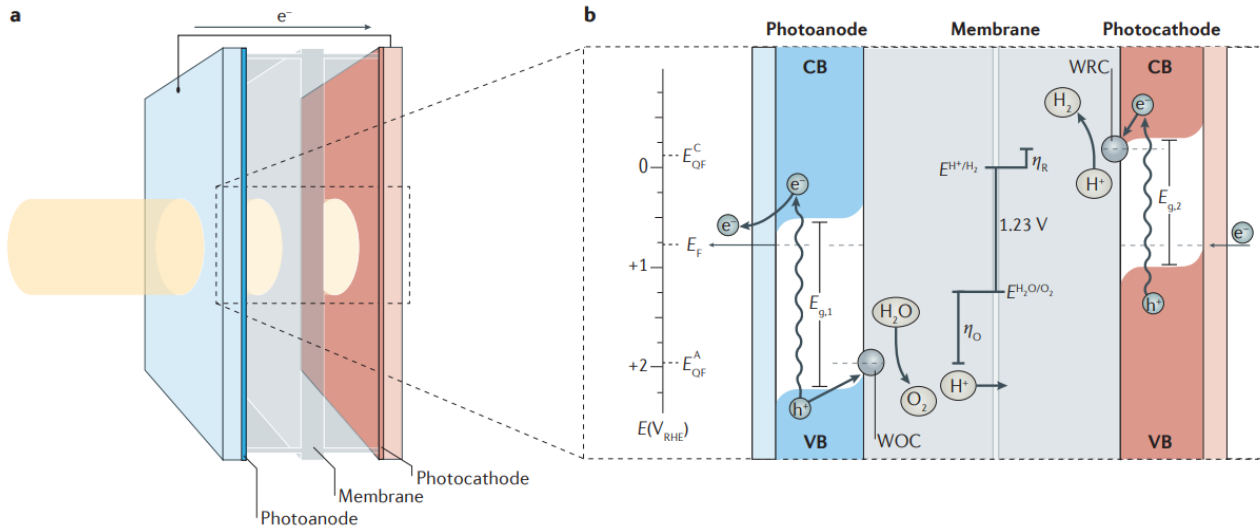
The first demonstration was done by Fujishima and Honda<sup>47</sup> in 1972, by using  $\text{TiO}_2$  as a semiconductor material. Despite the great  $\text{TiO}_2$  stability, the  $\eta_{\text{STH}}$  efficiency is limited to less than 2%<sup>13</sup> due to its 3.2 eV band gap that does not allow to harvest a large part of the solar spectrum. Different cell configurations are foreseeable, such as single light absorber, dual light absorber side-by-side or dual light absorber-stacked (**Figure 1.8**) with a theoretical maximum  $\eta_{\text{STH}}$  conversion efficiency<sup>41</sup> of 11%, 15.5% and 23% respectively. The best performing band gap characteristic calculated by Shaner *et al.*<sup>41</sup>, are (i) 2.26 eV band gap for single light absorber, (ii) two semiconductors with a band gap of 1.59 eV for dual light absorber side by side, (iii) a bottom and top absorber having a band gap of 1.23 eV and 1.84 eV for dual light absorber stacked.



**Figure 1.8.** Schematic of PEC cells configuration (a) single light absorber (b) dual light absorber side by side (c) dual light absorber-stacked. Extracted from Ref<sup>25</sup>.

In order to increase the STH efficiency, a technology called tandem cell (i.e. dual light absorbers-stacked) has been developed, utilizing the combination of a top photoanode (n-type semiconductor) for the oxidation reaction, a bottom photocathode (p-type semiconductor) for the reduction reaction, and a membrane to separate the product of the two-half reactions (**Figure 1.9**). Although a potential of 1.23 eV is necessary to perform the overall water splitting potential, the actual

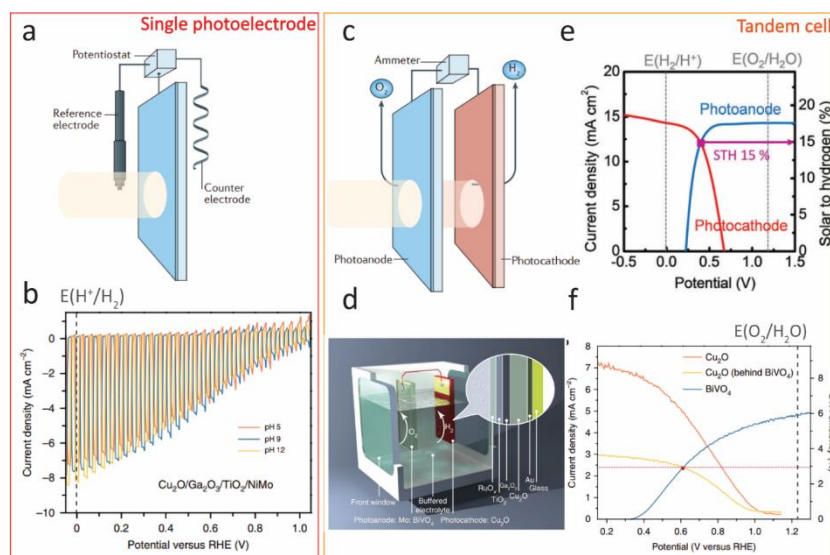
photogenerated potential must be around 1.5-1.8 V to drive the overall water splitting due to kinetic overpotential. For a tandem or dual-absorber cell, this potential threshold will be achieved by combining the photovoltage generated by the photocathode and the photoanode.



**Figure 1.9.** (a) Schematic of a PEC tandem cell and different processes ref<sup>34</sup>.

Decoupling the different components contribution is essential to make progress, especially in the material development point of view. A single semiconductor material can be studied independently by utilizing a photoelectrode on one side and a catalytic electrode on the other side. Usually the performances are evaluated in a three electrodes setup where the photocurrent for HER or OER under illumination is measured (**Figure 1.10a,b**) yielding a current-potential curve (J-V curve). In this case, the cell needs an extra bias in operation to compensate for overpotential and other losses.

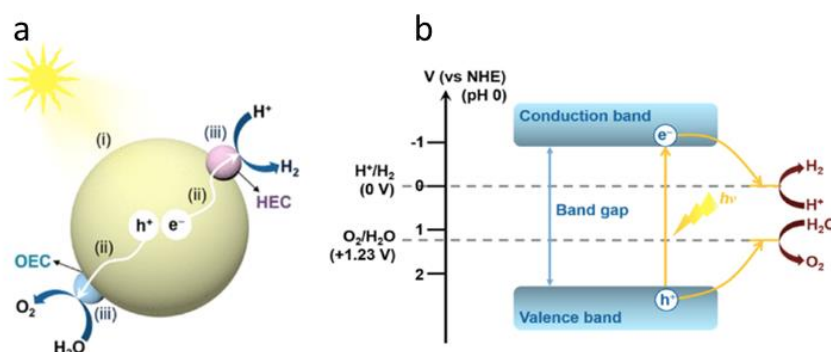
The tandem cell performance is evaluated by combining a photocathode and a photoanode (**Figure 1.10c,d**). It is essential for the sum of the photovoltage to be higher than 1.6 - 1.8 V and that both electrodes exhibit a photocurrent  $> 10 \text{ mA.cm}^{-2}$  at the same operating condition (**Figure 1.10e-f**). Pan *et al.*<sup>48</sup> demonstrated an all-oxide unassisted solar water splitting tandem device using state-of-the-art  $\text{BiVO}_4$  as the photoanode, and  $\text{Cu}_2\text{O}$  as a photocathode, achieving  $\approx 3\%$  STH conversion efficiency. Undoubtedly, the performance and the stability of each photoelectrode must be improved to reach the tandem cell target for commercial use of STH efficiency  $> 10\%$  and stability  $> 10$  years.



**Figure 1.10.** (a-b) Single photoelectrode case (a) schematic of a three-electrode setup used for single photoelectrode testing (b) Typical LSV curves obtained for  $\text{Cu}_2\text{O}$  photocathodes under chopped illumination (c-f) tandem cell case (c) schematic of a tandem cell setup (d) schematic of an actual  $\text{BiVO}_4/\text{Cu}_2\text{O}$  tandem cell (e) Typical characteristic of a tandem cell (f) characteristic of a  $\text{BiVO}_4/\text{Cu}_2\text{O}$  tandem cell. The figures (a,c), (e), and (b,d,f) are extracted from ref<sup>34</sup>, ref<sup>25</sup>, and ref<sup>48</sup>, respectively.

### 1.3.3 Photocatalyst (PC) systems

Photocatalyst (PC) systems gained a lot of interest due to their simplicity. Indeed, the system is solely composed of photocatalyst particles, possibly stabilized by a surfactant in water; thereby there is no need for complex cell engineering (see **Figure 1.11**). The system relies on (i) absorption of photons with energy  $E > E_g$  and generation of electron-hole pairs, (ii) charge separation and diffusion to the active sites, (iii) HER and OER with the assistance of co-catalysts. As the light absorption and the catalytic process would occur on the same particle, this could lower the final hydrogen cost. Indeed, the estimated hydrogen cost using such technology could be close to 1.6-3.5 US\$/kg with a STH between 5-10%.



**Figure 1.11.** (a) Schematic of the phenomena occurring during PC (b) band diagram for photocatalyst overall water splitting, extracted from ref<sup>49</sup>.



Despite the simplicity of the system, the control of the charge carriers is also limited as no bias is applied. Moreover, it is worth noting that back-reactions<sup>25</sup> are possible ( $\text{H}_2$  oxidation and  $\text{O}_2$  reduction), as they are more favorable than their counterpart occurring on the same particle.

Similarly, to work done with  $\text{TiO}_2$  in PEC cell, Schrauzer *et al.*<sup>50</sup>, demonstrated the possibility to generate hydrogen using  $\text{TiO}_2$  with UV irradiation. Later on, in order to increase light absorption, Domen *et al.*<sup>51</sup>, demonstrated photocatalytic overall water splitting under visible light using a solid solution  $(\text{Ga}_{1-x}\text{Zn}_x)(\text{N}_{1-x}\text{O}_x)$  and core-shell  $\text{Rh@Cr}_2\text{O}_3$  co-catalyst. Thus, a broad range of inorganic materials combined with co-catalyst such as  $\text{m-BiVO}_4/\text{RuO}_2$ ,  $\text{C}_3\text{N}_4/\text{Cdots}$ ,  $\text{RhCrO}_x+\text{CoO}_x/\text{Al-SrTiO}_3$  were evaluated exhibiting  $\eta_{\text{STH}}$  of 3.2%, 2% and 0.4% respectively. It is difficult to find a single material able to perform overall water splitting. Thereby strategies using two photocatalysts in a Z-scheme were developed. In this case, HER is performed on one type of photocatalyst particle and OER is performed on another type, while the extra hole and electron recombine via an aqueous shuttle redox mediator<sup>25,52</sup> such as  $\text{IO}_3^-/\text{I}^-$ . More recently, a proof of concept using Al-doped  $\text{SrTiO}_3$  particles in photocatalyst panels showed outstanding stability at large scale<sup>53</sup>. However, the STH remain quite low (0,76%) due to the low light absorption of the material.

Currently, inorganic photocatalysts dominate the field, however organic semiconductor bulk heterojunction photocatalysts could play a key role in the future. Indeed, being close to the photosynthetic compounds, composed of carbon, hydrogen and heteroatoms, are able to absorb a large portion of the visible range. Similarly, to PEC system, it is possible to decouple photocatalytic OER and HER by using a scavenger able to extract electrons or holes respectively. For instance, it is possible to study photocatalytic HER decoupled to the more difficult OER in presence of ascorbic acid as a hole scavenger. Kosco *et al.*<sup>54</sup> demonstrated a remarkable hydrogen production rate of  $60 \text{ mmol.h}^{-1}.\text{g}^{-1}$  using PTB7-Th as the polymer donor and EH-IDTBR as a non-fullerene small molecule acceptor stabilized with sodium 2-(3-thienyl)ethyloxybutylsulfonate (TEBS) surfactant and ascorbic acid as the hole scavenger.

Performance bottleneck remains a brake on PC systems development. Hence, progress is urgently needed to improve light absorption capacity, charge separation/migration, and catalytic surface reaction.

#### 1.3.4 Photocatalytic materials

- Water oxidation

In recent years, several light-driven photocatalytic materials have been investigated as photoanodes for OER and photocathodes for HER. In the selection process of the ideal semiconducting material, the major requirements are (i) suitable band gap energy and band positions (ii) efficient charge carrier separation and transportation in the semiconductor and (iii) strong catalytic activity and stability.<sup>35</sup>

Water oxidation is more kinetically demanding because it requires the coupling of four electrons to four protons in the cleavage of four O–H bonds and the formation of two O–O bonds<sup>55</sup>. The oxide

semiconductors photoanode such as  $\text{TiO}_2$ ,  $\text{WO}_3$ ,  $\text{Fe}_2\text{O}_3$  and  $\text{BiVO}_4$  dominate the field due to their stability.  $\text{BiVO}_4$  received a lot of attention due to its optical properties (band gap of  $E_g=2.4$  eV and favorable valence band maxima  $E_{vb}=2.4$  V vs. NHE, Normal Hydrogen Electrode), visible-light-response photoactivity, and its high theoretical maximum photocurrent density<sup>56</sup> of nearly  $7.5 \text{ mA.cm}^{-2}$ . Choi *et al.*<sup>57</sup> demonstrated a  $\text{BiVO}_4/\text{NiOOH-FeOOH}$  photoanode with a record  $5 \text{ mA.cm}^{-2}$  at 1.23 V vs. RHE (Reversible Hydrogen Electrode). Extensive studies<sup>58–62</sup> have been also conducted on hematite ( $\alpha\text{-Fe}_2\text{O}_3$ ) due to its ideal band position and band gap (1.9 – 2.2 eV), long-term chemical stability, and earth abundance (Fe is the 4<sup>th</sup> most abundant element on earth). Metal oxides are promising solutions, especially in terms of stability but their poor optical properties (large and indirect band gap) and poor conductivity might limit their performance.

Despite their lower stability, carbon-based photoanodes could also play a key role to increase light absorption properties as well as performances. Indeed several studies have been conducted<sup>63–65</sup>, Cho *et al.*<sup>66</sup> demonstrated a bulk heterojunction (BHJ) photoanode (FTO/mZnO/BHJ/PTAA/LIO) exhibiting  $\text{O}_2$  production with a photocurrent  $J_{ph} > 2 \text{ mA.cm}^{-2}$  at 1.23 V vs. RHE.

As water oxidation has sluggish reaction kinetic, more progress needs to be done on materials research and development regarding semiconductors, the different under and over layers as well as catalyst selection.

- Water reduction

A plethora of photocathode materials have been investigated such as high-performance crystalline GaInP/GaAs monolithic multijunction semiconductors, chalcogenides (Copper Indium Gallium Selenide), transition metal dichalcogenides (TMDs) such as  $\text{WSe}_2$ <sup>67</sup>, metal oxide such as  $\text{Cu}_2\text{O}$ <sup>68,69</sup>, and carbon-based materials<sup>63,70,71</sup>.

P-type  $\text{WSe}_2$  is a promising candidate for HER evolution due to its ideal band gap (1.2 - 1.6 eV), high absorption coefficient, anisotropic transport properties and finally its stability. First attempts have been done on  $\text{WSe}_2$  single crystal, starting from the discovery of the optical transition<sup>72</sup>, its use as a n-type photoanode<sup>73</sup>, pursued by the first use of p-type  $\text{WSe}_2$  into PEC cell<sup>74</sup>, to the record STH efficiency (7%,  $24.5 \text{ mA.cm}^{-2}$  at 0 V vs. RHE) reached by McKone<sup>75</sup> in 2013. However, high pressure and high temperature were still mandatory to obtain photoactive films. The interest for this type of material did not vanish, and a new thin film device generation came out, driven by the discovery of the TMDs' outstanding optoelectronic properties. Although the performance and the processability of the photoelectrode have been improved by recent techniques, the major weak point of this material remains its bulk and surface imperfections. Indeed, the defects such as internal and external defects (vacancies), surface imperfections (step edges) act as recombination center for the  $e^-$  and  $h^+$  generated and contribute to lower the performance of the device. Yu and al<sup>76–78</sup> developed, a solution-based method for  $\text{WSe}_2$  photocathode fabrication using  $\text{WSe}_2$  bulk powder exfoliation and a liquid-liquid interfacial self-assembly (LLISA) method of deposition. In this work, three key aspects to ensure the performance of the photocathode were highlighted: flake size<sup>77</sup>, defect mitigation<sup>78</sup>, catalyst deposition<sup>76,78</sup>.



Cu<sub>2</sub>O have been widely studied as a photocathode material<sup>69</sup> due to its ideal band gap (2.0 eV) and its ease of fabrication. However, the Pourbaix diagram highlights the main limitation of Cu<sub>2</sub>O which is prone to photocorrosion in aqueous solution and under applied potential. To tackle this issue, scientists have developed buried junctions and protective layers<sup>79–81,48</sup>, ensuring the stability over a few hours of the Cu<sub>2</sub>O-RuO<sub>x</sub><sup>81</sup> photocathode. More recently, a coaxial nanowire structure implementing a Cu<sub>2</sub>O/Ga<sub>2</sub>O<sub>3</sub>-TiO<sub>2</sub>-buried p-n junction reached an outbreking performance of  $\approx 10 \text{ mA.cm}^{-2}$  at 0 V vs. RHE<sup>48</sup>.

Although organic semiconductors were broadly studied for organic solar cells (OPVs.) applications, they are emerging for PEC applications. BHJs are particularly interesting in different aspects: (i) solution-processability adapted for fabrication scale-up (ii) high charge mobility (ii) high light absorption and tunable optical properties. Despite their lack of stability, promising performance were obtained for photocathode applications<sup>82–84</sup>. The charge diffusion length in such material is around 10 nm which leads to charge recombination limitation in single organic semiconductor. A blend of two organic semiconductors having different energy levels tackles the issue of charge separation. An electron is photoexcited upon illumination in the “donor” material and is transferred to the acceptor, if the materials are blended at the nanoscale due to exciton diffusion length ( $\approx 10\text{nm}$ ). The blend is called a bulk heterojunction (BHJ). The first attempts<sup>85</sup> were done on poly(3-hexylthiophene) (P3HT) donor and a fullerene based acceptor such as phenyl-C61-butyric acid methyl ester (PCBM). Poly([2,6'-4,8-di(5-ethylhexylthienyl)benzo[1,2-b;3,3-b]dithiophene]{3-fluoro-2[(2-ethylhexyl)carbonyl]thieno[3,4b]thiophenediyl}) (PTB7-Th) is also well-studied as polymer donor<sup>83</sup>. PCBM suffers from stability issue, as it is prone to dimerization and photodegradation under operating conditions<sup>86</sup>. Overlayers such as TiO<sub>2</sub> can be deposited by atomic layer deposition (ALD) to act as a charge extraction layer and protective layer. Steier *et al*<sup>59</sup>. reported several hours stability with a device composed of P3HT:PCBM coated with TiO<sub>2</sub> layer. Recently, Yao *et al*.<sup>87</sup> reported a polymer BHJ composed of PTB7-Th polymer donor and perylene diimide-based non-fullerene polymer acceptor (PDI-V) photocathode combined with RuO<sub>2</sub> catalyst that exhibits  $8.2 \text{ mA.cm}^{-2}$  at 0 V vs. RHE, retaining 85% of its photocurrent after 8 h. By replacing PCBM by a polymer acceptor, the stability of the photocathode was improved.

Although PEC water splitting is a promising solution for hydrogen production, the need for low-cost, robust, and high-performing semiconducting materials hinders the industrial-scale development of such technology. The issue of costs remains a limitation, while the earth-abundant materials such as the oxide semiconductors suffer from poor performance and organic semiconductors suffer from low stability under PEC conditions. Moreover, the final device is often composed of under/overlayer and non-earth abundant catalyst that participate in the overall performance. Their optimization is undeniably a key point to increase the device performance.

In conclusion, the current requirements in terms of performance and stability does not satisfy the target to be economically viable. However, the enthusiasm for renewable hydrogen production might help to reach this goal in the foreseeable future.

## 1.4 PEM-PEC systems: motivation and objectives

### 1.4.1 PEM-PEC cells early research

Taking inspiration from both PEC and PEM technologies, the idea of a PEM-PEC or solid-state PEC device began with studies on membrane electrode assembly (MEA) combining a  $\text{TiO}_2$  photoanode, a Nafion membrane and Pt HER catalyst<sup>88–93</sup>. The  $\text{TiO}_2$  layer was either coated directly on the PEM membrane, or a substrate (e.g., Ti discs or carbon paper) using anodization<sup>94</sup>, drop-casting<sup>91</sup>, or electrophoretic deposition<sup>90</sup> to perform water splitting under UV illumination. This novel compact device architecture allows simple product separation, minimizes electrolyte resistance thanks to the solid PEM<sup>88</sup> and operates at elevated temperature and pressure, preventing gas bubble formation (i.e. the typical limitations in PEC cell). In principle the water feedstock for PEC could come from rainfall or seawater<sup>95</sup>, however it poses additional challenges such as water supply in dry areas and water desalinization systems. Thus, using simple natural air convection to perform gas phase water splitting is a promising alternative.

It is obvious that the PEC system cannot be directly transposed to PEM-PEC technologies as it operates in the liquid phase, requiring typical flat conductive substrate (e.g. FTO glass). However, as the PEM-PEC cell operates in the gas phase, a porous and high-surface area substrate must be used to (i) maximize reactant supply at the electrode surface<sup>17,96</sup> and (ii) facilitate gas diffusion and proton diffusion<sup>97</sup>. Stoll *et al.*<sup>96</sup> successfully demonstrated a PEM-PEC cell using a Ti felt coated with  $\text{TiO}_2$  nanotubes arrays through anodization as the photoanode, a Pt-C as the cathode and a Pt/C reference electrode (allowing comparison with the PEC system).

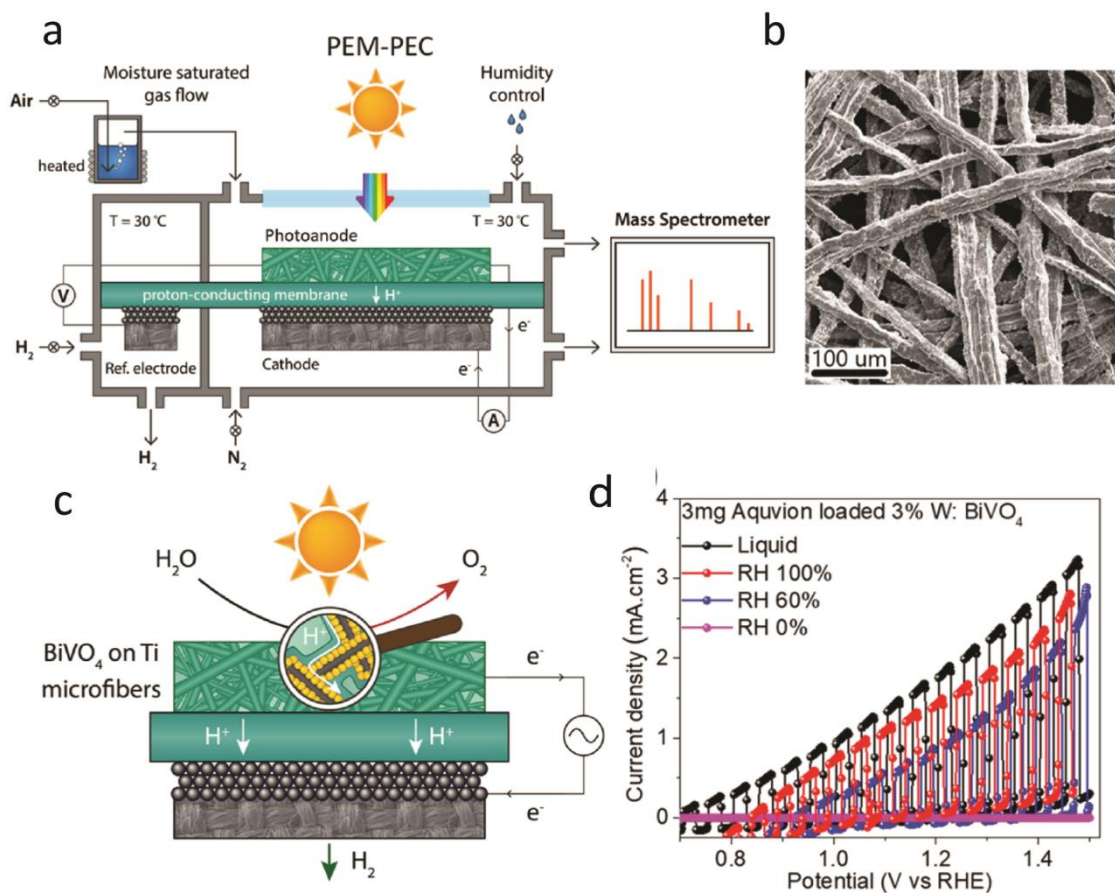
With the aim of improving light harvesting, a  $\text{WO}_3/\text{BiVO}_4$  heterojunction photoanode was investigated by different research groups<sup>98,99</sup>.  $\text{WO}_3/\text{BiVO}_4$  can be coated on porous Ti felt by combining electrochemical anodization of sputtered W layers and  $\text{BiVO}_4$  formation via SILAR (Successive Ionic Layer Adsorption and Reaction) or by simple dip-coating processes<sup>99</sup>. Stoll *et al.*<sup>98</sup> obtained similar performance in the liquid and gas phase,  $\approx 1.9 \text{ mA}\cdot\text{cm}^{-2}$  at 1.23 V vs. RHE. More recently, W-doped  $\text{BiVO}_4$  coated on Ti felt<sup>100</sup> exhibited a photocurrent density of  $2.1 \text{ mA}\cdot\text{cm}^{-2}$  at 1.23 V vs. RHE in liquid electrolyte. It is the highest reported for  $\text{BiVO}_4$  on porous substrates. The photocurrent in the gas phase was  $1.55 \text{ mA}\cdot\text{cm}^{-2}$  at 1.23 V vs. RHE (**Figure 1.12**).

Amano *et al.*<sup>95</sup> highlighted the importance of an additional Nafion coating on the photocatalyst surface. The Nafion coating allows a triple phase boundary (i.e. gas/electrolyte/semiconductor) to increase PEC water oxidation performance. A PEM-PEC cell composed of Nafion/ $\text{WO}_3$  nanoparticles coated on the Ti felt photoanode/Nafion membrane/Pt-C cathode was used to demonstrate that Nafion coating improves proton conductivity and moisture absorbance. The same effect was observed for  $\text{TiO}_2$  coated Ti felt photoanodes<sup>101,102</sup>. Zafeiropoulos *et al.*<sup>103</sup> further studied the impact of the photoanode functionalization with ionomers (Nafion and Aquivion) for PEM-PEC application. They demonstrated that an Aquivion spray-coating on the photoanode ( $\text{TiO}_2$  coated Ti felt or  $\text{WO}_3$

coated W mesh) was able to perform at low humidity (60%) conditions, retaining more water uptake and demonstrating more stability than Nafion.

Similarly,  $\text{SrTiO}_3$  on Ti felt has also shown promising performance after ionomer functionalization<sup>104</sup>. By replacing  $\text{TiO}_2$  by  $\text{SrTiO}_3$ , the external voltage could be decreased and the gradual decomposition of the ionomer coated on the photoanode could be suppressed, exhibiting a better stability.

Most of the studies on PEM-PEC deal with a photoanode and a cathode. The only attempt of full photocatalytic PEM-PEC system was done by Xu *et al.*<sup>105</sup> combining  $\text{TiO}_2$  photocatalyst/Nafion membrane/ $\text{C}_3\text{N}_4$  photocatalyst without GDL. However, a poor photoresponse was obtained ( $5\text{--}10 \mu\text{A}\cdot\text{cm}^{-2}$ ).



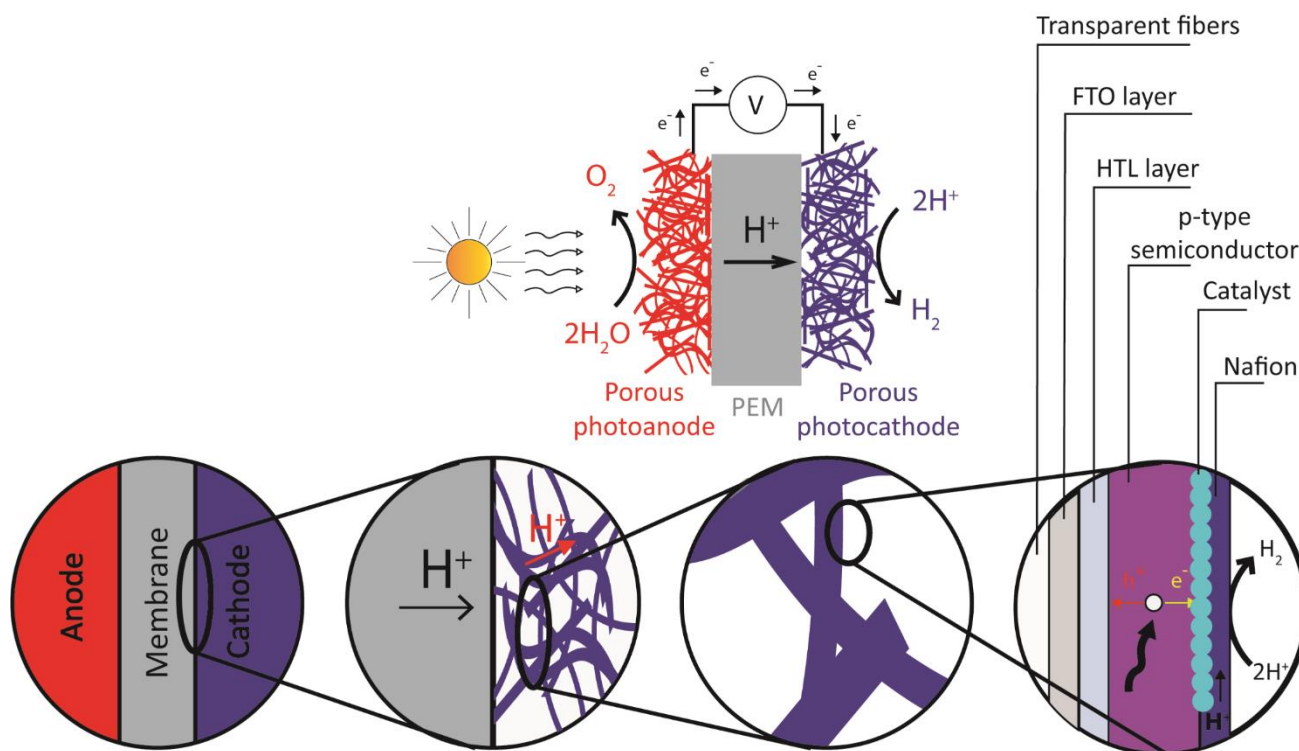
**Figure 1.12.** (a) PEM-PEC experimental configuration used for evaluating the photoanodes with a standard hydrogen reference electrode with the capability to operate under a humidified air (b) SEM features of W:BiVO<sub>4</sub> deposited on the Ti-felt (c) Schematic of MEA with BiVO<sub>4</sub> photoanodes, PEM and Pt/C cathode (d) LSV curves of functionalized W:BiVO<sub>4</sub> under chopped light illumination at various RH. Extracted from ref<sup>106</sup>.

#### 1.4.2 The PEM-PEC cell: general motivation

The goal of this project is to build a PEM-PEC operating in gas phase. To do so, the project aims for the development of three components: the photoanode, the photocathode and the PEM assemblies. This work places special focus on the PEM-PEC photocathode development. The main principle is to combine existing PEM technology with the PEC system. Indeed, Spurgeon *et al.*,<sup>107</sup>

reported a PEM electrolyzer sustained by vapor water. They demonstrated that an efficient solar photoelectrolyzer could be operated only with water vapor as the feedstock, even at low operating temperatures that may occur in the absence of active heating. Thus, the cell will work as a PEM cell, except that the electrode will be composed of semiconductors materials able to reduce/oxidize water under light illumination.

One of the main goals is to produce hydrogen from sunlight and humidity in the air using a novel photoelectrochemical device. The device envisioned is a tandem device as seen in **Figure 1.13**. The high energy photons from the incident sunlight are absorbed by a photoanode that oxidizes vapor water to produce oxygen gas. The low energy photons are thus transmitted through the photoanode to the photocathode bottom absorber, which produces hydrogen gas from protons transported through the PEM. Efficient operation of the device requires good electrical contact to the photoanode and photocathode materials, optimal transmission of the low-energy photons to the photocathode, and efficient mass transport of ionic species between both electrodes and to the gas phase. To meet these requirements, the semiconducting light absorbers of both photoelectrodes must be deposited on porous, electrically conducting and optically transparent scaffolds. More precisely, the photocathode will require the deposition of a p-type semiconductor with an appropriate band gap and an efficient catalyst for HER.



**Figure 1.13.** Envisioned tandem device for photoelectrochemical water splitting (FTO: Fluorine-doped tin oxide and HTL: Hole Transporting Layer).

### 1.4.3 PEM-PEC photocathode engineering

- Gas diffusion layer (GDL) for PEM-PEC system

One of the challenges addressed is the need for a transparent porous conductive GDL. GDLs are typically used in electrochemical applications (fuel cells or electrolyzers), where the reactant and/or the product are gaseous species, to reduce mass transport limitations (gas flow and ionic resistance), especially upon scale up.

In existing PEM technologies, GDLs used such as Ti felt and carbon fiber paper/cloth are opaque (**Table 3**). Ti felt possesses high mechanical strength and surface area, and carbon fiber paper is flexible; however, in addition to their low transmittance, both materials are unable to sustain highly oxidative conditions. W mesh, which is more transparent due to holes, has high mechanical properties, but suffers from poor surface area well as oxidation. However, in the case of the PEM-PEC cell, the incoming light should be absorbed primarily by the photoabsorber. It is crucial for the photoanode as the front electrode to be transparent to transmit the low-energy photons to the photocathode. Moreover, the transparency of the photocathode support would also allow light absorption on both side of the electrode, maximizing the number of photons transmitted through the entire electrode surface.

**Table 3.** Characteristics of typical commercial porous conductive substrates.

	Ti felt	Carbon cloth	W mesh
Transparency	opaque	opaque	opaque (light transmission through the holes)
Surface area	High	Medium	Poor
Mechanical properties	High	Flexible	High
Stability	Oxidize at high positive potential	Oxidize at high positive potential	Oxidize at high positive potential

- PEM-PEC photocathode

Although several parts of the cell such as the photoanode, photocathode, and the PEM assemblies need to be studied, this work will focus predominantly on the development of the photocathode.

As mentioned in section 1.4.2., a p-type material able to reduce water to hydrogen is required as a photoabsorber coating for the photocathode. Over the past decades, a plethora of p-type semiconductors have been developed for PEC applications. Several promising materials have been identified by the European Sun-to-X consortium, including WSe<sub>2</sub>,<sup>67,108,109</sup> Cu<sub>2</sub>O,<sup>48,68,79,80,110</sup> and BHJ (organic semiconductor).<sup>63,87</sup>

The most promising material in terms of HER performance and processability will be selected to be implemented in the PEM-PEC cell. Apart for the material choice, the material deposition is a key challenge to ensure a high performing photocathode. Indeed, most methods are optimized to

process these materials into films on a flat, transparent conductive substrate such as FTO-coated glass (i.e., certain methods cannot be applied to a porous substrate). Accordingly, the appropriate HER catalyst will be chosen depending on the material used. The method of deposition of the catalyst could also be a challenge, due to the novelty of the porous substrate. Thus, solution process engineering for both semiconductor and catalyst deposition will be required. The HER in the liquid phase will have to exhibit acceptable photocurrent to guarantee the performance in the gas phase. Indeed, in the gas phase some limitations such as lower amount of electrolyte, proton transport through the membrane, and mass transport that potentially drops the overall performance must be mitigated. Finally, the integration in the PEM-PEC cell will be evaluated to demonstrate the possibility to produce hydrogen using humid air and solar energy.

## Chapter 2     A novel Transparent Porous Conductive Substrate for photoelectrode application

The idea of combining an existing technology such as polymer exchange membrane (PEM) electrolyzer with a photoelectrochemical (PEC) system, could lead to an effective way to use directly solar energy to convert water vapor (e.g. in humid air) to hydrogen.<sup>111</sup> The PEC technology uses semiconductor photoelectrodes that absorb sunlight to generate photo-potential to drive water electrolysis. For such technology, a gas diffusion layer is required as the core of the electrode. Gas diffusion layers (GDLs) are porous substrates with a high specific surface that are electrically conductive and have sufficient pore size to not restrict gas flow through the support ( $> 1 \mu\text{m}$ ). GDLs are typically used in electrochemical applications (e.g., fuel cell or electrolyzer) where a high surface area is needed to ensure a large rate of electrocatalysis and the flow of gaseous species. The structure of the GDL reduces mass transport limitations such as gas flow and ionic resistance,<sup>112</sup> especially upon scale up. However, the existing GDLs are not transparent, while it is a key requirement for a PEM-PEC photoelectrode substrate. Thus, we developed a novel type of transparent porous conductive substrate (TPCS) based on FTO-coated quartz fibers. The transmittance, porosity, conductivity, and robustness of the support was characterized with a view to evaluate the TPCS potential and scope for growth. The TPCS exhibits  $> 35\%$  transmittance, and a resistivity of  $20 \Omega \cdot \text{sq}^{-1}$ . Moreover, using hematite ( $\alpha\text{-Fe}_2\text{O}_3$ ) as a model semiconductor material, we demonstrated for the first time, the use of the TPCS as a support for photoelectrode applications. The hematite-TPCS photoanode exhibited a photocurrent of  $1.6 \text{ mA} \cdot \text{cm}^{-2}$  at  $1.6 \text{ V}$  vs. RHE in liquid  $1\text{M NaOH}$  electrolyte.

This chapter is based on the following patent: Scalable Method for the Production of Transparent Gas Diffusion Layers EP21306880, M. Caretti, H. Johnson, JH. Yum, E. Mensi, S. Kinge, K. Sivula. Patent submitted (21.12.2021)

## 2.1 State of the art

In a traditional PEM electrolyzer cell, GDLs are typically carbon-based or metallic (e.g. Ti felt, Ni foam) porous supports, which are intrinsically non-transparent.<sup>17</sup> For PEM application, the conductivity and the porosity of the electrode are essential; however, there is no requirement in terms of transparency. The non-transparent nature of the available GDL is limiting in photo-electrochemical applications. For example, light absorption by the GDL itself represents a parasitic light loss, and it prevents configurations where two photoelectrodes are placed one in front of the other, in a so-called tandem configuration,<sup>113</sup> since the light cannot reach the back electrode.

Therefore, in the case of a PEM-PEC cell, the need for the gas diffusion layer to be transparent is crucial, especially for the front photoanode side. Similar to a standard PEC tandem cell, the photoanode is placed as a front absorber in a PEM-PEC cell (see section 1.4.3, Figure 1.13). The electrode substrate must be transparent enough to let a sufficient number of photons reach the photocathode surface. Similarly, the conductive support used for the photocathode side must be transparent to limit the parasitic absorption by the electrode support and then to maximize the absorption of the semiconductor. Thus, the few attempts<sup>96,111,114–116</sup> for performing water splitting in the gas phase using a PEM-PEC cell were limited to a single photoanode configuration with a Pt/C cathode. In this case, a metal felt (Ti or W-based) coated with n-type semiconductor such as  $\text{TiO}_2$ ,<sup>96,111,114–116</sup>  $\text{WO}_3$ ,<sup>111</sup>  $\text{SrTiO}_3$ ,<sup>117</sup> or  $\text{BiVO}_4$ <sup>106,118</sup> were used as photoanode to perform water oxidation in the gas phase while a Pt/C electrode was used for hydrogen production.

In a traditional liquid electrolyte tandem PEC device, the front photoelectrode material is coated on a conductive monolithic flat substrate such as fluorine-doped tin oxide (FTO) coated glass. FTO glass is used in the design of PEC tandem cell for its high transmittance (80%) and sufficient conductivity ( $5 - 100 \text{ } \Omega \cdot \text{sq}^{-1}$ ).<sup>119</sup> However, FTO glass is not porous, and subsequently cannot be used as a gas diffusion layer. Another disadvantage of monolithic substrates compared with GDLs, is the lack of material surface area. When charge carriers are generated in photo-absorbing materials, they have a limited diffusion length before the electrons and holes recombine. The thickness of the film must be less than the diffusion length to prevent loss of performance due to charge recombination. For materials with a low light absorption coefficient and low diffusion length, this means multiple layers of the material must be deposited onto individual monolithic substrates to absorb the maximum amount of light. However, this quickly becomes impractical when multiple layers are required particularly when considering a scaled device. In contrast, a GDL intrinsically provides a high specific surface area which allows a large amount of light-absorbing materials compared to a monolithic substrate.

In summary, in the current PEM electrolyser technology the available substrates are not transparent while in the traditional PEC water splitting cells, the employed substrates are not porous. Therefore, there is a clear need to develop a transparent GDL to enable the PEM-PEC technology and expand the options for implementation of direct solar-to-hydrogen technologies. Herein, we report a facile method to fabricate transparent porous conductive substrates (TPCSs) using quartz fibers template followed by FTO coating. We evaluated the key factors to achieve our best TPCS, such as



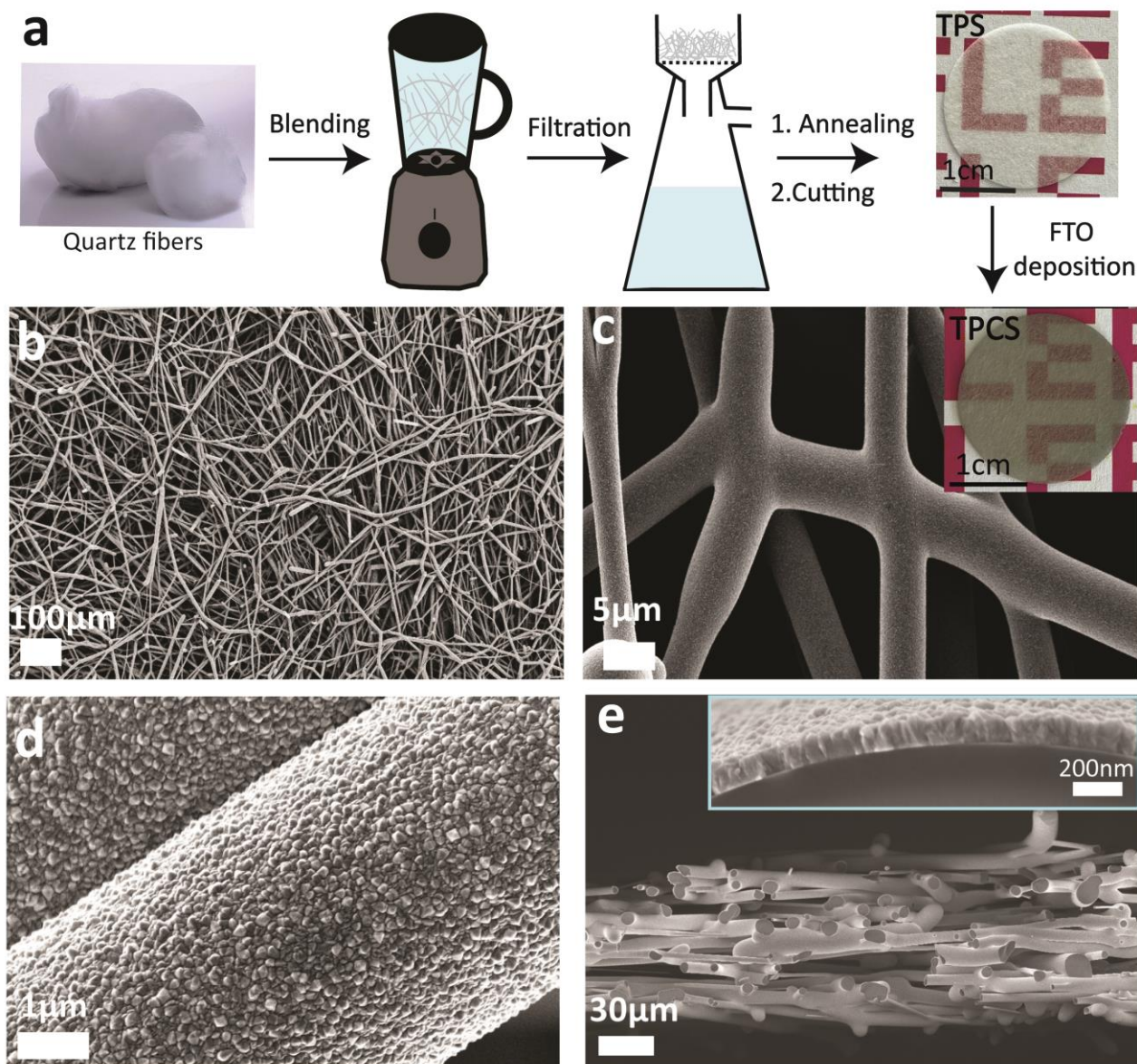
optimization of the TPS processing and FTO coating. The characteristics in terms of transparency, conductivity, porosity, and robustness were determined to gain insight into physical properties of the novel transparent support. Next, we chose hematite ( $\alpha\text{-Fe}_2\text{O}_3$ ) as an appropriate model material to evaluate the possibility of using the TPCSs as a large surface area template for photoelectrode applications. Hematite has been widely investigated as n-type semiconductor<sup>60,61,120–125</sup> (band gap,  $E_g = 2.0\text{--}2.2$  eV) photoanode material for water oxidation due to its earth-abundance, light absorption properties and chemical stability. However, as metal oxide, hematite suffers from poor optoelectronic properties such as poor majority carrier conductivity and short minority carrier diffusion length (2–4 nm) that limits its performance.<sup>121</sup> We showed that the use of the TPCS is a potential route to overcome these charge carrier diffusion length limitations with hematite photoanodes.

## 2.2 TPCS as a new photoelectrode template

### 2.2.1 TPCS fabrication

We developed a process to fabricate a novel type of GDL composed of quartz fibers coated with FTO. The first step aims to produce a transparent porous template that could be coated afterwards by a conductive layer. We used a fused quartz fiber template to ensure transparency and mechanical strength of the support. The quartz fibers are composed of  $\text{SiO}_2$  and show high-temperature resistance (up to 1300 °C) and chemical stability.

The preparation of the transparent porous substrates (TPSs) is illustrated in **Figure 2.1**. Briefly, the fibers are processed by a blending step (30 seconds) of a quartz fiber (i.e., commercial quartz wool) aqueous suspension to reduce the fiber length (e.g., to  $256 \pm 176$   $\mu\text{m}$ , figure S2.1). Then, the quartz fiber suspension is filtered, and the resulting filter cake is annealed at 1350 °C. At high temperature, the quartz will deform, transitioning from solid to a plastic-like behaviour, also called softening point, when the sample has lost the sharpe edge.<sup>126</sup> The annealing step is essential to improve interconnection among the fibers in a robust 3D-network (see Appendix 2, Figure S2.2). As quartz is an electrically insulating material, the TPS were made electrically conductive by coating a transparent conductive layer. Fluorine-doped tin oxide (FTO), a well-known transparent conductive oxide was selected as the conductive layer. FTO is widely used as conductive coating for semiconductors and solar industry and can be easily deposited by Atmospheric Pressure Chemical Vapor Deposition (APCVD).



**Figure 2.1.** Illustration of TPCS process (a) schematic of the TPCS procedure (b-e) SEM image of a TPCS, (b-d) top view, (e) cross-sectional image and zoom on a fiber cross section.

Therefore, the FTO deposition was conducted on the TPCS by APCVD. The FTO deposition set-up (Appendix 2, Figure S2.3) consists of a two-zones oven. The precursors (MBTC for monobutyltin trichloride and trifluoroacetic acid) are pre-heated in the first zone in presence of  $O_2$  and water. The deposition takes place on the substrate in the second zone at 600 °C. In **Figure 2.1**, we can see the photographs of the TPS and TPCS, before and after FTO deposition respectively. After FTO coating, the TPS becomes conductive and will be henceforth identified as the transparent porous conductive substrate (TPCS). The high transparency was well maintained after FTO deposition, and the quantitative analysis will be discussed later. Scanning electron microscopy (SEM) was used to study the morphology of the resulting TPS and TPCS. SEM images were taken after FTO deposition for a better resolution. We can see that the TPCS has an open porous morphology in **Figure 2.1b**. Additionally, due to the thermal treatment, the fibers are well connected (Appendix 2, Figure S2.3).

After FTO deposition, the FTO grains appear homogeneously coated on the fibers surface (**Figure 2.1d**). In **Figure 2.1e**, the TPCS cross-section exhibits a FTO layer coating through the entire thickness. Indeed, the quartz internal part appears darker and highlights well the lighter FTO coating on the fibers surface. The FTO layer thickness on the TPS, determined by SEM is around 100 nm (zoomed image **Figure 2.1e**).

### 2.2.2 Thickness effect

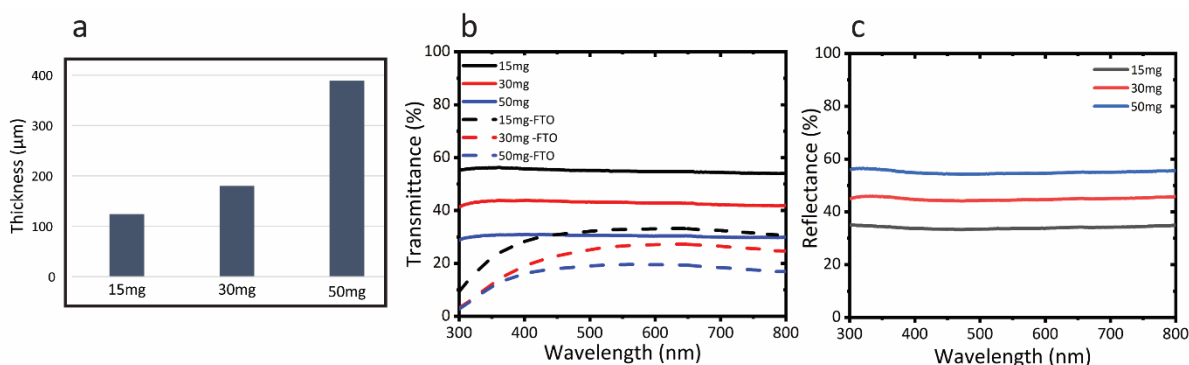
Subsequently, in **Figure 2.2 a**, we compared different thicknesses of TPSs prepared with an increase amount of quartz fibers, from 15 mg to 50 mg for a 22 mm diameter cake, to study the impact on the substrate transparency. The TPS thickness was evaluated by SEM cross-section after FTO coating for the reason mentioned previously. We can see in Figure S2.4 (appendix 2) that the FTO deposition for the thick TPSs does not penetrate the entire thickness resulting in partially coated support for 30 and 50 mg.

Transmittance and total reflectance measurements were performed to characterize the transparency of the TPS and are shown in **Figure 2.2b,c**. The direct transmittance evolves from 35% to 55% for 15 mg and 50 mg over 300 - 800 nm range, respectively. The transmittance loss exhibited by the TPSs comes from the higher reflectance of the 3D-network. Indeed, the total reflectance goes from 34% to 60%. It is not surprising that by increasing the thickness, the transmittance decreases due to additional reflection losses.

The morphology is not impacted by the thickness of the TPS, in Figure S2.5 (appendix 2), we can see that the structure remains highly porous, and the fibers are well-connected. Moreover, we also studied the impact of the FTO coating on the transmittance. In **Figure 2.2b**, we can see that for every fiber loading, the transmittance decreases after FTO coating. For our typical condition (15 mg), the transmittance drops from 55% to 30%.

For the rest of the study, we scaled-up the TPS process, by making a large TPS (7 cm diameter) and cut it in smaller TPSs (Appendix 2, Figure S2.6) to maximize the production of substrates and allow to tune the shape and size easily. Indeed, tuning the size and shape of the support can be appealing to fit in different types of applications/cells. Then, we used a condition of  $4 \text{ mg.cm}^{-2}$  fiber loading corresponding to 120 - 150  $\mu\text{m}$  thick TPS (i.e., close to 15 mg for a 22 mm-diameter TPS).

A low loading was chosen to maximize the transparency of the support. In addition, we demonstrated the conductivity of the support by measuring the sheet resistance average using a four-point probe set-up. The TPCS exhibits a value of  $20 \pm 3 \text{ } \Omega.\text{sq}^{-1}$  for the standard TPCS condition ( $4 \text{ mg.cm}^{-2}$ ), which is close to the  $14 \text{ } \Omega.\text{sq}^{-1}$  of commercial FTO glass.



**Figure 2.2.** TPS thickness tuning from 15 mg, 30 mg and 50 mg (a) Thickness variation (b) Transmittance measured over a range 300 - 800 nm for TPS and TPCS (dashed line) (c) Reflectance measured over a range 300 - 800 nm for TPS.

### 2.2.3 Annealing temperature effect

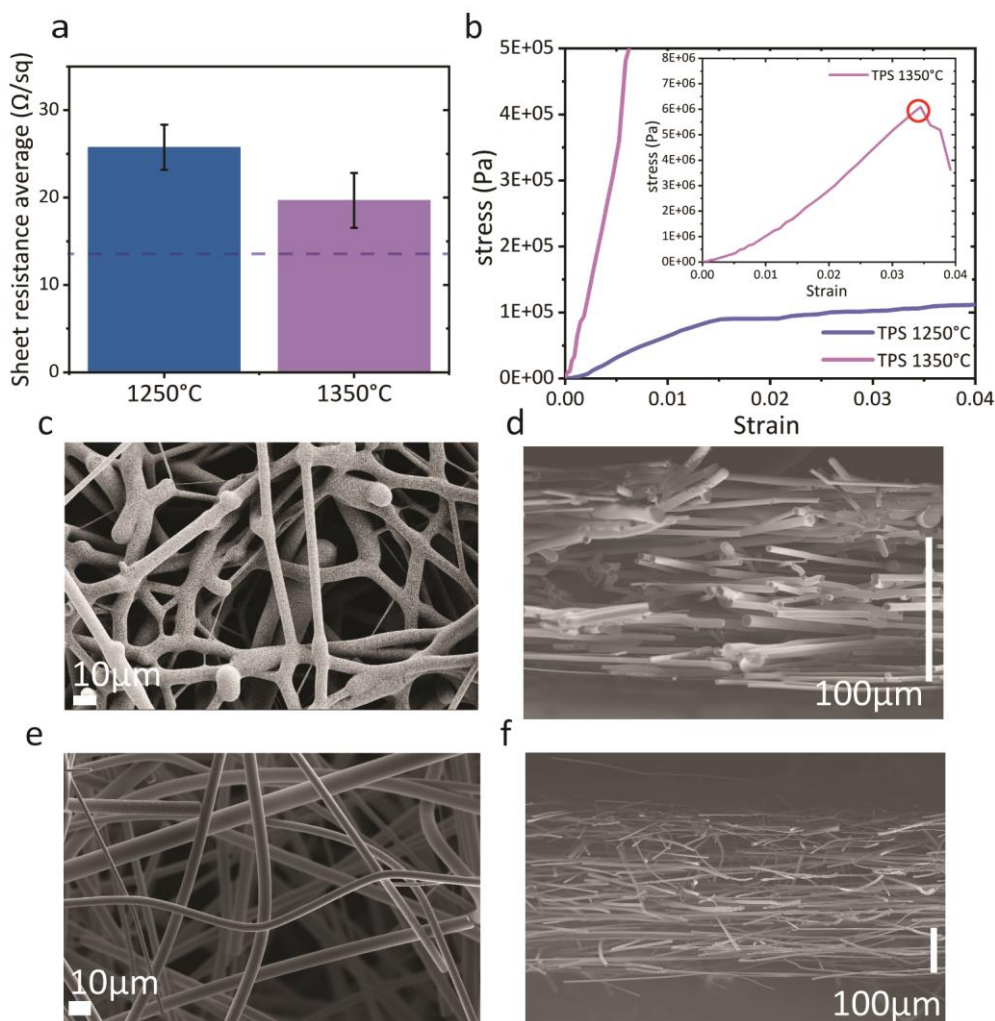
In order to study the possibility to tune the TPS morphology, we evaluated the impact of the annealing temperature. The TPSs annealed at 1250 °C and 1350 °C exhibit similar sheet resistance average after FTO coating. In **Figure 2.3a**, both TPCSs have sufficient conductivity with a sheet resistance average of  $26 \pm 3$  and  $20 \pm 3 \Omega \cdot \text{sq}^{-1}$  for 1250 °C and 1350 °C respectively.

Interestingly, for the same fiber loading ( $4 \text{ mg} \cdot \text{cm}^{-2}$ ) the morphology obtained differs in terms of thickness and fiber connectivity. The TPCS annealed at 1250 °C appears thicker ( $400 \mu\text{m}$ ), less dense and the connection of the fibers was relatively poor, as shown in **Figure 2.3 c-f**.

We hypothesized that the temperature is too low for the quartz to soften sufficiently and form a good network of fibers. In order to qualify and quantify the mechanical property, a biaxial flexure test was performed. It is a common method that consists in the flexural test of a disk to evaluate the robustness of a specimen. Following the procedures developed elsewhere<sup>127,128</sup>, we build an home-made set-up where the substrate is supported along its perimeter on a ring (glass vial with round border). The loading is done at the center by a small circular ring (a stainless-steel tube) operated by a screw-driven linear actuator (see Appendix 2, Figure S2.7).

The annealing temperature plays a key role in mechanical properties of the TPS. Indeed, the TPS annealed at 1250 °C exhibits a malleable structure. Similar to a plastic material, the TPS 1250°C requires a little amount of stress to produce a deformation. Instead of breaking, the sample wraps the load rod, resulting in a slight increase a stress when the strain increases **Figure 2.3b**. In contrast, the TPS annealed at 1350 °C, exhibits the typical strain-stress linearity for a brittle material, meaning that it breaks after a small plastic deformation. The Young's Modulus can be extracted by fitting the linear region before the failure point and characterise the stiffness of the material (see Appendix 2, calculation biaxial flexure text). The greater the Young's Modulus, the stiffer the material. A Young's Modulus of 0.20 GPa was calculated from the TPS annealed at 1350°C. The failure point, which is the maximum amount of stress a material can handle before fracture, can be read in **Figure 2.3b** (red circle). The failure point for the TPCS annealed at 1350°C is  $6.1 \times 10^6 \text{ Pa}$ , while it is  $1.1 \times 10^5 \text{ Pa}$  for the TPS annealed at 1250 °C. The effect of the annealing temperature is highlighted by this

experiment and demonstrates the possibility to tune the mechanical properties of the substrate. The malleable structure of the TPCS annealed at 1250 °C could be interesting in a cell using a compression-based electrical contact. However, the investigation was pursued with the TPCS annealed at 1350 °C as it will be easier to connect electrically and will be explained further.



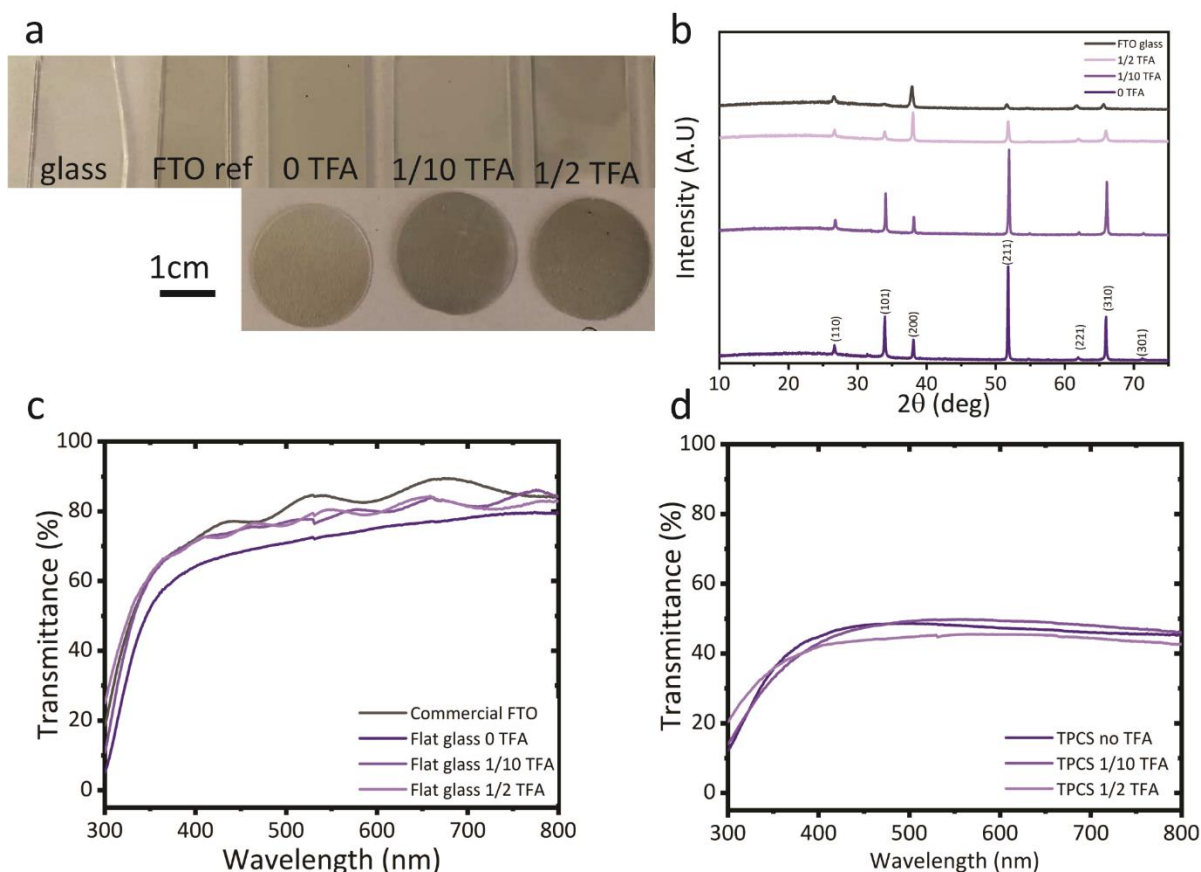
**Figure 2.3.** Comparison annealing temperature (a) sheet resistance average (b) stress-strain curve from bi-axial flexure test, showing the failure point (red circle) (c-d) SEM images top view and cross sectional for TPCS 1350 °C (e-f) SEM images top view and cross sectional for TPCS 1250 °C.

#### 2.2.4 FTO deposition study

Since the deposition of the FTO clearly affects the transparency of the resulting TPCS, the conditions of the FTO deposition were further investigated to optimize the conductivity and the transparency on both flat aluminium-borosilicate glass (as a control) and TPS ( $3 \text{ mg}\cdot\text{cm}^{-2}$  loading). Lower fiber loading was used to minimize the impact of the thickness and maximize the effect of the FTO coating on the resulting transmittance. In **Figure 2.4a**, a photograph of commercial borosilicate glass, FTO glass, and of the samples prepared by our APCVD setup for different conditions are displayed. Indeed, we can tune the F-doping of the FTO layer by tuning the amount of trifluoroacetic acid (TFA), one of the APCVD precursors, during the deposition. The TFA plays a key role as it is responsible for



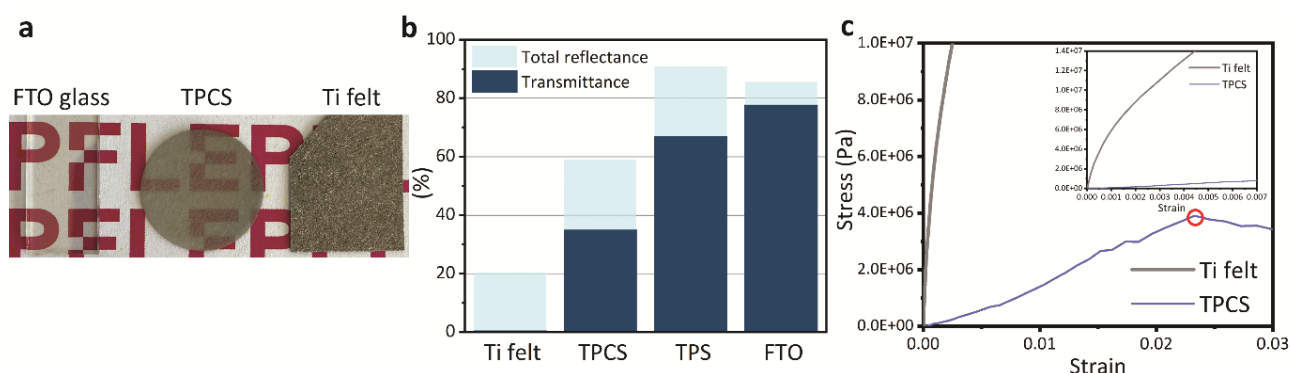
the F-doping (e.g., conductivity) of the tin oxide layer. Moreover, it has been shown that for high fluorine doping, the FTO layer become less transparent<sup>129</sup>. Indeed, we observed that by increasing the amount of TFA in the mixture TFA/water, the samples appear darker, which could be detrimental for the transparency. However, the transmittance is relatively less dependent on the TFA amount for the TPCSs than flat FTO glass as it can be seen in **Figure 2.4a**. The **Figure 2.4b** shows the XRD patterns of the films deposited and the FTO commercial reference. Typical SnO<sub>2</sub> peaks exhibits orientation in (110), (101), (200), (211), (221), (310), and (301). Fluorine doping affects the grain orientations together with the film thickness, as it has been reported previously<sup>130,131</sup>. By increasing the TFA amount, the peaks orientation evolves and give a similar spectrum than the commercial FTO glass. The intensity of the (200) diffraction peak becomes more intense with TFA content compared to the (211) and (101) peak. In figure S2.8 (appendix 2), the resistivity measurement shows that all the samples have a great conductivity, between 5 - 10±2 Ω.sq<sup>-1</sup> for flat substrates and 12 - 29±4 Ω.sq<sup>-1</sup> for TPCSs, similar to commercial FTO glass (14 Ω/sq). The optimized condition in term of F-doping used for this work is water:TFA at 1:2 (v:v). However, further optimizations will have a potential to balance the crystallinity and the transmittance.



**Figure 2.4** (a) Photograph of samples, flat borosilicate glass, commercial FTO glass reference, flat glass substrate, and TPCS deposited with different amount of TFA in the mixture water/FTA (v/v), (0, 1/10, 1/2) (b) XRD diffractograms of deposition on flat glass substrate and FTO glass commercial reference (c) Direct transmittance measurement for flat substrate (d) Direct transmittance measurement for TPCS.

## 2.3 Comparison between conductive substrates

Although a significant loss of transmittance can be observed upon FTO coating as shown in **Figure 2.5a,b** compared to the TPS, the transmittance of the TPCS (35%) is still higher than the commercial Ti felt (0%). FTO glass remains the best support in terms of transparency, but it is not porous, therefore not adapted as a gas diffusion layer. The TPCSs are so far the only existing GDL able to transmit up to 35% of the light. Characterizations of the typical TPCS were conducted to be able to identify any point of improvement. The porosity was estimated at  $90 \pm 5\%$  using Archimedes principle<sup>132,133</sup>, which matches well with the calculation using quartz density (i.e, 89%, see Appendix 2, porosity calculation). A specific surface area of  $0.41 \text{ m}^2 \cdot \text{g}^{-1}$  was measured by Brunauer-Emmett-Teller (BET) theory. Therefore, a typical TPCS is a circle with a diameter of 22 mm and composed of 15 mg of quartz fibers, which means that it has an effective surface area of  $60 \text{ cm}^2$  for geometrical area of  $3.8 \text{ cm}^2$ . The resistivity was measured using a 4-probes set-up. The FTO coating leads to a highly conductive 3D porous substrate with a resistivity of  $20 \pm 3 \Omega \cdot \text{sq}^{-1}$  while it is  $14 \Omega \cdot \text{sq}^{-1}$  for commercial FTO glass. The TPCSs have a slightly higher resistivity than commercial FTO; however, it is completely suitable for photoelectrode applications. In terms of robustness, we compared the stress-strain curves of a Ti felt and a TPCS using our bi-axial homemade biaxial flexure test. The stress-strain graph highlights a clear difference between the Ti felt and the TPCS as it can be seen in **Figure 2.5c**. Ti felt shows great mechanical properties. As Titanium has a Young's Modulus of 120 GPa,<sup>134</sup> the set-up was not adapted to characterize such highly robust material, however it was useful as a method of comparison. We could determine the Young's Modulus of the TPCS after fitting the linear region of the stress-strain curve, ca. 0.18 GPa and a failure point at  $3.9 \times 10^6 \text{ Pa}$ . After FTO deposition, the robustness seems to decrease slightly (Figure S2.9, appendix 3). In conclusion, the mechanical properties of the TPCS could be a point of improvement in future work in order to ensure long-term mechanical stability.



**Figure 2.5.** Figure Conductive support comparison between commercial FTO glass, TPS ( $4 \text{ mg} \cdot \text{cm}^{-2}$ ), TPCS ( $4 \text{ mg} \cdot \text{cm}^{-2}$ ) and Ti felt (a) photograph (b) Transmittance and total reflectance measurement (c) stress-strain curve from bi-axial flexure test.

## 2.4 TPCS as photoelectrode support: hematite model

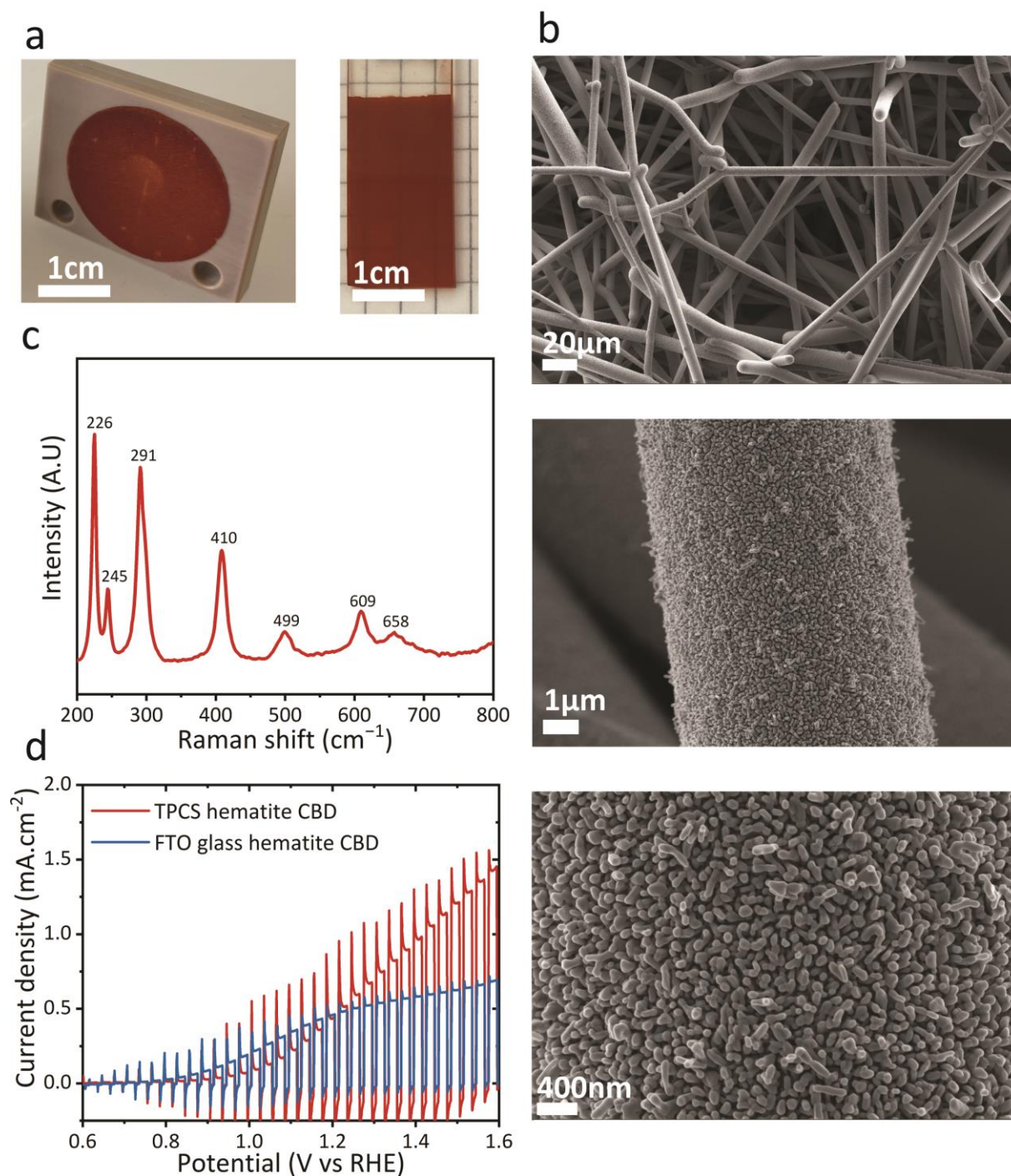
Hematite ( $\alpha\text{-Fe}_2\text{O}_3$ ) was chosen as model material to verify the utility of the TPCS as GDL for photoelectrode application. Indeed, hematite is a well-known n-type semiconductor for the PEC

oxygen evolution reaction. The ideal thickness suggested by the small carrier harvesting depth would be a 10/20 nm-thick film. As the light absorption would be decreased in this case, scientist developed nanostructured morphology deposited by spray pyrolysis<sup>135</sup>, electrodeposition<sup>136,137</sup>, Atmospheric Pressures Chemical Vapor Deposition<sup>60,61,138</sup> (APCVD) or Chemical Bath Deposition<sup>139,140</sup> (CBD). This type of structure provides a direct path for photogenerated charge carrier through the vertically oriented structure such as nanowires arrays. Moreover, the issue of the majority charge carrier transport and collection was solved by doping incorporation such as  $\text{Sn}^{4+}$ ,  $\text{Si}^{4+}$ ,  $\text{Ge}^{4+}$ . Despite the performance improvement by combining nanostructuring, doping and surface treatment, the photocurrent obtained is still far behind the theoretical value ( $12.6 \text{ mA}\cdot\text{cm}^{-2}$ ).<sup>60</sup> Another strategy would be to coat an extremely thin absorber<sup>121</sup> (ETA) layer on large surface area template. Lin *et al*<sup>141</sup> demonstrated a nanonet-based hematite heteronanostructures composed of  $\text{TiS}_2$  nanonet coated with hematite by atomic layer deposition (ALD), exhibiting  $1.6 \text{ mA}\cdot\text{cm}^{-2}$  at 1.23 V vs. RHE. In a recent study<sup>142</sup>, hematite was coated by aerosol assisted chemical vapor deposition (AA-CVD) onto highly-conductive and bulk porous  $\text{SnO}_2$  (Sb-doped) ceramic substrates, which could be more difficult to implement on the TPCS. Among all the deposition method, chemical bath deposition<sup>139</sup> (CBD) was applied for the TPCSs due to its process simplicity.

Following a procedure developed elsewhere, we successfully coated a homogenous hematite layer on FTO glass and on TPCS, as shown in **Figure 2.6a**. A teflon holder was used to maintain the TPCS vertically during the CBD (see appendix 2, Figure S2.10). The optimized condition was 10 min CBD at  $100^\circ\text{C}$  to obtain a thin hematite film on the TPCSs. The typical hematite nanowires cover the entire surface of the TPCS, as shown in the SEM images in **Figure 2.6b**. Thus, CBD seems to be an appropriate method to coat large surface area templates. After electrode fabrication, the samples were annealed at  $800^\circ\text{C}$  for 15 min. The Raman spectra exhibits the typical hematite characteristic Raman vibrations of hematite<sup>143</sup> as displayed in **Figure 2.6c**. We evidenced the with three oxygen-based vibrations at 226, 245,  $291 \text{ cm}^{-1}$ , three iron-based vibrations at 410, 499, and  $609 \text{ cm}^{-1}$ , and a symmetry-forbidden vibration appears at  $658 \text{ cm}^{-1}$ . The same deposition process was applied to flat FTO substrates in order to compare the PEC performance on flat substrate and the 3D-network such as the TPCSs.

To compare the PEC performance on the two different substrates, we examined the LSV characteristics in 1 M NaOH, under chopped 1-Sun illumination for both electrodes. A special clip composed of Au or Ta mesh was used to electrically contact the TPCS (see appendix 2, Figure S2.11). Firstly, the TPCS-hematite electrode exhibits photocurrent of  $1.5 \text{ mA}\cdot\text{cm}^{-2}$  at 1.6 V vs. the reversible hydrogen electrode (RHE). Therefore, the TPCS as photoelectrode substrate is validated by the hematite model experiment. Moreover, the performance is higher for TPCS compared to flat FTO, which might be due to the larger surface area of the TPCS. In addition, the thickness of the film determined by SEM, is around 130 nm (appendix 2, Figure S2.12a). It is important to mention that an extremely thin hematite layer of 20 nm would be more appropriate to benefit from the whole 3D-network surface area, maintaining electrode transparency.

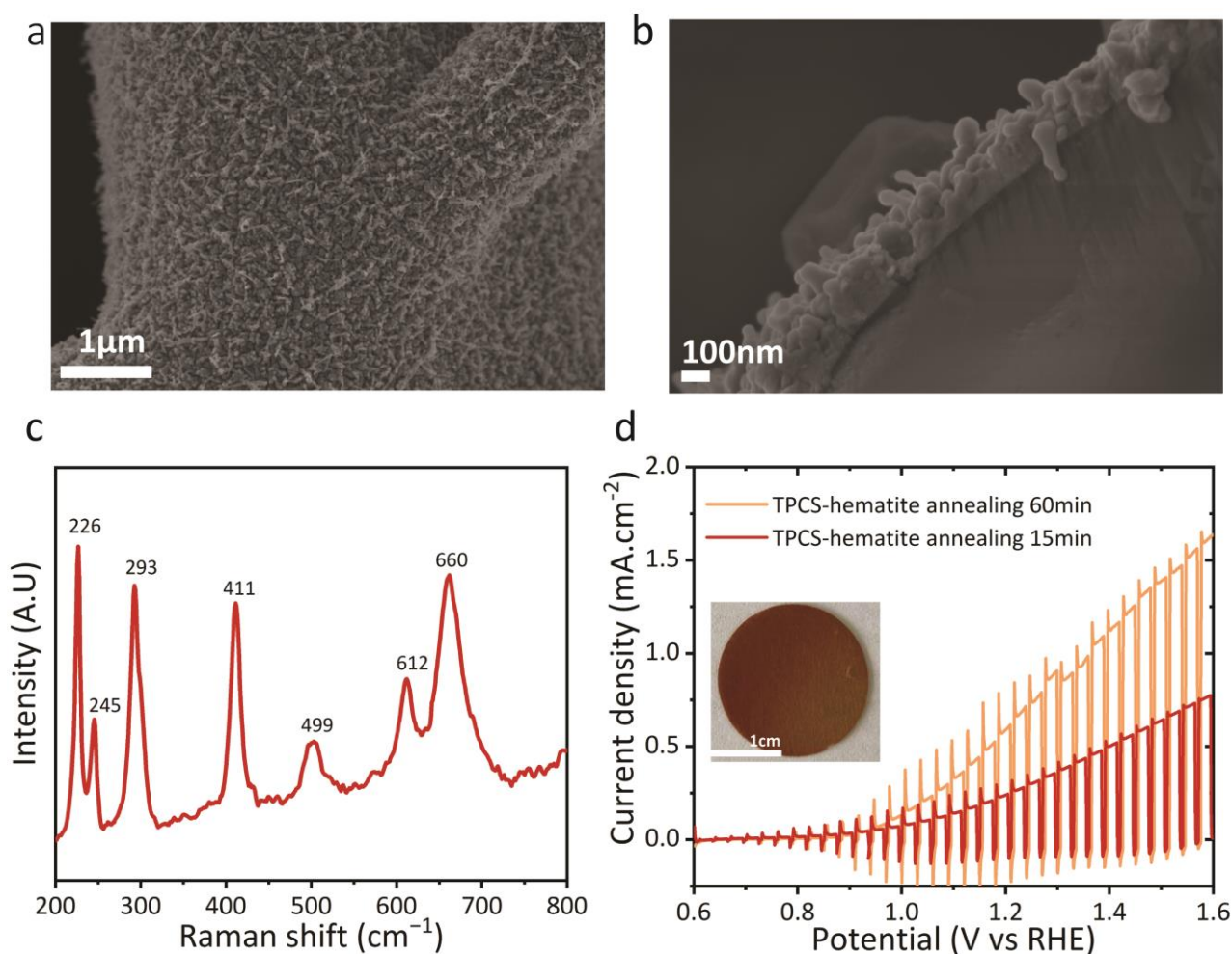




**Figure 2.6.** (a) photograph of hematite samples on TPCS and FTO glass (b) SEM image of hematite-coated TPCS (c) Raman spectra of the hematite film (d) LSV curves obtained in NaOH pH 13.6 under 1 sun illumination.

We coated a homogenous thinner hematite layer on the TPCS by CBD, following the procedure developed by Yang *et al.*<sup>140</sup> In their study they synthesized ITO@ $\alpha$ -Fe<sub>2</sub>O<sub>3</sub> core-shell nanowire array with a 34 nm thick hematite layer. In **Figure 2.7c**, The Raman spectra confirmed the formation of hematite with the characteristic Raman vibrations at 226, 245, 293, 411, 499, 612, and 660 cm<sup>-1</sup>. By following their procedure, we managed to decrease the size of the nanowire ca. 60 - 90 nm (appendix 2, Figure S2.12b). However, the nanowires length was not homogeneous throughout the

TPCS surface as it can be seen in **Figure 2.7a,b**. This could explain the decrease in the photocurrent obtained as not all the surface is covered by the photoactive material. Indeed, the hematite thin film on the TPCS reached  $0.7 \text{ mA.cm}^{-2}$ , while the thicker hematite version exhibited a photocurrent of  $1.5 \text{ mA.cm}^{-2}$  at  $1.6 \text{ V vs. RHE}$ . Interestingly, by increasing the annealing time from 15 min to 60 min, a great enhancement of the photocurrent, up to  $1.6 \text{ mA.cm}^{-2}$  was observed. Annealing at high temperature leads to Sn-doping of the hematite film by Sn (from FTO) diffusion as it has been highlighted in previous reports.<sup>120,144</sup> We hypothesized that the increase of the photocurrent correlated with the annealing time (Figure S2.13, appendix 2) is due to an higher doping of the hematite film or to a higher crystallinity, produced during a longer annealing time. As shown in **Figure 2.7d**, a higher photocurrent was obtained for TPCS compared to standard FTO glass (Figure S2.13b, appendix 2) for 15 min hematite annealing time. In conclusion, further experiments must be performed to improve the homogeneity of the thin hematite layer. Other method of deposition such as APCVD<sup>138</sup> or atomic layer deposition (ALD)<sup>124</sup>, to form an ultra-thin hematite layer on the TPCS should be investigated.



**Figure 2.7.** (a-b) SEM image of hematite-coated TPCS (thin version) (c) Raman spectra of the thin hematite film (d) LSV curves obtained in NaOH pH 13.6 under 1 sun illumination and photograph of the thin hematite-coated TPCS.

## 2.5 Conclusion

We demonstrated the fabrication of a novel transparent porous conductive substrate (TPCS). The TPCS consists in a typical circular electrode ( $4 \text{ mg.cm}^{-2}$  fiber loading) with a thickness of 120-150  $\mu\text{m}$ . However, the shape and the size could be tuned easily. The TPCS has a higher transparency than the commercial state of the art Ti felt, exhibiting a transmittance of 35% while Ti felt is opaque. The transparency could be improved by tuning the FTO deposition precursor conditions (e.g., F doping), the thickness of the FTO layer and the thickness of the TPS. Moreover, we also characterized the porosity, conductivity and the robustness of this support. The TPCS has an open porosity of  $90\pm 5\%$  and a resistivity of  $20\pm 3 \Omega.\text{sq}^{-1}$ , which makes it a good candidate for gas diffusion layer applications. Nevertheless, the mechanical strength must be improved in future work as we did not fully explore every condition to make different structure types. However, we also validated this support for photoelectrode applications with the hematite model. Hematite was successfully coated by chemical bath deposition on the fibrous support. The electrode exhibited a maximum photocurrent of  $1.6 \text{ mA.cm}^{-2}$  at 1.6 V vs. RHE in liquid 1M NaOH electrolyte. To conclude, the TPCSs could be used as a novel gas diffusion layer, especially in a gas phase solar-driven water-splitting cell where the transparency of the support is detrimental for the performance. Undoubtedly, the TPCSs would be useful in any electrolyzer or fuel cell system where stable large surface area electrode are required.

## 2.6 Experimental part

### 2.6.1 Chemicals

Quartz wool (2-5 $\mu\text{m}$ , Technical Glass Product), n-Butyltrichlorotin (98.0%, Fluorochem), Trifluoroacetic acid 99% (Sigma-Aldrich), Iron chloride  $\text{FeCl}_3.6\text{H}_2\text{O}$  (99+%, Acros), Iron nitrate  $\text{Fe}(\text{NO}_3)_3.9\text{H}_2\text{O}$  (99+% ) sodium nitrate  $\text{NaNO}_3$  (99+%, Acros), Sodium hydroxide NaOH (pure Reactolab) were used as received. Ti felt and FTO glass substrates were purchased from Bekaert and Solaronix, respectively.

### 2.6.2 TPS preparation

1 g of quartz wool (2-5  $\mu\text{m}$ ) was dispersed in 1 L of deionized (DI) water. The suspension was placed in a commercial blender for 30 seconds to reduce the wool to fibers. The fibers suspension was then filtered to remove the water, leaving a dry powder. A certain amount of the powder was redispersed in water, typically between 15 and 50 mg in 20 mL of DI water. The suspension was filtered to form a filter cake (22 mm diameter). The cake was annealed at 1350  $^{\circ}\text{C}$  (or 1250  $^{\circ}\text{C}$  if specified) for 2 hours, which is sufficient to connect the fibers at the intersections, whilst not melting the structure, forming a TPS. The scale up of this process allows to use larger fibers loading, after the blending step, typically 125 mg of fibers was redispersed in 1 L of DI water. The filtration of the suspension forms a 7 cm-diameter filter cake that is annealed at 1350  $^{\circ}\text{C}$ . After annealing, the large TPS can be cut into smaller pieces if relevant.

### 2.6.3 FTO deposition

The FTO deposition is performed by Atmospheric Pressure Chemical Vapor Deposition adapting a procedure developed elsewhere<sup>145,146</sup>. Briefly, a two-zone oven is used with a pre-heating zone at 200 °C and a deposition zone at 600 °C. The air flow (300 mL/min) bubbling in a diluted trifluoroacetic acid solution (TFA) (1/2 v/v TFA/water) directed into the pre-heating zone. In the pre-heating zone, the monobutyltin trichloride was vaporized at 200 °C. The gas precursor mixture is deposited on the substrate placed at the 600 °C zone inlet. The substrate can be a borosilicate glass with or without a TPS. For FTO deposition on a TPS, the glass piece acts as a support. The corrosive gas mixture is neutralized in a NaOH 1 M solution, located at the outlet.

### 2.6.4 Hematite model

Flat FTO substrate and TPCS were positioned vertically using a Teflon holder, in an aqueous solution containing 0.15 M iron chloride hexahydrate and 1 M sodium nitrate. A precursor film of  $\beta$ -FeOOH nanowires were grown by chemical bath deposition at 100 °C for 10min in a universal oven (Memmert UF 30 plus). The substrate immersed in the precursor solution was placed in the oven at room temperature and removed after the heating program when the oven cooled down to room temperature. After rinsing with deionized, these  $\beta$ -FeOOH thin films were introduced into a tube furnace (MTI OTF-1200X-S) preheated at 800 °C for 15 min to be transformed into hematite nanowires. For thin hematite layer coating, the precursor solution was prepared by mixing 0.02M  $\text{Fe}(\text{NO}_3)_3 \cdot 9\text{H}_2\text{O}$  in deionized water. The TPCS was placed in the precursor solution and kept at 90 °C for 2 h. Then, the  $\text{Fe}(\text{OH})_3$  compact thin films grown on the TPCS was washed with deionized water and the sample was introduced into a tube furnace (MTI OTF-1200X-S) preheated at 800 °C for 15 or 60 min to be transformed into hematite nanowires.

### 2.6.5 Characterizations

#### PEC characterization

Photoelectrochemical measurements were carried out with a computer controlled (EC-LAB V11.12) potentiostat (Bio-Logic SP-300) with a 3-electrode configuration: a hematite working electrode, a platinum counter electrode (0.25 mm diameter, 99.99%, chemPUR), and an Ag/AgCl reference electrode (ALS RE-1CP). For FTO glass, a cappuccino-type cell with an active geometric area of 0.25 cm<sup>2</sup> for the working electrode was used. The electrolyte used was NaOH 1M. For TPCS, a glass cell was used, and the current density was corrected by measuring the area exposed (0.4 - 1.3 cm<sup>2</sup>). A xenon arc lamp (Newport 66921, 450 W), calibrated to provide simulated AM 1.5 G solar irradiation.

#### TPCS characterization

UV-Visible spectroscopy was performed with a UV-vis spectrophotometer Shimadzu UV-3600. Resistivity measurement was done by a 4-probe set-up controlled by a LabVIEW program. Bragg-Brentano XRD measurements were carried out using a Bruker D8 Vario diffractometer equipped with a Johansson  $\text{K}\alpha_1$  ( $\lambda = 1.5406 \text{ \AA}$ ). SEM images were recorded with a Zeiss Merlin microscope.

Raman spectra were obtained with a LabRam spectrometer (Jobin Yvon Horiba). The excitation line was provided by an argon laser (532.19nm).

For measuring porosity, we used Archimede's principle<sup>132,133</sup> : "A body wholly or partly immersed in a fluid is buoyed up by a force equal to the weight of the fluid displaced". The measurement consists in measuring the mass of the specimen in air and in a fluid (water). The porosity can be calculated using the equation as follows:

$$V_{\text{apparent}} = \frac{W_{\text{air}} - W_{\text{soaked}}}{\rho_{\text{water}}}$$

$$\phi = 1 - \frac{\text{Solid phase volume}}{\text{Total bulk volume}} \times 100 = 1 - \frac{V_{\text{apparent}}}{V_{\text{total}}} \times 100 \quad (\%)$$

With  $W_{\text{air}}$  is the mass of the sample in air (mg),  $W_{\text{soaked}}$  is the mass of the sample in water (mg),  $\rho_{\text{water}}$  is the density of water,  $V_{\text{apparent}}$  is the volume of immersed sample (without the pores) (mm<sup>3</sup>),  $V_{\text{total}}$  is the volume total (pores included) of the sample (mm<sup>3</sup>) and  $\phi$  porosity of the sample.

Brunauer-Emmett-Teller (BET) surface area was calculated from N<sub>2</sub> physisorption isotherms collected with a Micromeritics 3Flex instrument. Before measurements, all materials were degassed overnight under vacuum (<10<sup>-3</sup> mbar) at 120 °C (10 °C/min ramp rate).

Robustness test was performed with a homemade bi-axial flexure test following the procedure developed elsewhere.<sup>128</sup> Briefly, the test was performed on circular TPS/TPCS or Ti felt, supported by an annular glass ring and loaded at the center. A stainless-steel rod was used as a circular loading device and the velocity was fixed at 1 mm.min<sup>-1</sup> using a dip coating system. The change in mass was monitored using a balance until the failure point (i.e., crack). The calculation used can be found in Appendix 2 (section Calculation biaxial flexure text).

## Chapter 3    Transparency and morphology control of Cu<sub>2</sub>O photocathodes via an *in-situ* electro-conversion

Cu<sub>2</sub>O is a model p-type semiconductor for photocathodes in photoelectrochemical (PEC) water splitting cells. However, major challenges remain in controlling its deposition into thin and homogeneous semi-transparent films. Herein, we report a new route to construct thin homogeneous Cu<sub>2</sub>O layers on transparent fluorine doped tin oxide (FTO) substrates via the *in-situ* electro-conversion of CuSCN to Cu<sub>2</sub>O. We highlight the morphology control of the resulting converted Cu<sub>2</sub>O thin-films while demonstrating that they maintain promising performance for solar-driven hydrogen production with a maximum incident photon to current efficiency (IPCE) reaching 60% (at 0 V vs. RHE and 450 nm) for a 180 nm-thick film and integrated solar photocurrents up to 4 mA.cm<sup>-2</sup>. In addition, altering the deposition conditions (e.g., applied potential, electrolyte compositions and pH) gives important insight into the mechanism and operation of the electro-conversion process.

This chapter is based on the following publication: “Transparency and morphology control of Cu<sub>2</sub>O photocathodes via an in-situ electro-conversion”, M. Caretti, L. Lazouni, M. Xia, R.A. Wells, S. Nussbaum, D. Ren, M. Grätzel, K. Sivula. ACS Energy Letters, 2022.

### 3.1 Cu<sub>2</sub>O photocathode progress and challenges

Cuprous oxide, Cu<sub>2</sub>O, is a promising candidate as a photocathode material due to its band gap energy ( $E_g = 2.0\text{-}2.1$  eV), atomic abundance, and facile preparation by low-cost methods (e.g., electrodeposition<sup>10</sup>). As such, its ability to operate as the light-harvesting material in H<sub>2</sub>-producing or CO<sub>2</sub>/N<sub>2</sub> reducing photocathodes has been widely investigated.<sup>11–15</sup> Stabilized operation and water-reducing photocurrent densities close to the theoretical maximum for this material have been achieved by using electron transport layer (ETL) and protective over-layers (e.g. Ga<sub>2</sub>O<sub>3</sub>/TiO<sub>2</sub>)<sup>16–18</sup> and nano/micro-structuring approaches,<sup>19,20</sup> respectively. However, in order to assemble a high-STH-efficiency PEC tandem cell, the Cu<sub>2</sub>O photocathode should be used in a stack as the top cell given its  $E_g$  (while a photoanode with  $E_g = 1.2\text{-}1.5$  eV would serve as the bottom cell).<sup>5,21</sup> Thus, control of the Cu<sub>2</sub>O thickness and morphology is essential in order to tune light absorption and transmission.

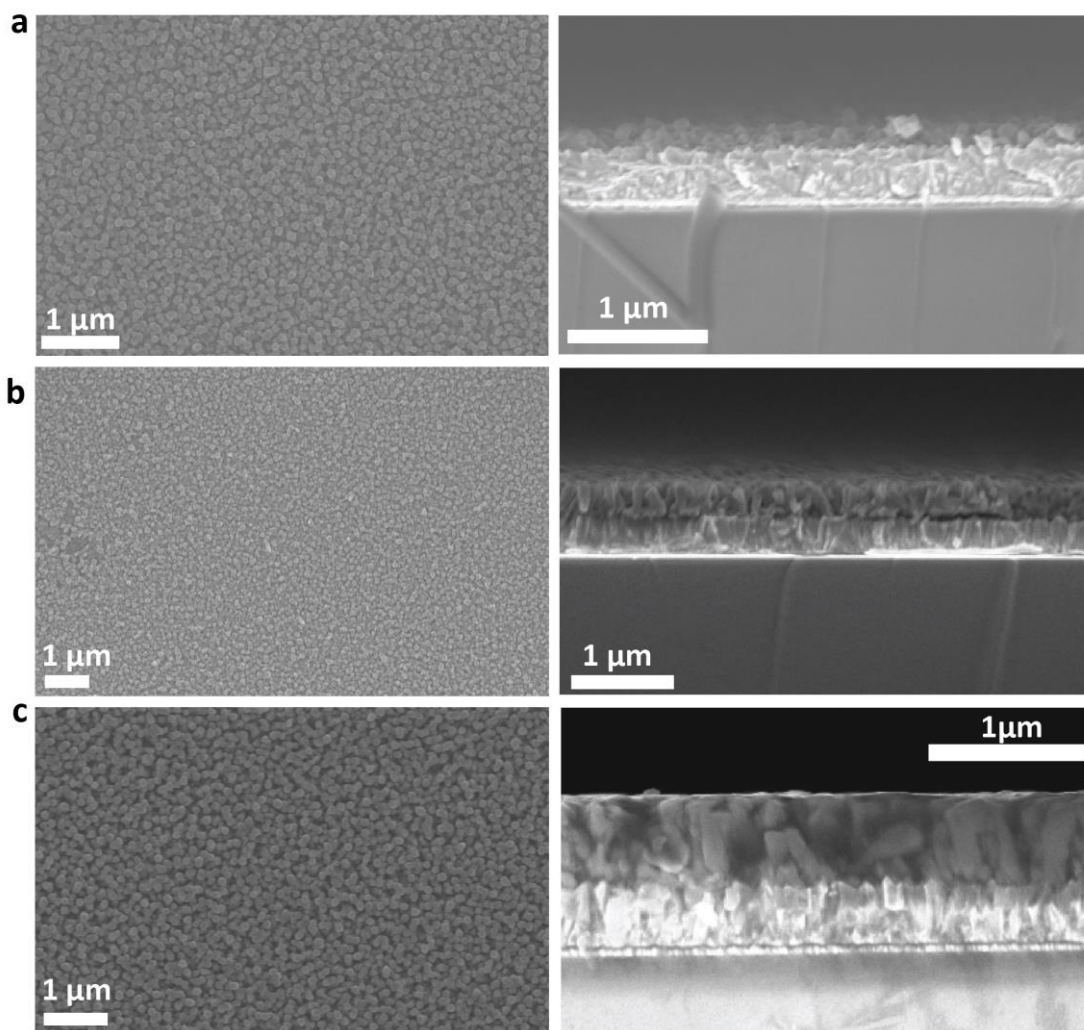
Typically, Au-coated substrates are used to electrodeposit Cu<sub>2</sub>O since this interface forms a low-resistance ohmic contact and also provides a suitable surface for the electrodeposition of Cu<sub>2</sub>O, leading to homogeneous nucleation and good coverage. However, opaque Au substrates are not suitable as the top-cell in a tandem configuration.<sup>22</sup> As such, alternative transparent underlayers for Cu<sub>2</sub>O have been recently developed.<sup>23,24</sup> Nevertheless, electrodeposited Cu<sub>2</sub>O generally results in the formation of micron-sized cubic crystals<sup>25</sup> that strongly scatter incident light. Since this light scattering can lead to significant losses in transmission to the bottom cell, as demonstrated with Cu<sub>2</sub>O<sup>26</sup> and other oxide semiconductor photoelectrodes,<sup>27</sup> there remains a general need to develop methods to control the morphology and transparency of Cu<sub>2</sub>O formed by electrodeposition. This is especially important for the application of Cu<sub>2</sub>O in extremely-thin-absorber type photoelectrodes, where a large surface area conductive template is coated with an ultrathin Cu<sub>2</sub>O layer. While promising performances have been obtained with Cu<sub>2</sub>O grown on an opaque Cu 3D-network,<sup>28,29</sup> the demonstration of a highly photo-active ultrathin (< 200 nm) Cu<sub>2</sub>O layer electrodeposited on transparent conductive substrates has not been yet achieved.

### 3.2 Potential drop identification

Herein we report that electrodeposited CuSCN can be used as precursor for the electro-conversion into Cu<sub>2</sub>O under specific electrochemical conditions. Our discovery resulted from work on the CuSCN/Cu<sub>2</sub>O heterojunction, which has been established in photocathodes<sup>24,30</sup> and in photovoltaic devices.<sup>31</sup> However, our efforts to investigate conditions for the subsequent electrodeposition of Cu<sub>2</sub>O on CuSCN led to the surprising observation of an electro-conversion process. We show that the electro-conversion allows for a novel morphological control of Cu<sub>2</sub>O film on transparent conductive substrates and we further investigate the key parameters required to drive the *in-situ* CuSCN electro-conversion. Finally, we highlight the optoelectronic and photoelectrochemical advantages of the converted Cu<sub>2</sub>O photocathode over the direct deposition on transparent substrates.

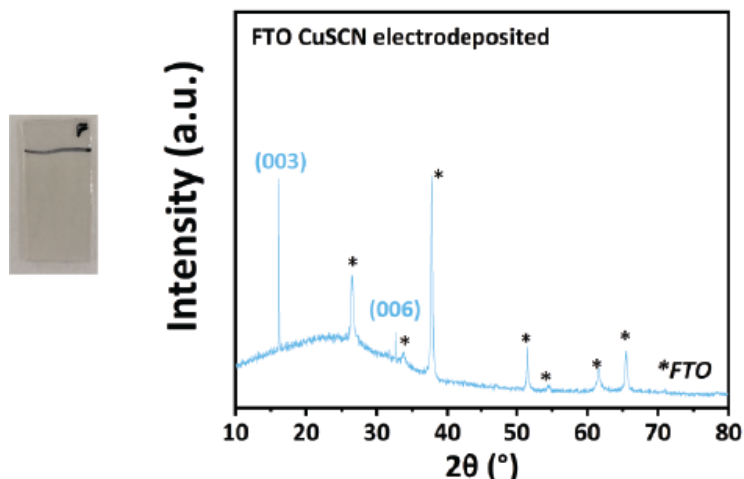


Following common procedures (see experimental methods section 3.6) a layer of CuSCN was first electrodeposited on transparent F-doped SnO<sub>2</sub> (FTO) coated glass substrates using a constant applied potential of  $-0.3$  V vs. Ag/AgCl with a CuSO<sub>4</sub> and KSCN-based electrolyte. The resulting layer exhibits a nanopillar structure (see scanning electron micrograph, SEM, **Figure 3.1**) and the crystal structure is verified by X-Ray diffraction (XRD), as shown in **Figure 3.2**. The thickness can be tuned by varying the deposition time with a 2-min and 10-min electrodeposition leading to thicknesses of 140 nm and 570 nm, respectively (**Figure 3.1**).



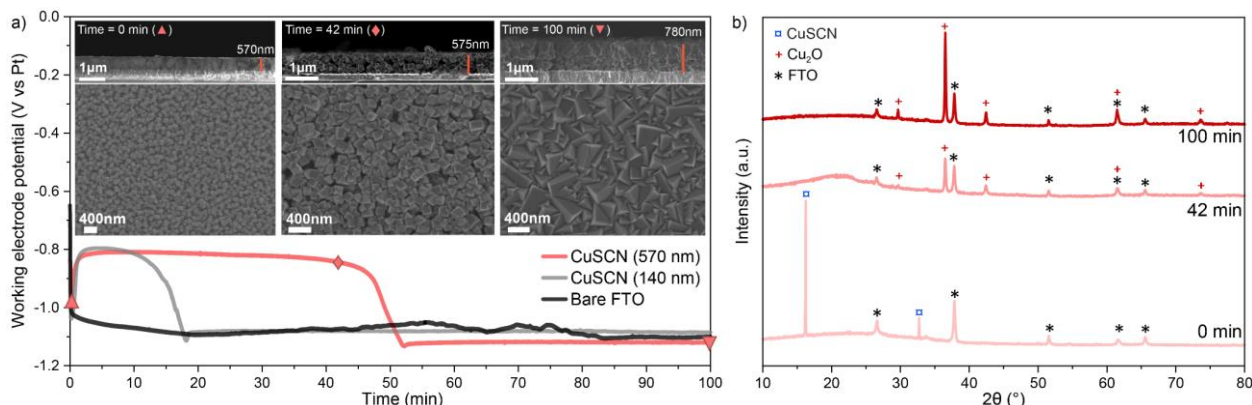
**Figure 3.1.** SEM images (top view, left, and cross-section, right) of CuSCN films deposited at  $-0.3$  V vs. Ag/AgCl for various times (a) 2 min (b) 5 min (c) 10 min.





**Figure 3.2.** Photograph (left, substrate width 12 mm) and XRD pattern of 5 min-electrodeposited CuSCN film.

During the subsequent electrodeposition of Cu<sub>2</sub>O with a copper(II) lactate complex, but using a higher pH of 12 compared to previous work,<sup>24</sup> an interesting behavior is observed during constant-current electrodeposition as shown by chronopotentiometry ( $-0.1 \text{ mA.cm}^{-2}$ ) in **Figure 3.3a** for electrodeposition on bare FTO glass compared to thick (570 nm) or thin (140 nm) layers of CuSCN on FTO.

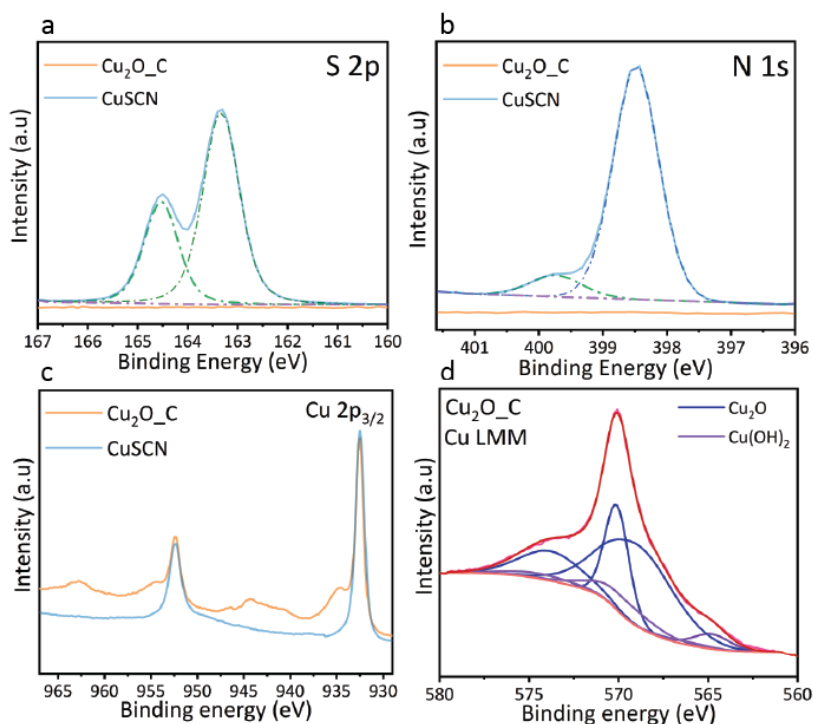


**Figure 3.3.** (a) Potential evolution during Cu<sub>2</sub>O electrodeposition by chronopotentiometry at  $-0.1 \text{ mA cm}^{-2}$  on bare FTO, and FTO/CuSCN substrates with different thicknesses of CuSCN. SEM images (top-view and cross section) are shown in the insets for the FTO/CuSCN (570 nm) substrate at various times during the electrodeposition (0, 42, and 100 min) and the corresponding points on the chronopotentiometry curve are indicated. (b) XRD patterns of 570 nm CuSCN film during in-situ electro-conversion at time = 0 min, 42 min and 100 min.

For the same current density during the electrodeposition ( $-0.1 \text{ mA.cm}^{-2}$ ), the potential evolves differently for bare FTO and CuSCN/FTO substrates. When bare FTO is used, the potential remains constant at ca.  $-1.1 \text{ V vs. Pt}$  during a 100 min deposition. However, a less negative potential ( $-0.8 \text{ V}$ ) is initially observed for CuSCN-coated FTO followed by a shift to  $-1.1 \text{ V}$  at around 15 and 48 min for the thin (140 nm) and thick (570 nm) CuSCN substrates, respectively. The obvious correlation

between the duration of the less negative potential segment of the deposition to the thickness of the CuSCN layer suggests a process involving the CuSCN is occurring during the low potential phase of the deposition. In order to gain insight into this process, we examined the morphology of the substrate at different deposition times in the thick CuSCN layer case as shown by top-down and cross-sectional SEM image insets in **Figure 3.3a**. Before the electrodeposition (time = 0) the substrate is composed of the typical CuSCN nanorods with a thickness of 570 nm as expected. Interestingly, at time = 42 min, before the shift in potential, the rounded CuSCN nanorods seem to have changed shape, appearing more cubic with a size of 100-200 nm; however, the thickness of the film remains largely unchanged. Continuing the electrodeposition after the potential shift, at t = 100 min, the thickness of the resulting film increases to 750 nm and the typical micron-sized cube morphology of electrodeposited Cu<sub>2</sub>O is observed on the top of the small-cube layer. XRD of the 0, 42, and 100-minute samples (**Figure 3.3b**) show the dominant peaks of Cu<sub>2</sub>O at  $2\theta = 29.6, 36.5, 42.3, 61.4$  and  $73.5^\circ$  corresponding to the (110), (111), (200), (220), (311) planes<sup>32</sup> emerging after 42 min and becoming more intense after 100 min while the characteristic (003) CuSCN peak is already absent after 42 min.

In **Figure 3.4**, X-ray photoelectron spectroscopy (XPS) further confirms the total transformation of CuSCN to Cu<sub>2</sub>O. Indeed, neither sulfur nor nitrogen was detected in the Cu<sub>2</sub>O prepared from the CuSCN layer, in contrast to the original CuSCN film (**Figure 3.4 a,b**). The Cu 2p 3/2 signal exhibits two features at 932.5 and 934.5 eV (**Figure 3.4c**). The 932.5 eV signal cannot be attributed to Cu<sup>0</sup> considering the fit of the LMM auger transition spectrum (**Figure 3.4d**) using the Biesinger method.<sup>33</sup> The peak at 934.5 eV is attributed to Cu(OH)<sub>x</sub> species present due to air exposure of the Cu<sub>2</sub>O surface, therefore it is not present in the CuSCN sample. Moreover, energy-dispersive X-ray (SEM-EDX) mapping obtained in analytic mode (see Appendix 3, Figure S3.1) shows only copper (Cu), oxygen (O), element signals, and no sulfur signal (no peak at 2.307 keV) indicating the complete transformation of CuSCN to Cu<sub>2</sub>O. Overall, the SEM, EDX, XRD, XPS results support the view that the CuSCN layer can be converted to Cu<sub>2</sub>O during electrodeposition at pH 12. Furthermore, the chronopotentiometry results suggest that the electro-conversion of CuSCN to Cu<sub>2</sub>O occurs at a potential of -0.8 V vs. Pt.



**Figure 3.4.** XPS spectra of Cu<sub>2</sub>O thin film prepared from converting a CuSCN film (deposited with a charge of 120 mC cm<sup>-2</sup>) “Cu<sub>2</sub>O\_C” compared to the original CuSCN substrate (a) for S2p spectra (b), N 1s spectra (c), Cu 2p spectra (d) Cu Auger LMM.

### 3.3 Parameters identification

In order to identify the parameters essential for driving the formation of Cu<sub>2</sub>O via the observed in-situ electro-conversion of CuSCN, and to gain insight into the transformation mechanism, we performed additional experiments by varying the processing conditions. First, to understand the importance of pH on the stability of the CuSCN layer we investigated the impact of a 1-min dipping of an FTO/CuSCN film in copper lactate-based electrolyte at different pH (without any applied potential). As shown in Figure S3.2 (appendix 3) at pH 12 the CuSCN (003) XRD peak is still present, however the shape and density of the CuSCN nanopillars are slightly changed. This change is more intense at pH 13 than pH 12. Indeed, at pH 13, the FTO substrate is partially visible via top-view SEM (appendix 3, Figure S3.2), and the (003) CuSCN XRD peak vanishes, suggesting that the CuSCN is dissolved/corroded in the electrolyte under these conditions. However, we also observed weak reflections of Cu<sub>2</sub>O or Cu(OH)<sub>2</sub> on the XRD spectra (Figure S3.2), which become more intense at pH 13 compared to pH 12. Furthermore, photographs of the films (Figure S3.3) show a color change occurring during the dipping process, from the typical colorless CuSCN to a yellowish film, when FTO/CuSCN substrates are dipped in pH 12 or 13 electrolyte while at pH 11 the film does not change. Thus, we conclude that at pH  $\geq$  12 the CuSCN layer can undergo dissolution and conversion to a highly amorphous phase, likely based on a Cu<sub>2</sub>O or Cu(OH) stoichiometry. Indeed, the formation of a Cu<sub>2</sub>O-Cu(OH)<sub>2</sub> nanocomposite has been suggested to form in alkaline media when using CuSCN as precursor,<sup>34</sup> confirming the possibility of CuSCN conversion. However, in our experiments there is

no evidence of the full conversion to Cu(OH)<sub>2</sub> or Cu<sub>2</sub>O. This can be explained by the presence of lactate ion which complexes Cu<sup>2+</sup> ions and likely leads to the dissolution of the CuSCN. In fact, after a prolonged dipping time the material at the surface of the FTO glass is completely dissolved for both pH 12 and pH 13 (Figure S3.3).

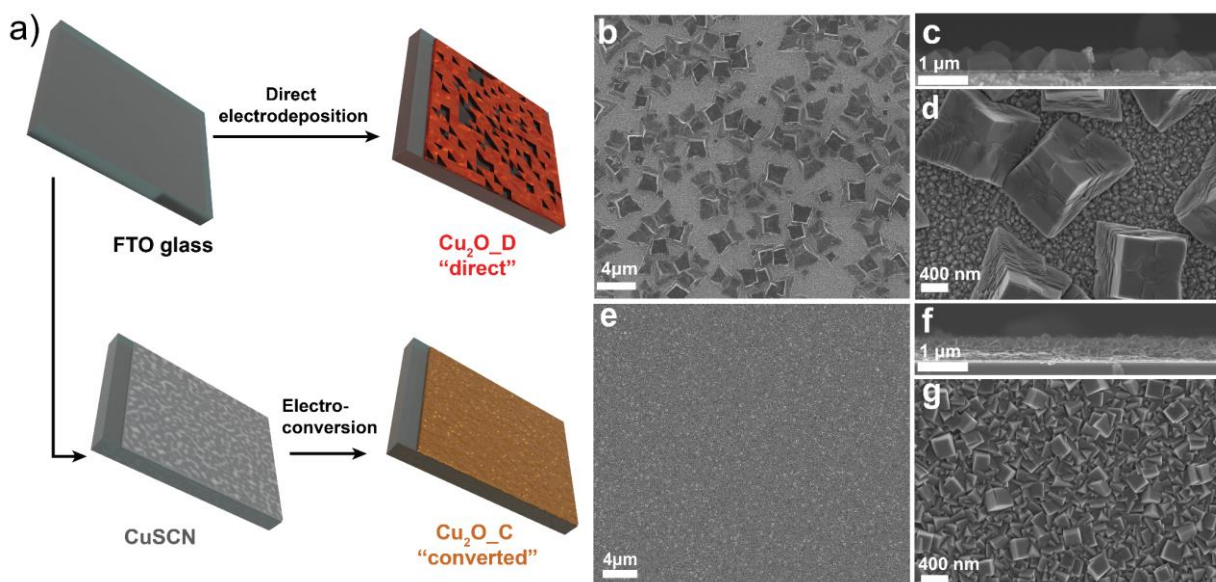
The importance of the presence of the copper ion in the electrolyte is further illustrated in Figure S3.4 (see appendix 3) where XRD and SEM images of FTO/CuSCN films are shown after 1-min dipping in the electrolyte at pH 12 without Cu<sup>2+</sup>. In the case without both copper and lactate (pH 12 adjusted with NaOH) the density of the CuSCN nanorods decreases and some needle-like structures are formed, while in the electrolyte without Cu ions but with lactate, the nanorods are slightly dissolved as some small pores can be observed. For both cases some weak Cu<sub>2</sub>O or Cu(OH) reflections appear in the XRD spectra at 36° and 42° (for dipping in NaOH). The latter result suggests that the Cu ions are not essential for the phenomenon to take place without applied potential. However, comparing the results from Figures S3.3 and S3.4 (see appendix 3), the presence of lactate in the solution appears to be key to control the morphology. Overall, with the dipping experiments, we can conclude that the formation of Cu<sub>2</sub>O pure films cannot arise from a simple solid-liquid reaction, as the cathodic polarization seems to be crucial for the transformation to occur.

While it is clear that applying a cathodic current is necessary to afford the CuSCN conversion to Cu<sub>2</sub>O, it is also important to note that the electrolyte composition plays a role in the electro-conversion. This is illustrated by additional electrodeposition experiments in pH 12 electrolyte without Cu ions (Figure S3.5, appendix 3). In both cases of electrolyte with or without lactate, after 100 min of chronopotentiometry at -0.1 mA cm<sup>-2</sup>, solely weak Cu<sub>2</sub>O XRD peaks are visible at 42°. Likewise the preceding dipping experiment, these minor traces are not comparable to the cubic Cu<sub>2</sub>O layer obtained with typical Cu<sub>2</sub>O electrodeposition electrolyte (Cu ions, lactate, K<sub>2</sub>SO<sub>4</sub>), in **Figure 3.3**. Rather the CuSCN nanopillars are transformed into amorphous structures. The applied potential is also found to affect the conversion, as shown by performing the electrodeposition in copper lactate electrolyte (pH 12) at different potentials ranging from -0.1 V to -1.1 V (vs. Pt) for a 100-min deposition on an FTO/CuSCN substrate. In Figure S3.6 (appendix 3), we can see that at -0.1 V, the conditions are not sufficiently negative to drive the transformation; the CuSCN is almost totally dissolved. The same conclusion can be made at -0.5 V, however the dissolution seems slower as more CuSCN nanorods are visible by SEM after 100 min. At the more negative potential of -0.8 V, which is the typical potential for a Cu<sub>2</sub>O chronopotentiometry deposition (see **Figure 3.3**), the substrate surface is fully covered with Cu<sub>2</sub>O. Thus, we conclude that both the proper electrolyte (copper and lactate ions at pH ≥ 12) and a sufficiently negative potential must be applied to drive the *in-situ* electro-conversion.

### 3.4 Electro-conversion study

Further insight is gained into the mechanism of the electro-conversion by comparing Cu<sub>2</sub>O films prepared by the two methods shown in **Figure 3.5**. The “Cu<sub>2</sub>O\_D” film is grown directly on bare FTO and “Cu<sub>2</sub>O\_C” is prepared via CuSCN electro-conversion, terminating just as the conversion transitions to the standard electrodeposition (which is easily monitored via the potential during the deposition). A 180 nm thick-film of CuSCN (corresponding to 25 mC cm<sup>-2</sup> of charge passed during the CuSCN electrodeposition) was used to prepare the Cu<sub>2</sub>O\_C film. For both the Cu<sub>2</sub>O\_C and Cu<sub>2</sub>O\_D films, the Cu<sub>2</sub>O film was deposited at -0.1 mA cm<sup>-2</sup> for 20 min (120 mC cm<sup>-2</sup>). The morphology difference between the Cu<sub>2</sub>O prepared by the two routes is shown in the SEM images in **Figure 3.5b-g**. While the Cu<sub>2</sub>O\_C film is evenly coated (has an FTO coverage of 100%) the coverage is incomplete for the Cu<sub>2</sub>O\_D film and is estimated at 46% by inspection of the SEM images. The absence of a favorable back contact such as gold for the Cu<sub>2</sub>O\_D sample can explain the uneven coverage. It should be noted that by increasing the deposition time for the Cu<sub>2</sub>O\_D film, the surface becomes increasingly covered (Figure S3.7, appendix 3). However, after 90 min the coverage is still not 100%.

In addition to substrate coverage, the cube size and the film thickness are different for the two preparation routes (keeping the same deposition current of 120 mC.cm<sup>-2</sup>): the cube edge length is 300-400 nm and 1.5-2 μm for Cu<sub>2</sub>O\_C and Cu<sub>2</sub>O\_D, respectively, while the average film thickness is around 180 nm and 400 nm, respectively. Consistent with our observations in **Figure 3.3**, the thickness of the film remains the same during the electro-conversion. Considering the density of CuSCN and Cu<sub>2</sub>O are, respectively, 2.8 and 6.0 g cm<sup>-3</sup>, it appears that the mass of the film doubles during the in-situ electro-conversion. Moreover, despite the fact that the Cu<sub>2</sub>O\_C sample passes more current during the electrodeposition (25 mC cm<sup>-2</sup> during the CuSCN deposition plus 120 mC cm<sup>-2</sup> during the electro-conversion), both electrodes appear to contain similar amounts of Cu<sub>2</sub>O. Indeed, comparing the coverage of the Cu<sub>2</sub>O\_D film (46%) and its average thickness of 400 nm suggests an amount of Cu<sub>2</sub>O equivalent to a 180 nm-thick continuous film, which is the same as for the Cu<sub>2</sub>O\_C film (see below UV-vis data for further support). Since CuSCN already contains Cu(I) it could be reasonable to consider that only one Cu(II) ion from the electrolyte needs to be reduced and incorporated into the converting CuSCN film to give Cu<sub>2</sub>O. This does not appear to be the case. Indeed, considering the constant film thickness together with the different densities of CuSCN and Cu<sub>2</sub>O and the observations of the dissolution of the CuSCN upon exposure to pH 12 without the applied potential suggest a mechanism wherein the dissolution of the CuSCN occurs during the electrodeposition of Cu<sub>2</sub>O. As Cu<sub>2</sub>O is thermodynamically stable at pH 12 at the applied potential, it results in the deposition of Cu<sub>2</sub>O cubes. We suggest that the CuSCN acts as an intermediate—reducing the required potential to deposit the Cu<sub>2</sub>O and acting as a morphological template, leading to the smaller cube size observed in the Cu<sub>2</sub>O\_C films. However, additional investigation is needed to fully elucidate the complex reduction mechanism occurring during the electro-conversion process.

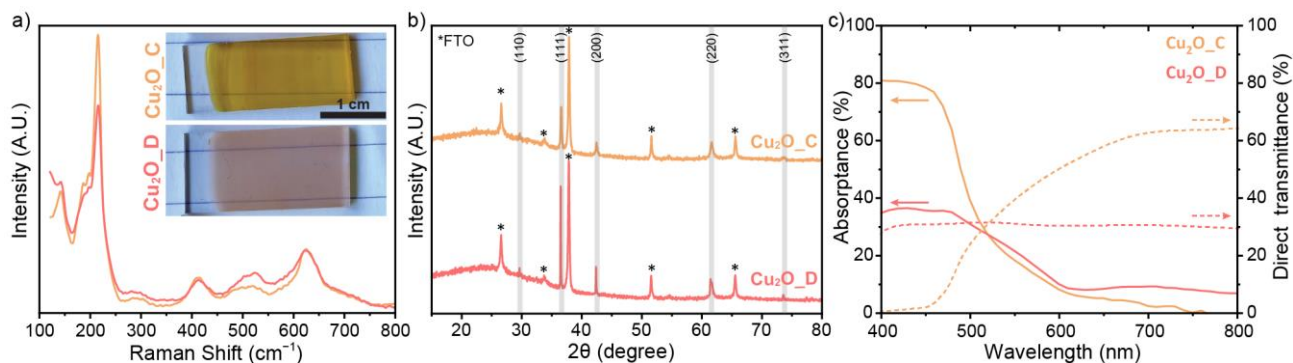


**Figure 3.5.** (a) Schematic of the possible routes to make Cu<sub>2</sub>O by direct Cu<sub>2</sub>O electrodeposition (Cu<sub>2</sub>O-D) and by CuSCN electrodeposition followed by in-situ electro-conversion to Cu<sub>2</sub>O (Cu<sub>2</sub>O-C), (b-g) SEM images of (b-d) Cu<sub>2</sub>O\_D direct deposition (e-g) Cu<sub>2</sub>O\_C converted film.

Nevertheless, given the distinct morphology differences between the Cu<sub>2</sub>O formed by the electro-conversion method, with smaller sized nanocubes and smoother crystal facets (with apparently fewer defects compared to the traditional electrodeposition directly on FTO, see additional SEM images Figure S3.8, appendix 3), we speculated that the electro-converted films would offer higher transparency and improved photocathode performance compared to the standard deposition on bare FTO. To assess this and further characterize the converted CuSCN samples, we performed UV-Visible spectroscopy, Raman spectroscopy, and XRD on the films. **Figure 3.6a** shows the Raman spectra of Cu<sub>2</sub>O\_D and Cu<sub>2</sub>O\_C where the typical Cu<sub>2</sub>O resonance peaks between 100-250 cm<sup>-1</sup> are seen in both cases. Similarly, the XRD analysis in **Figure 3.6b** shows nearly identical diffraction patterns with Cu<sub>2</sub>O peaks at  $2\theta = 29.6, 36.5, 42.3, 61.4$  and  $73.5^\circ$  corresponding to the (110), (111), (200), (220), (311) planes. The smaller crystallinity in the Cu<sub>2</sub>O\_C films is evident by the increased full width at half maxima (FWHM). However, the optical properties are quite different as evident from the photographs of the films (**Figure 3.6a**, inset) and the total absorptance and direct transmittance spectra (**Figure 3.6c**). Both samples have an absorption onset around 600 nm, typical for Cu<sub>2</sub>O, and a similar absorptance at 550 nm—further suggesting that both films have the same amount of Cu<sub>2</sub>O deposited, as suggest above. We verified this by calculating the theoretical absorptance of the Cu<sub>2</sub>O\_D film taking into account the film coverage, average thickness and the Cu<sub>2</sub>O absorption coefficient<sup>35</sup> at 550 nm (See SI, theoretical calculation). We estimate an absorptance of 20%, which is on good agreement to the measured value (21%). The difference between the Cu<sub>2</sub>O\_D and Cu<sub>2</sub>O\_C films at shorter wavelengths is attributed to the increase of the absorption coefficient, the coverage of the Cu<sub>2</sub>O, and the morphology of the Cu<sub>2</sub>O cubes. Indeed, the absorptance of the Cu<sub>2</sub>O\_D film is lower at wavelengths smaller than 500 nm due to the direct



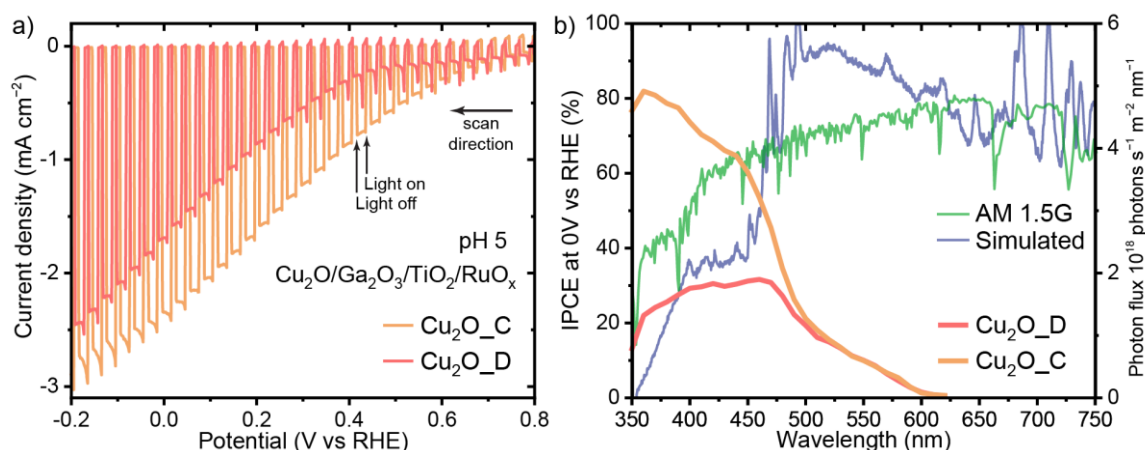
passing of photons through the uncoated parts of the FTO surface. The incomplete coverage and large crystal size of the Cu<sub>2</sub>O\_D film also leads to more light loss by scattering. The direct transmittance is around 50-70% in the range 600-900 nm for Cu<sub>2</sub>O\_C, while it is only 30% for Cu<sub>2</sub>O\_D. Thus, the Cu<sub>2</sub>O\_C samples exhibit higher transparency for non-absorbed photons despite the full surface coverage.



**Figure 3.6.** Characterization of thick Cu<sub>2</sub>O films obtained by direct deposition (Cu<sub>2</sub>O\_D) and by the in-situ electro-conversion (Cu<sub>2</sub>O\_C): (a) Raman spectra (inset) photograph of the electrodes (b) XRD spectra (c) UV-visible total absorbance and direct transmittance spectra.

### 3.5 Photoelectrochemical test

In order to establish the ability of the electro-converted Cu<sub>2</sub>O to perform as a photocathode for H<sub>2</sub> production, we fabricated complete photoelectrodes by adding protective and co-catalyst layers following the route established by Pan *et al.*<sup>20</sup> (Ga<sub>2</sub>O<sub>3</sub>/TiO<sub>2</sub> by atomic layer deposition (ALD) and RuO<sub>2</sub> catalyst by photoelectrodeposition<sup>36</sup>). We compared the HER performance with linear scanning voltammetry (LSV) under intermittent (simulated) solar illumination of the Cu<sub>2</sub>O\_D and Cu<sub>2</sub>O\_C photoelectrodes described in **Figure 3.5** and **Figure 3.6** (with approximately the same amount of Cu<sub>2</sub>O). The LSV curves are shown in **Figure 3.7a**.



**Figure 3.7.** (a) Linear scanning voltammetry of Cu<sub>2</sub>O-based photocathodes for H<sub>2</sub> production under intermittent simulated solar illumination (1 sun) LSV at pH 5 for HER. (b) IPCE spectra of the Cu<sub>2</sub>O photocathodes at 0V vs. RHE at pH 5 are shown next to the standard solar spectrum (green) and the simulator solar spectrum produced by the light source used during the LSV tests (blue).

In terms of photocurrent density, higher performance was obtained for Cu<sub>2</sub>O\_C (2.5 mA cm<sup>-2</sup> at 0 V vs. RHE) compared to Cu<sub>2</sub>O\_D (2 mA cm<sup>-2</sup> at 0 V vs. RHE) under simulated 1 sun illumination. The qualitatively higher fill-factor of the LSV curve in the Cu<sub>2</sub>O\_C photocathode suggests that the semiconductor layer benefits from an improved electrical contact to the FTO substrate compared to the Cu<sub>2</sub>O\_D photocathode. While using CuSCN as an underlayer is known to improve the contact with the substrate, it is notable that a similar improvement is seen with the electro-converted film, despite no detectable CuSCN remaining in the film.

Incident photon-to-current efficiency (IPCE) measurements, taken with monochromatic light at 0 V vs. RHE further highlight the performance difference between converted and direct depositions (**Figure 3.7b**). While the IPCE for both cases is similar in the wavelength range from 500-600 nm, due to the similar light absorption in this region, Cu<sub>2</sub>O\_D exhibits lower IPCE for wavelengths < 500 nm due to the incomplete film coverage. Specifically, the IPCE at 450 nm is 32% and 60% for Cu<sub>2</sub>O\_D and Cu<sub>2</sub>O\_C, respectively. The IPCE of the Cu<sub>2</sub>O\_C photocathode reaches 80% at 350 nm, which, together with the measured absorbance at that wavelength, suggests an internal quantum efficiency of close to 100% under these conditions. Integration of the IPCE data with the standard solar spectrum (**Figure 3.7b**, green trace) gives an estimated photocurrent density of 4.0 mA cm<sup>-2</sup> at 0 V vs. RHE with the Cu<sub>2</sub>O\_C photocathode compared to 2.4 mA cm<sup>-2</sup> for the Cu<sub>2</sub>O\_D photocathode (See Figure S3.9, appendix 3) confirming the improved performance of the Cu<sub>2</sub>O\_C. The discrepancy between the photocurrent measured under simulated solar conditions in **Figure 3.7a** and the predicted solar photocurrent from the IPCE measurements is attributed to the deficiency of UV photons in the solar simulator employed for the LSV measurements (see blue trace in **Figure 3.7b**). This difference together with the fact that the Cu<sub>2</sub>O\_C photocathode shows a linear response of photocurrent to light intensity (See Figure S3.10, appendix 3) indicates that the integrated IPCE results give a more accurate estimation of the true solar photocurrent. Overall, given the considerable difference in photocathode performance in the 350-500 nm range, and the drastically improved transmittance of the Cu<sub>2</sub>O\_C layer in the 550-800 nm range (as shown in **Figure 3.6c**) compared to the availability of solar photons in this wavelength range, we conclude that the Cu<sub>2</sub>O\_C films are well-suited for the coating of high surface transparent scaffolds or as top cells in tandem devices for overall water splitting. The exploitation of these prospects is under development in our lab.

### 3.6 Conclusion

To conclude, we have demonstrated a novel method to control Cu<sub>2</sub>O thin film morphology for semi-transparent photocathode applications. By first electro-depositing a nanostructured CuSCN layer and then electro-depositing Cu<sub>2</sub>O under specific conditions, the CuSCN acts as a sacrificial template and catalyst to lower the required potential for Cu<sub>2</sub>O deposition. This electro-conversion process allows homogeneous Cu<sub>2</sub>O coverage on transparent FTO substrates while similar depositions directly on the FTO give inhomogeneous films with poor transparency due to light scattering. Control experiments revealed that key parameters are essential for the *in-situ* electro-conversion: pH ≥ 12 electrolyte containing Cu-lactate complexes and the application of a sufficiently negative



current/potential. By comparing films with similar amounts of Cu<sub>2</sub>O, we found that the photocathode performance (for H<sub>2</sub> evolution) of electro-converted Cu<sub>2</sub>O (Cu<sub>2</sub>O\_C) was superior to Cu<sub>2</sub>O films directly deposited on the FTO (Cu<sub>2</sub>O\_D), due to improved substrate interaction and higher quantum efficiencies at low wavelengths. Thus, the Cu<sub>2</sub>O deposition by electro-conversion is a promising alternative to coat homogenous and thin Cu<sub>2</sub>O layer without scattering losses and without compromising the transparency of the electrode.

### 3.7 Experimental methods

#### 3.7.1 Chemicals

Copper(II)sulfate pentahydrate CuSO<sub>4</sub>·5H<sub>2</sub>O (99% Acros organics), Ethylenediaminetetraacetic acid C<sub>10</sub>H<sub>16</sub>N<sub>2</sub>O<sub>8</sub> (99% Acros organics), Potassium thiocyanate KSCN (99% Acros organics), Potassium sulphate K<sub>2</sub>SO<sub>4</sub> (99% Carl ROTH), DL-lactic acid (90% abcr), Potassiumhydroxide KOH (pure Reactolab), Sodium sulfate NaSO<sub>4</sub> (99% Sigma aldrich), Potassium phosphate, monobasic, KH<sub>2</sub>PO<sub>4</sub> (99% Acros organics), Sodium hydroxide NaOH (pure Reactolab) and Potassium perruthenate K<sub>2</sub>RuO<sub>4</sub> (98% strem chemicals) were used as received.

#### 3.7.2 CuSCN deposition

FTO glass (2.5 cm × 1 cm) were cleaned with detergent (20 min), deionized (DI) water (20 min), isopropanol (IPA) (20min). CuSCN is deposited following a procedure developed elsewhere.<sup>24</sup> Briefly, CuSCN electrodeposition is performed in an aqueous solution containing 12mM of CuSO<sub>4</sub>, EDTA and KSCN added in this specific order to avoid the precipitation of Cu(SCN)<sub>2</sub>. A standard three-electrode configuration was used for electrochemical deposition with Pt counter electrode and Ag/AgCl/sat. KCl reference electrode. Chronoamperometry at −0.3 V vs. Ag/AgCl is applied for a defined duration/charge passed. In the potential drop experiment (**Figure 3.3**) thin and thick film correspond to an electrodeposition time of 2 and 10 min. For the rest of the study, in order to keep the amount of CuSCN deposited constant for each condition, thin CuSCN and thick CuSCN correspond to a charge passed of 50 mC and 100 mC respectively.

#### 3.7.3 Cu<sub>2</sub>O deposition

Cu<sub>2</sub>O films were deposited on bare FTO (Cu<sub>2</sub>O\_D) or on CuSCN (Cu<sub>2</sub>O\_C) with a method developed elsewhere<sup>16</sup>. Cu<sub>2</sub>O was electrodeposited in a copper-lactate rich electrolyte at pH 12. The electrolyte contains 4 g of CuSO<sub>4</sub>·5H<sub>2</sub>O, 33.8 g of Lactic acid, and 10.9 g of K<sub>2</sub>SO<sub>4</sub> in 250 mL of DI water. The pH was adjusted to 12 by adding 2 M KOH. The final volume of the electrolyte is 500 mL. A piece of platinum was used as a counter electrode. The electrodeposition is performed by chronopotentiometry at a current density of −0.1 mA.cm<sup>−2</sup>. The temperature was maintained at 30°C using a water bath. The deposition time was varied depending on the film thickness expected. For *in-situ* electro-conversion on CuSCN, the chronopotentiometry was started just after sample immersion in the electrolyte to avoid CuSCN dissolution. 20 nm of Ga<sub>2</sub>O<sub>3</sub> and 20 nm of TiO<sub>2</sub> layers were deposited on the Cu<sub>2</sub>O film using a Savannah 100 (Cambridge Nanotech) thermal ALD system. The chamber was stabilized at 150°C and flushed with 10 sccm nitrogen gas (99.9995%, Carbagas).

Gallium oxide was deposited using bis( $\mu$ dimethylamino)tetrakis(dimethylamino)digallium (98%, Stream Chemicals) and TiO<sub>2</sub> was deposited using tetrakis(dimethylamino)titanium (99.999%, Sigma). RuO<sub>x</sub> catalyst was photoelectrodeposited by chronopotentiometric method at 28  $\mu\text{A}\cdot\text{cm}^{-2}$  under illumination in presence of 1.3 mM K<sub>2</sub> RuO<sub>4</sub> aqueous solution for 5min. Pt wire was used as counter electrode.

#### 3.7.4 Material characterization

UV-Visible spectrometry was performed with a UV-3600 (Shimadzu) spectrometer equipped with an integrating sphere. Bragg-Brentano XRD measurements were carried out using a Bruker D8 Vario diffractometer equipped with a Johansson K $\alpha$ 1 ( $\lambda = 1.5406 \text{ \AA}$ ). SEM images were recorded with a Zeiss Merlin microscope. Raman spectra were obtained with a LabRam spectrometer (Jobin Yvon Horiba). The excitation line was provided by an argon laser (532.19nm). XPS measurements were carried out on an Axis Supra (Kratos Analytical) instrument, where a monochromated K $\alpha$  X-ray line of an aluminum anode was used. The pass energy was set to 20 eV with a step size of 0.1 eV. The samples were grounded to the sample holder by connecting the FTO underlayer to the sample stage.

#### 3.7.5 Photoelectrochemical characterization

PEC experiments were performed by using a three-electrode setup, with carbon rod as counter electrode and Ag/AgCl/KCl sat as reference electrode. PEC performances were measured in a pH 5 buffer solution containing 0.5M Na<sub>2</sub>SO<sub>4</sub>, 0.1 M sodium phosphate. The surface area of the film in contact with the electrolyte was in the range 0.1-0.2 cm<sup>2</sup>. The electrochemical behavior was monitored with a SP-200 potentiostat (biologic), while the light was provided by a xenon arc lamp (450W) calibrated with the AM 1.5G spectra to provide one sun of illumination (1000 mW cm<sup>-2</sup>). A mechanical shutter was used to chop the light. All experiments were carried out at ambient temperature and electrode potentials were converted to the RHE scale using  $E_{\text{RHE}} = E_{\text{Ag/AgCl}} + 0.059 \text{ pH} + 0.197$ . Incident photon to current efficiencies (IPCE) were obtained using an Optical Building Blocks Corporation tunable PowerArc illuminator for illumination where the photon flux was calibrated with a Thorlabs Model S120VC Photodiode Power Sensor. The photocurrent was recorded in the same three-electrode potentiostatic configuration described above at 0 V vs. RHE. The working electrodes were illuminated from the substrate side in all cases.

## Chapter 4    WSe<sub>2</sub> processing conditions evaluation for nanostructured photocathode

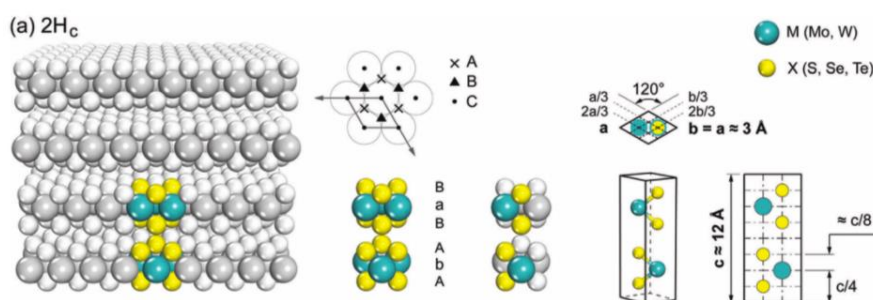
WSe<sub>2</sub> is a promising candidate for the solar-driven hydrogen evolution reaction due to its ideal band gap, band position, high absorption coefficient, raw-material availability and stability.<sup>147,148</sup> Moreover, WSe<sub>2</sub> photocathodes can be prepared by simple solution-based approaches such as exfoliation and deposition of WSe<sub>2</sub> nanoflakes. However, the performance of these photocathodes remains well below the state of the art with single crystal-based devices. Herein we gain insight into the factors important to the operation of WSe<sub>2</sub> nanoflake based photocathodes. Water and/or O<sub>2</sub> can have a strong influence on the exfoliation process by interacting with the solvent and the nanoflakes. NMP is prone to degradation during sonication under oxidation conditions. The influence of the sonication media during the exfoliation process and the film processing conditions were modified with a view to facilitate the WSe<sub>2</sub>-coated TPCS photocathode fabrication. A 2 hours exfoliation step in NMP(H) was used to avoid full degradation of the NMP solvent while ensuring promising photoactivity. Finally, using this exfoliation condition, we demonstrated that electrophoretic deposition (EPD) could be used for WSe<sub>2</sub> coating on FTO glass conductive substrates. The WSe<sub>2</sub> photocathodes exhibited a photocurrent of ca. -1 mA.cm<sup>-2</sup> at 0 V vs. RHE under 1 Sun illumination.

## 4.1 WSe<sub>2</sub>, a promising semiconductor photocathode

TMDs represent a broad family of more than 60 compounds, including 40 TMDs with layered structure<sup>149</sup>. The interest in these inorganic graphene analogues started with the discovery by Mak<sup>150</sup> in 2010, of the tunable band gap of semiconducting MoS<sub>2</sub> nanosheets with respect to thickness, and a transition from a direct to an indirect band gap from bulk to monolayer (the stronger the light emission, the higher the luminescence quantum efficiency). The study of Kis<sup>151</sup> *et al*, on high electron mobility in the MoS<sub>2</sub> single layer transistor, complemented this work and further expanded the application field for TMDs.

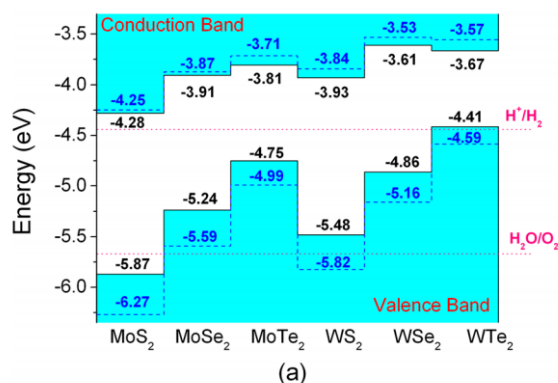
TMDs, according to their chemical composition, crystal structure, morphology and dimensionality can be used in a wide range of applications, from optoelectronics to energy conversion, including sensors, catalysis or other emerging technologies<sup>152</sup>. Their versatility makes TMDs promising and attractive candidates to study.

The crystal structure consists of three atomic layers X-M-X covalently bonded, with MX<sub>2</sub> monolayers coupled by weak Van der Waals forces. As all the bonding orbitals are involved in intralayer interactions, only the antibonding orbitals remain accessible on the basal plane, which leads to an absence of dangling bonds. Furthermore, different polytypes exist (1T, 2H, 3R); however, we will focus on the hexagonal crystal lattice, known as the 2H phase<sup>153</sup> (see the crystallographic structure in **Figure 4.1**), since this is a semiconducting version of the material.



**Figure 4.1.** Crystallographic structure of 2H phase TMDs extracted from ref <sup>152</sup>.

In order to develop an economically viable PEC device, the semiconducting material has to exhibit certain qualities such as low-cost, robustness and high performance. One of the advantages of these materials is their high stability, as shown by their high melting point (1200°C), due to the Coulombic forces, which hold the layered structures together<sup>152</sup>. Thermodynamically the photocatalytic ability of a semiconductor material depends on the position of the valence and conduction band edge (**Figure 4.2**), which, for example, determine if the electrons generated by light absorption have enough energy to reduce water (e.g. the energy conduction band edge must be higher than the potential  $E_{H_2/H^+}$ ). To drive the photochemical reaction, the material must also exhibit a catalytic surface, otherwise, a co-catalyst is needed.



**Figure 4.2.** Electronic structure of various TMDs to be compared with the water splitting potential required, extracted from ref<sup>154</sup>.

Thus, p-type WSe<sub>2</sub> is a promising candidate for HER evolution, due to its ideal bandgap (1.2-1.6 eV), high absorption coefficient, anisotropic transport properties and last but not least its stability<sup>148</sup>. Contrary to high-performance p-type material such as CdSe, CdS, GaAs, ZnO the optical transition does not affect the material chemical reactivity, because the band gap is composed of 2-d bands which do not affect the semiconductor chemical bonds. Nevertheless, the material performance is limited by several key aspects such as the particle size and morphology, the internal and external defects. Thus, the aim is to prevent recombination of the photogenerated charge carriers, due to edge/defect site, while ensuring the light absorption and processability of the material for large scale applications. Some progress was made for solar hydrogen generation using WSe<sub>2</sub> photocathode, starting from studies of single crystal properties, followed by the investigations on polycrystalline films made by high-temperature annealing, to the new generation of devices appropriate for large-scale applications such as solution-processed method.

In the view of utilizing the WSe<sub>2</sub> nanoflakes as the p-type semiconductor for the TPCS photocathode, the solution-processability of the material needs to be evaluated. Using the methods developed by Yu *et al.*,<sup>108,109</sup> two steps are required to make a photoelectrode, namely the exfoliation step and the film deposition. The exfoliation step will be studied by assessing the processability and photoactivity of the materials using an already developed (LLISA) liquid-liquid self-assembly deposited film. After studying the exfoliation impact on the film processing and photoactivity, a method of deposition that could be applicable to the TPCS will be investigated.

## 4.2 Effort to implement WSe<sub>2</sub> nanoflakes photocathodes

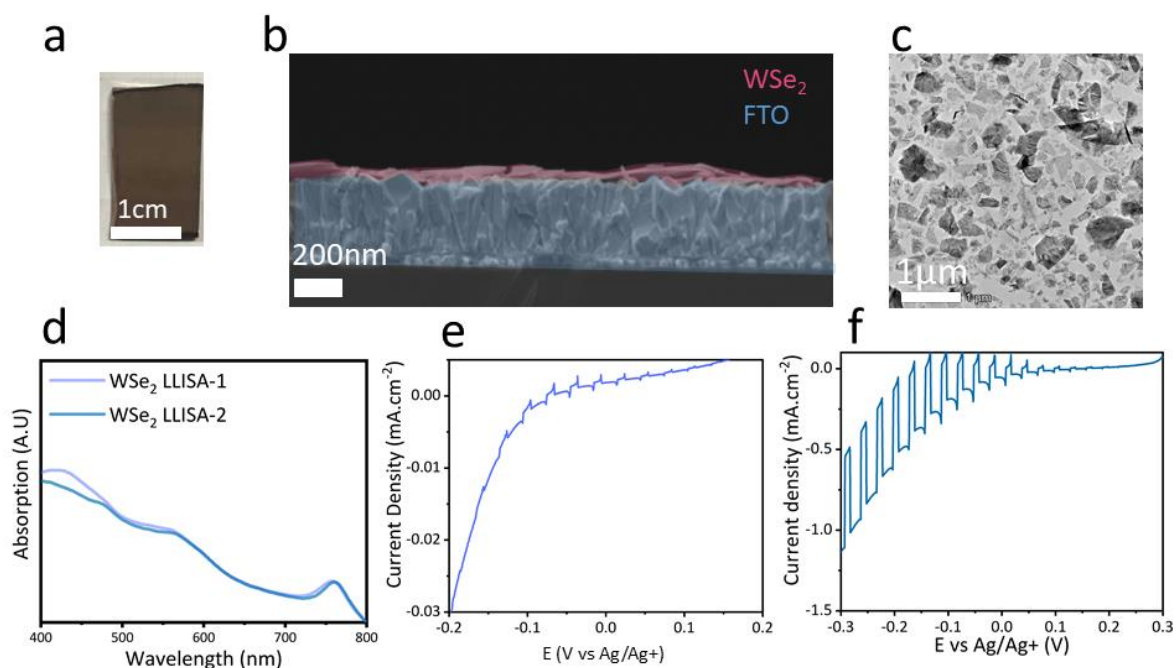
The WSe<sub>2</sub> thin film fabrication by a solution-processable method previously developed<sup>76</sup> was studied. Firstly, the fabrication of the WSe<sub>2</sub> nanosheets suspension is performed by liquid-phase exfoliation of WSe<sub>2</sub> bulk powder in N-Methyl-2-pyrrolidone (NMP) solvent in order to obtain a suspension, at a concentration of 1 mg.mL<sup>-1</sup> of few-layer nanosheets ranging from 200 - 1000 nm in

the lateral dimension. The size selection is performed by a centrifugation step: a first centrifugation step at low speed removes the non-exfoliated flakes, and a second centrifugation step at high speed provides a pellet with a desirable size distribution and a supernatant suspension containing the smallest flakes in the original sonication solvent.

In order to process the TMD dispersion, a system with two immiscible solvents is used. The suspension is injected at the interface where the flakes become confined within the two non-solvents and align with the 2D interface. Then, the top solvent and the bottom solvent are removed, individually. The last step is to dry the film in order to remove solvent traces and improve adhesion. Yu *et al.*,<sup>76</sup> showed that the spatial confinement caused by the thin film deposition process plays a key role in the WSe<sub>2</sub> photocathode performance for HER.

Initial experiments showed that the reproducibility of the PEC performances exhibited by samples made with the liquid exfoliation and LLISA deposition method proved to be challenging, therefore it was an essential aspect to determine the source of this variation. Several questions remained such as the influence of the sonication media and the processing conditions. By unraveling the effect of all these parameters, we would have better chance to apply the procedure to the transparent porous conductive substrates (TPCSs).

As an example, and to motivate the studies in this work we show typical results from WSe<sub>2</sub> nanoflake photocathodes in **Figure 4.3**. The fabricated photocathodes exhibit the typical morphology and optical properties of solution-processed WSe<sub>2</sub> photoelectrode (**Figure 4.3a**). The cross-sectional SEM (**Figure 4.3b**) confirms the alignment of the nanoflakes as a single layer on the FTO substrate. In **Figure 4.3d**, the TEM image shows exfoliated flakes coherent with the measurement obtained previously, with a flake lateral size between 200-1000  $\mu\text{m}$ . The UV-visible spectra (**Figure 4.3d**) exhibits the typical optical properties (i.e., several transition modes and an overall onset at 800 nm).<sup>76</sup> The PEC performances were evaluated in sacrificial chloranil (tetrachloro-1,4-benzoquinone) electrolyte for its favorable potential and facile one-electron reduction as it was used in previous studies.<sup>155,156</sup> Chloranil (Q) can be reduced to tetrachloro-semiquinone (QH<sup>-</sup>) in a saturated chloranil solution (i.e., in acetonitrile with 0.1 M NBu<sub>4</sub>PF<sub>6</sub> supporting electrolyte). Some electrodes exhibited poor photocurrent (**Figure 4.3e**) while some electrode showed up to  $-0.5 \text{ mA.cm}^{-2}$  at  $-0.2 \text{ V}$  vs. Ag<sup>+</sup>/Ag (**Figure 4.3f**). At this stage the reason of the variability of the PEC performance is not known, hence a study to identify the source of PEC disparity was next launched.



**Figure 4.3** WSe<sub>2</sub> film characterizations (a) photograph (b) cross sectional SEM image (c) TEM image (d) UV-visible spectrum, comparison between two sample having different PEC performances (e) LSV curves under intermittent illumination (1 Sun) in sacrificial chloranil saturated solution in acetonitrile (MeCN).

The sonication media could change the quality of the resulting flakes (oxidation, adsorption phenomenon) due to H<sub>2</sub>O/O<sub>2</sub> presence. Recently, Jawaid *et al.*<sup>157</sup> introduced a new exfoliation mechanism based on autooxidation of NMP to NMS (N-methyl-succinimide) during sonication, in presence of oxidative species such as O<sub>2</sub>, H<sub>2</sub>O, leading to the formation of hydroperoxides. According to this work, the edge sites are oxidized by hydroperoxides species, which leads to an accumulation of negative charges at the edges causing a coulombic repulsion between the layers. They emphasized this theory by another study on the redox exfoliation mechanism<sup>158</sup>, in which they reported the TMDs exfoliation in mild condition without sonication required. They suggested the use of a weak oxidizing agent (mimicking the degradation product of NMP) can dissolve the TMD edge sites by forming in situ anionic polyoxometalates on the flake surface. The resulting negative charge generated at the surface drives the exfoliation by Coulombic repulsion and stabilizes electrostatically the suspension. The final step requires the use of a diluted reductant solution to drive the dispersion by partial reduction. Gupta *et al.*<sup>159</sup> proposed another mechanism, by considering solvent-solvent interaction in such a way as adsorption of H<sub>2</sub>O molecules on the Mo-edges leads to a strongest interaction between NMP and TMD nanoflakes due to hydrogen bonding. In their work, they used bath-sonication, so it would be more relative to explain the suspension stability for the suspension after probe sonication-assisted exfoliation due to interaction H<sub>2</sub>O-NMP with taking into account that it can also prevent chemical erosion of the flake edge leading to resulting flakes with largest average lateral size and less defective. For Manna *et al.*<sup>160</sup> the heteroassociation of NMP and water can form polymeric species called clathrate, for precise water amount as co-solvent, which can prevent the recombination of the flakes and reduce the

sedimentation velocity by viscosity enhancement. Overall, it has been reported that H<sub>2</sub>O/O<sub>2</sub> could have an impact on exfoliation yield but also on flake size and defect densities.

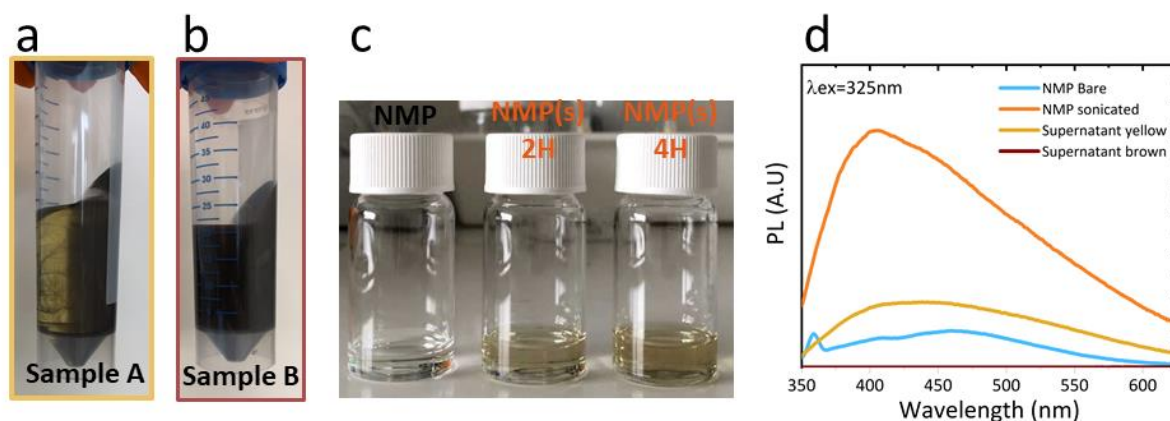
Taking into account the recently published results on TMDs exfoliation in NMP solvent, one of the first goals of this work is to be able to identify the parameters affecting the different steps of the process and to establish a protocol to overcome these fluctuations in quality of exfoliated materials and device results. For the exfoliation part, it is known that several parameters such as, the temperature, process time, volume, the initial concentration<sup>161</sup>, the H<sub>2</sub>O/O<sub>2</sub> amount in the media<sup>159,159,162</sup> have an influence on the process, and might lead to a difference in nanoflakes quality. Herein, we will investigate the impact of the sonication time and media on the WSe<sub>2</sub> exfoliation step to ensure optimum PEC performance of WSe<sub>2</sub> photocathode, in the aim to coat this material onto the TPCS. Electrophoretic deposition (EPD) could be an alternative to the LLISA deposition for WSe<sub>2</sub> photocathode fabrication. EPD will be beforehand validated on flat FTO glass to guarantee the PEC performance of the photoelectrodes.

### 4.3 Nanoflake suspension characterizations

#### 4.3.1 Solvent degradation during exfoliation

The first parameter we explored is the solvent degradation during the exfoliation. Specifically, we have observed, by performing a seemingly identical exfoliation for 12 hours in NMP on two different occasions, two different results. In one case, after centrifugation, all the nanoflakes are sedimented and agglomerated together leaving an almost clear supernatant (**Figure 4.4a**), while in another case, using the same centrifugation speed, a pellet containing non-exfoliated flakes is formed and a darkly colored brown supernatant suspension remains that contains the desired nanoflake dispersion (**Figure 4.4b**). This observed flake agglomeration difference between the seemingly identically processed samples could come from variability in the presence of water or oxygen in the solvent, which cases different amounts of degradation during the sonication-assisted exfoliation. Indeed, we have observed the nanoflakes tend to be less dispersible in sonicated discolored NMP compared to fresh NMP (data not shown). Several studies have confirmed the effect of sonication media,<sup>157,159,160,162</sup> specially the effect of H<sub>2</sub>O and O<sub>2</sub> on NMP autoxidation. As a matter of fact, NMP, a lactam known for its hygroscopic nature, could be influenced by the presence of water, and possibility leading to its degradation.





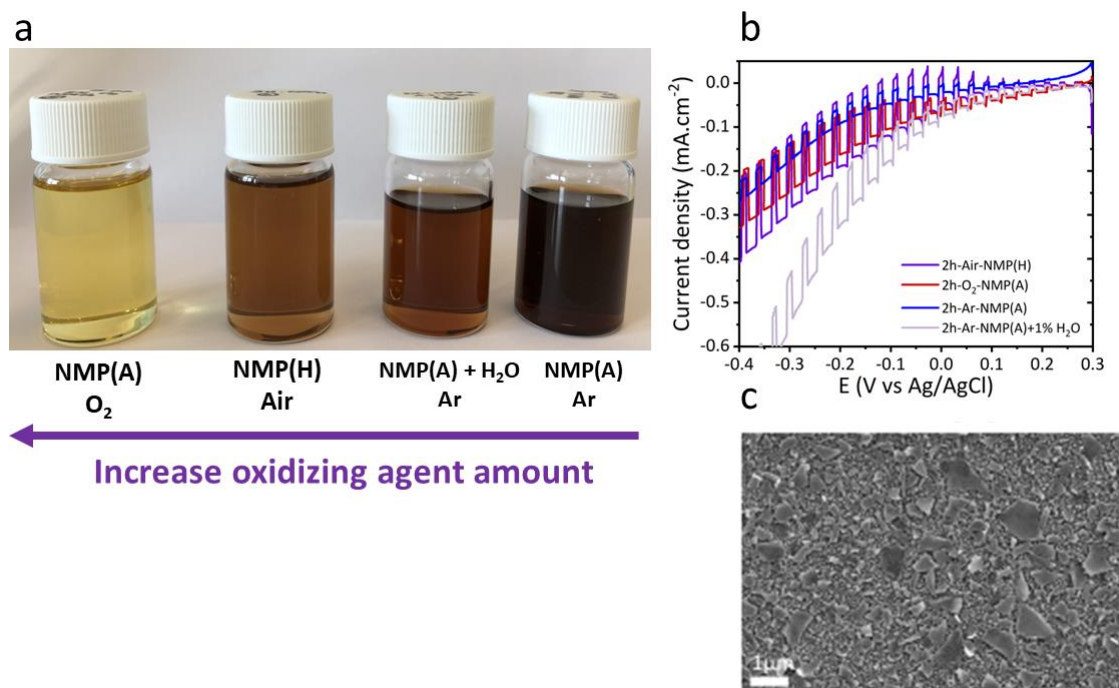
**Figure 4.4.** (a) Photograph of NMP without WSe<sub>2</sub>, bare, after 2h sonication, after 4 hours sonication (b) WSe<sub>2</sub> suspension after 12 hours exfoliation, flakes aggregated together (c) WSe<sub>2</sub> suspension after 12 hours exfoliation, flake separation succeeded (d) PL measurement of pristine NMP, NMP solvent sonicated for 4 hours, yellow supernatant from sample a, brown supernatant from sample b, with  $\lambda_{excitation} = 325$  nm.

In order to identify the impact of the sonication process on the solvent itself, various sonication times have been applied to NMP. A clear change of the optical properties with the yellow discoloration of the solvent after several hours of sonication (**Figure 4.4c**) have been observed, which can be due to the presence of amine group of new species. Moreover, the increase of the PL intensity and red-shift has been linked with NMP degradation due to the apparition of new species<sup>163</sup> such as hydroperoxides<sup>157,158</sup> or sonopolymer<sup>162</sup>. In **Figure 4.4d**, we can see that the PL intensity is higher for NMP solvent sonicated for 4 hours compared to pristine NMP. In addition, the PL signal for the yellow NMP supernatant (sample A with flake separation impossible) is different from the brown NMP supernatant (sample B, allowing flakes separation). Indeed, the PL signal of NMP supernatant from sample B is higher, which could confirm the presence of species also present in NMP solvent sonicated, possibly due to degradation of the solvent. To understand how to improve the control on WSe<sub>2</sub> exfoliation procedure in NMP, different exfoliation conditions were investigated.

#### 4.3.2 Exfoliation media investigation

The composition of the sonication media can have a strong influence on the exfoliation. In order to gain insight into the mechanism leading to the non-separation of the flakes, different environments have been designed and tested. The exfoliation was performed for different conditions (O<sub>2</sub> bubbling, Argon (Ar) bubbling, air) and with different solvent specifications (NMP(H) for a hydrated solvent stored in ambient atmosphere, NMP(A) for an argon-sealed anhydrous solvent, NMP(A) anhydrous with 1%v/v water addition). The standard procedure to produce WSe<sub>2</sub> standard suspensions required 12 hours of sonication, nevertheless only 2 hours exfoliation was used to study the solvent degradation mechanism. The goal was to be able to distinguish samples for different sonication

media conditions, while avoiding to reach fully degradation of the solvent for all conditions, as the NMP degradation increases with sonication time.



**Figure 4.5.** Picture (a) NMP supernatant for different sonication media with O<sub>2</sub> bubbling, in air, with Ar bubbling and addition of 1%v/v of H<sub>2</sub>O, with Ar bubbling (b) LSV curves under intermittent illumination (1 Sun) in sacrificial chloranil saturated solution in MeCN (c) SEM image of a LLISA deposited film after 2 hours exfoliation.

As mentioned in section 4.2.1, prior to the film deposition, the size selection is performed by a centrifugation step: a first centrifugation step at low speed removes the non-exfoliated flakes, and a second centrifugation step at high speed provides a pellet with a desirable size distribution and a supernatant suspension containing the smallest flakes in the original sonication solvent. As it is shown in **Figure 4.5a**, the supernatant containing the smallest size fraction of the flakes in sonicated NMP exhibits different optical properties, a gradually increase from yellow to brown is observed by increasing the inertness of the sonication media. Indeed, when the exfoliation is performed in an oxidative environment (presence of O<sub>2</sub> and/or H<sub>2</sub>O) the supernatant becomes yellow and the flakes cannot be separated, except if a washing step is used (see Appendix 4, Figure S4.1).

The PEC performance for different exfoliation conditions were tested in sacrificial chloranil electrolyte. Interestingly, using a reduced time (2 hours) for exfoliation to avoid fully degradation of the solvent, the photocurrent was in the typical photocurrent range for a bare WSe<sub>2</sub> photoelectrode. The best result was obtained with NMP(H) in air (**Figure 4.5b**). Several phenomena could be responsible for the difference in performance, due to flakes oxidation or ligand attachment, however the goal was in the first time to establish the best conditions to make a TPCS-based photoelectrode. More investigations were done by FT-IR or zetapotential measurements, highlighting the possible degradation of NMP in highly oxidative condition and different ligands

attachment phenomena on the nanoflakes (see appendix 4, Figure S4.2 and Table S4.1). FT-IR measurement suggests the presence of NMP degradation species resulting from ring-opening transformation or moisture absorption. The origin of the negative charge measured by zeta-potential needs to be studied further, but we hypothesize that it could come from hydroxyl group bonded to a defect site or an oxidized site<sup>164</sup>, or due to polyoxometalate species<sup>157,158</sup> (POM) resulting from solvent degradation, adsorbed onto the flake surface. In the view of replacing the NMP solvent, a dihydrolevoglucosenone or Cyrene, a bio-based solvent derived from cellulose has been identified as NMP alternative to exfoliate graphene.<sup>165</sup> We successfully exfoliated WSe<sub>2</sub> in Cyrene, however the PEC performance were lower than with NMP solvent (see appendix 4, Figure S4.3). Therefore, in order to avoid any solvent degradation issue and ensure photoactivity, 2 hours exfoliation in NMP(H) was kept as the standard condition.

Without discounting the impact of the sonication media on the PEC performance, one of the reasons for the lack of reproducibility potentially originates from the poor adhesion of the WSe<sub>2</sub> onto the FTO substrate. Yu *et al.*<sup>166</sup> used a polymer cross-linked underlayer in order to improve the attachment of the film. The PvPh cross-linked layer has been used as gate dielectrics for organic field effect transistors<sup>167</sup>. The polymer (polyvinylphenol) is cross-linked with a bi-functionalized chlorosilane in order to make a thin layer (thickness below 20 nm) insoluble in organic solvents. Effectively, a better adhesion of the film in presence of the PVP underlayer was observed, as evidenced by WSe<sub>2</sub> electrode before and after testing (see appendix 4, section PVP underlayer, Figure S4.4-7).

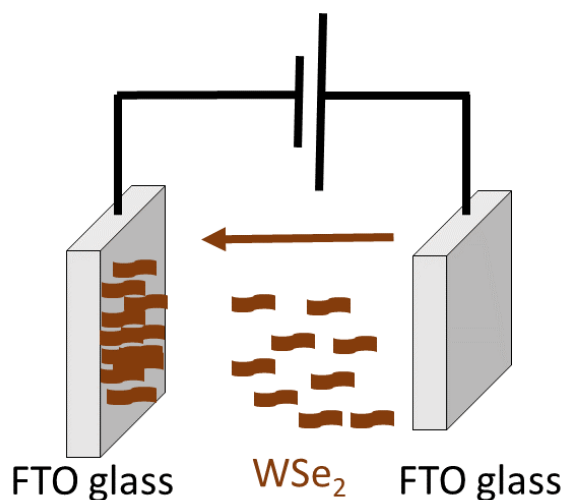
As mention throughout this chapter, we also have to take into account the variability related to the fabrication of WSe<sub>2</sub> photoelectrodes. Thus, further investigations on the sonication media are required to understand the mechanism behind the exfoliation process. The current procedure will need to be further investigated in the future, to establish the impact of exfoliation in different environment on the flake photoactivity as well as the electrical contact between the substrate and the flakes. However, we highlighted the major aspects to allow WSe<sub>2</sub> photoelectrodes fabrication.

From the best of our experience, NMP is prone to degradation during sonication under oxidative conditions that impedes flakes separation. To prevent this phenomenon, some precautions are implemented such as 2 hours exfoliation conditions. In addition, nanoflakes adhesion (electrical contact with the substrate) onto the substrate is a crucial aspects that leads to performance decrease and variability.

#### 4.4 Electrophoretic deposition for WSe<sub>2</sub> photocathode fabrication

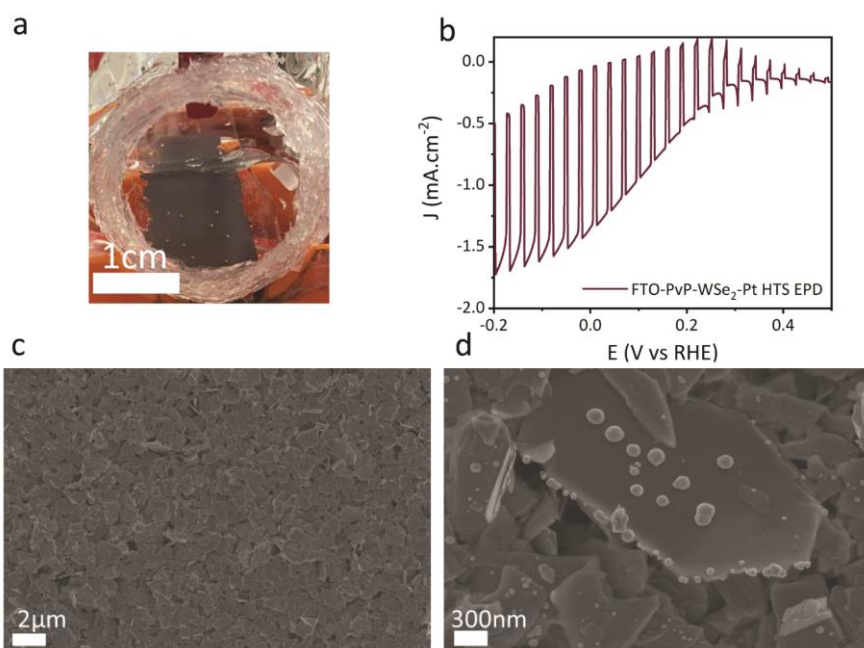
In the view of finding a method of deposition adapted to a 3D-fribrous network such as the TPCS, we evaluated electrophoretic deposition (EPD). Using this method, Liu *et al.*,<sup>168</sup> demonstrated the uniform coating of MoSe<sub>2</sub> hydrothermal exfoliated nanosheets on flexible carbon cloth to form a 3D binder-free electrode for hydrogen evolution reaction (HER).

Thus, we investigated the EPD of WSe<sub>2</sub> liquid exfoliated nanosheets on FTO glass. In the EPD technique, an electric field is applied between two electrodes (a working electrode and a counter electrode) immersed in a liquid containing charged particles such as the WSe<sub>2</sub> nanosheets (**Figure 4.6**). The negatively charged particles, driven by the electric field, are deposited onto the working electrode. We used two FTO glass as working electrode and counter electrode and a WSe<sub>2</sub> suspension in NMP as the electrolyte.



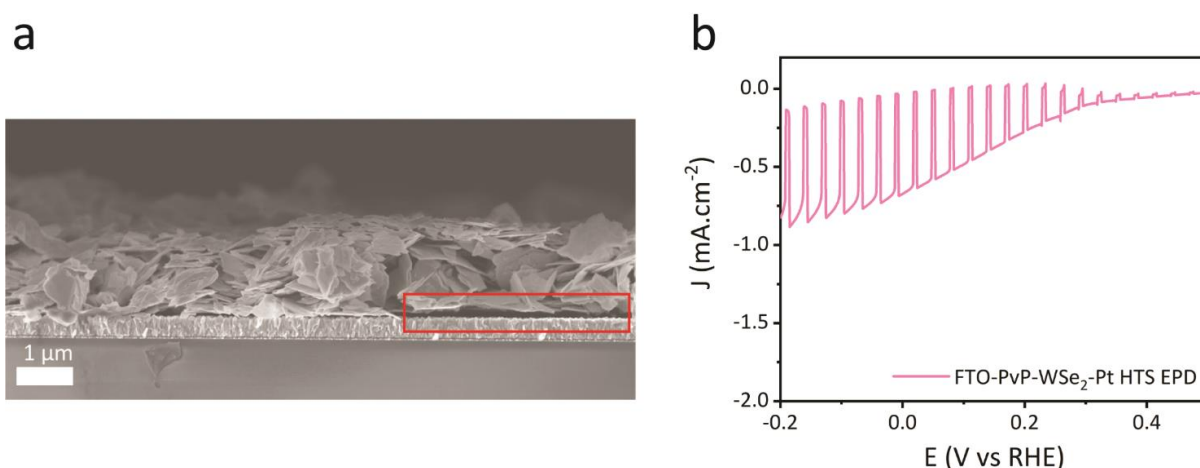
**Figure 4.6.** Schematic of the EPD set-up.

After applying 10 V for 1 hour, we observed the formation of the thick film on the working electrode side (**Figure 4.7a**). The film formed is homogeneously coated with WSe<sub>2</sub> nanoflakes as we can see in the SEM image (**Figure 4.7c**). In order to assess the photoactivity of the film towards HER, we fabricated a device using PVP underlayer, silane post treatment<sup>166</sup> and platinum (Pt) catalyst deposition. The Pt catalyst particles are well coated on the flakes by photoelectrodeposition (**Figure 4.7d**). A typical photoelectrode exhibits 1.3 mA.cm<sup>-2</sup> at 0 V vs. RHE (**Figure 4.7b**), which confirms that this method could be used for photoelectrodes fabrication.



**Figure 4.7.** (a) Photograph of EDP-deposited WSe<sub>2</sub> photocathode under operation (b) LSV curve under intermittent light (1 Sun) in H<sub>2</sub>SO<sub>4</sub> adjusted at pH 1 (c-d) SEM pictures.

Unfortunately, we noticed a decrease in the photocurrent after several LSV scans (**Figure 4.8b**), which could be attributed to flake detachment. The SEM cross-sectional shows that some parts of the film do not contact well with the conductive substrate (**Figure 4.8a**). Indeed, Yu et al.<sup>108</sup> demonstrated the importance of the spatial confinement for PEC performance, highlighting the decisive role of the contact between the flakes and the conductive substrate. Successive layers of flakes could prevent charge transport to the conductive substrate. Flake detachment could be solved by depositing a thinner film and will be implemented during the deposition on the TPCS.



**Figure 4.8.** (a) SEM cross sectional of EPD-WSe<sub>2</sub> film, highlight on the nanoflakes detachment (b) LSV curve under intermittent light (1 sun) in H<sub>2</sub>SO<sub>4</sub> adjusted at pH 1 after 4 scans.

## 4.5 Conclusion

Firstly, the method used to produce nanoflake WSe<sub>2</sub> photocathode leads to a lack of reproducibility because of the numerous parameters involved in the fabrication, from the exfoliation process to the film deposition. Moreover, the performances variability for WSe<sub>2</sub> material have been highlighted in numerous studies, from the single crystal form to the polycrystalline film. Water and/or O<sub>2</sub> can have a strong influence on the exfoliation process by interacting with the solvent and the nanoflakes. NMP is prone to degradation during sonication under oxidation conditions. In order to tackle this issue, some precaution can be implemented such as 2 hours exfoliation conditions. However, it would be essential to understand deeply the mechanism behind this phenomenon, to move forward with alternative sonication conditions (solvent such as cyrene, time, power, bubbling).

The film deposition is also an important parameter as it determines the nanoflakes alignment and the contact with the FTO substrate. The use of an underlayer such as a PvPh crosslinked layer allow improving slightly the reproducibility of the PEC performances and the adhesion of the film to the substrate. It is important to point out that even if the PVPPh underlayer is not the best option for the device performance due to its insulating characteristics. In the view of depositing WSe<sub>2</sub> nanoflakes onto the TPCS, EPD was evaluated to fabricate WSe<sub>2</sub> photocathode on FTO substrate. We successfully deposited the material on the support and obtained a photocurrent of  $-1.3 \text{ mA.cm}^{-2}$  at 0 V vs. RHE using Pt catalyst. Nevertheless, we pointed out the issue of flakes detachment that could be detrimental for the HER performance. In the next step, the parameters must be optimized for deposition onto the TPCS, notably in terms of electrical contact and film thickness.

## 4.6 Experimental methods

### 4.6.1 WSe<sub>2</sub> electrode fabrication

#### Sonication-assisted liquid exfoliation

The commercially available WSe<sub>2</sub> powder (AlfaAesar, <10  $\mu\text{m}$  in size) was exfoliated by ultrasonication in N-Methyl-2-pyrrolidone (NMP) (with/without additives). In a typical exfoliation, 250 mg of WSe<sub>2</sub> powder was dispersed in 50 mL of NMP and exposed to a Qsonica Model Q700 probe sonicator (50% amplitude, 10 s/2 s on/off cycle) for 2 or 12 h in a 0 °C bath. The sonicated dispersion was centrifuged at 2000 rpm for 30 min to remove large aggregates and then at 7830 rpm for 30 min to remove un-exfoliated particles and soluble impurities, respectively. The final dispersion used for thin film fabrication was in NMP solvent, and the concentration was adjusted to be  $1 \text{ mg.mL}^{-1}$ .

#### Liquid-liquid interfacial self-assembled thin film deposition

WSe<sub>2</sub> thin films were deposited by using the liquid-liquid interfacial self-assembly (LLISA) method based on a liquid/liquid interface. Before WSe<sub>2</sub> deposition, F:SnO<sub>2</sub> coated glass substrates (Solaronix) were coated with a layer of cross-linked poly(4-vinylphenol) (cPVPh) by first spin coating

a precursor solution (5 mg.mL<sup>-1</sup> PVPh plus 5 mg.mL<sup>-1</sup> 1,6 bis(trichlorosilyl)hexane in THF) at 3000 rpm for 60s, then heating at 110 °C for 20 min. To tolerate NMP dispersions, H<sub>2</sub>O:MeCN (85:15, v/v), was used as the bottom phase. Briefly, a fractionated WSe<sub>2</sub> dispersion in NMP was injected gradually at the heptane/H<sub>2</sub>O:MeCN interface until complete nanoflake coverage was attained. The top and bottom phases were then sequentially aspirated to deposit the self-assembled WSe<sub>2</sub> film on a substrate (for the electrodes, F:SnO<sub>2</sub>-coated glass substrates from Solaronix were used). Films were allowed to dry under ambient conditions and then at 250 °C for 30 min under air to remove all adsorbed NMP solvent.

#### Electrophoretic deposition

WSe<sub>2</sub> nanoflakes were coated by electrophoretic deposition using, a FTO glass as working electrode and a FTO glass as counter electrode. The electrolyte was composed of WSe<sub>2</sub> exfoliated flakes in N-Methyl-2-pyrrolidone (NMP) resulting from the exfoliation, diluted to 0.5 mg.mL<sup>-1</sup>. The potential applied was 10 V for 1 hour (or 6 hours). Some WSe<sub>2</sub> films deposited on the cPVPh/ F:SnO<sub>2</sub>/glass substrates were treated by 1%vol hexyl-trichlorosilane solution in toluene at room temperature. After 10 min of soaking, the electrodes were rinsed with toluene and isopropanol sequentially, followed by drying in air at 70 °C for 10 min.

#### 4.6.2 WSe<sub>2</sub> nanomaterial characterizations

##### UV-Visible spectroscopy

The absorption spectra of the thin films were recorded by using a UV-VIS-NIR UV-3600 (Shimadzu) spectrophotometer that was equipped with an integrating sphere (used to account for specular and diffuse reflection in films).

##### Contact angle measurement

The water contact angle was measured on the surface of a WSe<sub>2</sub> film by using a drop shape analyser DSA25 with the pendant drop, and sessile drop mode

##### Dynamic light scattering method

Zeta potential measurements were made with a Malvern Zetasizer Nano ZS, using a 660 nm laser. Samples were tested in stoppered glass having a 10 mm path length. The measurement was taken in the classical arrangement mode at an angle of 90°. Values for solvent viscosity at 25 °C, as provided by the solvent suppliers, were entered into the software.

The DLS technique can provide the value of the zetapotential.<sup>169</sup> It is an essential characteristic to assess the stability of a colloidal suspension and the effective surface charge associated with the double layer of a colloidal particle. To perform the measurement an electrical field is applied across the sample to induce the movement of charged particles. The particles are illuminated with laser

light and therefore scatter light. The frequency of the scattered light is a function of particle velocity, which will leave the electrophoretic mobility ( $\mu_e$ ), defined as:

$$\mu_e = \frac{V}{E}$$

with  $V$  = particle velocity ( $\mu\text{.ms}^{-1}$ )  $E$  = electric field strength ( $\text{V.cm}^{-1}$ )

Zeta potential is calculated from electrophoretic mobility. Subsequently, the Hückel equation is chosen when the thickness of EDL (electric double layer) is much bigger than the particle itself,  $f(Ka)$  is taken as 1. This equation is adapted for small particles, low concentration ( $10^{-5}\text{M}$ ) in organic solvent:

$$\mu_e = \frac{2\epsilon_r\epsilon_0\zeta f(Ka)}{3\eta}$$

with  $\epsilon_r$  = relative dielectric constant,  $\epsilon_0$  = permittivity of vacuum,  $\zeta$ = zetapotential,  $f(Ka)$  = Henry's function,  $\eta$ = viscosity

In the case of big particles (up to  $1\text{ }\mu\text{m}$ ), the electric double layer is smaller compare the particle radius,  $f(Ka)$  is taken as 1.5. For high concentration ( $10^{-2}\text{M}$ ), aqueous solutions, Helmholtz-Smoluchowski equation could be used instead:  $\mu_e = \frac{\epsilon_r\epsilon_0\zeta}{\eta}$

#### Electronic microscopy: SEM-TEM

The morphology of the LLISA thin films prepared with fractionated WSe<sub>2</sub> flakes were characterized using a Talos transmission electron microscopy (TEM) via direct LLISA deposition on a carbon-coated TEM grid at 200kV.

SEM pictures were taken with a Zeiss Merlin microscope at 100 pA.

#### ▪ Photoelectrochemical activity

#### Sacrificial electrolyte testing

WSe<sub>2</sub> LLISA films deposited on F:SnO<sub>2</sub> glass or cPVPh-F:SnO<sub>2</sub> substrates were used as photocathodes (working electrode) in the three-electrode PEC measurement with a Pt counter electrode and a Ag/Ag<sup>+</sup> reference electrode for measurement in an organic electrolyte (saturated chloranil and 0.1 M NBu<sub>4</sub>PF<sub>6</sub> in MeCN). Linear scan voltammetry (LSV) measurements were carried out with a BioLogic SP-50 potentiostat with an electrode active area of 0.25 cm<sup>2</sup>. The applied voltage was swept from positive to negative with a scan rate of 10 mV.s<sup>-1</sup>, intermittent illumination of white light was provided and projected onto the substrate side by a 450 W Xe arc lamp solar simulator (Muller GmbH Elektronik-Optik), the illumination power was adjusted to match the photon density flux to the standard AM1.5G flux up to a photon energy of 1.66 eV.

#### HER testing



Prior to testing, Pt catalyst was deposited by photoelectrodeposition in a set-up composed of the sample as the working electrode, Pt wire counter electrode and an Ag/AgCl reference electrode. The electrolyte is an aqueous solution of 1mM H<sub>2</sub>PtCl<sub>6</sub> at pH 0.5. The deposition was done at E=0.05V vs. Ag/AgCl under illumination until 14 mC.cm<sup>-2</sup> charge has been passed. WSe<sub>2</sub> EPD films deposited on F:SnO<sub>2</sub> glass or cPVPh-F:SnO<sub>2</sub> substrates were used as photocathodes (working electrode) in the three-electrode PEC measurement with a Pt counter electrode and a Ag/AgCl reference electrode for measurement in H<sub>2</sub>SO<sub>4</sub> adjusted at pH 1.

Linear scan voltammetry (LSV) measurements were carried out with a BioLogic SP-50 potentiostat with an electrode active area of 1-1.4 cm<sup>2</sup>. The applied voltage was swept from positive to negative with a scan rate of 10 mV s<sup>-1</sup>, intermittent illumination of white light was provided and projected onto the substrate side by a 450 W Xe arc lamp solar simulator (Muller GmbH Elektronik-Optik), the illumination power was adjusted to match the photon density flux to the standard AM1.5G flux up to a photon energy of 1.66 eV.

## Chapter 5     Developing photocathode coatings on the TPCS

The TPCSs developed for photoelectrode application offer a versatile platform for semiconductor coating. In the view of fabricating a TPCS-based photocathode for PEM-PEC application, we studied the coating of p-type semiconductors and an organic semiconductor (OS) blend: WSe<sub>2</sub>, Cu<sub>2</sub>O and several bulk heterojunction (BHJ) blends. These semiconductors were chosen for their ability to perform HER in liquid electrolyte. WSe<sub>2</sub> nanoflakes were coated by electrophoretic deposition but the difficulty in coating a uniform thin film on a 3D substrate resulted in poor PEC performances. In contrast, Cu<sub>2</sub>O was uniformly coated on the TPCS through an *in-situ* electro-conversion. Despite the coating of a protective layer, photocorrosion of the photocathode was observed, possibly due to charge accumulation, in the absence of HER catalyst. Finally, the best performance for PEC test in liquid electrolyte was obtained for a TPCS coated with a CuSCN hole transporting layer and an organic BHJ. CuSCN was successfully coated by electrodeposition while the BHJ was coated by a dip-coating method. The importance to use a high boiling point solvent for the BHJ dip-coating was highlighted to avoid any “coffee ring effect”. In addition, prior to PEC testing, a pre-wetting step was implemented to ensure contact of the electrolyte with the electrode surface. The best performing device exhibited a photocurrent of  $-6 \text{ mA.cm}^{-2}$  at 0 V vs. RHE in sacrificial Eu<sup>3+</sup> electrolyte under 1 Sun illumination.

## 5.1 Semiconductor coatings for photoelectrodes application

In chapter 2, a transparent porous conductive substrate (TPCS) has been developed and implemented for photoelectrode application using hematite as a model semiconducting material. In the view of integrated a TPCS-based photocathode in the PEM-PEC cell, a photocathode coating must be investigated.

WSe<sub>2</sub> is a p-type semiconductor with an appropriate band gap<sup>148</sup> (1.6 eV) and conduction band position for the HER. Indeed, WSe<sub>2</sub> can be used as a photocathode for water reduction. As mentioned in chapter 4 section 4.1, Lewis and coworkers,<sup>75</sup> showed that a WSe<sub>2</sub> single crystal coated with a Pt-Ru catalyst can exhibit a conversion energy efficiency superior to 7% for HER and a photocurrent density of over 15 mA.cm<sup>-2</sup> at 0 V vs. RHE under mildly acidic conditions. Although this result is promising, the use of a single crystal is not feasible from an industrial point of view, due to the cost necessary to produce this type of structure and the inability to grow WSe<sub>2</sub> single crystals larger than a few mm. Despite considerable research, traditional methods to deposit WSe<sub>2</sub> thin films (e.g., by chemical vapor deposition) are prohibitively expensive and not suitable for large areas. Therefore, sonication-assisted exfoliation technique associated with thin-film self-assembly,<sup>156,170</sup> was developed because it is versatile and suitable for large-scale applications. Yu *et al.*<sup>170</sup> developed a method to process WSe<sub>2</sub> nanosheets into thin films. Firstly, the fabrication of the WSe<sub>2</sub> nanosheets suspension is performed by liquid-phase exfoliation to obtain a suspension of few-layer nanosheets ranging from 200-1000 nm in the lateral dimension at a concentration of 1 mg.mL<sup>-1</sup> in NMP (N-methylpyrrolidone). They demonstrated the formation of WSe<sub>2</sub> nanosheets thin film by a liquid-liquid self-assembly (LLISA) technique, where the film is formed in the interface between two non-miscible liquids. However, this method is also not adapted for porous substrates such as the TPCS, as it would not homogeneously coat the 3D network, but only the top of the substrate surface. In contrast, WSe<sub>2</sub> could be deposited on TPCS by electrophoretic deposition (EPD), similarly than on flat FTO glass, as demonstrated in chapter 4 section 4.3. The feasibility of this process and the coating homogeneity on TPCS need to be evaluated.

Cu<sub>2</sub>O is an ideal candidate as a photocathode material due to its band gap (2.0 eV), abundance and low price. Moreover, its ability to reduce water has been widely investigated.<sup>80,81,69</sup> However, some limitations hinder the development of this material, such as its low stability and low light harvesting ability. To tackle the issue of stability, protective layers<sup>48,79,80</sup> deposited by atomic layer deposition (ALD) have been developed while nanostructuring<sup>48,171</sup> allows to efficiently absorb sunlight. In chapter 3, we identified a strategy to control the morphology of electrodeposited cubic-Cu<sub>2</sub>O for deposition on flat FTO glass. The method consists in pre-depositing a CuSCN layer by electrodeposition and then to convert it to Cu<sub>2</sub>O by an *in-situ* electroconversion. Although, Cu<sub>2</sub>O can be directly deposited on bare FTO, it exhibits a defined morphology composed of large inhomogeneous cubes. On the other hand, if a CuSCN layer is first deposited, and then converted to Cu<sub>2</sub>O, it allows a fine morphology control. Depending on the thickness of the CuSCN layer, the size of the cubes and the thickness of the film can be tuned. Herein our goal is to demonstrate the

Cu<sub>2</sub>O deposition on the TPCS and show the effect of the *in-situ* electro-conversion on the morphology of Cu<sub>2</sub>O on the high surface area substrates such as the TPCSs.

Recently, organic conjugated polymer semiconductors have become promising candidates for solar energy conversion for solar cell<sup>172,173</sup> or PEC applications.<sup>66,70,82–84,174,175</sup> Indeed, several of their intriguing properties such as earth-abundant elements composition, tunable band gap, and solution-processability are key advantages for photocathode application. A bulk heterojunction (BHJ) is composed of two organic semiconductors, an electron donor and an electron acceptor and is necessary to separate effectively photogenerated excitons into free charge carriers. The instability of organic semiconductors remains an important point toward further development of these materials. To address this issue of stability, two main strategies have been used: a thin TiO<sub>2</sub> ALD protective layer coating<sup>82–84</sup> or molecular engineering of the bulk heterojunction blend.<sup>66,174,176</sup> PTB7-Th:PCBM (phenyl-(C61)-butyric acid methyl ester) blend is a typical polymer donor/small molecule acceptor pair used in organic solar cell and photocathode applications<sup>83,177</sup>. Nevertheless, PCBM is a fullerene-based acceptor known for its instability due to dimerization upon operation that leads to generation of electron traps.<sup>178,179</sup> In the view of replacing PCBM, Yao *et al*<sup>174</sup> established few-hours stability for a photocathode composed of FTO glass as conductive substrate, MoO<sub>3</sub> as hole transporting layer (HTL), a molecular-engineered BHJ (PTB7-Th:PDI-V as a perylene diimide based non fullerene acceptor polymer) as the absorbing material, and RuO<sub>2</sub> as the HER catalyst. Taking inspiration from this work, the first step is to find a HTL that could be easily deposited on the TPCS. The second step is to find a method for coating the organic material onto a porous substrate. Spin-coating has been mostly used to coat homogenous organic semiconductor films onto flat substrates. However, this method is not adapted for a porous support; therefore, a new method of deposition must be developed.

In this chapter, we will evaluate the coating of two p-type semiconductor materials and some BHJs on the TPCS. While the BHJ consists of an electron donor and an electron acceptor, its behavior in the photocathode system is that of a p-type semiconductor, so to simply the discussion we refer to the BHJ as a p-type semiconductor in this chapter. The first step consists in determining the appropriate method of deposition for each material. Then, we will compare the optimized deposition procedure and PEC performances in liquid electrolyte. The PEC performances will be evaluated in liquid phase in the view to optimize the semiconductor coating without the difficulty to perform the reaction in the gas phase. To characterize solely the p-type semiconductor coatings (without catalyst), a sacrificial electrolyte could be used if possible (Eu<sup>3+</sup>). The main goal is to determine the semiconductor material best suited for the deposition on the TPCS and integration into a PEM-PEC cell.

## 5.2 WSe<sub>2</sub>-coated TPCS

Electrophoretic deposition<sup>168</sup> (EPD) can facilitate the coating processability on porous or irregular shape structure. Therefore, EPD was used in order to maximize the surface area coated with the

material. In the EPD technique, an electric field is applied between two electrodes (a working electrode and a counter electrode) immersed in a liquid containing charged particles such as the WSe<sub>2</sub> nanosheets (**Figure 5.1a**). The negatively charged particles, driven by the electric field, get deposited onto the working electrode. In order to improve the activity for HER, WSe<sub>2</sub> requires a catalyst<sup>75,170,180</sup> such as Pt, Pt/Ru, Pt/Cu. Platinum photoelectrodeposition was used because it allows to coat preferentially the semiconductor surface due to the “photo” interaction of the reaction. Moreover, it was used by Yu *et al*<sup>170</sup> in the same manner for WSe<sub>2</sub> solution-processable flat film. Overall, WSe<sub>2</sub> EPD and Pt photoelectrodeposition were demonstrated in the chapter 4 beforehand, on flat FTO substrate, exhibiting a photocurrent of 1.3 mA.cm<sup>-2</sup> at 0 vs. RHE.

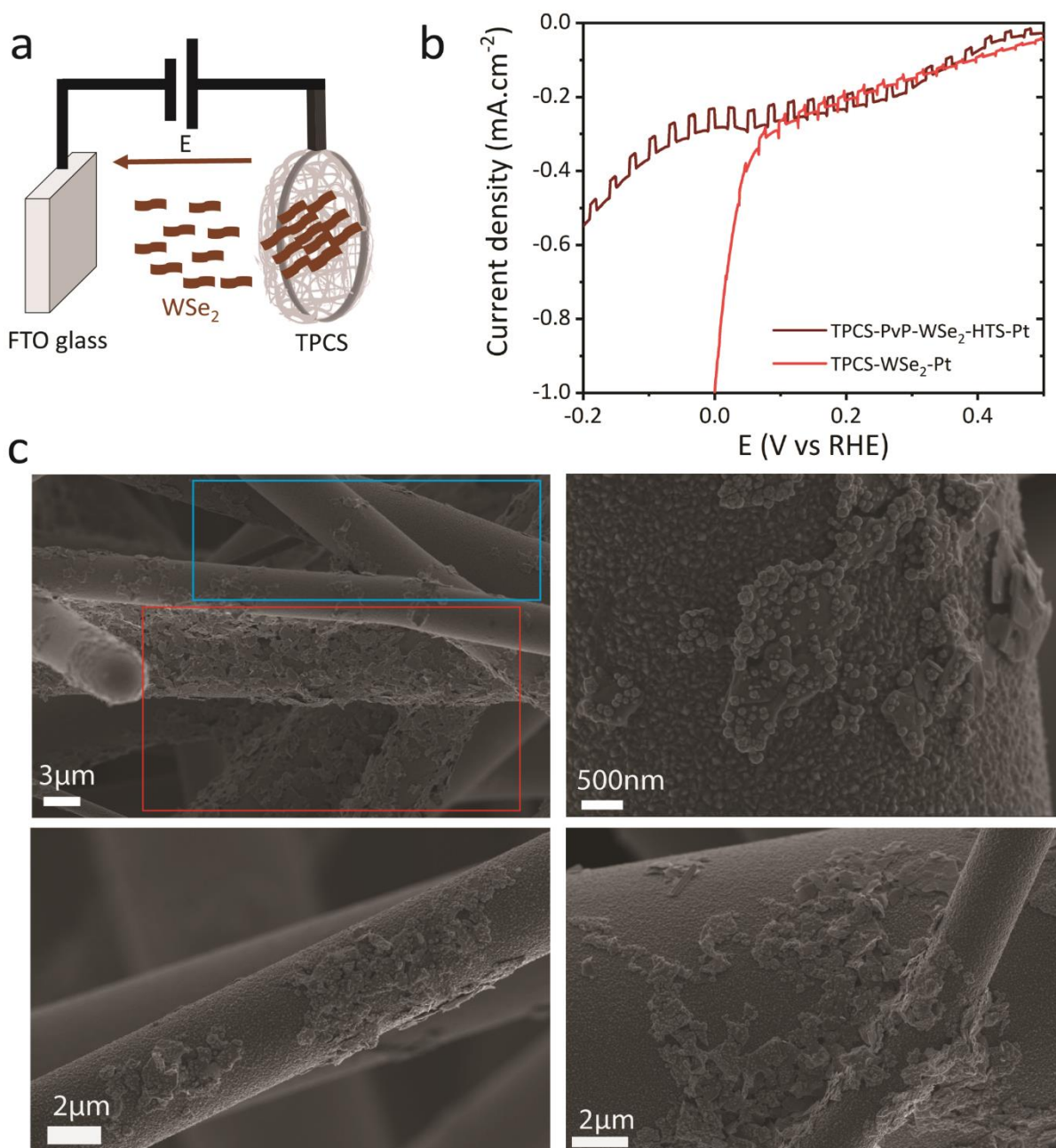
The same EPD (1 h) of WSe<sub>2</sub> nanoflakes was applied onto the TPCSs (see experimental section 5.5). **Figure 5.1c** shows three representative SEM images of the WSe<sub>2</sub> coated TPCS. The coating is not homogenous as the fibers are not fully coated by the nanosheets. Despite our efforts to improve the coating by increasing the EPD time up to 6 h, the fibers coverage remained unchanged (see Appendix 5, Figure S5.2). Prior to PEC testing, Pt catalyst was deposited by photoelectrodeposition. The Pt particles are visible on the WSe<sub>2</sub> nanoflakes.

The HER performance was evaluated in H<sub>2</sub>SO<sub>4</sub> electrolyte at pH 1. In **Figure 5.1b**, the response to intermittent illumination is weak, on the order of 10-30 μA.cm<sup>-2</sup> for TPCS-WSe<sub>2</sub>-Pt sample. Moreover, we observed flakes detachment in the electrolyte after testing (see Appendix 5, Figure S5.3). The flakes detachment from the support could be at the origin of a performance loss, as it was highlighted in chapter 4, for flat FTO substrate. In order to improve flakes adhesion, we deposited a cross-linked poly(4-vinylphenol) (PvP) underlayer by dipping. We observed the typical dark current decrease after PvP coating on bare TPCS (see appendix 5, Figure S5.1), as it was shown in chapter 4 (appendix 4). Hexyl-trichlorosilane (HTS) was also coated by dipping as a post-treatment to mitigate material defects, as reported elsewhere<sup>166</sup>. The dark and photocurrent only slightly increased but no tremendous effect was observed. The typical performance for WSe<sub>2</sub>-Pt photoelectrode deposited by EPD on flat FTO glass is around 0.5 - 1.3 mA cm<sup>-2</sup> at 0 V vs. RHE. Therefore, the low value of the photocurrent for the TPCS WSe<sub>2</sub> electrode shows that the porous electrode performs poorly compared to WSe<sub>2</sub> photoelectrode coated on flat FTO glass.

Several phenomena could explain the gap of performance between the WSe<sub>2</sub> photoelectrode coated on TPCS and flat FTO. The method of deposition and the electrical interface between the WSe<sub>2</sub> nanosheets and the conductive support could play a role. Although flat FTO samples were successfully coated by EPD in chapter 4, the limitation of this method was also highlighted (e.g., flakes detachment). Indeed, contrary to the LLISA deposition, where the nanoflake are homogeneously assembled into a 2D monolayer flakes film, relatively thicker films are formed with EPD. Similarly, the EPD used for the WSe<sub>2</sub> deposition on porous support does not allow uniform coating of the fibrous support. Some parts of the electrode are fully covered with WSe<sub>2</sub> nanosheets and some other parts are bare (**Figure 5.1c**).

In addition, it has been established that the adhesion between the 2D-nanoflakes and the conductive support are essential to ensure charge transport from the material to the electron

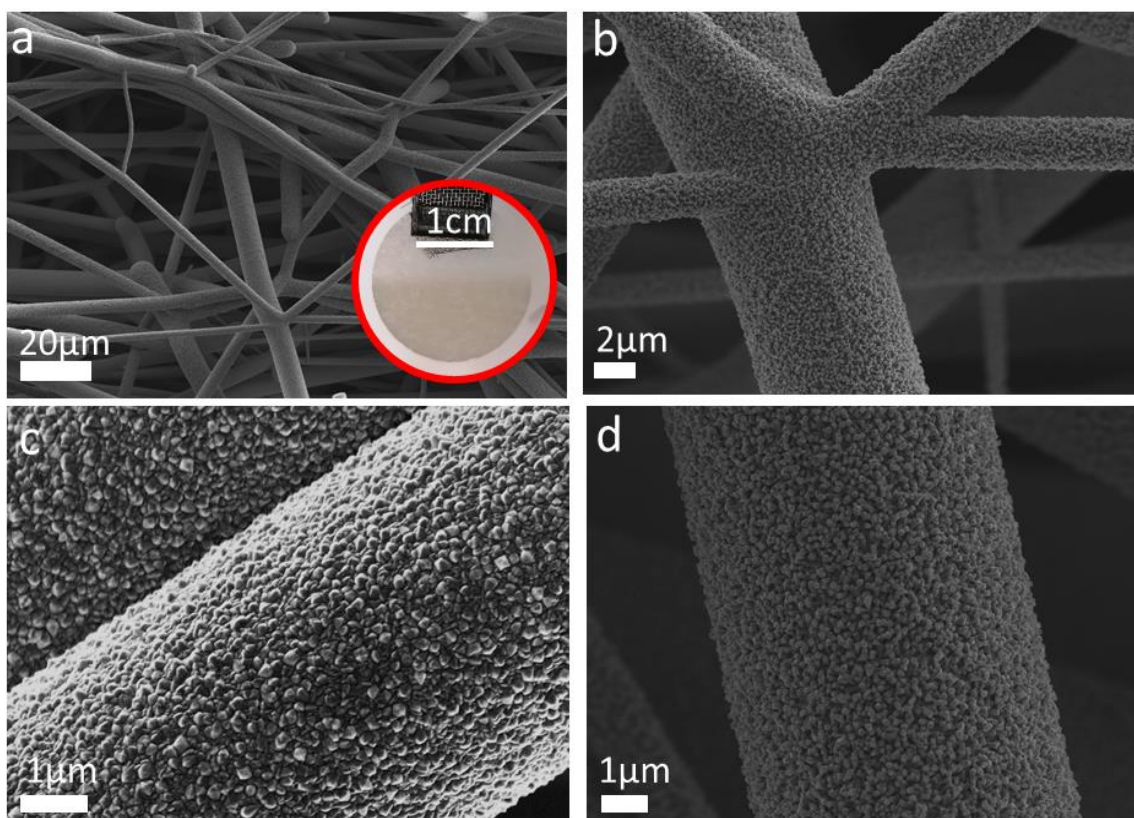
conducting back contact (FTO glass or TPCS). In the flat FTO case, the monolayer flakes are well-connected with the flat support thanks to LLISA deposition or well-coated with a thick nanoflakes film thanks to EPD. However, in the TPCS case, the fibrous morphology of the TPCS make the connection between the 2D-nanoflakes and the rounded conductive support more challenging. This morphology difference could be one of the reasons for the poor PEC performance of the  $\text{WSe}_2$ -Pt TPCS electrode.



**Figure 5.1** (a) Schematic of EPD set-up (b) LSV curve of  $\text{WSe}_2$ -Pt coated TPCS at pH 1 under 1 sun illumination (c) SEM picture of  $\text{WSe}_2$ -Pt coated TPCS, the red square shows the fully covered fibers and the blue square shows the uncoated fibers.

### 5.3 Cu<sub>2</sub>O-coated TPCS

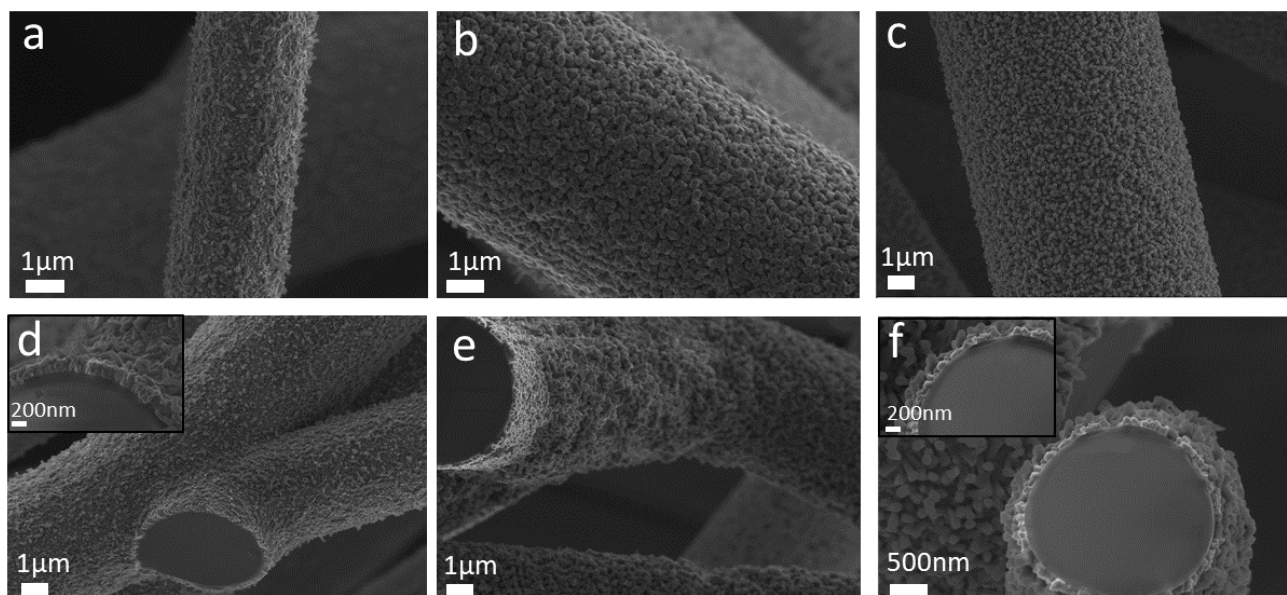
Cu<sub>2</sub>O is an ideal candidate for HER photoelectrode; therefore, we investigated the coating of Cu<sub>2</sub>O onto the TPCS surface. The TPCS was subject to CuSCN electrodeposition conditions (chronoamperometry at  $-0.3$  V vs. Ag/AgCl) as described in the experimental part. **Figure 5.2** shows the SEM images of the CuSCN-coated TPCS. The typical CuSCN nanorods are homogenously coated onto the TPCS fibers and the coated part appears a bit more contrasted on the TPCS photograph (red circle). **Figure 5.2c** shows the TPCS morphology before CuSCN deposition with the apparent FTO grains while in **Figure 5.2d**, the nanorods cover the fiber surface.



**Figure 5.2.** (a,b) SEM images and photograph of a CuSCN-coated TPCS (10min deposition) (c) SEM image of bare TPCS showing FTO grains (d) SEM image of CuSCN(10min)-coated TPCS showing CuSCN nanorods.

**Figure 5.3** shows the morphology of the CuSCN-coated TPCS for different CuSCN electrodeposition time. The different deposition times correspond to different number of charges passed,  $200 \text{ mC.cm}^{-2}$ ,  $400 \text{ mC.cm}^{-2}$  and  $600 \text{ mC.cm}^{-2}$  for 2min, 5min and 10 min respectively. In **Figure 5.3 a,d** and **Figure 5.3b,e**, by increasing the deposition time from 2 to 5 min for the same area coated, the density of the nanorods increased, leading to a homogenous fiber coverage. Moreover, the length of the nanorods increase from 220 to 250 nm. In **Figure 5.3c,f**, the deposition time is prolonged to 10 min, thereby the nanorods density and size are even more enhanced, forming a 300 nm thick CuSCN nanorods film.



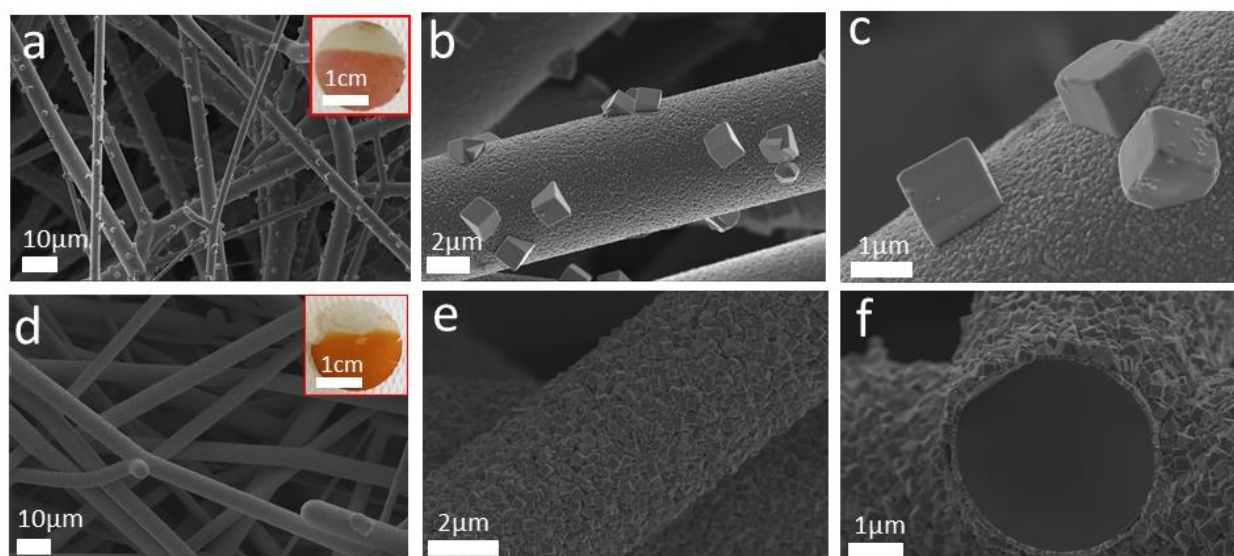


**Figure 5.3.** SEM images of CuSCN-coated TPCSs ( $3 \text{ cm}^2$ ) for different electrodeposition time (a,d) 2 min, (b,e) 5 min, (c,f) 10 min.

Given that our observation of homogeneous coating of the TPCS fibers, we can conclude that electrodeposition is an appropriate method to coat semiconductors on 3D conductive support with features sizes in the 1 to 10  $\mu\text{m}$  range like the TPCSs.

We optimized the parameters to coat uniformly  $\text{Cu}_2\text{O}$  on the TPCS by varying the charges passed during CuSCN and  $\text{Cu}_2\text{O}$  deposition (see appendix 5, Figure S5.4 and S5.5). Considering this result, we continued the investigation on the deposition parameters in the view to obtain a homogenous thin  $\text{Cu}_2\text{O}$  film. To do so, we performed an optimized  $\text{Cu}_2\text{O}$  deposition on bare TPCS, and TPCS-CuSCN( $250 \text{ mC.cm}^{-2}$ ) at  $-0.2 \text{ mA.cm}^{-2}$  for 50 min. As expected, based on the results demonstrated in chapter 3, for bare TPCS, we obtained a partial coverage of the TPCS fibers with large scattering cubes (**Figure 5.4 a-c**). This result raises two issues: (i) the large and light-scattering cubes obtained could generate scattering of the light, reducing efficiency and (ii) the full substrate surface potential is not exploited due to the uneven coverage. We continued our investigation on the deposition parameters to obtain a homogenous thin  $\text{Cu}_2\text{O}$  film. Therefore, we applied our *in-situ* electroconversion in the interest of obtaining thin and homogenous  $\text{Cu}_2\text{O}$  film on the TPCS. By applying this method on pre-deposited CuSCN-TPCS, the morphology of the  $\text{Cu}_2\text{O}$  coating was tuned, as shown before. We obtained a fully covered substrate surface (**Figure 5.4 d-f**) with smaller  $\text{Cu}_2\text{O}$  cubes (300-350 nm thick) which would prevent light scattering.

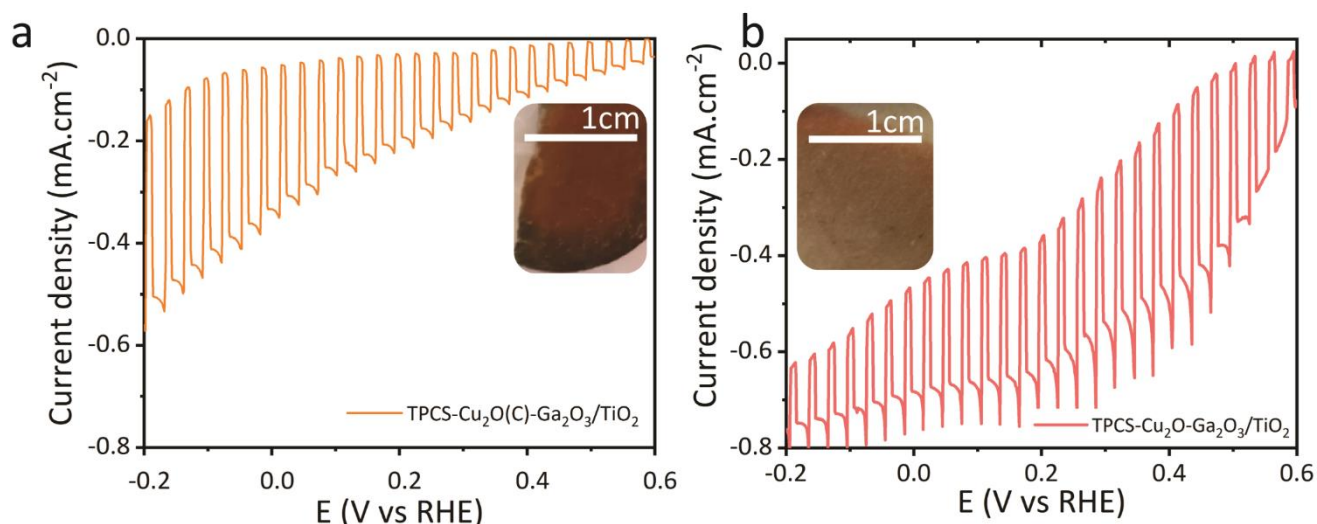




**Figure 5.4.** SEM pictures of  $\text{Cu}_2\text{O}$ -coated (50 min at  $-0.2 \text{ mA}\cdot\text{cm}^{-2}$ ) TPCSs on (a-c) bare TPCS (d-f) 5 min  $\text{CuSCN}$ -coated TPCS.

In order to test the  $\text{Cu}_2\text{O}$ -coated TPCS for HER, we deposited a protective layer composed of  $\text{Ga}_2\text{O}_3/\text{TiO}_2$  by ALD. We compared the samples coated on bare TPCS (TPCS- $\text{Cu}_2\text{O}$ ) and a sample made with the *in-situ* electroconversion (TPCS- $\text{Cu}_2\text{O}$ (c)) as seen in **Figure 5.4**. At pH 5, under intermittent solar illumination, the best sample (i.e., TPCS- $\text{Cu}_2\text{O}$ (c)) exhibits a current of  $-0.4 \text{ mA}\cdot\text{cm}^{-2}$  at 0 V vs. RHE (**Figure 5.5a**). By contrast, TPCS- $\text{Cu}_2\text{O}$  made with a direct electrodeposition showed a high dark current, typical from  $\text{Cu}_2\text{O}$  photocorrosion which is confirmed by the darker color of the electrode after testing (**Figure 5.5b**). While TPCS- $\text{Cu}_2\text{O}$ (c) exhibits less than flat  $\text{Cu}_2\text{O}$  photocathodes (best performance:  $10 \text{ mA}\cdot\text{cm}^{-2}$  with  $\text{RuO}_x$  catalyst), these results are a promising start for the deposition on the TPCS.

Indeed, the state of the art benchmark  $\text{Cu}_2\text{O}$  photocathode contained a HER catalyst such as  $\text{RuO}_x$ . However, we did not perform the  $\text{RuO}_x$  catalyst deposition because we noticed a drastic color change of the samples before and after testing (**Figure 5.5**). This colour change could come from  $\text{Cu}_2\text{O}$  disproportionation due to charge accumulation. Indeed, in the absence of catalyst, and without a homogenous electron selective layer coating, the photogenerated electrons would have more chances to accumulate at the surface and degrade the material. Our hypothesis is that the photocorrosion could originate from (i) the inhomogeneity of the protective layer due to the ALD coating and to the large surface area tested compared to what is usually used (i.e.,  $2.36 \text{ cm}^2$  vs.  $0.3 \text{ cm}^2$ , there will be more chances to test an area not well coated by the  $\text{TiO}_2$  protective layer)(ii) the absence of HER catalyst.

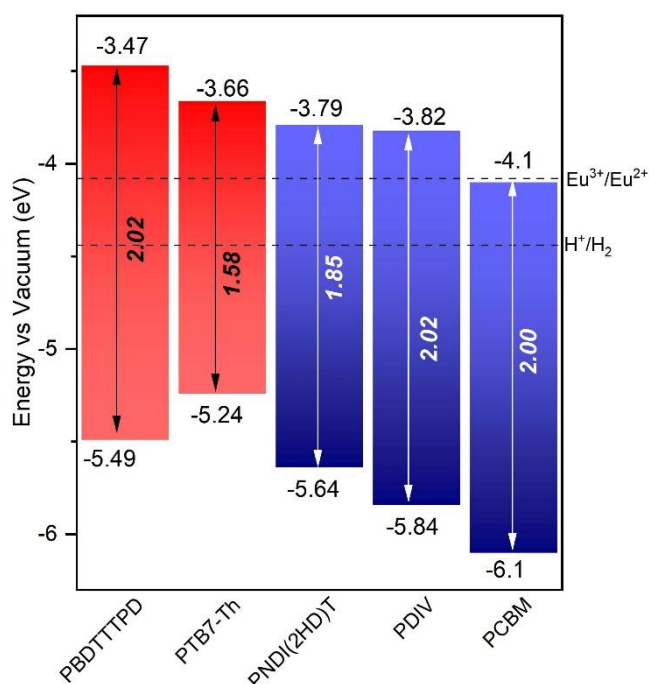


**Figure 5.5.** LSV curves of Cu<sub>2</sub>O-coated TPCS in liquid electrolyte at pH 5 under chopped (1 Sun) illumination and photograph of the sample after LSV testing (a) for TPCS, pre-deposited CuSCN (5 min), Cu<sub>2</sub>O (50 min at  $-0.2\text{mA}\cdot\text{cm}^{-2}$ ) and Ga<sub>2</sub>O<sub>3</sub>/TiO<sub>2</sub> (ALD) (b) for TPCS-bare, Cu<sub>2</sub>O (50 min at  $-0.2\text{mA}\cdot\text{cm}^{-2}$ ) and Ga<sub>2</sub>O<sub>3</sub>/TiO<sub>2</sub> (ALD).

## 5.4 Bulk heterojunction-coated TPCS

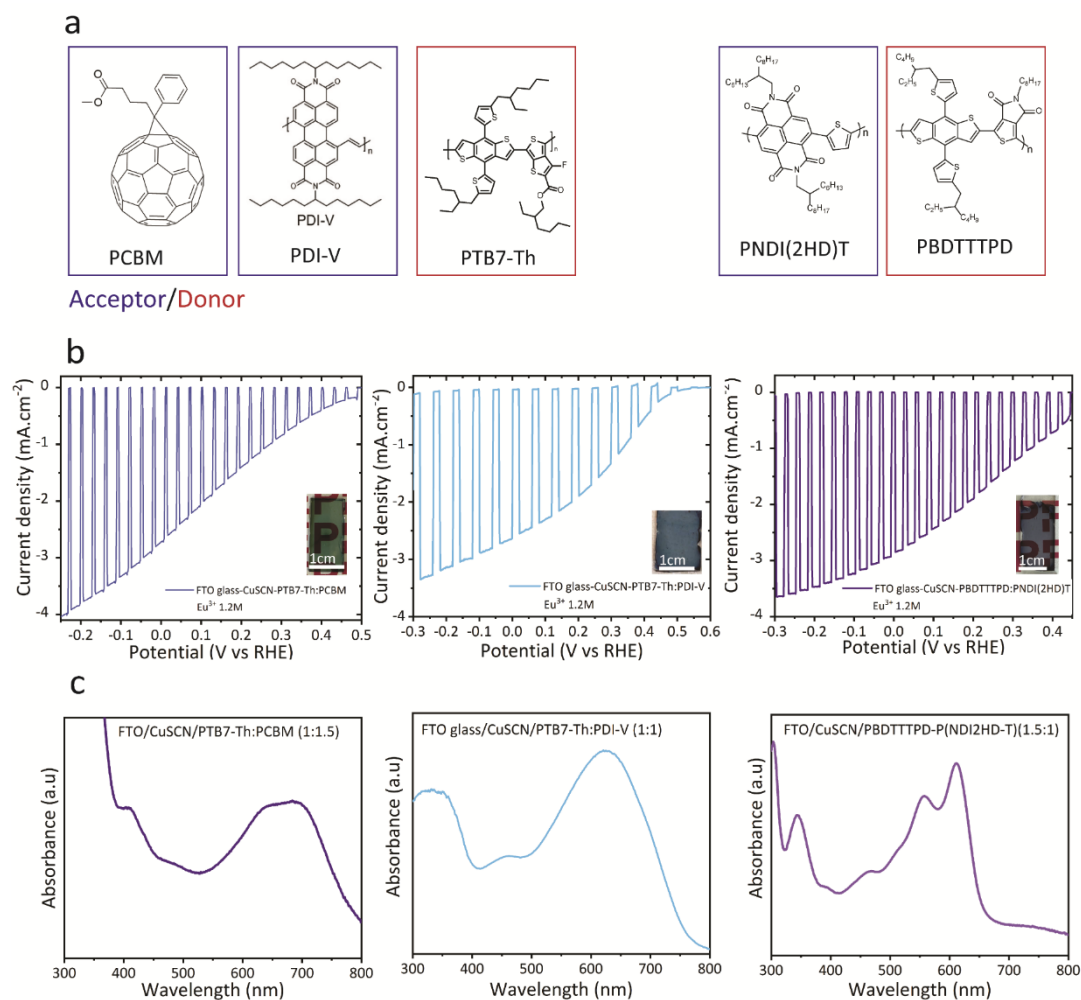
### 5.4.1 CuSCN : Hole transporting layer

The organic BHJ photoelectrodes requires the use of a hole transporting layer to optimize PEC performance.<sup>84</sup> Yao et al.,<sup>87</sup> deposited MoO<sub>3</sub> on flat FTO substrate by thermal evaporation. This method would be challenging to implement on the TPCS due to the fragility of the support. CuO<sub>x</sub>,<sup>84</sup> CuI<sup>82,175</sup> and NiO<sub>x</sub><sup>181</sup> have also been used as hole transporting layers for BHJ photocathode. These layers are deposited by spin-coating, which is a method mostly used to coat planar surface.<sup>182</sup> Copper thiocyanate is an HTL appropriate candidate due to its band position and its ease of deposition by electrodeposition.<sup>110</sup> The band diagram in **Figure 5.6** shows that it is possible to perform water reduction with diverse BHJ systems. To verify that, flat device were fabricated on FTO glass, using CuSCN as HTL and 3 different BHJ blends, namely PTB7-Th:PCBM (1:1.5 w:w), PTB7-Th:PDI-V (1:1 w:w) and a novel PBDTTTPD:PNDI(2HD)T (1:1 w:w) deposited by spin-coating (see chemical structure in **Figure 5.7a**). PBDTTTPD:PNDI(2HD)T and PTB7-Th:PDI-V are novel type of non-fullerene all polymers BHJs that could also be used to tackle the lack of stability of PCBM.



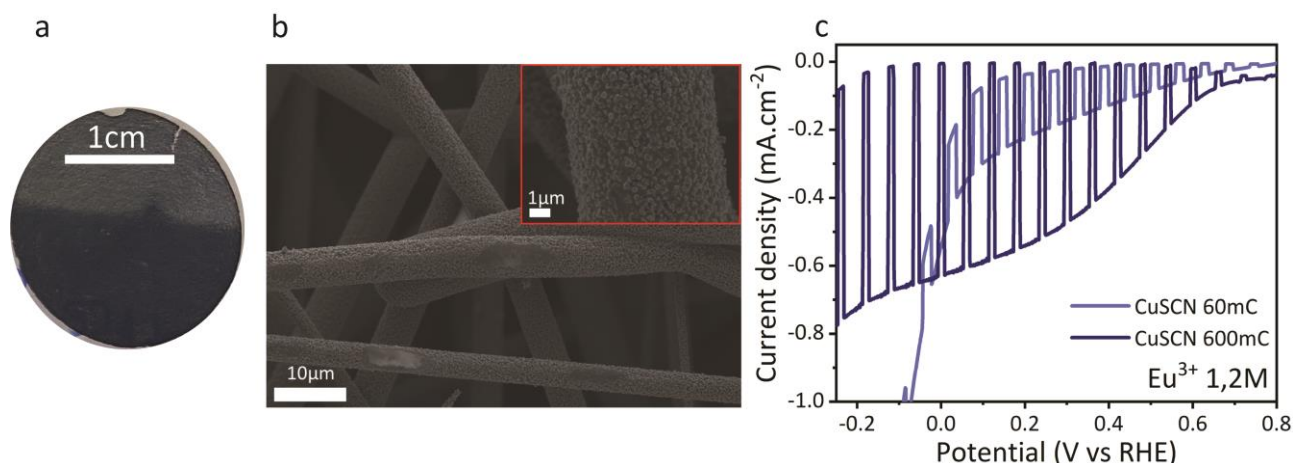
**Figure 5.6.** Band diagram for the BHJ systems studied.

The PEC performance was evaluated in sacrificial aqueous europium solution, following the procedure used by Yao *et al*<sup>174</sup>.  $\text{Eu}^{3+}/\text{Eu}^{2+}$  has a reduction potential ( $-4.08$  eV vs. vac) slightly lower than  $\text{H}^+/\text{H}_2$  ( $-4.44$  eV vs. vac), therefore, there is no need for an extra catalyst layer as the reaction is kinetically favorable. The photoelectrodes were tested in a  $\text{Eu}^{3+}$  1.2M solution and exhibited a promising photocurrent around  $3 \text{ mA}\cdot\text{cm}^{-2}$  at 0 V vs. RHE (**Figure 5.7b**). The devices coated on FTO glass absorb in the visible range (400 - 800nm) as seen in **Figure 5.7c**. For flat electrode, CuSCN was deposited by electrodeposition and the BHJ by the typical spin-coating method with optimized processing conditions (i.e., solvent and concentration). All the BHJ blends that were tested gave a similar photocurrent amplitude for  $\text{Eu}^{3+}$  reduction, however these blends showed diverse level of stability. The ideal BHJ blend should show the highest photocurrent as well as great stability for HER. Therefore, it could be chosen after further investigation on HER performance in liquid phase for the final cell device.



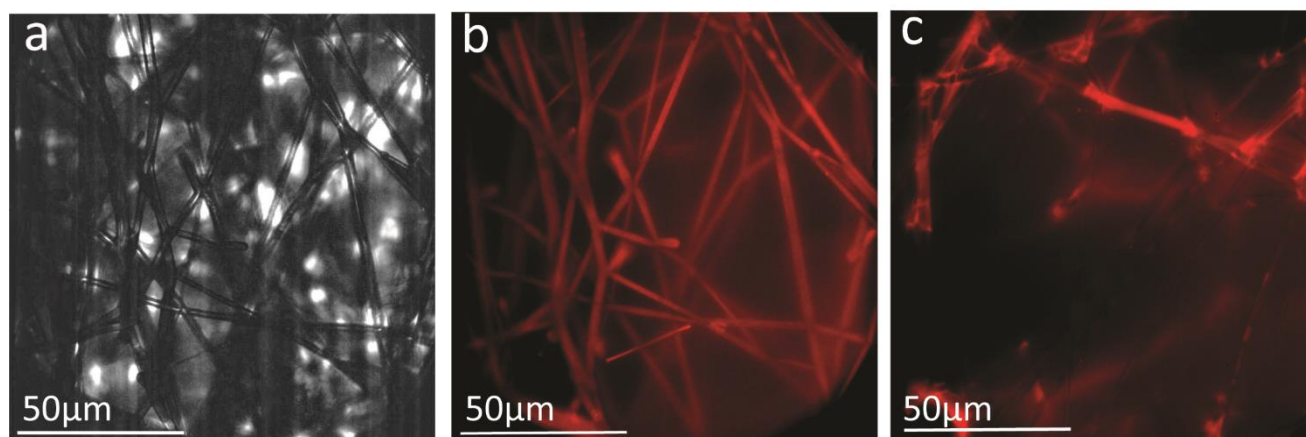
**Figure 5.7.** Characterizations of flat FTO-CuSCN(30 s)-PTB7-BHJ (a) polymers and small molecule chemical structure (b) LSV curves tested in  $\text{Eu}^{3+}$  (1 M) at pH 2 under chopped (1 Sun) (c) illumination UV-visible absorbance spectra.

We fabricated a TPCS(BHJ) photocathode by several steps (i) electrodeposition of CuSCN, (ii) immersion of the TPCS in a BHJ solution (PTB7:PDI-V, 1:1), (iii) annealing at 150 °C. The same annealing procedure were used for the devices made on FTO glass. After the total immersion of the TPCS in the BHJ solution, we could see a dark blue color appearing on the CuSCN-coated part while the uncoated section was light blue (**Figure 5.8**). This difference could come from a higher affinity of the BHJ blend with the CuSCN rather than FTO. In the SEM image we see the presence of the OS (dark patches) on the CuSCN nanorods, however it does not seem homogenously coated on all the fibers. In order to determine the performance of our TPCS-CuSCN-BHJ photocathode, we tested the samples for  $\text{Eu}^{3+}$  reduction (sacrificial electrolyte). In **Figure 5.8c**, we can see that the photoelectrodes are active. By tuning the amount of charge passed during the CuSCN electrodeposition from 60 to 600 mC (for 3 cm<sup>2</sup> surface), we could decrease the dark current while increased the photocurrent to 0.6 mA.cm<sup>-2</sup> at 0 V vs. RHE. The device architecture works but the CuSCN layer needs to be further optimized, and the BHJ coating will be investigated to increase the PEC performance.



**Figure 5.8.** (a) photograph of a TPCS samples coated with CuSCN-600mC and BHJ (PTB7-Th:PCBM, 1:1) 4mg.mL<sup>-1</sup> in chloroform (b) SEM images (c) LSV curve in Eu<sup>3+</sup> 1.2M under (1 sun) intermittent illumination.

To evaluate the BHJ coating homogeneity, we imaged the BHJ (PTB7-Th:PDI:V) by confocal microscopy ( $\lambda_{\text{excitation}} = 640 \text{ nm}$ ). In **Figure 5.9a**, we can see the bright field image of a TPCS-CuSCN (600 mC)-BHJ sample. The photoluminescence (PL) signal (in red) match with the bright field image (**Figure 5.9b**), suggesting that the BHJ is coated on all the sample surface area. In contrast, the sample without BHJ coating did not emit any PL and a sample prepared by drop-casted BHJ showed that the fibers are only partially coated (**Figure 5.9c**). In conclusion, the immersion method is the best to coat the entirety of the fibers.

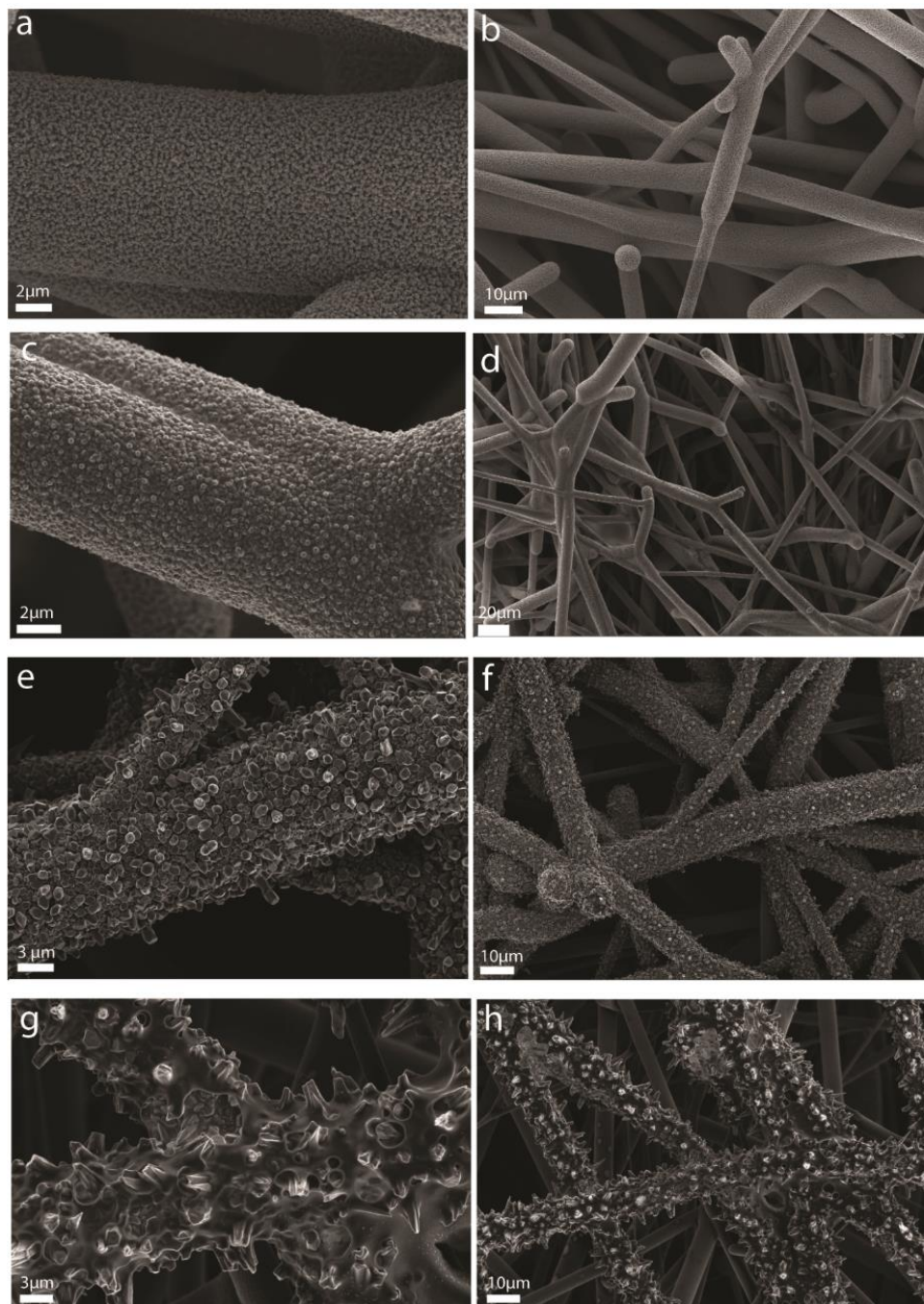


**Figure 5.9.** (a) Bright light microscope image of a TPCS-CuSCN-BHJ immersed confocal microscope image of (b) TPCS-CuSCN-BHJ immersed and (c) TPCS-CuSCN-BHJ drop-casted (for PL images, laser excitation: 640 nm and emission: from 800nm).

The morphology of the HTL can be tuned by changing the presence or absence of magnetic stirring during electrodeposition (**Figure 5.10**). Without stirring, the morphology is rough, and the deposition takes place mostly on the first outer layer of the TPSC. When the BHJ is then deposited (**Figure 5.10 (e,f)**), a thick BHJ layer adheres well onto the CuSCN-coated fiber layer but not the inner (deeper) fibers which are not well coated with CuSCN. Thus, the effect of the BHJ coating is limited



to the electrode's top surface. If stirring is used, a homogenous nanorod layer is obtained on the entire surface of the TPCS (**Figure 5.10 a,b**). This difference might come from a wettability issue, and will be discussed further in the next section. In order to ensure the consistency of the deposition, stirring was used for the rest of the study.



**Figure 5.10.** SEM pictures of CuSCN-coated TPCS (a,b) with stirring (c,d) without stirring coated with BHJ (e,f) with stirring coated with BHJ (g,h) without stirring coated with BHJ.

#### 5.4.2 BHJ Performance optimization

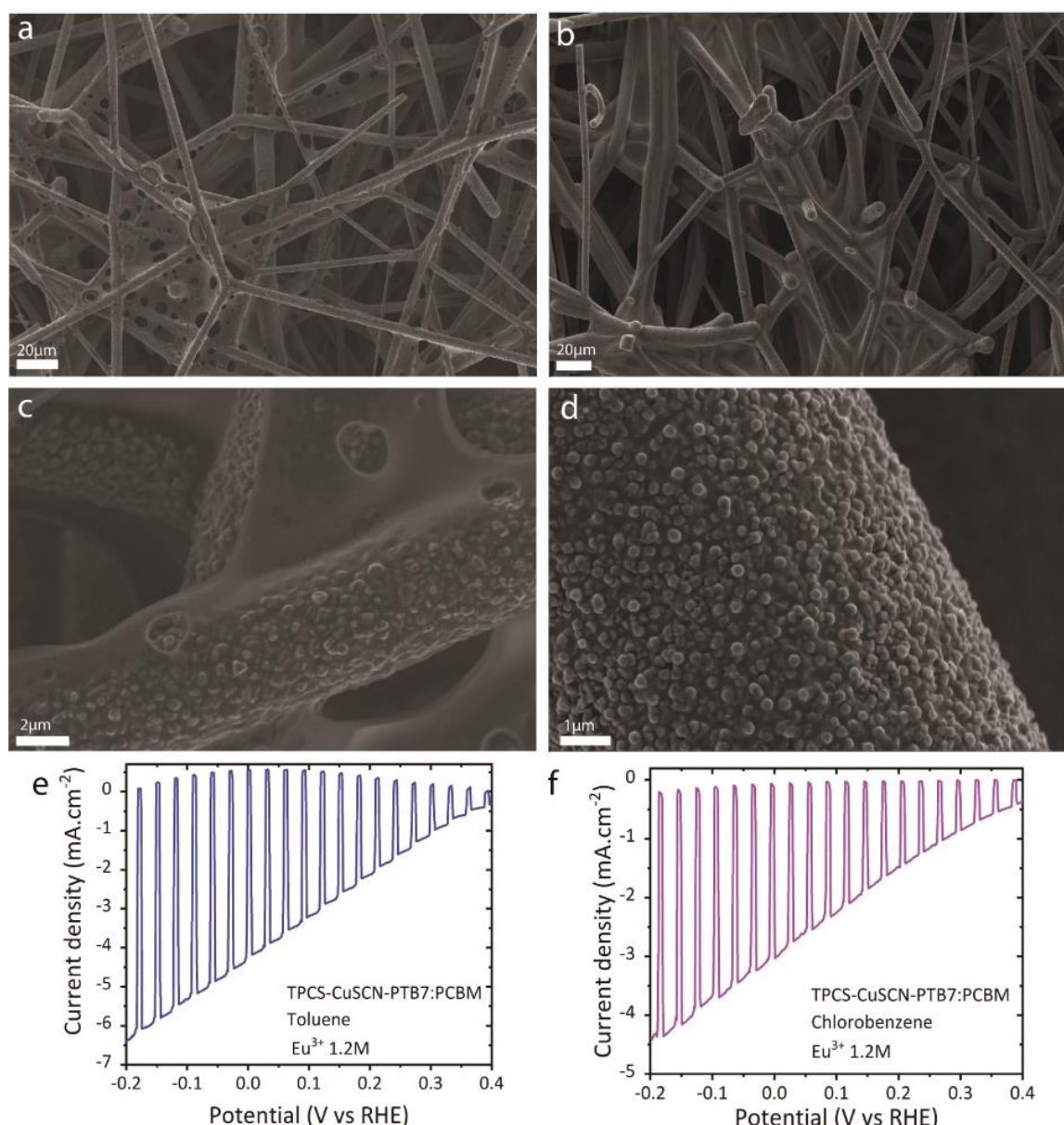
Commonly, organic semiconductor (OS) films are made on flat FTO glass. Spin-coating is used as the method of choice to process BHJ for solar cell or photoelectrode application<sup>71</sup> as it allows to form a thin and homogeneous layer. However, spin-coating might not be an applicable method for a 3D-network such as TPCSs. The challenge here was to find a novel way to coat the BHJ on the TPCS 3D network in the view of increasing PEC performance. An alternative method to spin-coating is dip-coating. Dip-coating<sup>183,184</sup> might be more adapted for 3D network coating as it allows to wet the entire substrate surface with the solution. We tested dip-coating methods using two solvents: a low boiling point solvent as chloroform (61 °C) and a high boiling point solvent as chlorobenzene (132 °C). As this study would require the use of a large amount of OS, commercially available materials (i.e. PTB7-Th:PCBM) were used in order to optimize deposition process for TPCS.

We investigated the best conditions for BHJ coating onto the TPCS and we found that the dip coating with a high boiling point solvent gave more homogeneous films compared to a dip coating with a low boiling point solvent (see Appendix 5, BHJ coating, Figure S5.6 and S5.7). In addition, we identified that a pre-wetting step is needed to ensure full contact with the electrolyte (see appendix 5, wettability of the electrode, Figure S5.8).

To further optimize the deposition process, several solvents with different boiling points were tried. Chloroform, toluene and chlorobenzene, with a boiling point of 61 °C, 110 °C and 132 °C respectively, were tested to process the BHJ solution. As it can be seen in Appendix 5, chloroform led to “coffee-ring” effects due to its fast evaporation rate; therefore, chlorobenzene was chosen for developing the dip-coating process and led to an improved coating. We wanted to evaluate another solvent like toluene in the aim to decrease the toxicity of the reagents used in the process.

To test this, we fabricated TPCS-CuSCN-BHJ using the same procedure (withdrawal speed = 60 mm.min<sup>-1</sup>, concentration = 16 mg.mL<sup>-1</sup>, annealing temperature=150 °C) with two different solvents, chlorobenzene and toluene. As it can be seen in **Figure 5.11** (a,c), the morphology obtained with toluene differs from the morphology obtained with chlorobenzene. With toluene, a BHJ web is formed in between the fibers. This morphology could lead to light loss because the BHJ web would absorb light without participating in photocurrent, since it is not in direct contact with the conducting substrate - the photogenerated charges cannot be extracted due to the size of the BHJ web (few microns length) compared to the diffusion length of the charges in the BHJ material (around 100 nm).

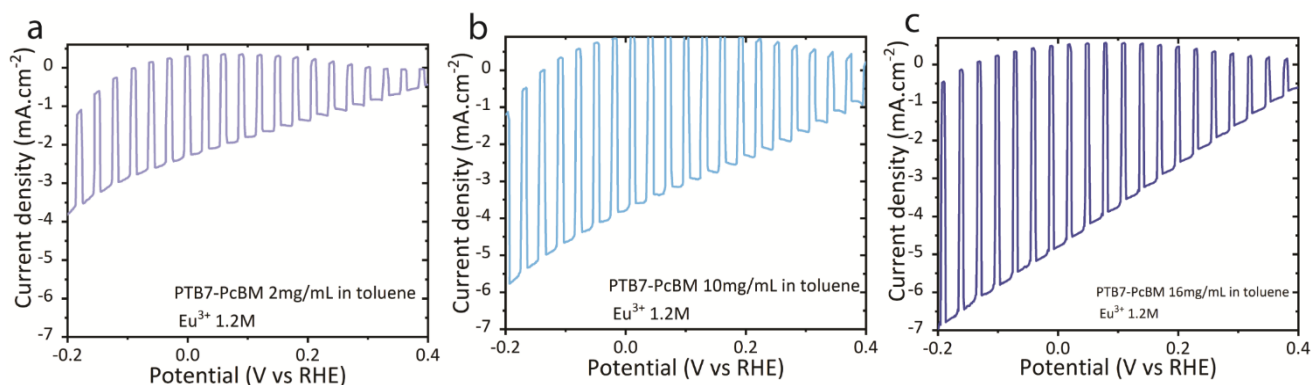
However, the performance of the electrode in sacrificial electrolyte is slightly higher for the toluene system. We obtained -4.5 mA.cm<sup>-2</sup> at 0 V vs. RHE for toluene and -3.5 mA.cm<sup>-2</sup> at 0 V vs. RHE for chlorobenzene. But this result needs to be put into perspective as the number of electrodes tested were limited. This difference could come from the variability of the electrode performance itself and would need to be verified. In conclusion, toluene could be used as a solvent, but the BHJ web formation should be avoided to maximize the final performance.



**Figure 5.11.** SEM pictures of TPCS-CuSCN-BHJ processed (a,c) with Toluene (b,d) with chlorobenzene, (e,f) PEC performance in sacrificial electrolyte  $\text{Eu}^{3+}$  1.2M.

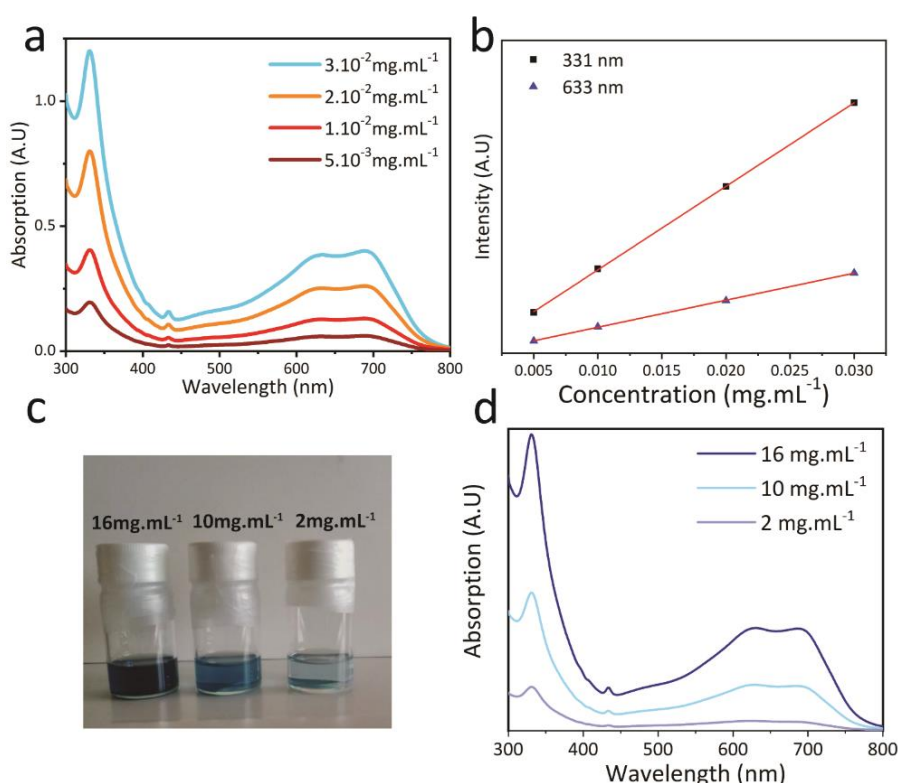
The impact of the BHJ concentration was evaluated by electrodes fabricated with different concentrations during the dip-coating process, ranging from 2 to 16  $\text{mg.mL}^{-1}$ . The electrode performance was also tested in sacrificial electrolyte  $\text{Eu}^{3+}$  1.2 M. **Figure 5.12** shows that the higher the BHJ concentration, the higher the photocurrent. By increasing the BHJ concentration, we could increase the amount of BHJ deposited on the TPCS due to the higher amount of material available and the higher solution viscosity. An increase of the solution viscosity could also promote the material coating onto a fibrous network such as the TPCS and will need to be further investigated in the future.





**Figure 5.12.** PEC performance in sacrificial electrolyte  $\text{Eu}^{3+}$  1.2M for electrode made with different BHJ concentration (a) 2  $\text{mg}\cdot\text{mL}^{-1}$  (b) 10  $\text{mg}\cdot\text{mL}^{-1}$  (c) 16  $\text{mg}\cdot\text{mL}^{-1}$ .

To verify that the BHJ amount was higher depending on the BHJ solution concentration used in the dipping process, a calibration curve for a PtB7-Th:PCBM (1:1.5) was established (**Figure 5.13 a,b**). The BHJ coated onto the surface of the TPCS for different concentration conditions (2, 10, 16  $\text{mg}\cdot\text{mL}^{-1}$ ) was dissolved by immersing the substrate in toluene for 2 h (**Figure 5.13 c**). After dilution, we measured the absorption properties of the three conditions. In **Figure 5.13 d**, we can see that the absorption intensity is gradually increasing with the BHJ concentration used, which proves that a higher amount of BHJ is deposited if the concentration is higher. Using the calibration curve, we estimated that 0.7 mg of BHJ was deposited on a  $3.8\text{ cm}^2$  TPCS.



**Figure 5.13.** (a) absorption spectra of solutions (PtB7:PCBM, 1:1.5) for different concentration (b) resulting calibration curve (c) photograph of the solution resulting from the BHJ dissolution on TPCSs (d) Absorption spectra of the solution.

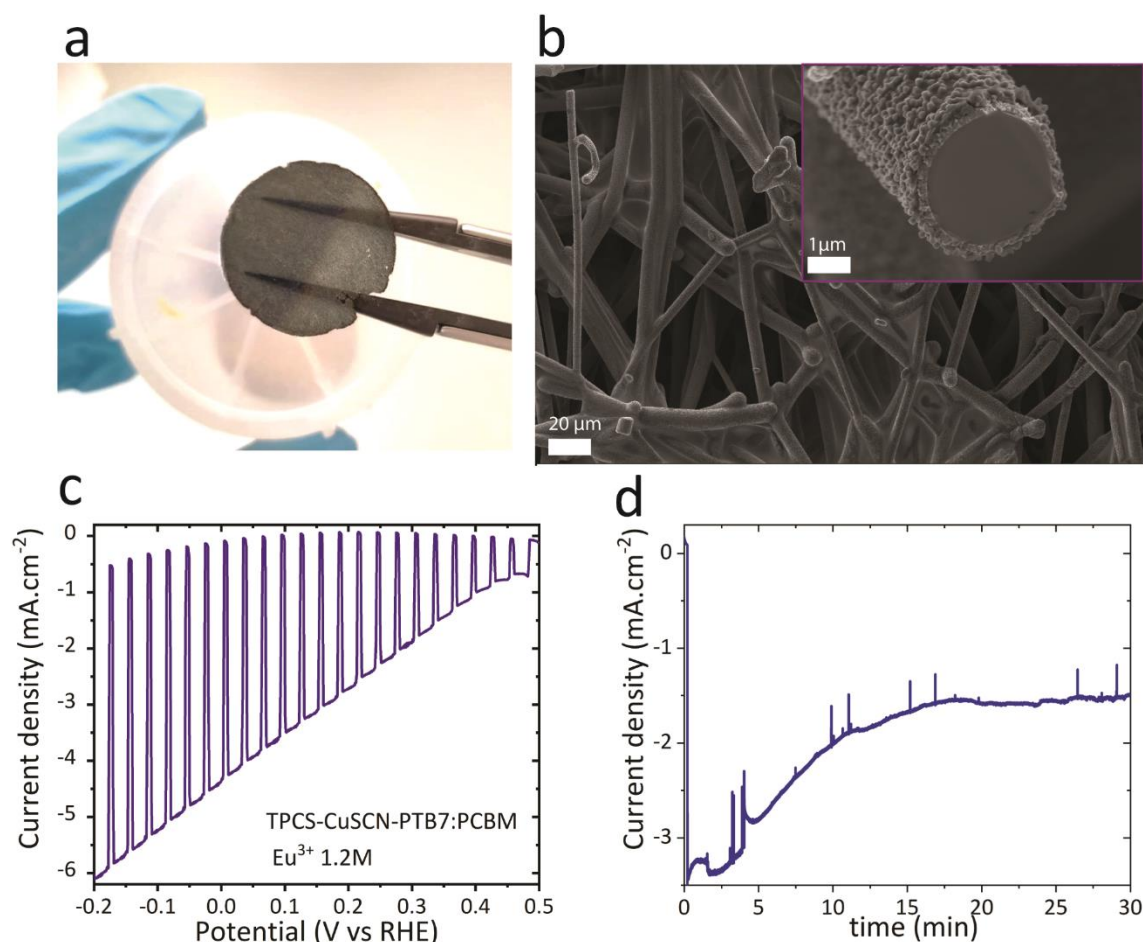
In further investigation, the concentration and solvent choice could be even further optimized. Nonetheless, the obtained photocurrent  $> 4.5 \text{ mA.cm}^{-2}$  already places this semiconductor choice above the other options discussed above.

### 5.4.3 Stability and further investigations

The best device composed of CuSCN (HTL) and PTB7-Th:PCBM (1:1.5) shows a photocurrent of  $4.5 \text{ mA.cm}^{-2}$  at 0V vs. RHE in sacrificial  $\text{Eu}^{3+}$  conditions at pH 2 (**Figure 5.14a-c**). The device in **Figure 5.14a** exhibits high transparency despite the successive coatings. Using scanning electron microscopy (SEM), the morphology of the device was highlighted (**Figure 5.14b**). The typical performance oscillates between  $3 - 4.5 \text{ mA.cm}^{-2}$ . The stability was also evaluated in **Figure 5.14d**, where the current initially decreases until reaching a steady state after 15 min.

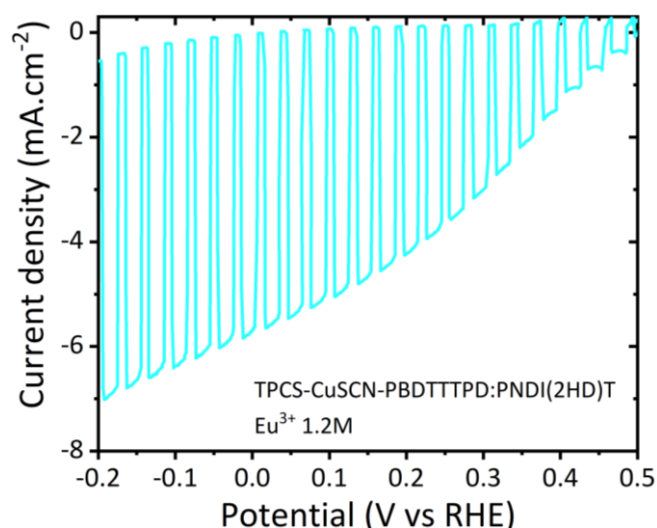
The fast photocurrent decrease could be attributed to several phenomena such as (i) HLT degradation as a similar CuI HTL is prone to oxidation/reduction phenomena in contact with water,<sup>82</sup> (ii) BHJ degradation<sup>83,174</sup> (iii) mass transport issue due to the wettability of the electrode. The stability of CuSCN should be investigated, especially in the final gas cell device that could be different from a liquid sacrificial electrolyte. The BHJ degradation could also participate to the photocurrent loss, especially for PCBM which is known to dimerize under operation. In addition, Yao *et al.*<sup>174</sup> observed an increase of the photocurrent and stability by increasing the  $\text{Eu}^{3+}$  concentration reaching a maximum at 1.2M. Therefore, a high concentration (1.2 M) was also used to test the BHJ-based TPCS performance. However, these substrates have a larger surface area than flat substrates which could require a higher electrolyte concentration to sustainably extract the photogenerated  $\text{e}^-$  at the BHJ/liquid interface. The hypothesis could not be verified as the Eu limit of solubility in water was already reached. In addition, in appendix 5, section wettability of the electrode, we highlighted the drastic impact of the electrode wettability on the performance.

The BHJ-based TPCS photoelectrode is highly hydrophobic due to the OS layer combined with a porous fiber network. A pre-wetting with an alcohol allows an increase of the photocurrent, possibly by increasing the electrode surface in contact with the electrolyte. However, the evolution of the wettability of the electrode is unknown at the moment. In addition, Iwata *et al.*<sup>185</sup> established how the hydrophobicity of a porous electrode could negatively influence the electrolysis performance. Although the photoelectrode still exhibits a photocurrent of  $1.5 \text{ mA.cm}^{-2}$  after 30 min, all the parameters cited could impact the performance and the long-term stability.



**Figure 5.14.** Characterization of a device TPCS-CuSCN-BHJ (a) Photograph of the device (b) Top view and cross sectional SEM features (c) LSV curve in sacrificial Eu<sup>3+</sup> at pH 2 under (1 Sun) chopped illumination (d) CA at 0 V vs. RHE in sacrificial Eu<sup>3+</sup> at pH 2 under (1 Sun) illumination.

As mentioned previously, PCBM is known to be unstable under operation due to the formation of dimers species acting as electron traps.<sup>174</sup> In order to maximize the device stability other OS blend could be used such as the all polymer blends PTB7-Th:PDI-V or PBDTTTPD:PNDI(2HD)T. The performance of PBDTTTPD:PNDI(2HD)T (1.5:1 w:w) BHJ in sacrificial electrolyte Eu<sup>3+</sup> 1.2 M showed a promising photocurrent of 6 mA.cm<sup>-2</sup> at 0 V vs. RHE under simulated 1 Sun illumination (**Figure 5.15**)., showing the realm of possibility to apply this approach to other types of BHJ blends.



**Figure 5.15.** LSV curve a TPCS-CuSCN-PBDTTTPD:PNDI(2HD)T sample in  $\text{Eu}^{3+}$  1.2M under chopped (1 sun) light illumination.

The combination of CuSCN (HTL) and BHJ (absorbing material) was also investigated on other types of porous supports such as carbon cloth and tungsten (W) mesh (see Appendix 5, section other porous substrates, Figure S5.9-12). We showed that the device architecture (i.e., substrate/CuSCN/BHJ) can be applied to a broad range of porous substrates. However, the TPCS is the most promising candidate due to the alliance of higher transparency and larger surface area. Indeed, the carbon cloth is opaque while the W mesh has poor surface area as it is composed of only one layer of meshes. Therefore, the further investigations will be pursued with the TPCSs.

## 5.5 Conclusion

In order to select the most promising photocathode material for the PEM-PEC cell, two p-type semiconductors and several BHJ blends coatings were screened:  $\text{WSe}_2$ ,  $\text{Cu}_2\text{O}$ , and organic BHJ. For each of these systems methods were developed to deposit the semiconductor on a porous substrate that will be suitable for implementation in the PEM-PEC cell. Despite the interesting discoveries made for each of the semiconductor systems, the organic BHJs are the most promising candidates with a simulated solar photocurrent of  $-6 \text{ mA}\cdot\text{cm}^{-2}$  at 0 V vs. RHE under sacrificial  $\text{Eu}^{3+}$  reduction in aqueous electrolyte when deposited on the porous quartz felt-based TPCSs.

While  $\text{WSe}_2/\text{Pt}$ -coated TPCS were successfully fabricated using EPD and photoelectrodeposition, the main limitation of this material come from the importance of the contact between the  $\text{WSe}_2$  and the conductive substrate. We conclude that the poor photoactivity measured results from the poor material coverage and the imperfect contact between the 2D-nanoflakes and fibrous TPCS substrate. Indeed, low photoactivity was obtained on the TPCS compared to a FTO glass substrate coated with a thick  $\text{WSe}_2$  film. The difficulty to coat homogeneously with an appropriate contact between the material and the substrate hinders the development of  $\text{WSe}_2$ -coated TPCS and the resulting photocurrent was not satisfactory.

Cu<sub>2</sub>O is an appealing p-type semiconductor for photocathode application due to its earth-abundant elements and ease of fabrication. Usually, Cu<sub>2</sub>O direct electrodeposition leads to uneven coverage of large scattering cubes. However, with the *in-situ* electroconversion, the Cu<sub>2</sub>O coverage is complete on different types of support (flat FTO glass and TPCS) and the cubes are smaller than for direct electrodeposition. We succeeded in coating homogeneously the TPCS with Cu<sub>2</sub>O, benefiting from the entire substrate surface area and avoids light loss due to scattering effect. The Cu<sub>2</sub>O photoelectrode instability has been tackled in the past and remediated through protective layer coating. The ALD method used on flat surface would need further development to be applied on porous substrate. However, we obtained promising results for high surface area template in terms of coating homogeneity and photocurrent extracted but with respect to the timescale of the project; we could not investigate these p-type semiconductors further. In conclusion, we obtained a fully coated Cu<sub>2</sub>O-TPCS substrate, but the observed photocorrosion needs to be mitigated.

The BHJ organic semiconductor coated TPCS photoelectrode was adapted from a previous work on flat substrates.<sup>174</sup> An alternative hole transporting layer, CuSCN, was developed for its ease of deposition on the porous substrates. Moreover, the BHJ was deposited by dip coating instead of spin-coating used for flat support to coat the 3D network. Then, dip-coating with high boiling point solvent (chlorobenzene) exhibited the best coating onto the fibers of the BHJ without “coffee-ring effect”. Finally, one of the key parameters to extract the maximum photocurrent of the BHJ TPCS photoelectrode was to establish an alcohol pre-wetting step in order to maximize the surface of contact between the fibers surface and the aqueous electrolyte, especially for the inner part of the substrate. The device composed of a TPCS as conductive support, CuSCN as HTL, and BHJ (PTB7-Th:PCBM, 1:1.5) exhibits a photocurrent of  $-4.5 \text{ mA.cm}^{-2}$  at 0 V vs. RHE in Eu<sup>3+</sup> sacrificial electrolyte. The photoelectrode could sustain  $-1.5 \text{ mA.cm}^{-2}$  at 0 V vs. RHE even after 30 min of operation in sacrificial electrolyte. While the best performing device (TPCS-CuSCN-PBDTTTPD:PNDI(2HD)T) in sacrificial electrolyte exhibited a photocurrent of  $-6 \text{ mA.cm}^{-2}$  at 0 V vs. RHE under 1 sun condition, the performance for flat films reaches  $-8 \text{ mA.cm}^{-2}$  for solar H<sub>2</sub> production at 1 Sun.<sup>174</sup> Thus, the roadmap for the further development of the TPCS-based BHJ photocathodes will be to (i) optimize the TPCS with respect to the fiber density and thickness, and (ii) tune the BHJ blend, the BHJ solution concentration, temperature, viscosity, the solvent, and the withdrawal speed during the coating process and (iii) evaluate the performance for water reduction using a HER catalyst. Moreover, the reproducibility and variability of the performance needs to be evaluated, as only a limited number of TPCS could be tested due to the number of steps required and the method lacks, for now, a high-throughput way to obtain the devices. In conclusion, the successful completion of p-type semiconductor and BHJ blends coating has led to a clear choice in the type of semiconductor to be employed for the PEM-PEC photocathode.

The effort will be focused on the BHJ organic photoelectrode, which is the most promising material so far, and we have identified parameters that will likely lead to an increase in the solar photocurrent operation in the view of integration in the PEM-PEC cell.

## 5.6 Experimental method

### 5.6.1 WSe<sub>2</sub>

#### Electrode fabrication

- Sonicated-assisted exfoliation

The commercially-available WSe<sub>2</sub> powder (AlfaAesar, <10  $\mu\text{m}$  in size) was exfoliated by ultrasonication in N-Methyl-2-pyrrolidone (NMP) (with/without additives). In a typical exfoliation, 250 mg of WSe<sub>2</sub> powder was dispersed in 50 mL of NMP and exposed to a Qsonica Model Q700 probe sonicator (50% amplitude, 10 s/2 s on/off cycle) for 2 in a 0 °C bath. The sonicated dispersion was centrifuged at 2000 rpm for 30 min to remove large aggregates and then at 7830 rpm for 30 min to remove un-exfoliated particles and soluble impurities, respectively. The final dispersion used for thin film fabrication was in NMP solvent, and the concentration was adjusted to be 1 mg.mL<sup>-1</sup>.

Layer of cross-linked poly(4-vinylphenol) (cPVPh) by dipping in a precursor solution (0.5 mg.mL<sup>-1</sup> PVPh plus 0.5 mg.mL<sup>-1</sup> 1,6-bis(trichlorosilyl)hexane in THF) then heating at 110 °C for 20 min.

- Electrophoretic deposition

WSe<sub>2</sub> nanoflakes were coated by electrophoretic deposition using, a TPCS as working electrode and a FTO glass as counter electrode. The electrolyte was composed of WSe<sub>2</sub> exfoliated flakes in N-methyl-2-pyrrolidone (NMP) resulting from the exfoliation, diluted to 0.5 mg mL<sup>-1</sup>. The potential applied was 10V for 1 hr.

Some WSe<sub>2</sub> films deposited on the TPCS were treated by 1% hexyl-trichlorosilane solution in toluene at room temperature. After 10 min of soaking, the electrodes were rinsed with toluene and isopropanol sequentially, followed by drying in air at 70 °C for 10 min.

- Catalyst deposition

Pt catalyst was deposited by photoelectrodeposition is a set-up composed of the TPCS as the working electrode, Pt wire counter electrode and a Ag/AgCl reference electrode. The electrolyte is an aqueous solution of 1mM H<sub>2</sub>PtCl<sub>6</sub> at pH 0.5. The deposition was done at E = 0.05V vs. Ag/AgCl under illumination until 14 mC charge has been passed.

#### PEC characterization

Photoelectrochemical measurements were carried out with a computer controlled (EC-LAB V11.12) potentiostat (Bio-Logic SP-300) with a 3-electrode configuration: a WSe<sub>2</sub> working electrode, a carbon counter electrode (0.25 mm diameter, 99.99%, chemPUR), and an Ag/AgCl reference electrode. The electrolyte used was H<sub>2</sub>SO<sub>4</sub> pH 1. For TPCS, a glass cell was used, and the current density was corrected by measuring the area exposed (0.4 - 1.3 cm<sup>2</sup>). A xenon arc lamp (Newport 66921, 450 W), calibrated to provide simulated AM 1.5 G solar irradiation.

### 5.6.2 Cu<sub>2</sub>O

#### Chemicals

Copper(II)sulfate pentahydrate CuSO<sub>4</sub>·5H<sub>2</sub>O (99% Acros organics), Ethylenediaminetetraacetic acid C<sub>10</sub>H<sub>16</sub>N<sub>2</sub>O<sub>8</sub> (99% Acros organics), Potassium thiocyanate KSCN (99% Acros organics), Potassium sulphate K<sub>2</sub>SO<sub>4</sub> (99% Carl ROTH), DL-lactic acid (90% abcr), Potassiumhydroxide KOH (pure Reactolab), Sodium sulfate NaSO<sub>4</sub> (99% Sigma aldrich), Potassium phosphate, monobasic, KH<sub>2</sub>PO<sub>4</sub> (99% Acros organics), and Sodium hydroxide NaOH (pure Reactolab) were used as received.

#### CuSCN deposition

CuSCN is deposited following a procedure developed elsewhere.<sup>110</sup> Briefly, CuSCN electrodeposition is performed in an aqueous solution containing 12mM of CuSO<sub>4</sub>, EDTA and KSCN added in this specific order to order to avoid the precipitation of Cu(SCN)<sub>2</sub>. A standard three-electrode configuration was used for electrochemical deposition with Pt counter electrode and Ag/AgCl/sat. KCl reference electrode. The TPCS working electrode was connect through a special clip, composed of Au mesh. Chronoamperometry at -0.3 V vs. Ag/AgCl is applied for a defined duration/charge passed. The optimum conditions is 5min deposition for a 3 cm<sup>2</sup> area exposed.

#### Cu<sub>2</sub>O photocathode formation

Cu<sub>2</sub>O films were deposited on bare TPCS or on CuSCN-coated TPCS with method developed elsewhere.<sup>79</sup> Cu<sub>2</sub>O was electrodeposited in a copper-lactate rich electrolyte at pH 12. The electrolyte contains 4 g of CuSO<sub>4</sub>·5H<sub>2</sub>O, 33.8 g of Lactic acid, and 10.9 g of K<sub>2</sub>SO<sub>4</sub> in 250mL of DI water. The pH was adjusted to 12 by adding 2M KOH. The final volume of the electrolyte is 500 mL. A large piece of platinum was used as a counter electrode. The temperature was maintained at 30 °C using a water bath. The electrodeposition is performed by chronopotentiometry at a current density of -0.1 mA.cm<sup>-1</sup> or -0.2 mA.cm<sup>-2</sup>. Deposition time was varied depending on the film thickness expected. The optimum condition is 50min deposition at -0.2mA.cm<sup>-2</sup> on a 5min-CuSCN TPCS. For *in-situ* electroconversion on CuSCN, the chronopotentiometry was started just after sample immersion in the electrolyte to avoid CuSCN dissolution. 20 nm of Ga<sub>2</sub>O<sub>3</sub> and 20 nm of TiO<sub>2</sub> layers were deposited on the Cu<sub>2</sub>O film using a Savannah 100 (Cambridge Nanotech) thermal ALD system. The chamber was stabilized at 150 °C and flushed with 10 sccm nitrogen gas (99.9995%, Carbagas). Gallium oxide was deposited using bis(μdimethylamino)tetrakis(dimethylamino)digallium (98%, Stream Chemicals) and TiO<sub>2</sub> was deposited using tetrakis(dimethylamino)titanium (99.999%, Sigma).

#### PEC analysis

PEC experiments were performed by using a three-electrode setup, with carbon rod as counter electrode and Ag/AgCl/KCl sat as reference electrode. PEC performances were measured in a pH 5 buffer solution containing 0.5M Na<sub>2</sub>SO<sub>4</sub>, 0.1 M sodium phosphate. The surface area of the film is contact with the electrolyte was in the range 1.5 - 2.5 cm<sup>2</sup>. The electrochemical behaviour was monitored with a SP-200 potentiostat (biologic), while the light was provided by a xenon arc lamp

(450W) calibrated with the AM 1.5G spectra to provide one sun of illumination ( $1000\text{mW.cm}^{-2}$ ). A mechanical shutter was used to chop the light. All experiments were carried out at ambient temperature and electrode potentials were converted to the RHE scale using  $E_{\text{RHE}} = E_{\text{Ag/AgCl}} + 0.059 \text{ pH} + 0.197$ .

### 5.6.3 Bulk heterojunction

#### Materials

Europium(III) nitrate hexahydrate ( $\text{Eu}(\text{NO}_3)_3 \cdot 6\text{H}_2\text{O}$  ABCR, 99.9%), PTB7-Th (Ossila),  $\text{PC}_{61}\text{BM}$  (Ossila), Copper(II)sulfate pentahydrate  $\text{CuSO}_4 \cdot 5\text{H}_2\text{O}$  (99% Acros organics), Ethylenediaminetetraacetic acid  $\text{C}_{10}\text{H}_{16}\text{N}_2\text{O}_8$  (99% Acros organics), Potassium thiocyanate KSCN (99% Acros organics), were used as received. PDI-V, PBDTTTPD and PNDI(2HD)T were synthesized by LIMNO (EPFL). W meshes were purchased from Werson and carbon cloth were purchased from Fuel cell store.

#### CuSCN electrodeposition

On TPCS, CuSCN is electrodeposited on TPCS at  $-0.3 \text{ V}$  vs. Ag/AgCl until 300mC of charges is passed for  $1 \text{ cm}^2$ . On FTO glass, the electrodeposition time is set at 30 seconds for  $2 \text{ cm}^2$ .

#### BHJ coating

Organic semiconductor powders are dissolved in a solvent (table below) at a concentration from 4 to  $16 \text{ mg.mL}^{-1}$ . The OS weight ratio were 1:1 for PTB7-Th:PDI-V, 1:1.5 for PTB7-Th:PCBM and 1.5:1 for PBDTTTPD:PNDI(2HD)T. The solution is stirred overnight at  $50^\circ \text{C}$ .

	PTB7-Th:PCBM (1:1.5)	PTB7-Th:PDI-V (1:1)	PBDTTTPD:PNDI(2HD)T
FTO glass	16mg/mL in toluene	8mg/mL in chloroform	12mg/mL in chloroform
TPCS	16mg/mL in toluene	4mg/mL in chlorobenzene	12mg/mL in toluene

The BHJ blend is deposited on FTO glass by spincoating at 3000rpm for 40 seconds, before the annealing step at  $150^\circ \text{C}$  for 10 min in ambient atmosphere.

The BHJ blend is deposited on TPCS by a dip-coating method at a withdrawal speed of 60mm/min. After complete removal from the solution, the samples rest for 5 min, before the annealing step at  $150^\circ \text{C}$  for 10 min in ambient atmosphere.

#### PEC characterizations

Photoelectrochemical measurements were carried out with a computer controlled (EC-LAB V11.12) potentiostat (Bio-Logic SP-300) with a 3-electrode configuration: a BHJ working electrode, a carbon counter electrode (0.25 mm diameter, 99.99%, chemPUR), and an Ag/AgCl reference electrode. The electrolyte used was  $\text{Eu}^{3+}$  1.2M at pH 2. For FTO glass, a cappuccino cell with an exposed area of  $0.25 \text{ cm}^2$  was used. For TPCS, a glass cell was used, and the current density was corrected by



measuring the area exposed ( $0.4 - 1.3 \text{ cm}^2$ ) using Image J software. A xenon arc lamp (Newport 66921, 450 W), calibrated to provide simulated AM 1.5 G solar irradiation.

### Characterizations

SEM images were recorded with a Zeiss Merlin microscope. The water contact angle was measured by using a drop shape analyser DSA25 with the pendant drop, and sessile drop mode.

The PL microscope measurement was performed using a confocal microscope. The setup consists of a supercontinuum laser (SuperK Extreme EXR-15, NKT Photonics) coupled to a tunable band-passfilter unit (SuperK Varia, NKT Photonics) that operates between 400 and 830 nm at a 80 MHz pulse frequency. A short-pass filter (890 nm BrightLine, Semrock) was used to remove near-infrared contributions from the laser optical fiber. The excitation light passes through a 20 $\times$  objective (M Plan Apo NIR, NA 0.4 air, Mitutoyo Corporation) using silver-coated mirrors and a dichroic beam-splitter (LP 830nm, Semrock), resulting in an illumination spot of  $350 \times 350 \mu\text{m}^2$ . The emission is collected in the epi-direction and focused onto the entrance slit of a spectrometer (IsoPlane SCT-320, Princeton Instruments). The light is redirected into an InGaAs NIR camera (NIRvana 640 ST, Princeton Instruments) using a 70 lines.mm<sup>-1</sup> grating. Measurements were recorded with LightField (Princeton Instruments) in combination with a custom-built LabView (National Instruments) software for automation of the measurements.

## Chapter 6     Engineering bulk heterojunction photocathode for gas phase water splitting

The exploration of bulk heterojunction coating on the TPCS lead to a promising result for gas phase organic semiconductor photocathodes. After developing the method of fabrication, a device composed of TPCS as the conductive substrate, CuSCN as the hole transporting layer (HTL) and PTB7-Th:PCBM BHJ as the organic semiconductor, exhibited a current of  $-4.5 \text{ mA.cm}^{-2}$  at 0 V vs. RHE for sacrificial  $\text{Eu}^{3+}$  reduction. In this chapter, we evaluated the coating of hydrogen evolution reaction (HER) catalyst at the surface of the TPCS-BHJ photocathode. Pt catalyst was successfully coated by photodeposition and lead to a photocurrent between  $-1 - 2.2 \text{ mA.cm}^{-2}$  at 0 V vs. RHE in liquid electrolyte at pH 1. The BHJ-based TPCS photocathode was integrated in a PEM-PEC cell. A photocurrent of  $120 \text{ }\mu\text{A.cm}^{-2}$  and a hydrogen production ca.  $1 \text{ }\mu\text{mol.h}^{-1}$  was sustained for 1 hour, suggesting ca. 52% FE.

## 6.1 BHJ photoelectrode for water reduction in the gas phase

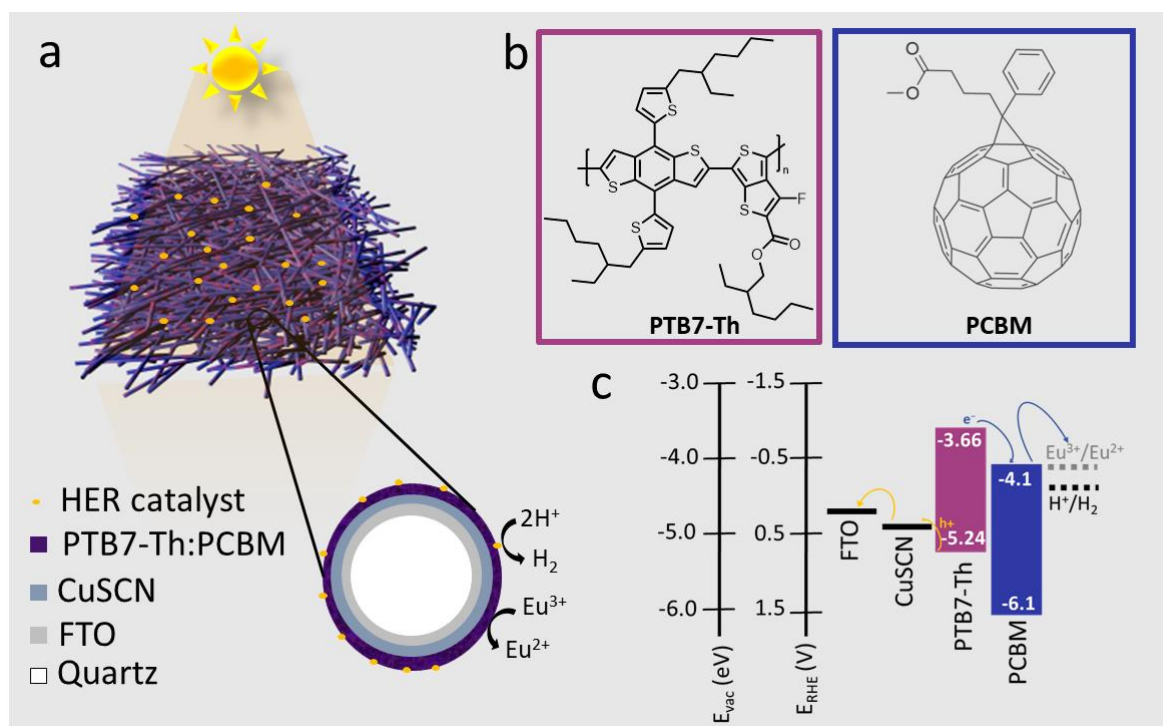
Hydrogen production by PEC water splitting system in liquid electrolyte has been studied extensively.<sup>113</sup> More recently, taking some inspiration from the mature proton-exchange membrane (PEM) electrolysis technology<sup>17,186,187</sup>, some attempts to perform water splitting in gas phase<sup>116,103,117,100</sup> using a proton-exchange membrane photoelectrochemical (PEM-PEC) cell have been reported. The goal of this approach is to tune the well-developed PEM electrolyser with GDL-type photoelectrode to replace the GDL-catalyst electrode. This novel compact device architecture allows simple product separation, minimizes electrolyte resistance thanks to the solid electrolyte<sup>88</sup> (i.e., PEM) and operates at elevated temperature and pressure, hindering gas bubbles formation (i.e. the typical limitations in PEC cell). It would also allow the use of simple natural air convection to perform gas phase water splitting as a promising alternative to liquid water feedstock. So far, the PEM-PEC cell reports were essentially focused on a photoanode coated on metal felt and a typical cathode (e.g., carbon cloth-Pt), due to the lack of transparent porous conductive substrate.

To integrate a photocathode in a PEM-PEC cell, the electrode substrate must be a gas diffusion layer-type electrode. Given the TPCS-BHJ photoelectrode demonstration in chapter 5, the investigation will be pursued to fabricate a complete photocathode for HER. For BHJ-based TPCSs fabrication, we selected a well-known BHJ blend<sup>83,177,188</sup> such as PTB7-Th polymer electron donor, and PCBM small-molecule acceptor due their commercial availability and cost. In addition, this type of electrode exhibits a promising photocurrent in sacrificial  $\text{Eu}^{3+}$  liquid electrode ( $4.5 \text{ mA.cm}^{-2}$  at 0 V vs. RHE).

To perform HER, the TPCS-BHJ photocathode should be coated with a HER catalyst. Therefore, the catalyst deposition needs to be evaluated and the performance for  $\text{H}_2$  production in liquid electrolyte must be verified prior to the integration in the PEM-PEC cell. In addition, a half PEM-PEC cell should be engineered. This device will consist in a photocathode operating in the gas phase, an anode and reference electrode operating in the liquid phase and a PEM separating the two sides. Firstly, the device will be investigated in the dark using a gas diffusion layer coated with a HER catalyst to verify the cell operation. Finally, the TPCS-BHJ-catalyst photocathode will be integrated in the half gas-cell test to investigate the feasibility of hydrogen production in a gas phase environment using the half PEM-PEC cell.

## 6.2 Photocathode for HER in liquid phase

In the previous chapter, we demonstrated a TPCS device with CuSCN HTL deposited by electrodeposition and a BHJ coating by dip-coating method (**Figure 6.1**). The photoelectrode is composed of quartz fibers, coated with FTO (100 nm), CuSCN nanorods (250 nm) and a BHJ film (40 nm). The best device shows a photocurrent of  $-4.5 \text{ mA.cm}^{-2}$  at 0 V vs. RHE in sacrificial conditions at pH 2 and the device could sustain a photocurrent of  $-1.5 \text{ mA.cm}^{-2}$  after 30 min of PEC testing in sacrificial conditions. Therefore, the catalyst deposition on the BHJ-based TPCS was investigated to establish the feasibility of HER on this novel photocathode morphology.

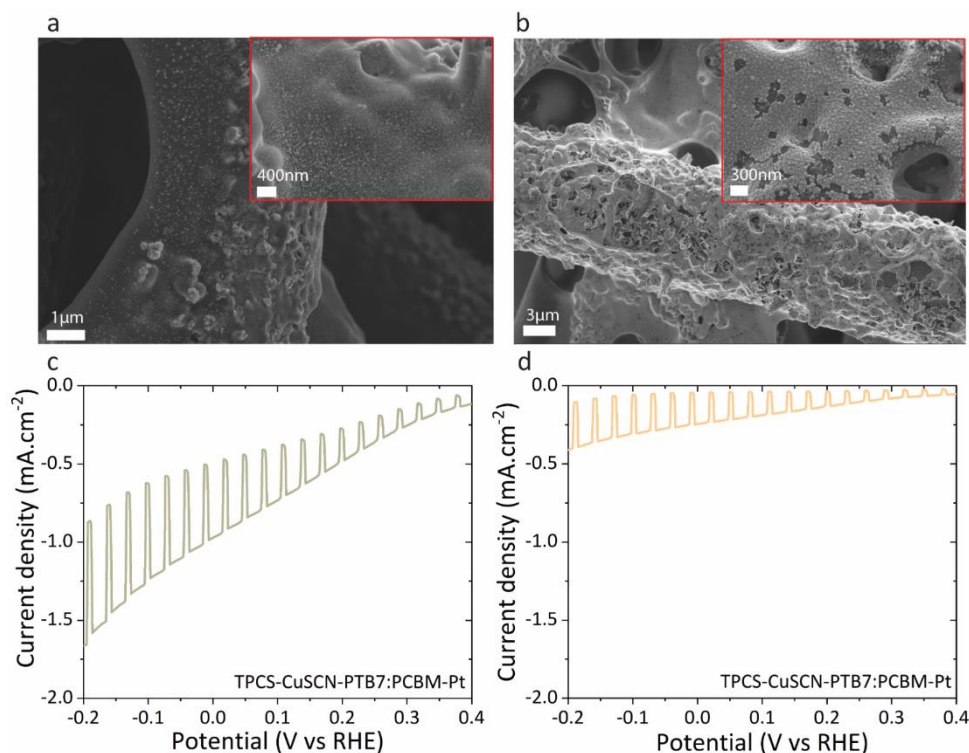


**Figure 6.1.** (a) Schematic of a TPCS-BHJ photocathode (b) Chemical structure of the donor polymer and small molecule acceptor (c) The energy levels of the photocathode components including FTO, CuSCN, PTB7-Th, and PCBM are shown versus vacuum energy or volts vs. the reversible hydrogen electrode (V RHE).

$\text{RuO}_2$  and Pt are mostly used as HER catalysts for BHJ-based photocathode. Our first attempt to coat  $\text{RuO}_2$  nanoparticles by spray coating following the procedure developed by Yao et al.<sup>174</sup> leads to an uneven coverage of the catalyst on the TPCS (see Appendix 6, Figure S6.1). A photocurrent of  $-0.4 \text{ mA}\cdot\text{cm}^{-2}$  at 0 V vs. RHE was obtained in the best case. The use of spray-coating could limit the coating of the inner part of the electrode, therefore a method to coat uniformly the catalyst should be investigated such as photoelectrodeposition or photodeposition. Moreover, the transparency of the catalyst layer could also be an issue for TPCS-based electrode. Yao et al.<sup>174</sup> coated a thick catalyst layer by spray-coating on the BHJ-photocathode with FTO glass substrate, therefore a back illumination was used. In contrast, a minimum transparency should be maintained for the TPCS photocathode to benefit from the illumination of the entire surface area.

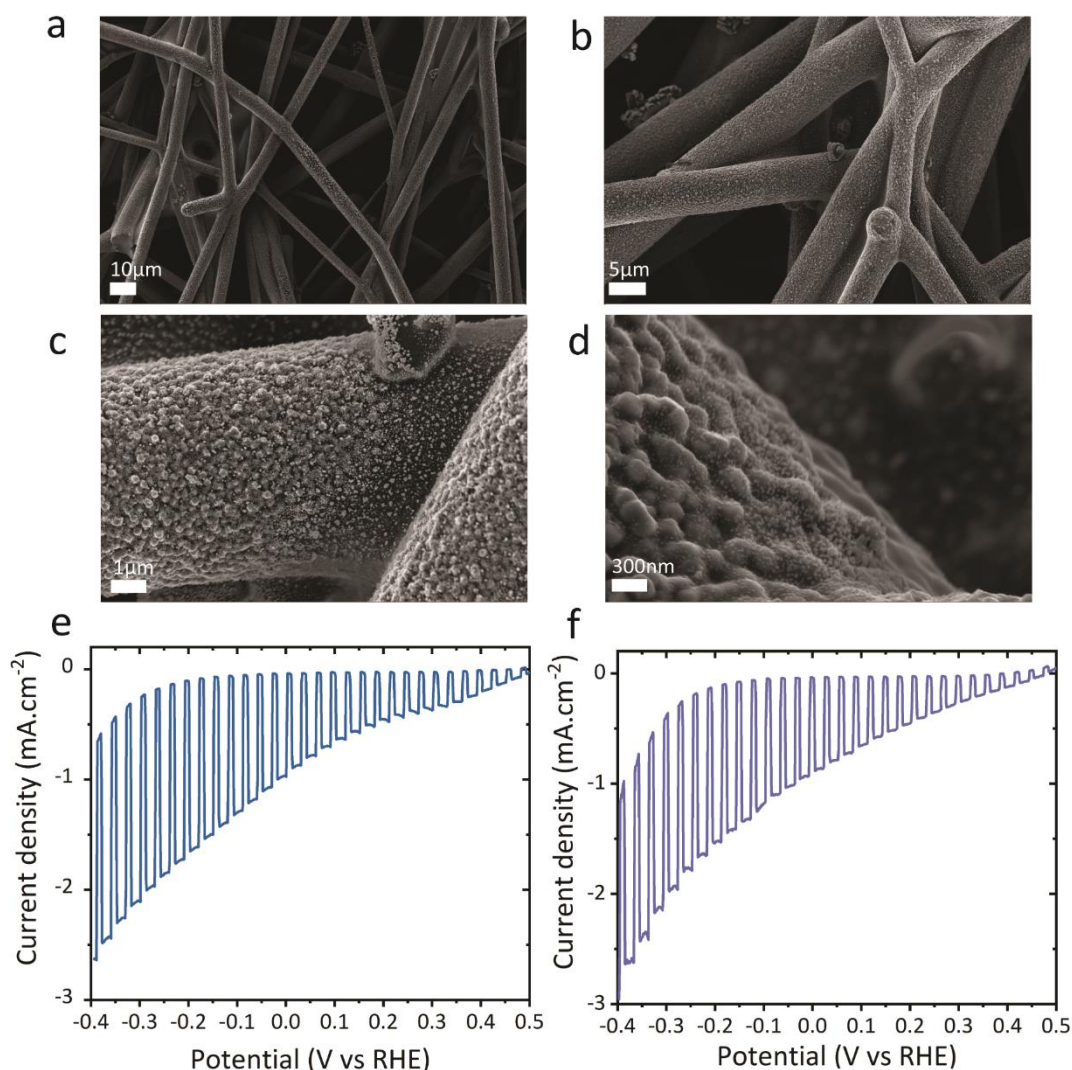
Pt photoelectrodeposition has been successfully performed on BHJ-based photocathode. A  $\text{TiO}_2$  protective layer deposited by ALD<sup>82,84</sup> is often required to improve charge extraction and catalyst adhesion onto the BHJ, leading to large increase in the performance and long-term stability. Given the fragile nature of the TPCS, the catalyst deposition was tested without protective layer deposition. The coating of Pt by photoelectrodeposition is visible by the scanning electron microscopy (SEM) analysis (Figure 6.2a,b). However, just like for spray-coating, the Pt catalyst was also unevenly coated. Some fibers appear only slightly coated (Figure 6.2a) whilst some fibers are completely covered with Pt particles (Figure 6.2b). This lack of homogeneity lead to a difference in terms of HER performance on the two electrode sides (Figure 6.2c-d). Indeed, on the backside, the

photocurrent and the dark current are higher (both around  $-0.5 \text{ mA}\cdot\text{cm}^{-2}$  at 0 V vs. RHE), while both decrease for the front side of the electrode ( $J_{\text{ph}} = -0.25 \text{ mA}\cdot\text{cm}^{-2}$  at 0 V vs. RHE). The complete coverage of the BHJ layer with Pt particles would lead to a blocking of the light absorption and could explain the lower photocurrent for the front illumination. The higher dark current in **Figure 6.2c** could come from the direct contact of large Pt particle with the conductive substrate. Overall, it seems difficult to control the photoelectrodeposition on the BHJ-coated TPCS.



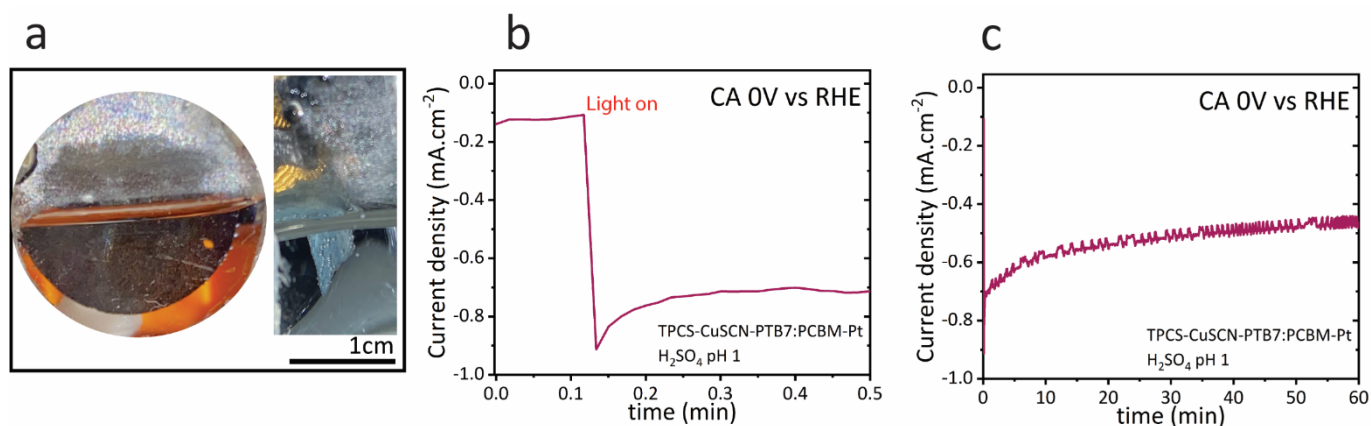
**Figure 6.2.** TPSC-CuSCN-BHJ-Pt(photoelectrodeposited) characterizations (a-b) SEM images of the electrode after Pt photoelectrodeposition (c-d) LSV curves in  $\text{H}_2\text{SO}_4$  at pH 1 under (1 Sun) chopped illumination for (e) back side (f) front side.

Interestingly, in photocatalysis Pt is photodeposited on BHJ photocatalyst nanoparticles<sup>54</sup> by using ascorbic acid as a hole scavenger and  $\text{K}_2\text{PtCl}_6$  as the Pt source. This method was tried on the TPSC-CuSCN-BHJ and gave more homogeneous coating (**Figure 6.3a-d**) and improved PEC performance with a current reaching  $-1 \text{ mA}\cdot\text{cm}^{-2}$  at 0 V vs. RHE (**Figure 6.3e,f**). The two sides of the electrodes exhibit similar photocurrent, highlighted the homogeneity of the Pt coatings.



**Figure 6.3.** (a-d) SEM features of a TPCS-CuSCN-BHJ-Pt after HER test, (e-f) LSV curves in  $\text{H}_2\text{SO}_4$  at pH 1 under (1 Sun) chopped illumination for (e) front side (f) back side.

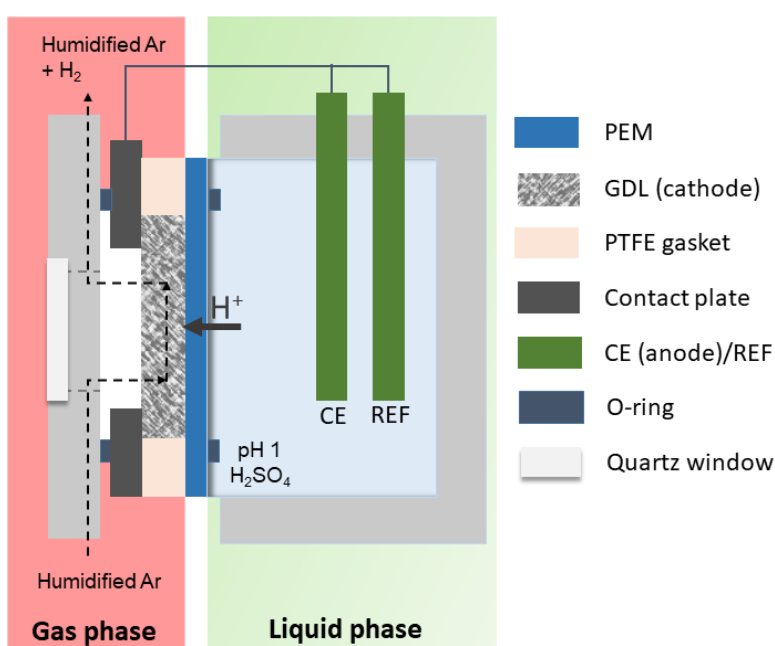
The long-term stability was evaluated in an acid solution at pH 1. First, bubbles were observed during the stability test, which suggests the production of  $\text{H}_2$  (**Figure 6.4**). The bubbles are formed on the electrode's edges and on the surface. A strong stirring was used to ensure electrolyte renewal, especially in the pores of the electrode, and to minimize the active sites' blockage by the bubbles. A photocurrent was sustained for 1 h with a decrease from  $-0.7 \text{ mA.cm}^{-2}$  to ca.  $-0.5 \text{ mA.cm}^{-2}$ . The faradic efficiency and nature of the bubbles were not verified by gas chromatography (GC), therefore the several degradation phenomena mentioned for the sacrificial testing cannot be discarded; however, the presence of bubbles proves that a certain amount of the current comes from water reduction. In addition, the comparison between the charges passed during the HER test (ca.  $18 \mu\text{mol of e}^- \cdot \text{h}^{-1} \cdot \text{cm}^{-2}$ ) with the amount of BHJ ( $0.12 \mu\text{mol.cm}^{-2}$  estimated from data of chapter 5, section 5.4.2, Figure 5.13) strongly suggests that the photocurrent cannot be just from the BHJ degradation. Despite the further optimization that could be made in term of photoelectrode performance and stability, we decided to pursue the investigation in a gas phase environment to determine the ability of such photoelectrode to operate in gas phase.



**Figure 6.4.** TPCS-CuSCN-BHJ-Pt long term stability characterizations (a) Photograph of the device during operation (b-c) CA at 0V vs. RHE in curves in H<sub>2</sub>SO<sub>4</sub> at pH 1 under (1 Sun) illumination.

### 6.3 Development of the half PEM-PEC cell

To test the TPCS electrodes in a gas phase environment, we designed a half gas phase cell (**Figure 6.5**). The goal is to study the ability of the electrode to carry out the HER in gas phase. The cell is composed of two compartments: the anode side operates in liquid for OER, then the protons are conducted through the PEM (Nafion) and will be reduced to hydrogen at the cathode, which operates in the gas phase. The reference Ag/AgCl and the counter carbon road are immersed in the liquid compartment. The photocathode is contacted electrically by an Au-coated Ti plate and fed by an argon flow that passes through water (20 mL.min<sup>-1</sup>) to keep the Nafion membrane hydrated (see Appendix 6, Figure S6.2).

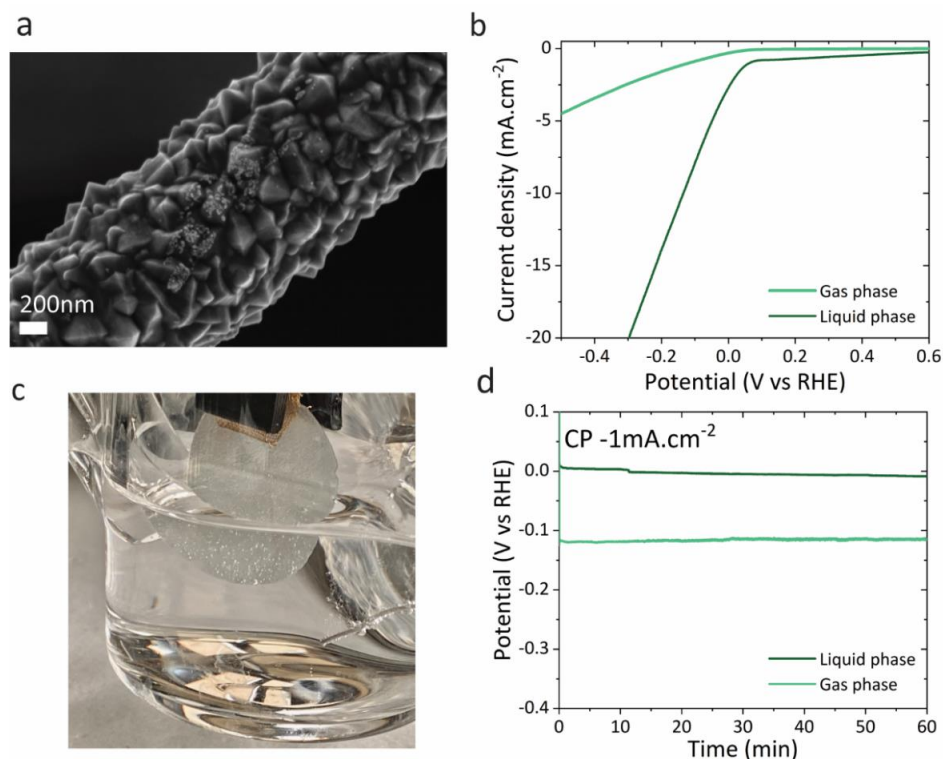


**Figure 6.5.** Schematic of the half gas cell.



The operation as PEM electrolyzer was first verified in the dark. Prior to the study on TPCS, the cell operation was verified on a commercial carbon cloth/platinum gas diffusion layer. The cell exhibited a current and a faradic efficiency for hydrogen production rate of ca. faradic efficiency (FE) 100% (see appendix 6, Figure S6.3 and S6.4). This last result suggests that the half gas cell system can be studied further on the TPCS. To do so, the TPCS were platinized, following a commonly used procedure<sup>189</sup> in the dye sensitized solar cell field. The substrates were dipped several times in a  $\text{H}_2\text{PtCl}_6$  1 mM solution and then annealed at 450 °C to form Pt nanoparticles. Even though the Pt coating does not seem homogenous, the presence of small Pt particles is visible on the FTO grains (**Figure 6.6a**). This option was chosen instead of Pt electrodeposition because the latter lead to the formation of large Pt particles that could be get more easily detached during operation (see Appendix 6, Figure S6.5).

The platinized TPCS exhibits a current of  $1.5 \text{ mA}\cdot\text{cm}^{-2}$  at 0 V vs. RHE (**Figure 6.6b**). Bubble formation was visible on the TPCS surface in the liquid phase (**Figure 6.6c**). In the gas phase, we assessed the operation of the cell; however, the current was lower than in the liquid phase, as seen in **Figure 6.6c** (e.g.,  $0.5 \text{ mA}\cdot\text{cm}^{-2}$  at 0 V vs. RHE). Lower performances in the gas phase could be expected as the transport of protons originates only from the contact between the membrane and the TPCS. Coating a Nafion layer on the TPCS surface could improve the protons transport on the entire substrate surface. The long-term stability was also investigated by a CP measurement at  $1 \text{ mA}\cdot\text{cm}^{-2}$  (**Figure 6.6d**). As the potential remained stable for minimum 1 h, in liquid and gas phase, the study could be pursued on the photocathode BHJ-based TPCS.

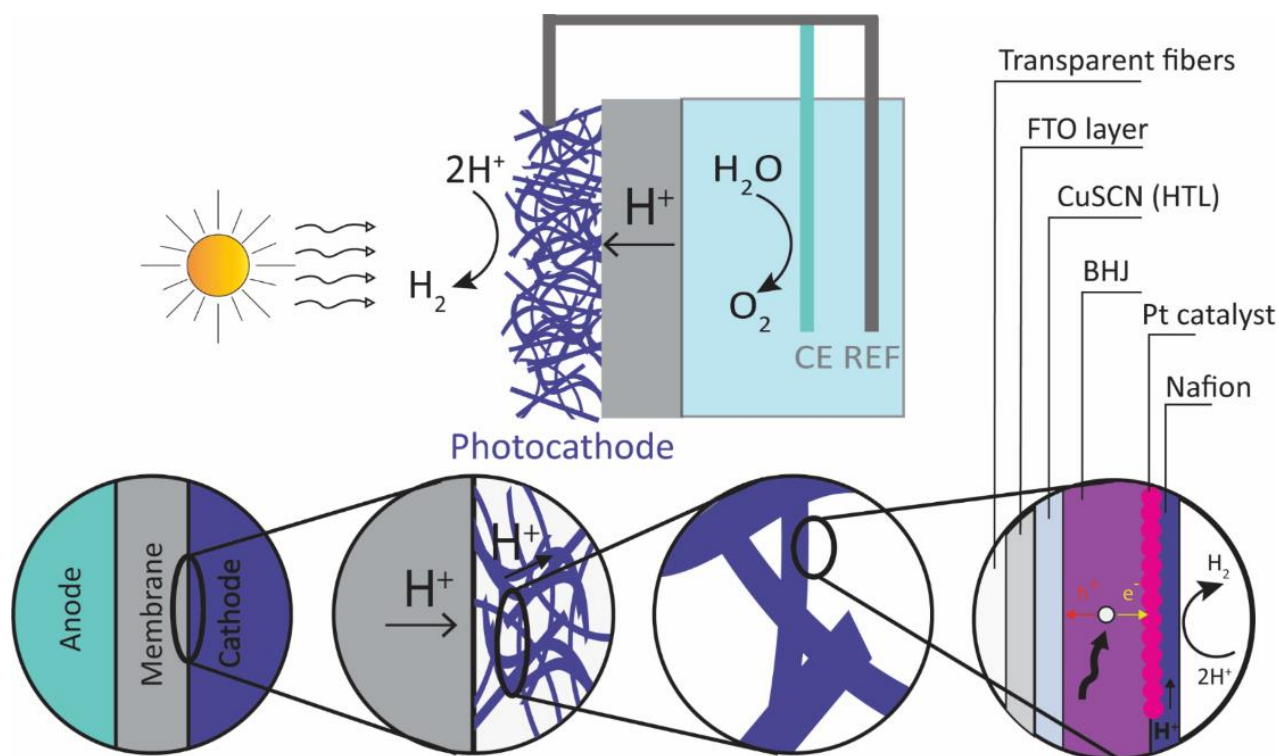


**Figure 6.6.** (a) SEM feature of a fiber from a platinized TPCS (b-d) characterizations of the platinized TPCS cathode in liquid (pH 1) and gas phase with humidified Argon ( $20 \text{ mL}\cdot\text{min}^{-1}$ ) (b) LSV curves (c) Photograph during the liquid phase testing (d) chronopotentiometry (CP) at  $-1 \text{ mA}\cdot\text{cm}^{-2}$ .



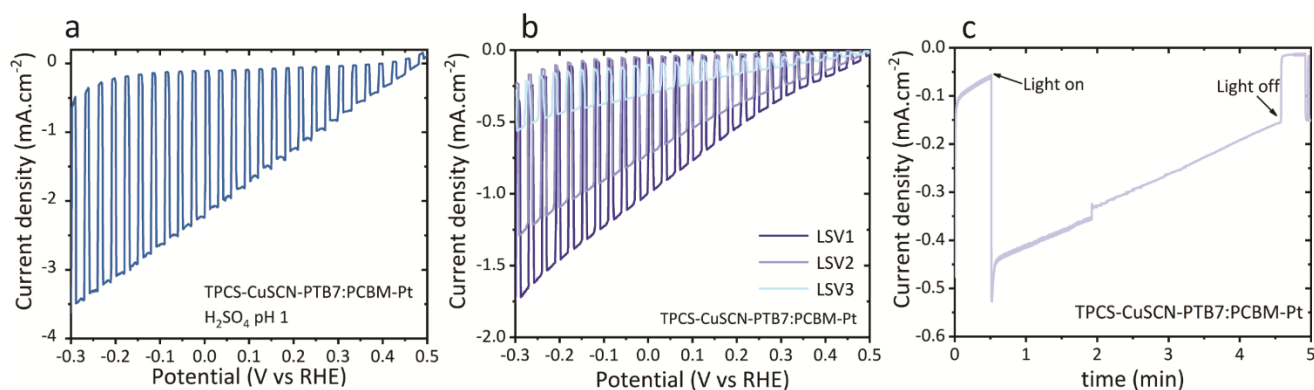
## 6.4 Photocathode for PEM-PEC operation

To determine the ability of the BHJ-based TPCS, the half gas cell developed was used. Indeed, in this system, the OER takes place in the liquid phase and the resulting protons travel through the PEM where they can be used by the photocathode upon illumination. In summary, if we have a close look to the photocathode (**Figure 6.7**), electrons and holes are photogenerated in the BHJ. The electrons can reach an active site (i.e, Pt particle) and reduce the protons transported by the PEM, while the holes can be extracted to the external circuit by the CuSCN HTL and the FTO layer.



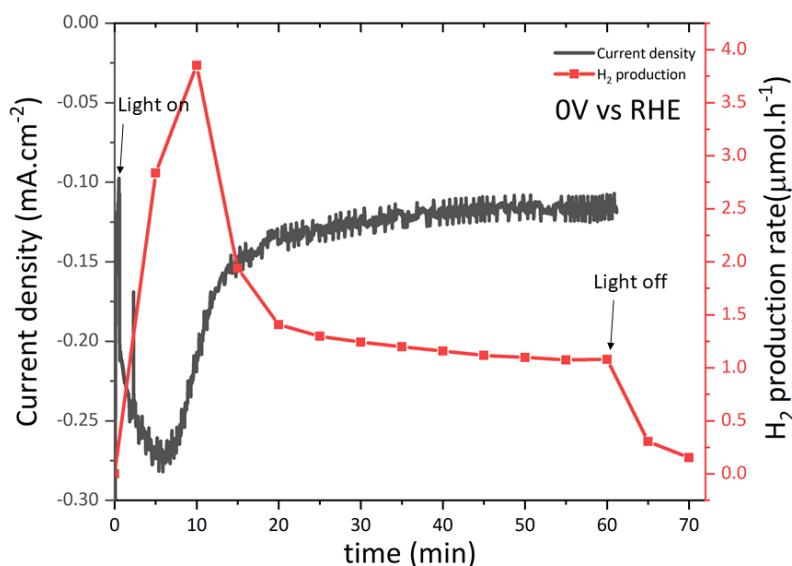
**Figure 6.7.** Illustration of the half PEM-PEC cell and photocathode composition.

Despite the variability of the platinum photodeposition on the BHJ-based TPCS, we evaluated the performance in the gas phase of our best performing photoelectrode (**Figure 6.8**). The photocurrent in the liquid phase at pH 1 reached  $2.2 \text{ mA}\cdot\text{cm}^{-2}$  at 0 V vs. RHE for the best device (**Figure 6.8a**). The photoelectrode was directly mounted into the PEM-PEC gas cell and tested upon chopped illumination. The photocurrent for the first scan (LSV1) was lower than the liquid phase and we observed a decrease of the current after successive scanning, from  $1.1 \text{ mA}\cdot\text{cm}^{-2}$  to  $0.4 \text{ mA}\cdot\text{cm}^{-2}$  for 3 scans (**Figure 6.8b**). In addition, we performed a CA measurement at 0 V vs. RHE, the photocurrent continued to decrease to  $0.15 \text{ mA}\cdot\text{cm}^{-2}$  after 4 min (**Figure 6.8c**).



**Figure 6.8.**TPCS-CuSCN-BHJ-Pt characterizations (a) LSV curve in  $\text{H}_2\text{SO}_4$  at pH 1 under (1 Sun) chopped illumination (b) Successive LSV curves in the gas phase at  $20\text{ mL}\cdot\text{min}^{-1}$  humidified argon under (1 Sun) chopped illumination (c) CA at 0 V vs. RHE in the gas phase following the successive LSVs.

The origin of the photocurrent decrease could be the same as the one cited for the liquid phase test (i.e., material degradation such as CuSCN and BHJ reduction or catalyst detachment). Moreover, the electrode was mounted on the half gas cell just after testing in liquid, therefore some liquid could remain in the pores and benefit the performance. Despite the low current obtain after few minutes of test, we performed a CA at 0 V vs. RHE for 1 h and we verified the hydrogen production by GC (**Figure 6.9**). After light illumination, up to  $4\text{ }\mu\text{mol}\cdot\text{h}^{-1}$  could be detected. Nevertheless, after 15 min the photocurrent decreased to  $120\text{ }\mu\text{A}\cdot\text{cm}^{-2}$  and a production ca.  $1\text{ }\mu\text{mol}\cdot\text{h}^{-1}$  was sustained for 1 h, suggesting ca.  $52\pm 1\%$  FE. Overall, we demonstrated that hydrogen was produced in the gas phase.



**Figure 6.9.** CA at 0 V vs. RHE and  $\text{H}_2$  production rate extracted from GC measurement for an electrode TPCS-CuSCN-BHJ-Pt tested in the half gas cell (area tested  $1\text{ cm}^2$ ).

The decrease observed in the photocurrent could obviously come from the TPCS-based photoelectrode (i.e., CuSCN degradation, PCBM dimerization, Pt detachment). A  $\text{TiO}_2$  could also be added as selective and protective layer (see appendix 6, Figure S6.6). Apart from the material point

of view, the stability of the cell depends also on the mass transport. We expect that the mass transport, which represents the number of protons reaching the TPCS electrode, could pose a limitation. We hypothesized that this is the major limiting factor as the unique proton channel was the contact between the PEM and fibrous TPCS. In future works, it will be essential to develop an ionomer coating able to efficiently transport the protons from the PEM to the BHJ layer. Recently, Tsampas *et al.*<sup>103</sup> developed diverse types of ionomer coating (e.g., Nafion or Aquivion) on Ti felt photoanode that could effectively solve the protons transport limitations. In addition, the material stability will also need to be investigated in the liquid and in the gas phase. However, in the view of the half gas cell operation in the dark, the bubbles formation observed in the liquid phase, and the H<sub>2</sub> detected by GC in the gas phase, we demonstrated that hydrogen production by the BHJ-TPCS likely contributes to the measured photocurrent.

## 6.5 Conclusion

The first demonstration of a gas-phase semi-transparent photocathode for photoelectrochemical H<sub>2</sub> production has been shown. CuSCN HTL and a PTB7-Th:PCBM BHJ are coated on a TPCS to form a gas diffusion-type photocathode. Pt catalyst was successfully coated by photodeposition and led to a photocurrent between  $-1 - 2.2 \text{ mA.cm}^{-2}$  at 0 V vs. RHE in liquid electrolyte at pH 1. A half gas phase PEM-PEC cell was developed in the view to test the novel BHJ-based TPCS photocathode. The photocathode, operating in the gas phase was engineered to ensure a good contact with the PEM and the contact plate (Au-coated Ti foil). The cell operation was conducted in the dark using a platinized TPCS to ensure the stability of the components for at least 1 h. We integrated the BHJ-based TPCS photocathode in the PEM-PEC cell, measured a photocurrent and H<sub>2</sub> was detected by GC measurements. A photocurrent of  $120 \text{ }\mu\text{A.cm}^{-2}$  and a hydrogen production ca.  $1 \text{ }\mu\text{mol.h}^{-1}$  was sustained for 1 hour, suggesting ca.  $52 \pm 1 \%$  FE. In order to enhance the cell performance and stability, the photocathode could be improved by (i) the replacement of PCBM by a non-fullerene acceptor (PDI-V, EH-IDTBR, ITIC), (ii) the coating of an electron-selective protective layer (TiO<sub>2</sub>) or (iii) the development of a reproducible HER catalyst coating. In addition, an ionomer coating onto the final photocathode seems mandatory to ensure protons transport through the fibers of the TPCSs and limit mass transport issue. Overall, a new type of photocathode, based on solution-processable methods and abundant materials (except for Pt) was developed and open the door to a broad range of applications.

## 6.6 Experimental part

### 6.6.1 Electrode fabrication

#### Materials

Europium(III) nitrate hexahydrate ( $\text{Eu}(\text{NO}_3)_3 \cdot 6\text{H}_2\text{O}$  ABCR, 99.9%), PTB7-Th (PCE, Ossila),  $\text{PC}_{61}\text{BM}$  (Ossila), Copper(II)sulfate pentahydrate  $\text{CuSO}_4 \cdot 5\text{H}_2\text{O}$  (99% Acros organics), Ethylenediaminetetraacetic acid  $\text{C}_{10}\text{H}_{16}\text{N}_2\text{O}_8$  (99% Acros organics), Potassium thiocyanate KSCN (99% Acros organics), Sulfuric acid (Fluka, 1M), Ruthenium(III) chloride hydrate (Fluorochem, 99%) Chloroplatinic acid hexahydrate ( $\text{H}_2\text{PtCl}_6$ , 38-40% Pt, 99.9%, ABCR), Potassium hexachloroplatinate(IV) ( $\text{K}_2\text{PtCl}_6$ , Fluka 98%), were used as received.

#### CuSCN electrodeposition

CuSCN is electrodeposited on the TPCSs at  $-0.3$  V vs. Ag/AgCl until 300mC of charges is passed for  $1\text{cm}^2$ . On FTO glass, the electrodeposition time is set at 30 seconds for  $2\text{cm}^2$ .

#### BHJ coating

Organic semiconductors powders are dissolved in a solvent toluene at a concentration of 16mg/mL. The OS weight ratio were 1:1.5 for PTB7-Th:PCBM. The solution is stirred overnight at  $50^\circ\text{C}$ . PTB7-Th has used has a molecular weight of 57 kDa.

The OS blend is deposited on TPCS by a dip-coating method at a withdrawal speed of 60mm/min. After complete removal from the solution, the samples rest for 5min, before the annealing step at  $150^\circ\text{C}$  for 10min in ambient atmosphere.

#### Catalyst deposition

Platinisation was performed by photoelectrodeposition, wherein the device was immersed into a 1mM  $\text{H}_2\text{PtCl}_6$  aqueous solution using a three-electrodes set-up with Pt as counter electrode and Ag/AgCl as reference electrode. The deposition potential was 0V vs. Ag/AgCl with a charge density of  $25\text{mC.cm}^{-2}$ . The solution was stirring and purged with argon during the deposition.

Platinisation was performed by photodeposition. The platinum solution at  $1\text{mg.mL}^{-1}$  was prepared by dissolving  $\text{K}_2\text{PtCl}_4$  salt in DI water and kept in the dark and in an inert atmosphere to prevent Pt particles formation. In a typical deposition, 1.58g of ascorbic acid was dissolved in 40mL of DI water. Once the ascorbic acid is dissolved, 100 $\mu\text{L}$  of the  $\text{K}_2\text{PtCl}_4$  is added to the solution. After immersion of the electrode in the solution, the system is purged under Argon for 30min. The deposition took placed under light illumination (1 Sun) for 30min. The electrode was rinsed with DI water and used for PEC testing.

## RuO<sub>2</sub>

RuO<sub>2</sub> nanoparticles were synthesized using a procedure developed elsewhere.<sup>174</sup> Briefly, RuO<sub>2</sub> was prepared by microwave-assisted hydrothermal synthesis. Ruthenium(III) chloride hydrate (80 mg) was added to 15 mL of water. The solution was transferred to a 30 mL microwave tube after sonicating for 5 min. A two-step microwave (Anton Paar Monowave) heat treatment was used for the synthesis: firstly a 5 min heating at 70 °C was performed to completely dissolve RuCl<sub>3</sub> and then a second heating at 160 °C for 30 min afforded the RuO<sub>2</sub> nanoparticles. After the reaction, the RuO<sub>2</sub> nanoparticles were washed with water three times. A RuO<sub>2</sub> catalyst ink was obtained by dispersing 50 mg solids in 50 mL isopropanol via sonication (2 h) using a tip sonicator (Q700 Qsonica). 1 mL catalyst ink (1 mg mL<sup>-1</sup> in isopropanol) was sprayed onto the TPCS-CuSCN-PTB7:PCBM in an ambient pressure environment. The organic BHJ film was placed on a hotplate at 80 °C beneath a custom external-mix two-fluid spray head.

### 6.6.2 PEC characterizations

Photoelectrochemical measurements were carried out with a computer controlled (EC-LAB V11.12) potentiostat (Bio-Logic SP-300) with a 3-electrode configuration: a BHJ working electrode, a carbon counter electrode (0.25 mm diameter, 99.99%, chemPUR), and an Ag/AgCl reference electrode. The electrolyte used was Eu<sup>3+</sup> 1.2M at pH 2. For FTO glass, a cappuccino cell with an exposed area of 0.25 cm<sup>2</sup> was used. For TPCS, a glass cell was used, and the current density was corrected by measuring the area exposed (0.4-1.5 cm<sup>2</sup>) using Image J software. A xenon arc lamp (Newport 66921, 450 W), calibrated to provide simulated AM 1.5 G solar irradiation.

### 6.6.3 PEM-PEC electrolysis

#### TPCS platinisation

The platinisation on bare TPCS was done by immersing a TPCS in H<sub>2</sub>PtCl<sub>6</sub> (1mg.mL<sup>-1</sup>) solution for 3 successive times. The electrodes were annealed at 450 °C for 10min to form Pt nanoparticles.

#### PEM-PEC characterisation

The TPCS (22mm diameter) was placed on the top of a Nafion<sup>®</sup> perfluorinated membrane (N117, Fuel Cell Store). The Nafion membrane was activated in H<sub>2</sub>SO<sub>4</sub> and hot water. A teflon gasket with a 2mm-hole was used to hold the circular TPCS positioned. A gold-coated titanium plate with a 18mm-hole was used to electrically contact the TPCS. The gas phase compartement was sealed and fed with a 20mL/min flow of humidified Argon. A quartz window allowed the illumination of the photoelectrode. The other side, in liquid phase, consists in a reference (Ag/AgCl) electrode and a counter (carbon rod) electrode immersed in H<sub>2</sub>SO<sub>4</sub> pH 1.

Photoelectrochemical measurements were carried out with a computer controlled (EC-LAB V11.12) potentiostat (Bio-Logic SP-300) with a 3-electrode configuration: the working electrode connected through the Au-coated Ti plate, the Ag/AgCl reference electrode and a carbon rod counter

electrode. For photoelectrode test, a xenon arc lamp (Newport 66921, 450 W), calibrated to provide simulated AM 1.5 G solar irradiation.

#### 6.6.4 Material characterizations

SEM images were recorded with a Zeiss Merlin microscope. The water contact angle was measured by using a drop shape analyser DSA25 with the pendant drop, and sessile drop mode.

## Chapter 7 Conclusion and outlook

Replacing fossil fuel by hydrogen could be a way to mitigate climate change by decreasing GHG emissions. However, the hydrogen production system must rely on renewable energy and abundant materials in the view of scaling-up this technology. The work conducted in this thesis aims to engineer the photocathode portion of a PEM-PEC cell to produce hydrogen from moist air and solar energy. A significant step towards this technology was reported in this thesis, namely the development of a novel TPCS. In addition, the deposition of various semiconducting materials was evaluated, showing the versatility of the new GDL-type support. The best photoelectrode performance in liquid phase was obtained with a bulk heterojunction-based photocathode. The photoelectrode has been integrated in a half PEM-PEC cell as a proof-of concept for solar-driven hydrogen production in gas phase. Except the Pt HER catalyst, all the materials used to construct the electrodes do not belong to the rarest family of elements on Earth, supporting the potential for scaling-up the device.

### 7.1 Transparent Porous Conductive Substrate

The TPCSs developed in this thesis are a versatile platform for any photoelectrode application. Indeed, we demonstrated for the first time, a novel gas diffusion layer able to transmit  $\geq 35\%$  of light, combining porous structure (ca. 90% porosity) and electrical conductivity (resistivity ca.  $20 \Omega \cdot \text{sq}^{-1}$ ). The main opportunity for improvement relates to the poor mechanical properties of the template compared to a standard metal felt. To increase the mechanical properties, several options can be considered. The first one being to tune the TPS process by changing the annealing temperature or the fiber blend to increase the cohesion of the structure. The second possibility could be a post sintering treatment using ceramic powders such as zirconia, alumina or silica to reinforce the support at the fiber-fiber connexion. However, the use of ceramic powders would require higher annealing temperature. The transparency of the electrode could also be improved by further optimizing the FTO deposition parameters, ensuring sufficient conductivity (i.e., resistivity  $< 30 \Omega \cdot \text{sq}^{-1}$ ). Finally, the surface area could be enhanced by creating a porosity gradient in the TPCS structure, having one side more porous with lower surface area and another side composed of a denser network of fibers, typical from the gas diffusion layer used in the PEM fuel cell.

## 7.2 Material coatings onto the TPCS for PEC application

Throughout this thesis work, we highlighted the scope of possibilities for material coating on the TPCS. FTO, Hematite, CuSCN/Cu<sub>2</sub>O, WSe<sub>2</sub>, and BHJ were coated by atmospheric pressure chemical vapor deposition, chemical bath deposition, electrodeposition, electrophoretic deposition, and dip-coating respectively.

The best performing hematite-TPCS photoelectrode exhibited a photocurrent of 1.6 mA.cm<sup>-2</sup> at 1.6 V vs. RHE in liquid electrolyte for OER. The performance could be optimized further by decreasing the thickness of the hematite nanorods while keeping an optimum fiber coverage. An optimization of the CBD procedure in terms of precursor's concentration or CBD temperature could be envisioned. In addition, hematite deposition by ALD could be an appropriate method to coat an extra-thin layer on a large surface area template such as the TPCS.

A thin Cu<sub>2</sub>O layer was coated on the TPCS thanks to the *in-situ* electro-conversion method, by pre-depositing a CuSCN layer by electrodeposition followed to the conversion to Cu<sub>2</sub>O. The method is adapted to coat homogeneously a large surface area template. After protective layer coating by ALD, a photocurrent of ca. -0.5 mA.cm<sup>-2</sup> at 0 V vs. RHE could be measured. However, in absence of HER catalyst, a drastic color change was observed after operation, typical of photocorrosion. In order to avoid any degradation of the Cu<sub>2</sub>O layer, the optimization of the protective layer and the deposition of a HER catalyst could be investigated.

The most promising photoelectrode is the organic semiconductor-based photocathode. The device is composed of different layers coated on the TPCS. The CuSCN is deposited by electrodeposition and acts as a hole transporting layer. The bulk heterojunction is deposited by dip-coating and the Pt HER catalyst is photodeposited on the BHJ. In liquid electrolyte, the photocathode exhibited a photocurrent between -1 - 2 mA.cm<sup>-2</sup> at 0 V vs. RHE in liquid electrolyte. Despite the photocurrent loss, the electrode exhibited -0.5 mA.cm<sup>-2</sup> at 0V vs. RHE after one hour of operation. The performance of the electrode could be improved by optimizing the thickness and coverage of the HTL and BHJ. In addition, the photoelectrode performance and stability could be improved by using a all-polymer BHJ (e.g., PTB7-Th:PDI-V), which has been proved to be more stable compared to PTB7-th:PCBM.<sup>87</sup> Moreover, the stability of the CuSCN HTL should also be investigated further. A TiO<sub>2</sub> layer acting as charge selective layer could be applied to the BHJ-TPCS photoelectrode as it has been done on BHJ photoelectrode coated on flat FTO glass.<sup>82</sup> The electron selective layer could prevent charge accumulations and the degradation of the BHJ layer. Finally, Pt is a rare element on Earth and its deposition on BHJ lacks of reproducibility. Moreover, the Pt detachment was identified as source of instability for BHJ-based electrode,<sup>190</sup> due to the delamination of Pt nanoparticles. Therefore, Pt could be replaced by another catalyst such as FeMoSx or MoSx, provided that it can be deposited homogeneously on the BHJ surface.



### 7.3 BHJ-photocathode for PEM-PEC application

The proof-of-concept of hydrogen production in presence of humidified argon and sunlight was demonstrated using a semi-transparent BHJ photocathode. A photocurrent of  $-120 \mu\text{A}\cdot\text{cm}^{-2}$  and a hydrogen production ca.  $1 \mu\text{mol}\cdot\text{h}^{-1}$  was sustained for 1 hour, suggesting ca. 52% FE. However, in order to increase the photocurrent amplitude and stability, the component of the photocathode could be further investigation, as mentioned in section 7.2.

The electrode wettability in the gas phase could be investigated as it has been identified as an important factor to guarantee the use of the full surface area of the electrode. In parallel, the development of an ionomer coating<sup>111</sup> (e.g., Nafion, Aquivion) could enhance the water uptake of the electrode and improve the protons transport through the fibers.

Finally, a full PEM-PEC cell could be developed, using the TPCS as photoelectrode support, a photoanode material (e.g.,  $\text{BiVO}_4$ ) and the BHJ TPCS photocathode. In the view of combining the BHJ photocathode with a photoanode in a bias-free device, both photoelectrodes must exhibit photocurrent at the operating point (e.g, intersect of the J-V curves). The operation point is limited by the photovoltages that can be obtained by both the photoanode and photocathode. It is essential for the sum of the photovoltage to be higher than 1.6 - 1.8 V. The onset potential of the photocathode developed in this work could be enhanced by using a catalyst such as  $\text{RuO}_2$  which showed a  $V_{\text{onset}}$  at 0.7 V vs RHE<sup>174</sup> in order to match with the selected photoanode. Finally, to realize a commercially viable PEM-PEC device, a solar-to-hydrogen efficiency of 10% and 10 years of stability are needed. Therefore, the development of high performing and robust semiconducting materials, ionomers and catalysts will be essential, as well as PEMs and bipolar plates.



## Appendix 2

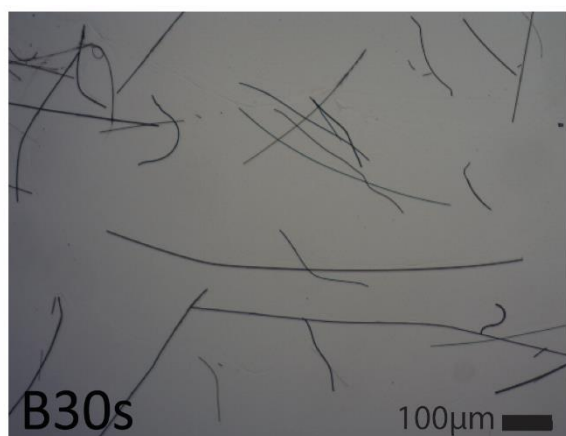


Figure S2.1. Microscope image of the quartz fibers blended for 30 s.

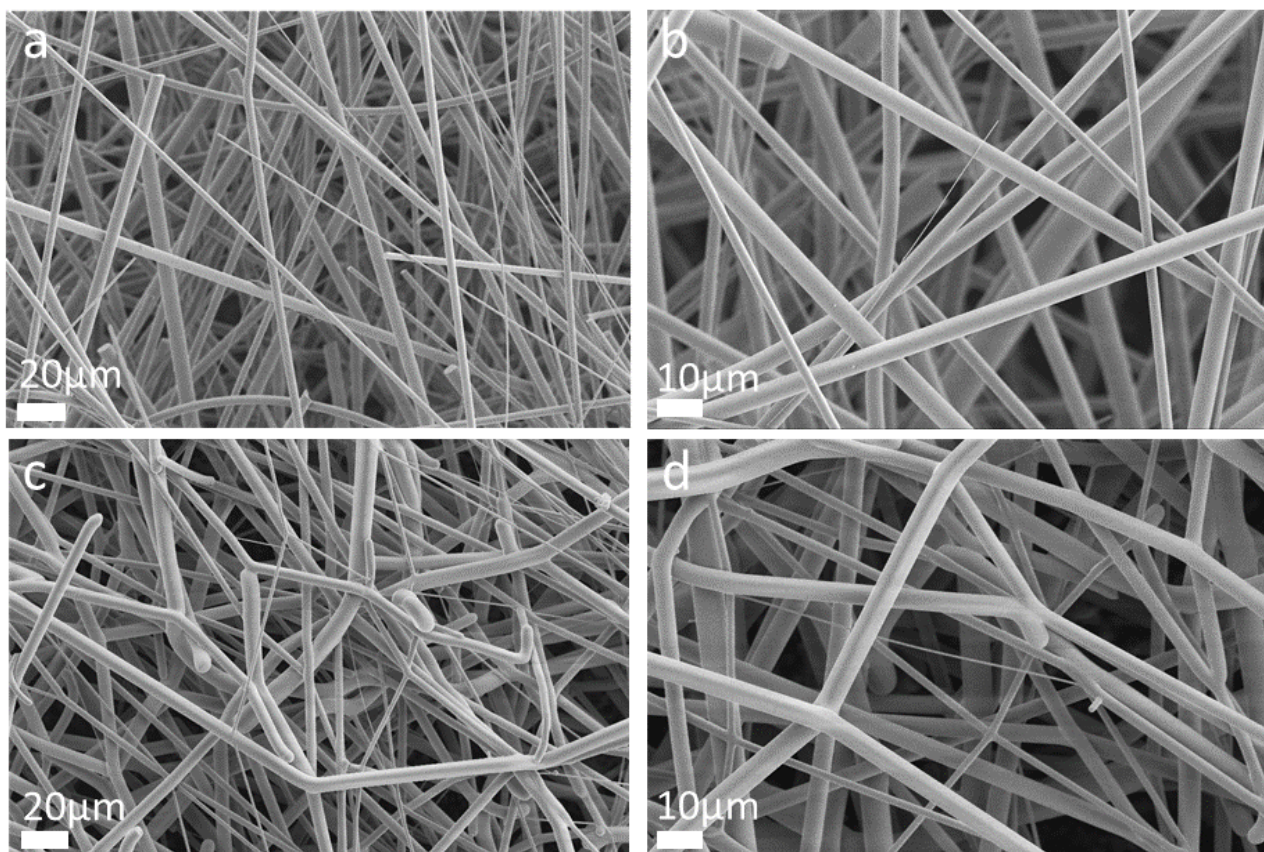


Figure S2.2. SEM of a TPS (a,b) before annealing (c,d) after annealing at 1350 °C.

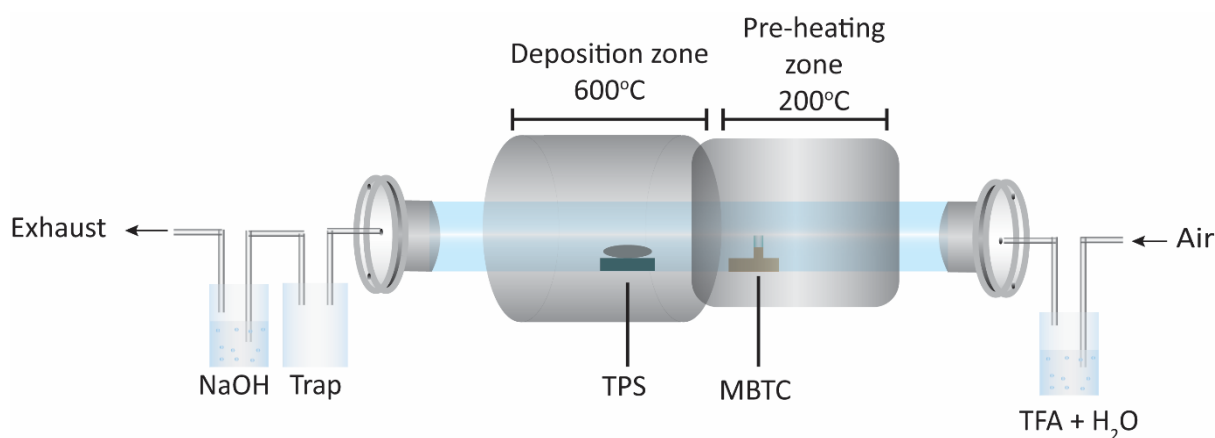


Figure S2.3. Schematic of FTO (APCVD) set up. TPS is the transparent porous substrate, MBTS is monobutyltin trichloride and TFA is acid trifluoroacetic.

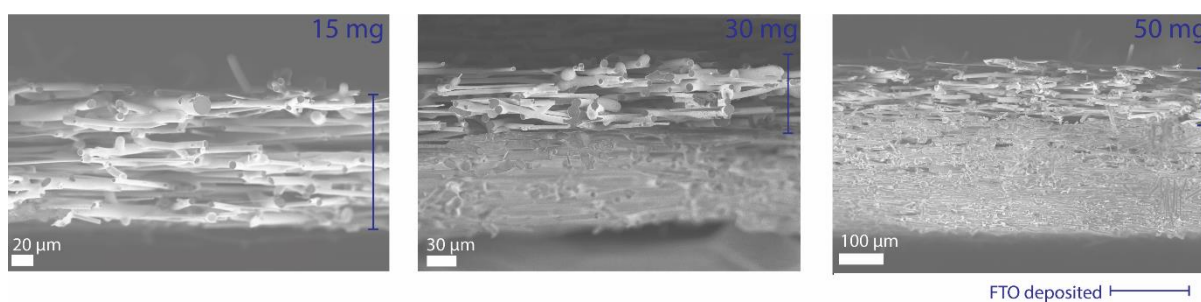


Figure S2.4. SEM cross-sectional of TPCS for different fibers amount (a)15 mg, (b)30 mg, (c)50 mg.

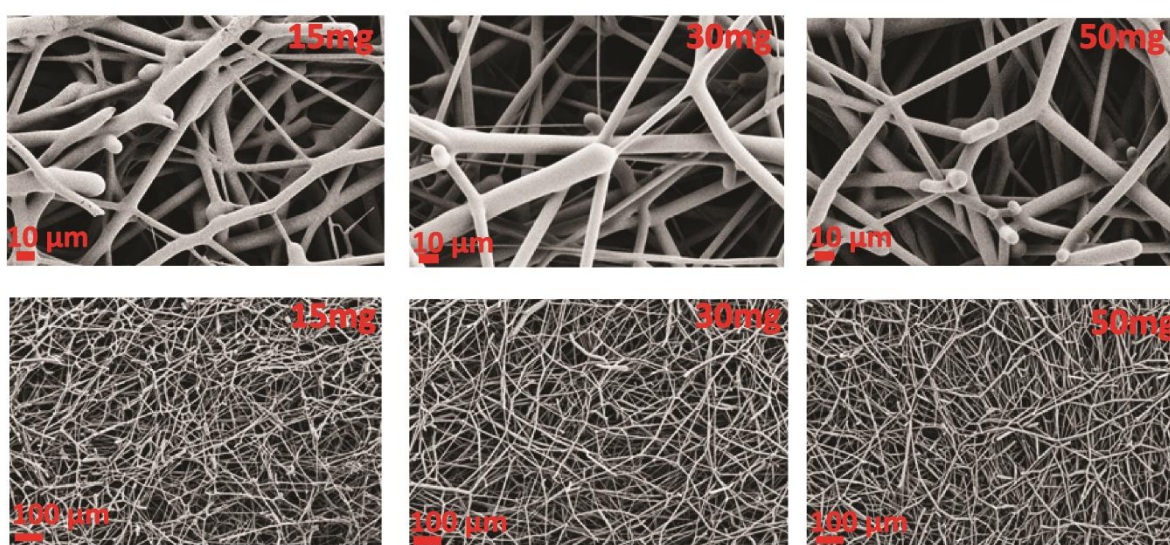


Figure S2.5. SEM pictures of TPCS for different fibers amount (a)15 mg, (b) 30mg, (c) 50 mg

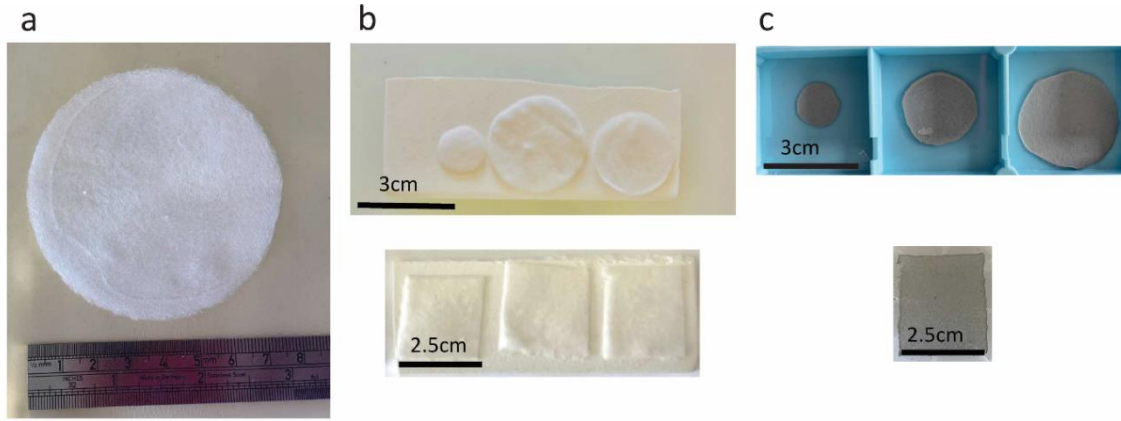


Figure S2.6. TPS and TPCS photograph (a) large TPS, (b) different TPS shape/size, (c) different TPCS shape/size after FTO coating.

Porosity calculation using quartz density:

Quartz density :  $2.65 \text{ g/cm}^3$

Volume(TPS) =  $A \times t$  with A the area and t the thickness of a TPS.

Volume(quartz fibers) =  $\frac{m}{d}$  with m mass of a TPS and d density of quartz.

$$\text{Porosity} = \frac{V_{\text{pore}}}{V_{\text{total}}} = \frac{V(\text{TPS}) - V(\text{quartz fibers})}{V(\text{TPS})} = 89\%$$



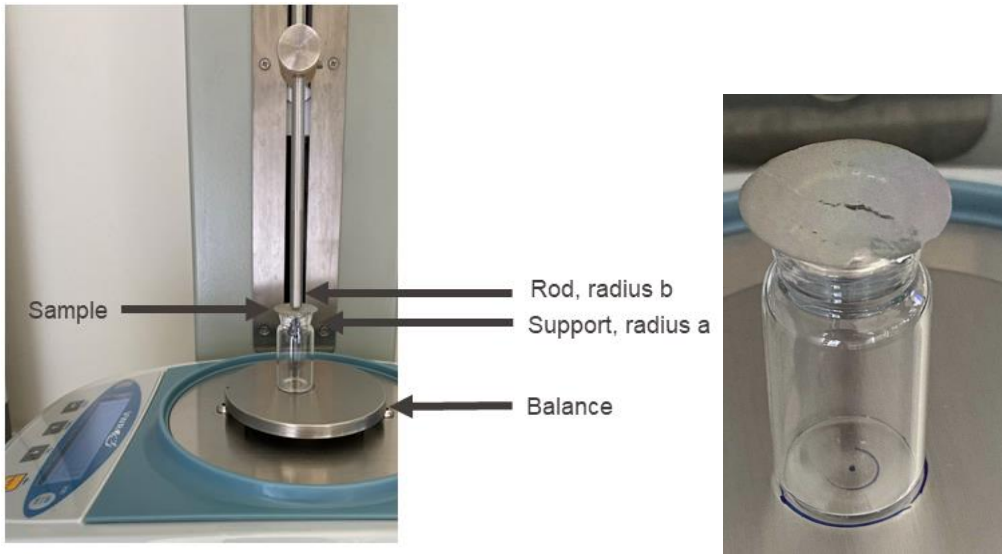


Figure S2.7. Photograph of the biaxial flexure test set-up and the sample after the test.

#### Calculation biaxial flexure text:

The following calculation were done to determine the Young's modulus and failure point; extracted from ref<sup>127,128</sup>:

Displacement (m)  $d = t \times v$  ; where t is the time and v the velocity of displacement.

Force/Load (N)  $F = m \times g$

where m is the mass measured and g the gravity of acceleration (9.81 m/s<sup>2</sup>).

Radius of curvature (m)  $\rho = \frac{\sqrt{a^4 - 2a^2b^2 + 2a^2d^2 + b^4 + 2b^2d^2 + d^4}}{2d}$

Where a, b are the radii of the support and the rod load, d is the displacement.

Strain (N.U)  $\varepsilon = \frac{\Delta L}{2L} = \frac{d}{\rho}$

Where d is the displacement and p the radius of curvature.

Stress (N/m<sup>2</sup> or Pa)  $\sigma = \frac{F}{A} = \frac{3}{4\pi h^2} \left\{ (1 - \nu) \left[ 1 - \left( \frac{b^2}{a^2} \right) \right] - 2(1 + \nu) \log \left( \frac{b}{a} \right) \right\} F$

Where F the force applied, A is the area of the substrate, h is the thickness of the substrated tested, v is the Poisson's ratio for foam, a and b are the radii of the support and the rod load.

The Young's modulus (N.m<sup>-2</sup> or Pa) is calculated by fitting the linear region of the stress-strain graph:

$$E = \frac{\text{stress}}{\text{strain}} = \frac{\sigma}{\varepsilon}$$

The failure point is the maximum stress point that the material can handle before the fracture.

	Flat substrate	TPCS
TFA 0	$10 \pm 2 \text{ } \Omega/\text{sq}$	$29 \pm 4 \text{ } \Omega/\text{sq}$
TFA 1/10	$6 \pm 1 \text{ } \Omega/\text{sq}$	$16 \pm 3 \text{ } \Omega/\text{sq}$
TFA 1/2	$5 \pm 1 \text{ } \Omega/\text{sq}$	$12 \pm 4 \text{ } \Omega/\text{sq}$

Figure S2.8. Resistivity measurement for flat substrate and TPCS coated using different amount of TFA in the mixture TFA/water (v/v).

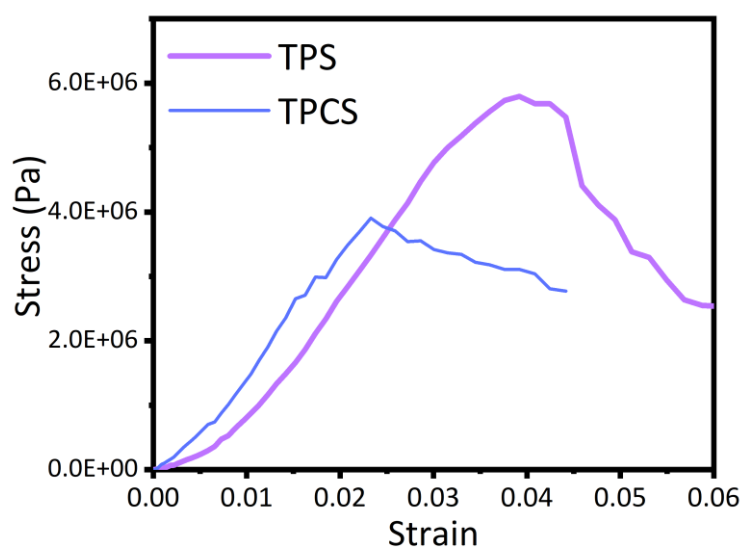


Figure S2.9. Stress-strain curve for the bi-axial flexure test for TPS and TPCS 1350 °C, ( $4 \text{ mg}\cdot\text{cm}^{-2}$  loading).

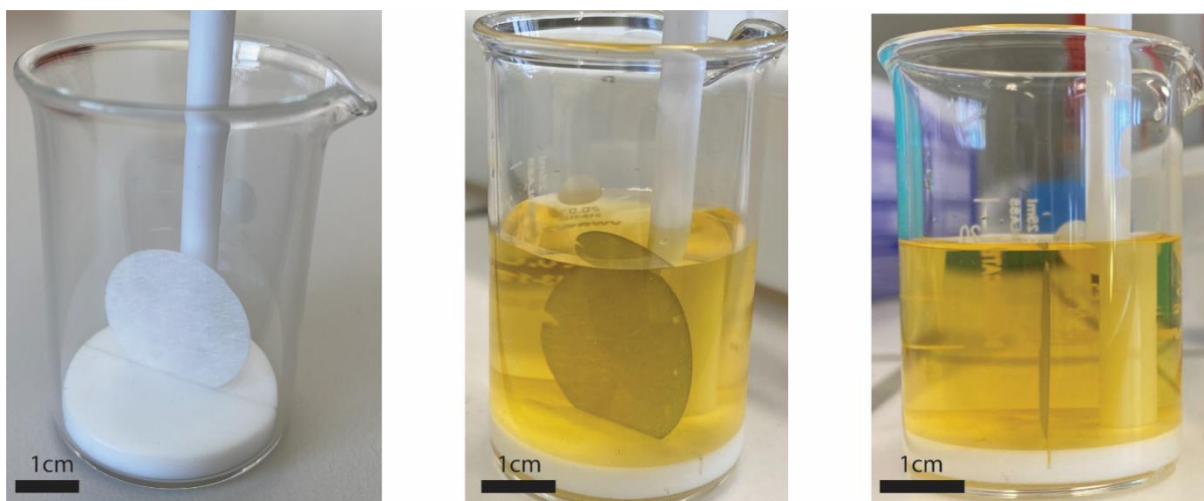


Figure S2.10. Photographs of the set-up used for CBD deposition on the TPCS, the holder is made of Teflon.

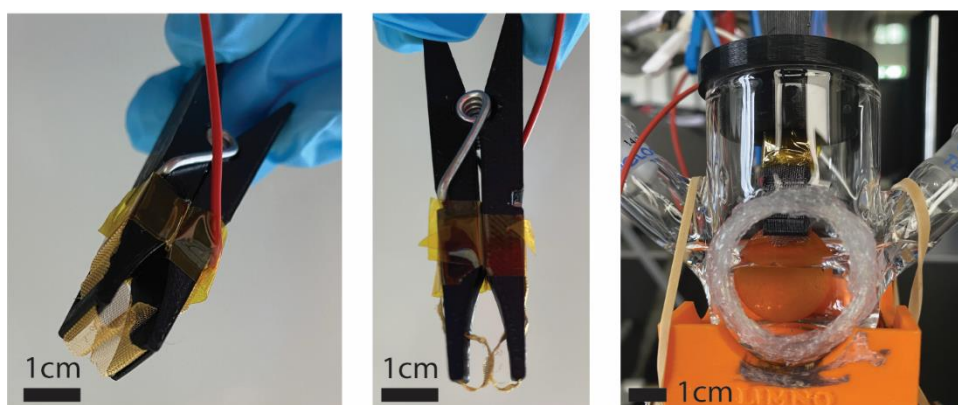


Figure S2.11. Photographs of the set-up used for PEC test, a clip composed a gold-mesh (or Ta mesh) contact and a glass cell for 3-electrodes testing.



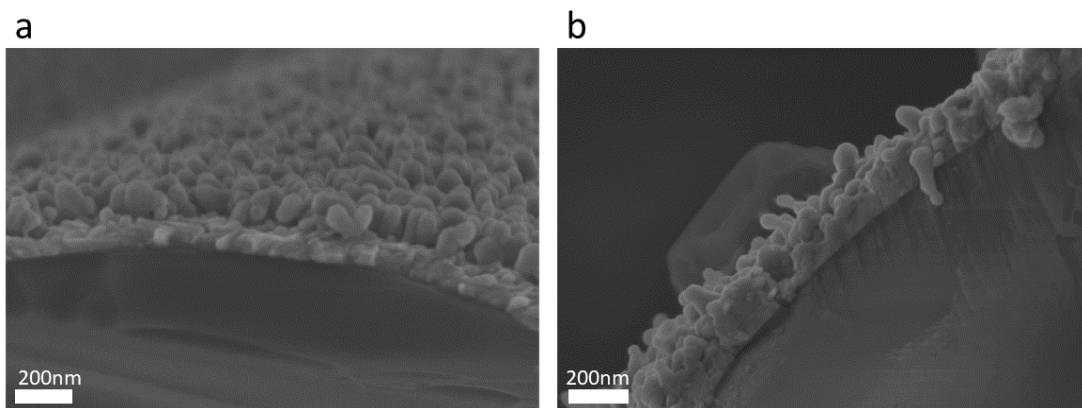


Figure S2.12. SEM cross-sectional images (a) Hematite-coated TPCS 10 min CBD at 100 °C (b) Hematite-coated TPCS 2h CBD at 90 °C.

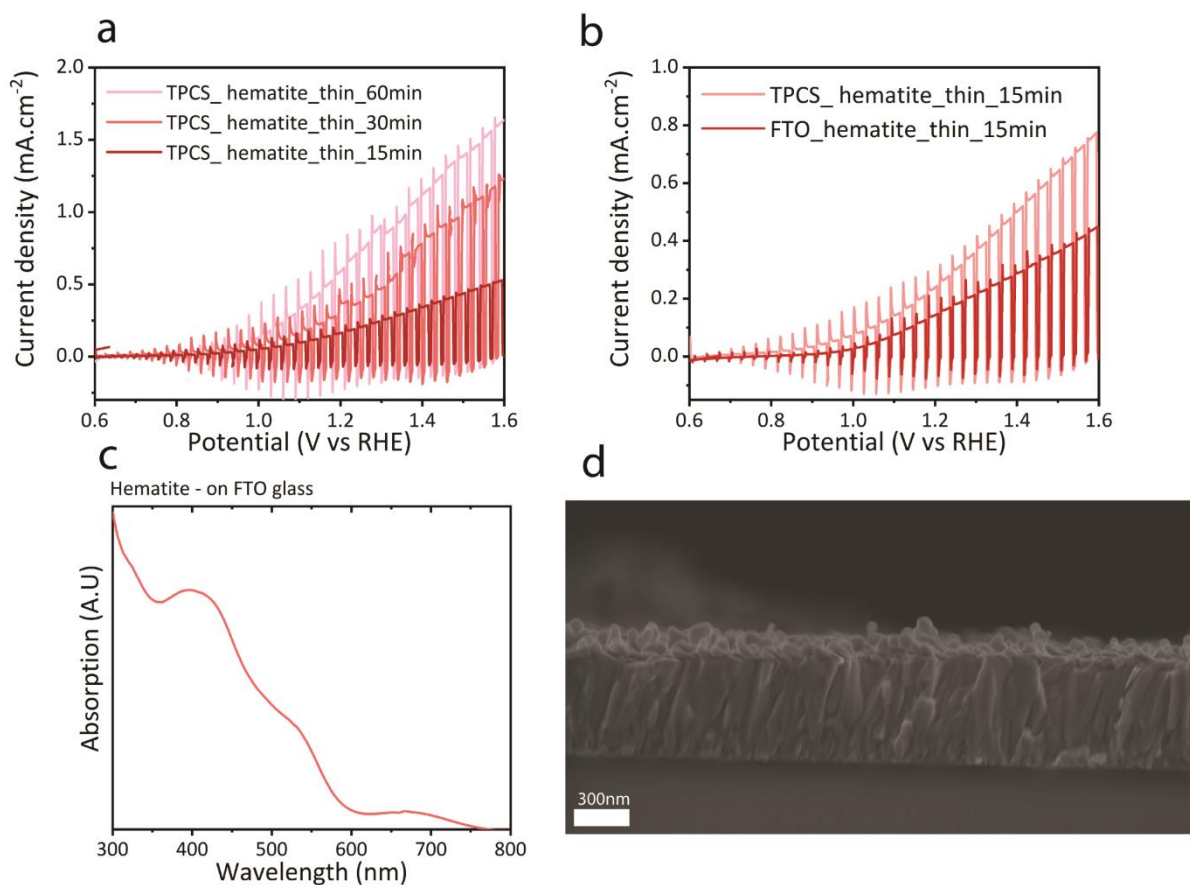


Figure S2.13. (a-b) LSV curves in NaOH, at pH 13.6 under 1 sun illumination for thin-hematite samples (a) on TPCS for different annealing temperatures (b) comparison between FTO and TPCS for 15 min annealing (c) UV-visible absorption spectra of thin hematite on FTO glass (d) SEM cross-sectional of thin hematite on FTO glass.

Our attempts to make a photoanode with a TPCS annealed at 1250 °C having more ductile properties did not withstand any photocurrent (Figure S15). We hypothesized that the connectivity between the fibers was not achieved despite the sheet resistance average measurement exhibiting 25  $\Omega/\text{sq}$ . As the sheet resistance measurement is based on a compression method, it can explain the value obtained. However, in a compression-based setup, a ductile structure could be useful and would require more investigations.

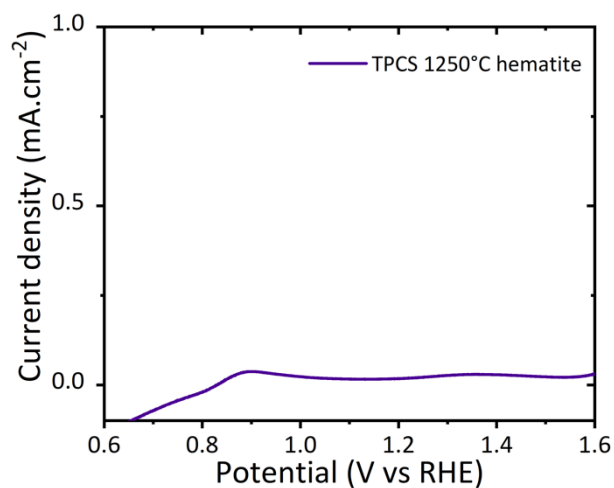
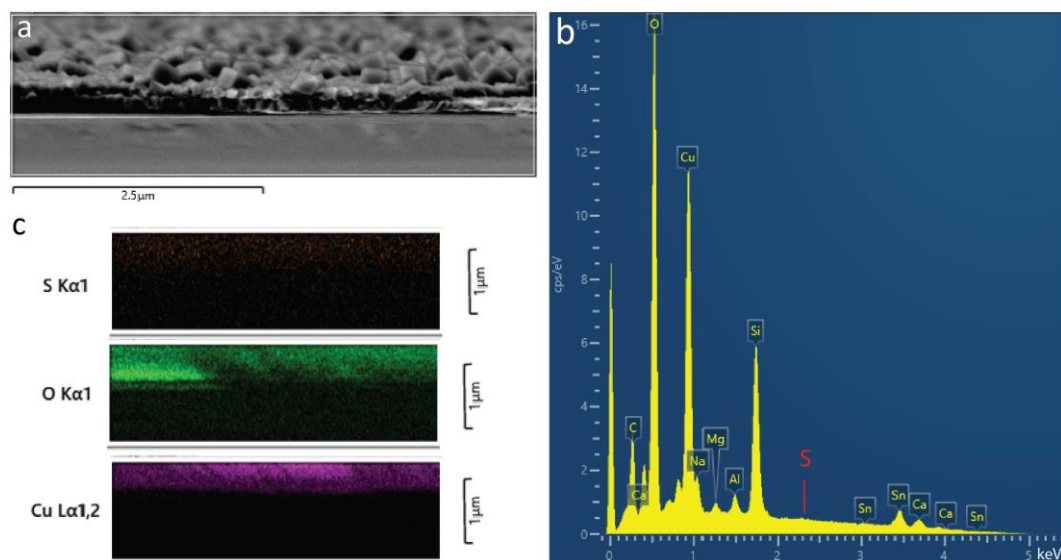
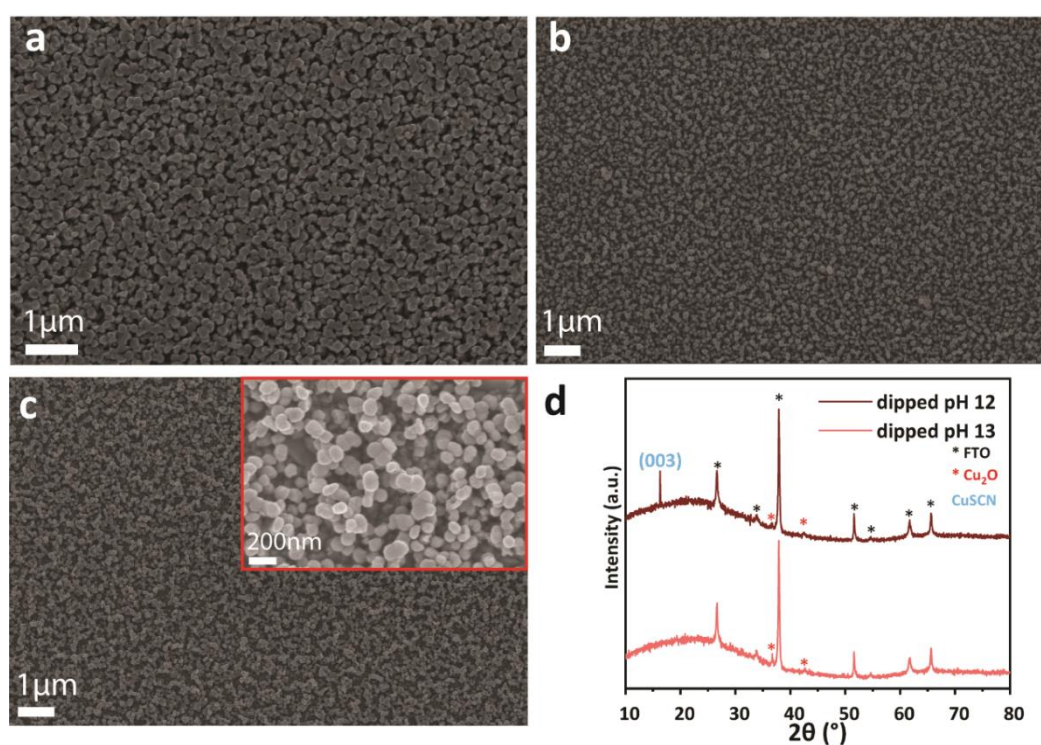


Figure S2.14. LSV curve in NaOH, at pH 13.6 under 1 sun illumination for thin-hematite film on TPCS 1250 °C.

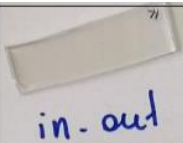
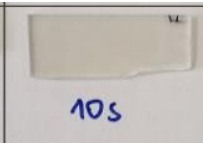
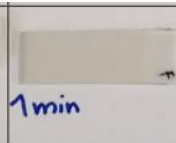

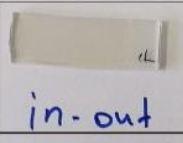
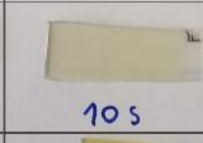
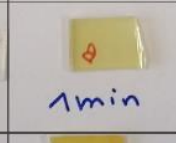
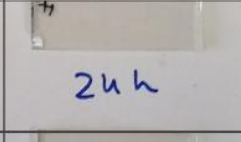

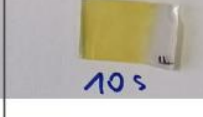
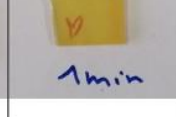
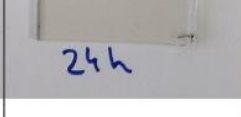
## Appendix 3



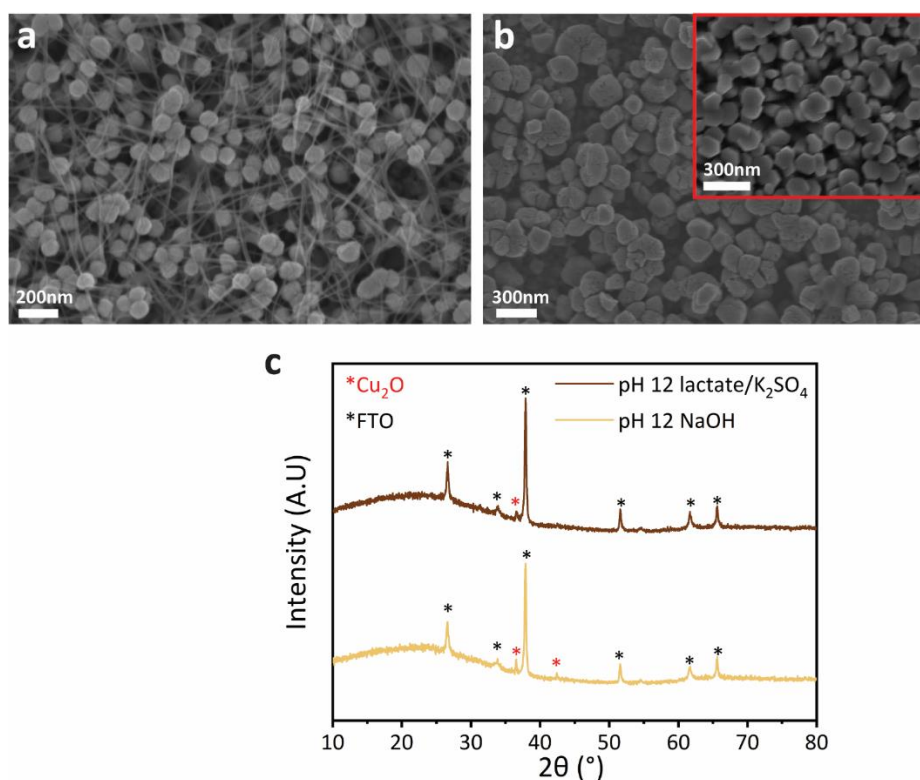
**Figure S3.1.** Characterizations of the  $\text{Cu}_2\text{O}$  deposited at  $-0.1\text{mA}\cdot\text{cm}^{-2}$  on CuSCN (2min electrodeposition) converted film (a) SEM image (b) Element mapping of S, Sn, O, Cu respectively (c) EDX spectrum showing the absence of S signal at 2.307 keV



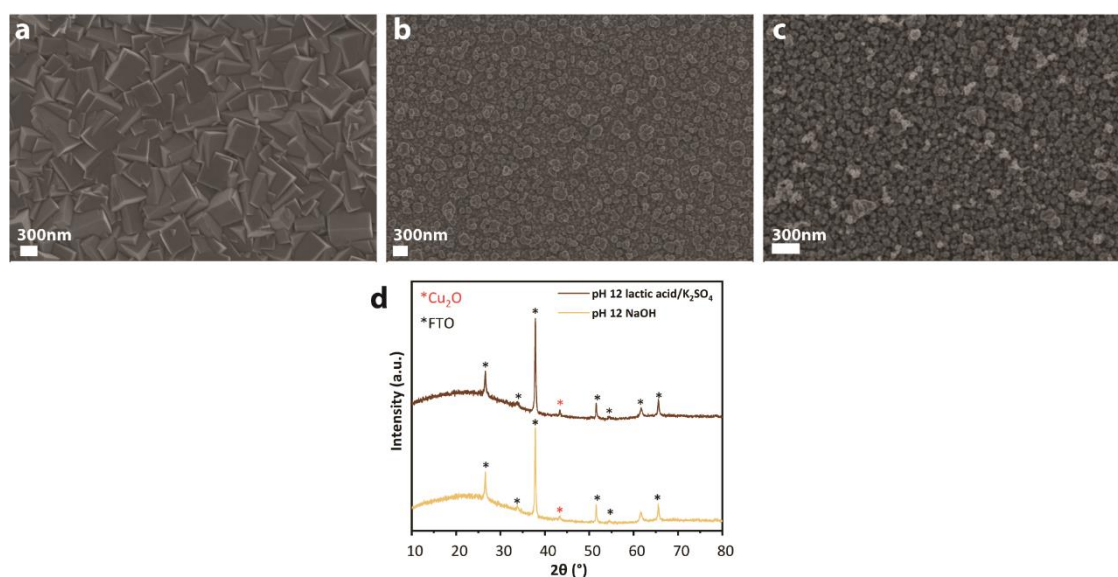
**Figure S3.2.** SEM top view of a 5 min-electrodeposited CuSCN film on FTO after dipping treatment in different electrolytes. (a) native FTO/CuSCN film (b) dipped for 1 min at pH 12 in Cu-lactate rich electrolyte (c) dipped for 1 min at pH 13 in Cu-lactate rich electrolyte (d) XRD spectra.

Cu <sub>2</sub> O electrolyte pH 11	 in-out	 10s	 1min	 24h
Cu <sub>2</sub> O electrolyte pH 12	 in-out	 10s	 1min	 24h
Cu <sub>2</sub> O electrolyte pH 13	 in-out	 10s	 1min	 24h

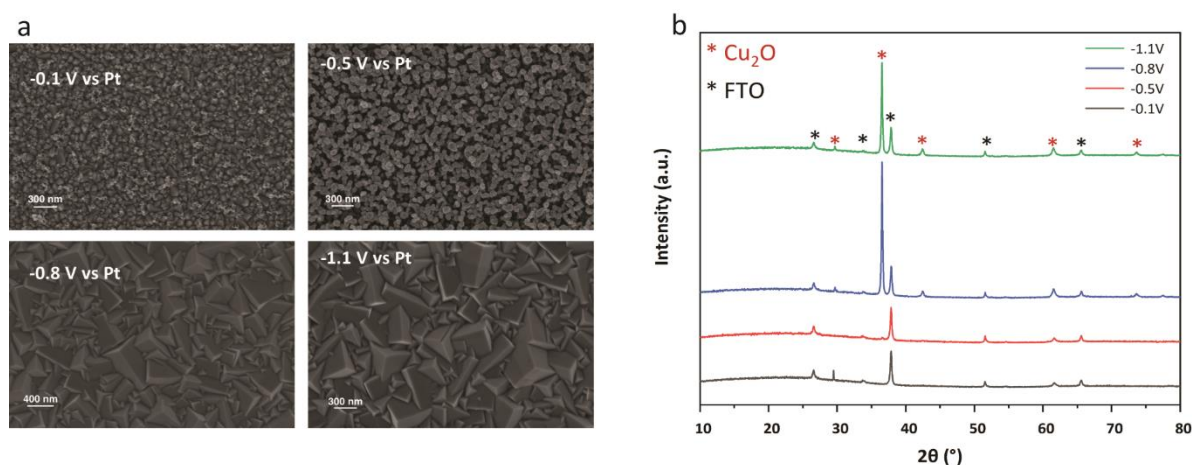
**Figure S3.3** Photographs of samples (FTO/CUSCN) after dipping in a standard electrolyte solution (CuSO<sub>4</sub>, Lactate, K<sub>2</sub>SO<sub>4</sub>, KOH) at pH 11, 12, 13 for < 1 s “in-out”, 10 s, 1 min, or 24h.



**Figure S3.4.** SEM of a 5 min-electrodeposited CuSCN film after 1 min dipping (a) in NaOH pH 12 (b) in electrolyte containing Lactate/K<sub>2</sub>SO<sub>4</sub>/KOH at pH 12 with a native CuSCN bare film for comparison (inset red frame) (c) XRD patterns of the films from (a) and (b).

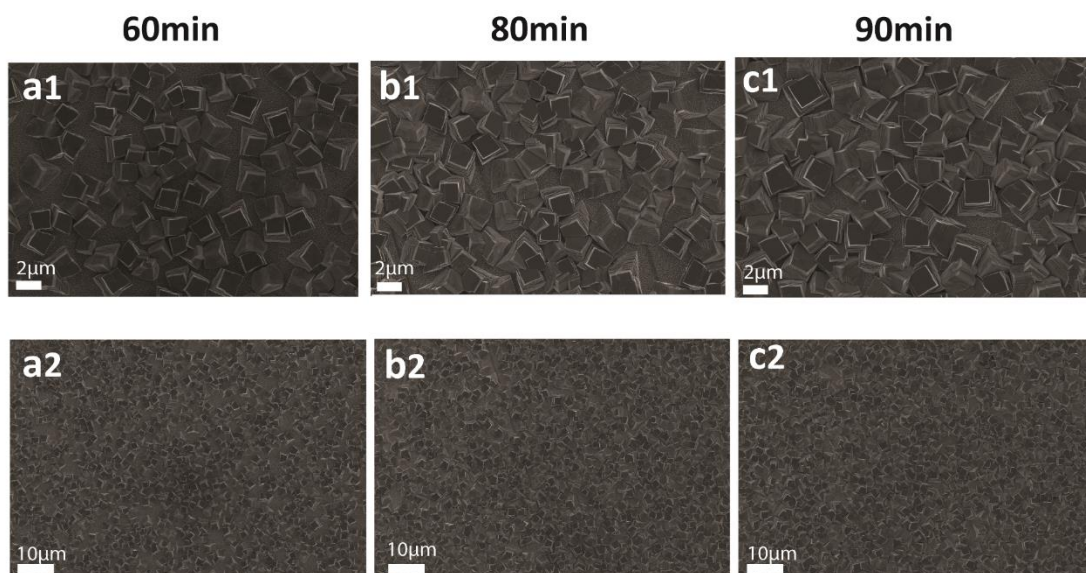


**Figure S3.5.** SEM of a 5 min-electrodeposited CuSCN film after 100 min electrodeposition ( $-0.1 \text{ mA cm}^{-2}$ ) in different electrolytes at pH 12 (a) standard electrolyte (lactic acid,  $\text{CuSO}_4$ ,  $\text{K}_2\text{SO}_4$ , KOH) (b) standard electrolyte without Cu ions (lactic acid,  $\text{K}_2\text{SO}_4$ , KOH) (c) NaOH pH 12 (d) XRD patterns from the film (b) and (c)

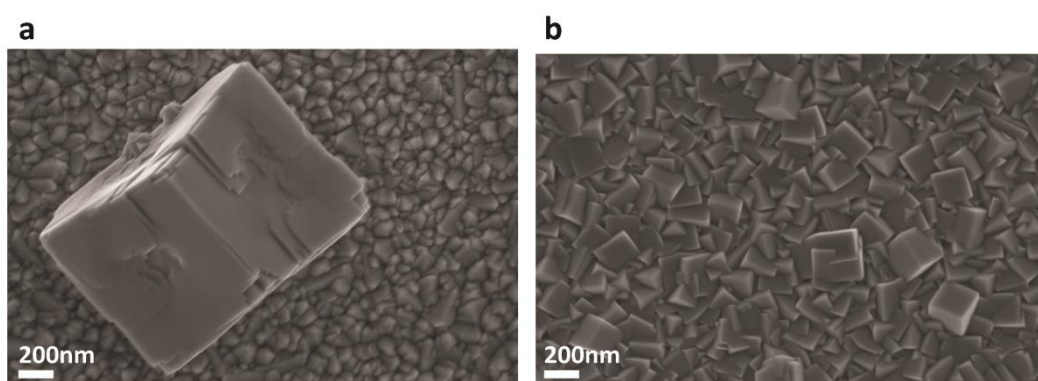


**Figure S3.6.** 2 min-electrodeposited CuSCN film after 100 min electrodeposition following  $\text{Cu}_2\text{O}$  standard procedure at the different potentials noted in the figure (a) Top view SEM (b) XRD patterns. We note the small sharp peak at  $2\theta = 29.5^\circ$  in the  $-0.1 \text{ V}$  sample is not consistent with  $\text{Cu}_2\text{O}$  and is attributed to an impurity present during the measurement.

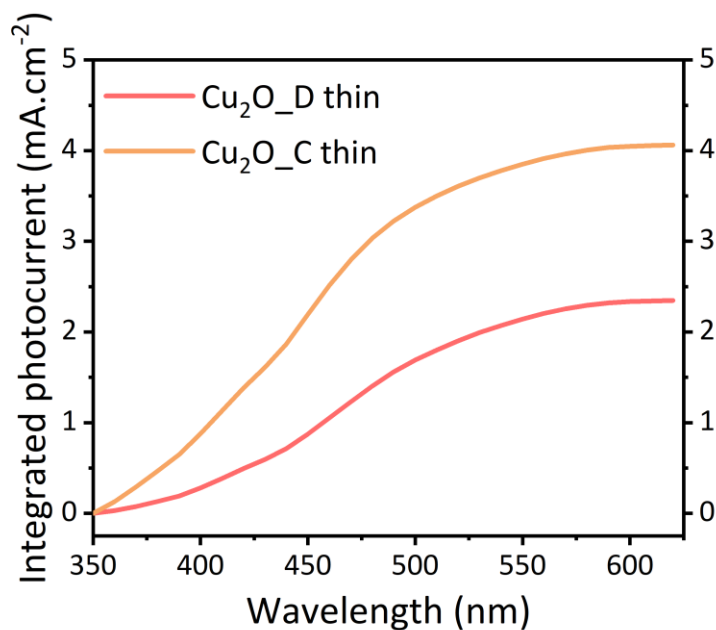




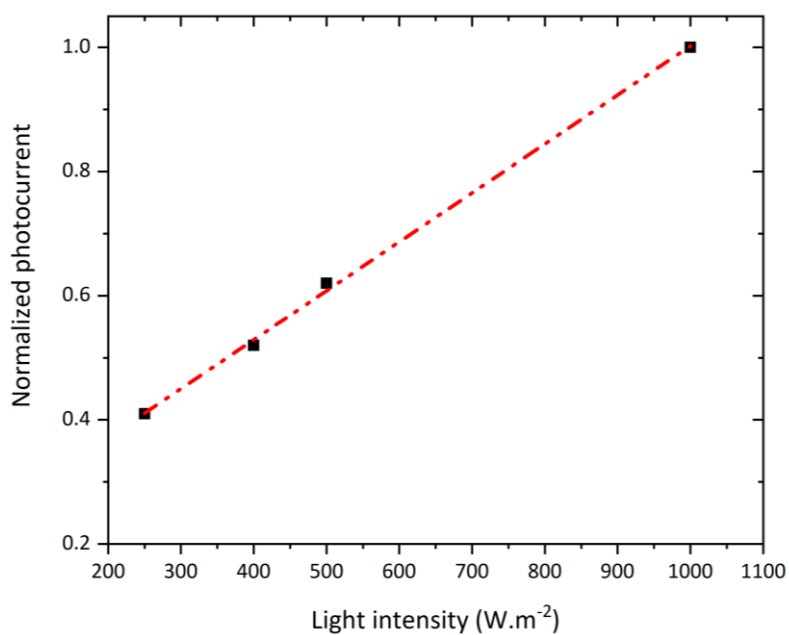
**Figure S3.7.** SEM images top view comparison of  $\text{Cu}_2\text{O}$  grown on bare FTO for various deposition time (a1,a2)  $\text{Cu}_2\text{O}_\text{D}$  60min, (b1,b2)  $\text{Cu}_2\text{O}_\text{D}$  80 min, (c1, c2)  $\text{Cu}_2\text{O}_\text{D}$  90 min



**Figure S3.8.** High magnification SEM images comparing  $\text{Cu}_2\text{O}$  samples (a)  $\text{Cu}_2\text{O}_\text{D}$  (b)  $\text{Cu}_2\text{O}_\text{C}$



**Figure S3.9.** Photoelectrochemical characterizations of the Cu<sub>2</sub>O\_D and Cu<sub>2</sub>O\_C electrodes at pH 5 (a) Integrated photocurrent during IPCE measurement at 0V vs. RHE considering the AM 1.5 G standard solar spectrum.



**Figure S3.10.** Normalized photocurrent of the Cu<sub>2</sub>O\_C photocathode at 0 V vs. RHE as a function of illumination intensity. The linear fit line is shown in red ( $R^2 = 0.99882$ ).

**Additional methods:** *Theoretical calculation for absorptance*

	Transmittance	Reflectance	Absorptance	Theoretical Absorptance
FTO glass	0.84	0.12	0.04	-
Cu <sub>2</sub> O Direct	0.58	0.21	0.21	0.20

$$\alpha = \frac{4\pi k}{\lambda}$$

$$T = (1 - R)e^{-\alpha d}$$

Then, the absorptance of a film with a coverage of 100% is:

$$A(\text{Cu}_2\text{O}) = 1 - T - R$$

If we take into account the coverage of the film:

$$A = A(\text{Cu}_2\text{O}) \times \%coverage(\text{Cu}_2\text{O}) + A(\text{FTO}) \times \%coverage(\text{FTO})$$

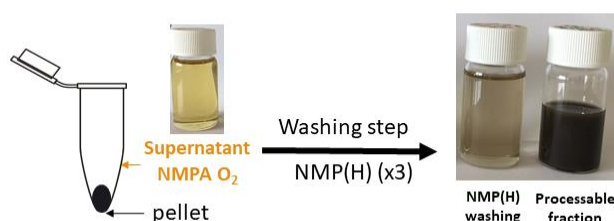
- $k(\text{Cu}_2\text{O})=0.02310$  at 550nm,  $\alpha = 5275 \text{ cm}^{-1}$  at 550 nm
- $\%coverage(\text{Cu}_2\text{O}_D)=46\%$



## Appendix 4

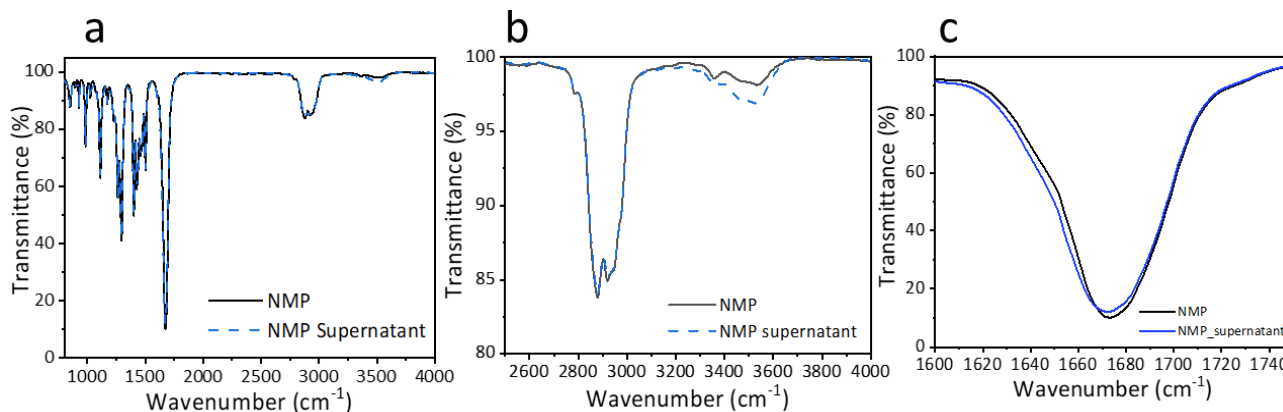
- Investigations on 2 h exfoliations in NMP

As it is always the case when the supernatant exhibits a yellow discoloration, the flake separation is difficult to process and only a low-concentration suspension can be obtained. Nevertheless, if the resulting flake residue is washed with fresh NMP(H), the separation step can be conducted, leading to a solution-processable suspension containing exfoliated WSe<sub>2</sub> nanoflakes. By washing the residue with fresh solvent, it is possible to redisperse the flakes which suggests that the exfoliation has been performed, even in an oxidative sonication media (NMP(H) with O<sub>2</sub> bubbling), but if the media is saturated with O<sub>2</sub>/H<sub>2</sub>O, it can lead to the formation of species which linked the nanoflakes together.



**Figure S4.1.** Illustration and photographs showing the washing step necessary to process the nanoflakes exfoliated in NMP(A) under O<sub>2</sub> bubbling.

To identify the species formed, investigation with FTIR was performed on bare NMP and on the supernatant from exfoliation under oxidative condition (**Figure S4.1**). This phenomenon could come from NMP degradation, like ring-opening transformation, as a red-shift of the carbonyl peak has been observed with FTIR analysis. Moreover, the peak corresponding to hydroxyl group (-OH) stretch is more intense at 3200-3500 $\text{cm}^{-1}$ , which suggest moisture absorption for the supernatant.



**Figure S4.2.** Comparson between NMP and NMP supernatant from exfoliation in oxidative conditions (a-b) IR spectra (b) –OH region of the IR spectra (d) –CO region of the IR spectra

We pursued our investigation by measuring zetapotential measurements. A negative charge on the flakes surface has been measured for all the fractions, which is coherent with the value reported for TMDs in the literature<sup>157,164,191,192</sup>. The negative charge measured could come from ion species adsorbed or linked to the flakes. The measurements (**Table S4.1**) were done on the different supernatant solutions containing a small amount of the smallest flakes, assuming that different ionic species were generated according to the sonication conditions (oxidative or inert). Measuring zetapotential in principal interprets the presence of different ionic species as the electric double layer thickness changes by ionic strength, leading to a change in zeta potential. For the four conditions (NMPH in air, NMPA with H<sub>2</sub>O addition and Ar bubbling, NMPA with Ar bubbling), the zetapotential shows a negative value, similar for each sample and coherent which the adsorption of negatively charges species (such as POMs). Jawaid *et al*<sup>158</sup>, proposed a mechanism in which the dissolution of the edge sites of MX<sub>2</sub> structure leads to the formation of polyoxometalate species adsorbed on the flake surface and responsible for the negative charge observed, which is consistent with this result. The origin of the negative charge needs to be studied further, but we hypothesize that it could come from hydroxyl group bonded to a defect site or an oxidized site<sup>164</sup>, or due to polyoxometalate species<sup>157,158</sup> (POM) resulting from solvent degradation, adsorbed onto the flake surface. However, the low value of the zetapotential for the yellow supernatant is not clearly explained, as it is challenging to compare the values due to the difference of conductance of the solution: the suspension formed in oxidative condition shows a higher conductance, which could be due also to the presence of ions in solution such as the degraded NMP species. Nonetheless, it is

clearly observed that the zeta potential values can be changed as different atmosphere in suspension media.

**Table S4.1. Zetapotential and conductance measurement for NMP supernatant for different sonication media with O<sub>2</sub> bubbling, in air, with Ar bubbling and addition of 1%v/v of H<sub>2</sub>O, with Ar bubbling.**

	NMPA_O2	NMPA_O2_ washed	NMPA_Ar	NMPA_Ar_1 %H <sub>2</sub> O
Zetapotential (mV)	-23±9	-52±12	-49±20	-42±11
Conductance (μS)	184	23	28	29

The hypothesis is that different species can be formed during exfoliation in NMP (e.g., sonopolymer, POM). In an oxidative environment, the sonopolymerisation of the NMP could occurred and leads to the flakes agglomeration, requiring a washing step to dissolve the sonopolymer and redisperse the exfoliated flakes. However, it is not clear how the presence of the polymer can affect the efficiency of the exfoliation, as it could reduce the flakes dispersibility. For the case of a brown supernatant, the assumption is the formation of POM species resulting from NMP degradation, thereby demonstrating the effective exfoliation. The POM formation theory and the effect on the exfoliation yield and flakes characteristics (flake size distribution, defectiveness, species adsorbed onto the surface) have to be further evaluated.

It is important to note that the suspension appears to be less stable and difficult to process for LLISA deposition, when the redispersion solvent is anhydrous NMP (NMPA), therefore the redispersion solvent used is always NMP(H). This side effect of anhydrous NMP has been observed by Jawaid *et al*<sup>157</sup>, showing that anhydrous NMP has lower dispersion ability than hydrated NMP.

Thereby, it is proved that the zetapotential measurement, apart of ensuring the reproducibility of the suspension characteristics, could also be used as a tool to characterize surface of WSe<sub>2</sub> nanoflakes. In fact, it can be used to understand the chemical surface environment of the flakes in suspension, which is essential to understand the liquid exfoliation phenomenon (possible adsorption of degradation species), and any ligand conjugation.

#### ▪ Exfoliation in Cyrene

For this study NMP has been used as solvent for exfoliation because it is one of the most efficient solvent to exfoliate TMD, due to his ability to solubilize graphene layered materials displayed by the amide structural unit (NC=O)<sup>152</sup>. Nevertheless, NMP exhibits several drawbacks as its instability, toxicity, high boiling point, thus the development of alternative high performance solvent<sup>193</sup> is

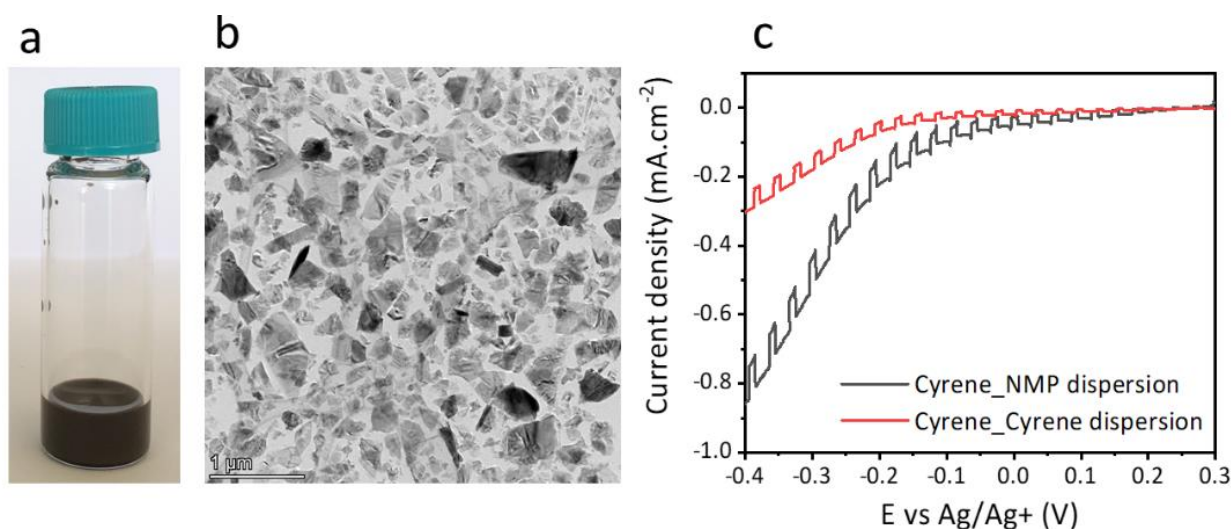
required to ensure the process sustainability. Recently, dihydrolevoglucosenone or Cyrene, a bio-based solvent derived from cellulose has been identified as NMP alternative to exfoliate graphene<sup>165</sup>. Indeed, it possess several advantages such as low acute and toxic toxicity, not mutagenic, safe to handle, stable to oxidation, and sustainable. In term of physical properties, its Hansen solubility parameters are close to the NMP (**table S4.2**).

The main difference is that Cyrene is more viscous than NMP, but it results in higher exfoliation yield, higher length and width of the flake, and reduction of defect<sup>165</sup>. These effects would lead to shorter sonication time, which is an essential aspect for large-scale application. Moreover, Pan *et al*<sup>194</sup>. demonstrated that in addition to the increase of the exfoliation yield, the graphene flakes exfoliated in Cyrene exhibits higher conductivity due to the reduction of defects generated by the process.

**Table S4.2.** Physical properties extracted from 63 for Cyrene and NMP and extracted from 11 for TMDs.

	Cyrene	NMP	TMDs
Dispersion solubility $\delta_D$ (MPa <sup>1/2</sup> )	18.8	18	17-18
Dipolar intermolecular forces $\delta_p$ (MPa <sup>1/2</sup> )	10.6	12.3	8-9
Hydrogen bonding $\delta_H$ (MPa <sup>1/2</sup> )	6.9	7.2	6.5-7.5
Boiling point (°C)	203	202	-
Mass volumic $\rho$ (g.mL <sup>-1</sup> )	1.25	1.03	-

We demonstrated the possibility to exfoliate WSe<sub>2</sub> bulk powder in Cyrene as we can see in **Figure S4.2 a,b**. The nanoflakes obtained were characterized by TEM and exhibit a size ranging from 100-1000nm. Moreover, we tested the PEC performance in chloranil sacrificial electrolyte using a PVP-coated FTO substrate. As Cyrene is more viscous than NMP, it is more difficult to process the cyrene suspension for LLISA deposition. Therefore, we prepared two samples, from the WSe<sub>2</sub> exfoliated in Cyrene by redispersing the nanoflakes in Cyrene and NMP. Both samples, exhibits photoactivity as we can see in **Figure S4.2c**. The redispersion in NMP (black curve) shows slightly higher photocurrent current and dark current. This different could come from the difficulty to perform LLISA deposition with a suspension dispersed in Cyrene. It would be interesting to exfoliate WSe<sub>2</sub> using Cyrene, in order to reduce the defects generated by sonication for instance. However, the exfoliation conditions should be further investigated in term of sonication time/power to unravel the best conditions using this novel solvent. Moreover, the LLISA deposition does not seem to be adapted to a Cyrene-based suspension due to the viscosity of the solvent.



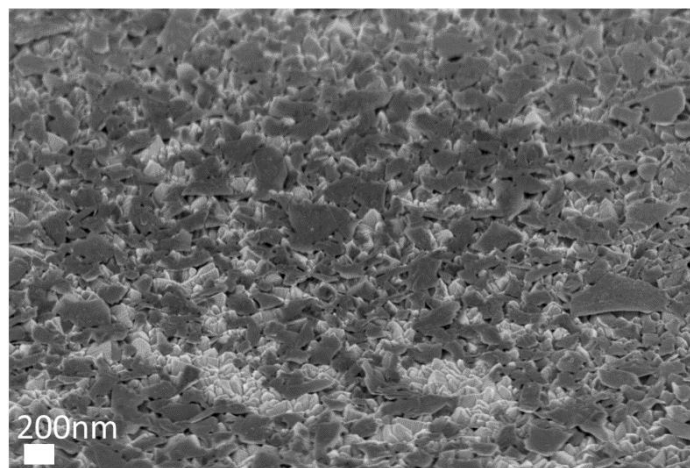
**Figure S4.3.** WSe<sub>2</sub> nanoflakes exfoliated in Cyrene (a) Photograph of the WSe<sub>2</sub> suspension exfoliated in Cyrene (b) TEM image (c) LSV curve in Chloranil electrolyte under intermittent (1 Sun) illumination.

▪ PvP underlayer

Using PVP underlayer could improve adhesion of the nanoflakes on the FTO conductive support (**Figure S4.3**). Apart from the adhesion issue, the PVP underlayer can help to reduce the dark current during PEC measurement. In fact, the coverage of the substrate was observed to be around 80% by the SEM tilted feature (**Figure S4.4**) and leads to the contact of the FTO substrate and the electrolyte.

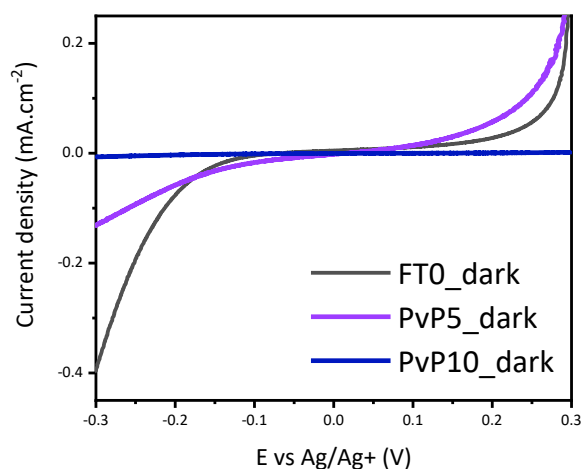


**Figure S4.4.** Pictures of the WSe<sub>2</sub> before and after testing.



**Figure S4.5.** SEM tilted feature of WSe<sub>2</sub> film on FTO substrate

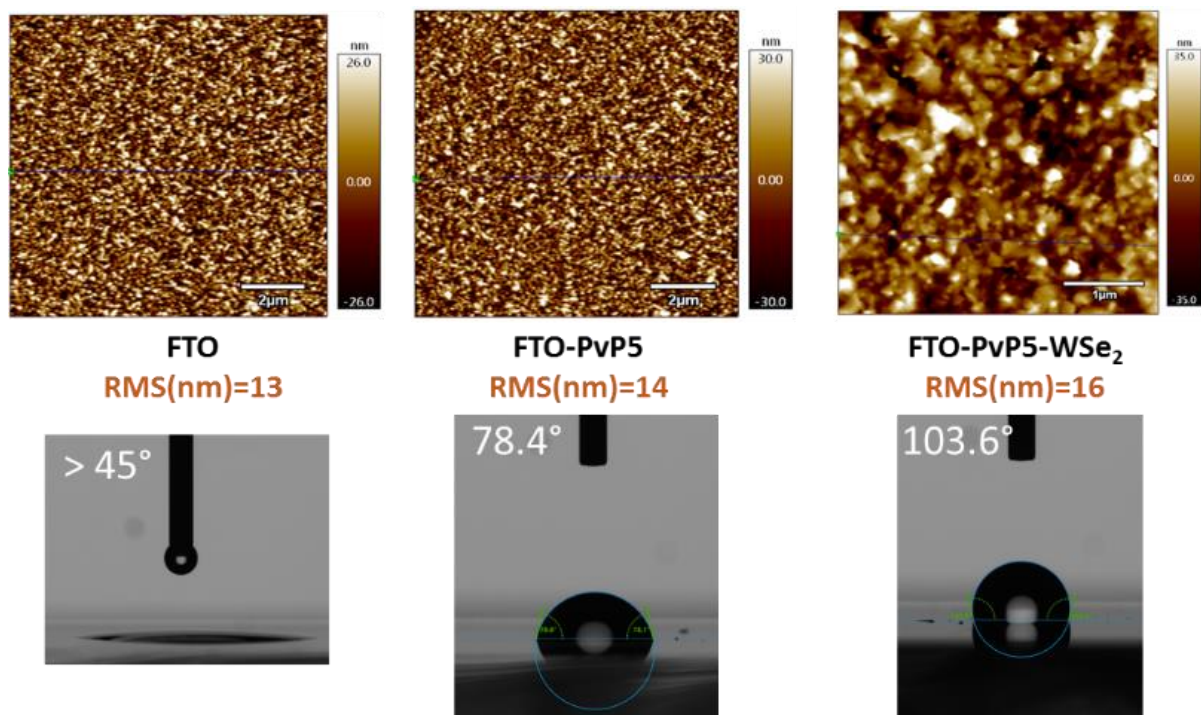
The PVP underlayer can be a barrier for electron to travel from FTO to electrolyte reducing therefore the dark current. In **Figure S4.5**, by increasing the PVP underlayer thickness (meaning increasing the PVP solution concentration) the dark current is lower but for PVP10 it seems that the charge transfer is blocked. As it is essential that the charge could travel through the PVP underlayer, the PVP5 underlayer condition will be used.



**Figure S4.6.** LSV curves in the dark of FTO and FTO coated with PVP for different PVP solution concentration (PVP5 for 5mg.mL<sup>-1</sup>, PVP10 for 10 mg.mL<sup>-1</sup>) in Chloranil saturated solution in MeCN.

The mechanism of attachment of the flakes on the PVP underlayer is likely not due to a planarization of the surface, e.g. the roughness (RMS) extracted from atomic force microscopy (AFM) features (**Figure S4.6**) does not show any change for different samples. However, it could come from the hydrophobic interaction as we can see in **Figure S4.6**, by contact angle measurement. The bare FTO surface is highly hydrophilic while the FTO-PVP5 and FTO-PVP5-WSe<sub>2</sub> surface are hydrophobic, exhibiting a contact angle of 78.4° and 103.6°, respectively. One of the hypothesis could also be an

interaction between the organic ligands which can be present onto the flake surface (due to the exfoliation process in NMP) and the PVP underlayer.



**Figure S4.7.** AFM (features and roughness) and surface angle analysis for different substrates, FTO, FTO-PVP, and FTO-PVP-WSe<sub>2</sub>.

PVP underlayer is not the most promising alternative, due to its insulating properties. Indeed, if the layer is too thick, the charge transfer could be blocked. Moreover, the cross-linking step required the use of a silane based component, which is sensitive to air, leading to a lack of reproducibility. However, it is the best architecture so far to ensure great flakes attachment and therefore higher reproducibility.

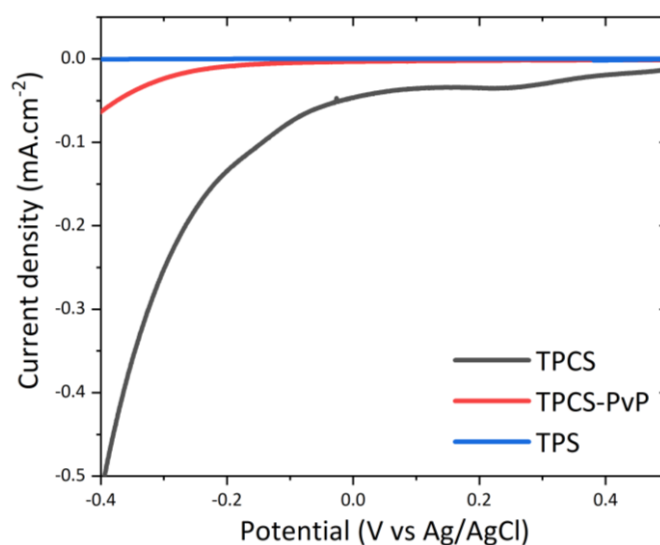


## Appendix 5

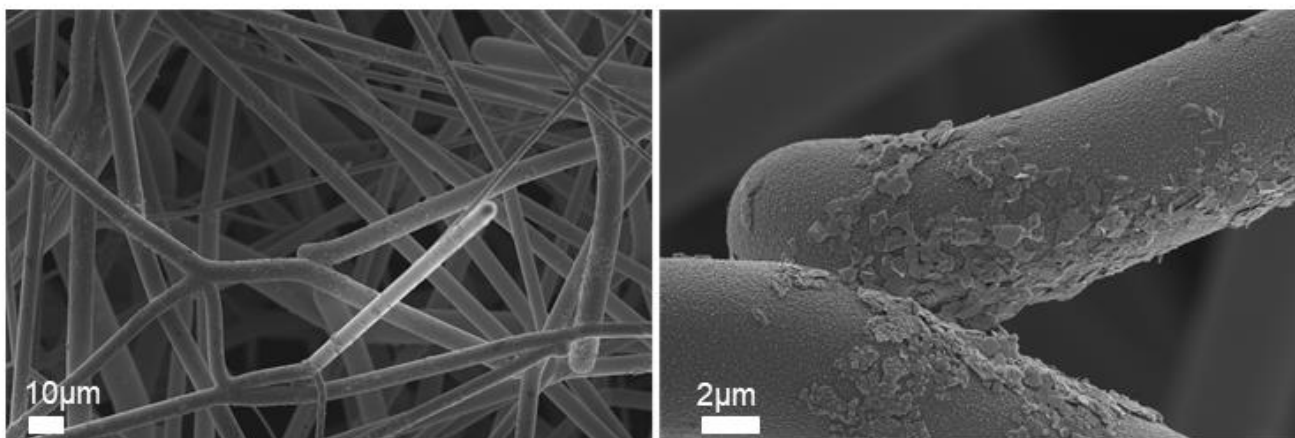
### ▪ WSe<sub>2</sub>-TPCS electrode

#### PvP coating on TPCS

PvP coating was verified by performing an LSV in H<sub>2</sub>SO<sub>4</sub> pH 1. A decrease in the dark current was observed for PvP-coted TPCS compared to the bare TPCS.



**Figure S5.1.** LSV curve in in H<sub>2</sub>SO<sub>4</sub> pH 1 for TPS (non conductive substrate), TPCS and PvP-coated TPCS



**Figure S5.2.** SEM of a TPCS-PvP-WSe<sub>2</sub>-Pt after 6hours EPD



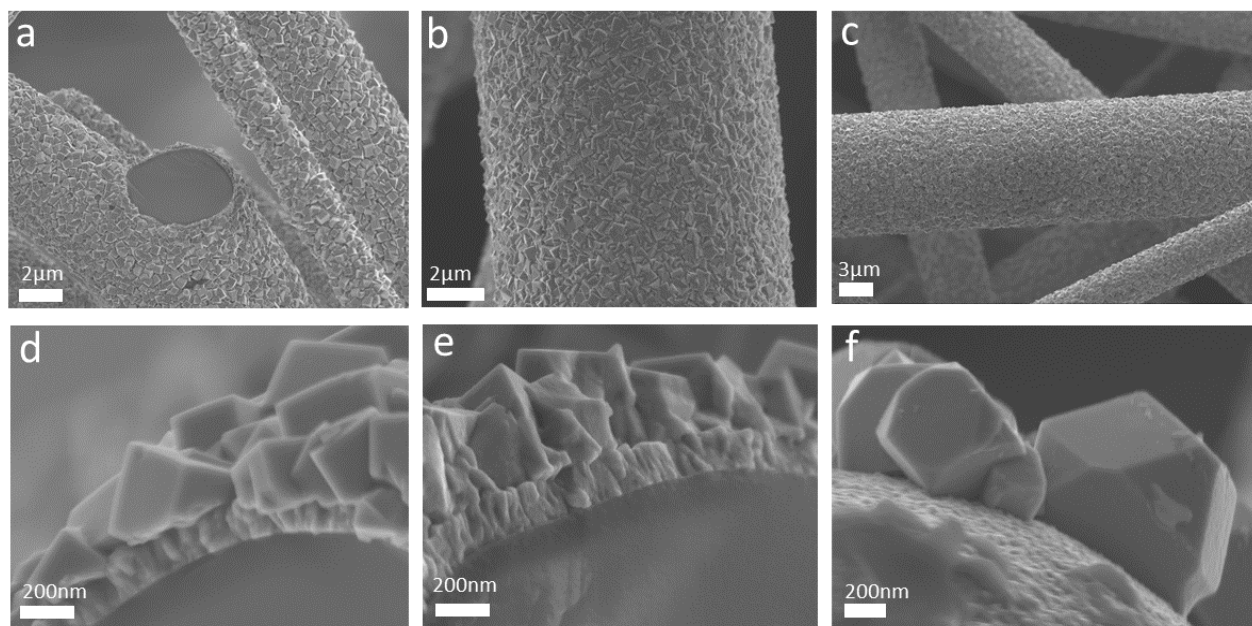


**Figure S5.3.** Photograph of the electrolyte after PEC testing showing the  $\text{WSe}_{\text{eds}}$  nanoflakes detachment

### ▪ **$\text{Cu}_2\text{O}$ -TPCS electrode**

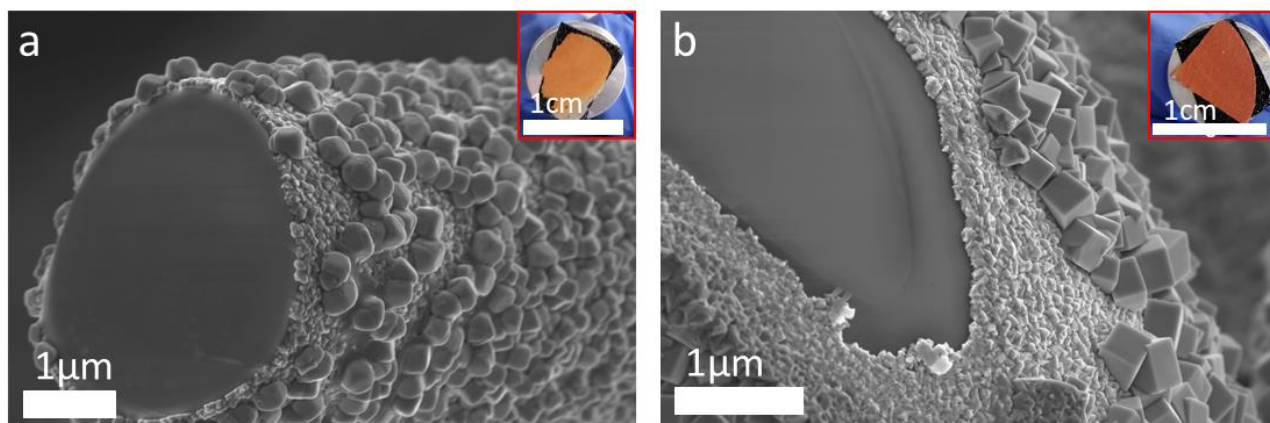
#### **$\text{Cu}_2\text{O}$ coating on CuSCN-coated TPCS**

The coating of the  $\text{Cu}_2\text{O}$  was next pursued using 100 min- electrodeposition of by chronoamperometry at  $0.1 \text{ mA}\cdot\text{cm}^{-2}$  for different CuSCN-coated TPCSs conditions ( $200 \text{ mC}\cdot\text{cm}^{-2}$ ,  $400 \text{ mC}\cdot\text{cm}^{-2}$ ,  $600 \text{ mC}\cdot\text{cm}^{-2}$  charged passed during CuSCN electrodeposition). In Figure S5.4(a,d) we can see that the fibers are well-coated with 300 nm-thick  $\text{Cu}_2\text{O}$  cubes and no CuSCN underlayer is present, as it was previously shown in chapter 3. In Figure S5.4(b-f), by changing the CuSCN layer thickness and nanorod density but maintaining the same  $\text{Cu}_2\text{O}$  deposition time and current density (e.g. 100 min at  $0.1 \text{ mA}\cdot\text{cm}^{-2}$ ), we demonstrated an enhancement of the  $\text{Cu}_2\text{O}$  film thickness, to 450 nm (CuSCN 5 min) and 730 nm (CuSCN 10min). This result confirms that CuSCN undergoes an *in-situ* electroconversion, as no CuSCN nanorods is visible on the SEM image and the increase of the CuSCN film thickness leads to an increase of the  $\text{Cu}_2\text{O}$  thickness (for the same amount of charge passed during  $\text{Cu}_2\text{O}$  deposition). For thick CuSCN film resulting in a 730 nm  $\text{Cu}_2\text{O}$  film,  $\text{Cu}_2\text{O}$  particles exhibits a truncated shape and seem to grow in a different orientation, but this is outside the scope of the project, so we did not investigate it more.



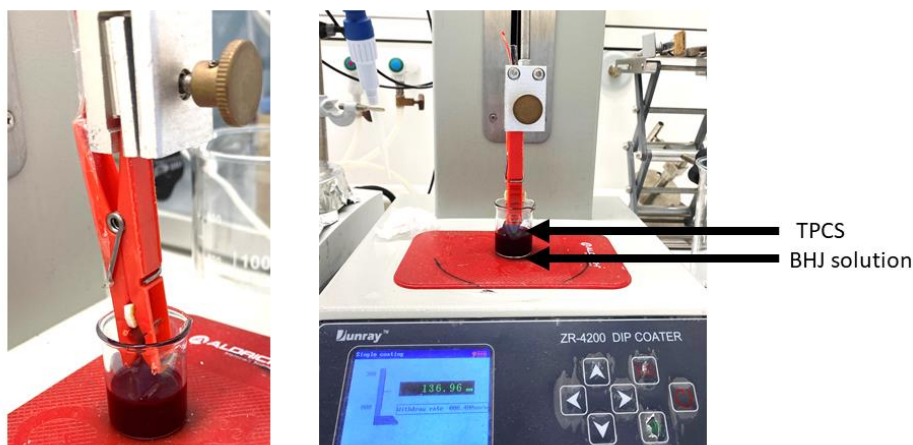
**Figure S5.4.** SEM images TPCSs ( $3\text{cm}^2$ ) after electrodeposition of varied time for CuSCN at  $-0.3\text{V}$  vs. Ag/AgCl, and 100min at  $0.1\text{mA}\cdot\text{cm}^{-2}$  for  $\text{Cu}_2\text{O}$  (a) CuSCN 5 min (b) CuSCN 10 min (c) CuSCN 15min.

Continuous investigation on TPCS-CuSCN (5 min) was performed using optimized chronopotentiometry conditions ( $-0.2\text{mA}\cdot\text{cm}^{-2}$  for 50 min). In order to gain some knowledge on the growth rate, we stopped the  $\text{Cu}_2\text{O}$  electrodeposition at different time points. In Figure S5.5, we can see that after 15 min the cubes are not totally formed, while after 50 min we obtained a homogenous coverage of  $\text{Cu}_2\text{O}$  cubes. The orange color of the samples is also more intense after 50min deposition compared to 15min.



**Figure S5.5** SEM images of CuSCN-coated TPCS (5min) after  $\text{Cu}_2\text{O}$  electrodepositon at  $-0.2\text{mA}\cdot\text{cm}^{-2}$  (a) after 15 min (b) after 50 min.

### ▪ BHJ-TPCS electrode

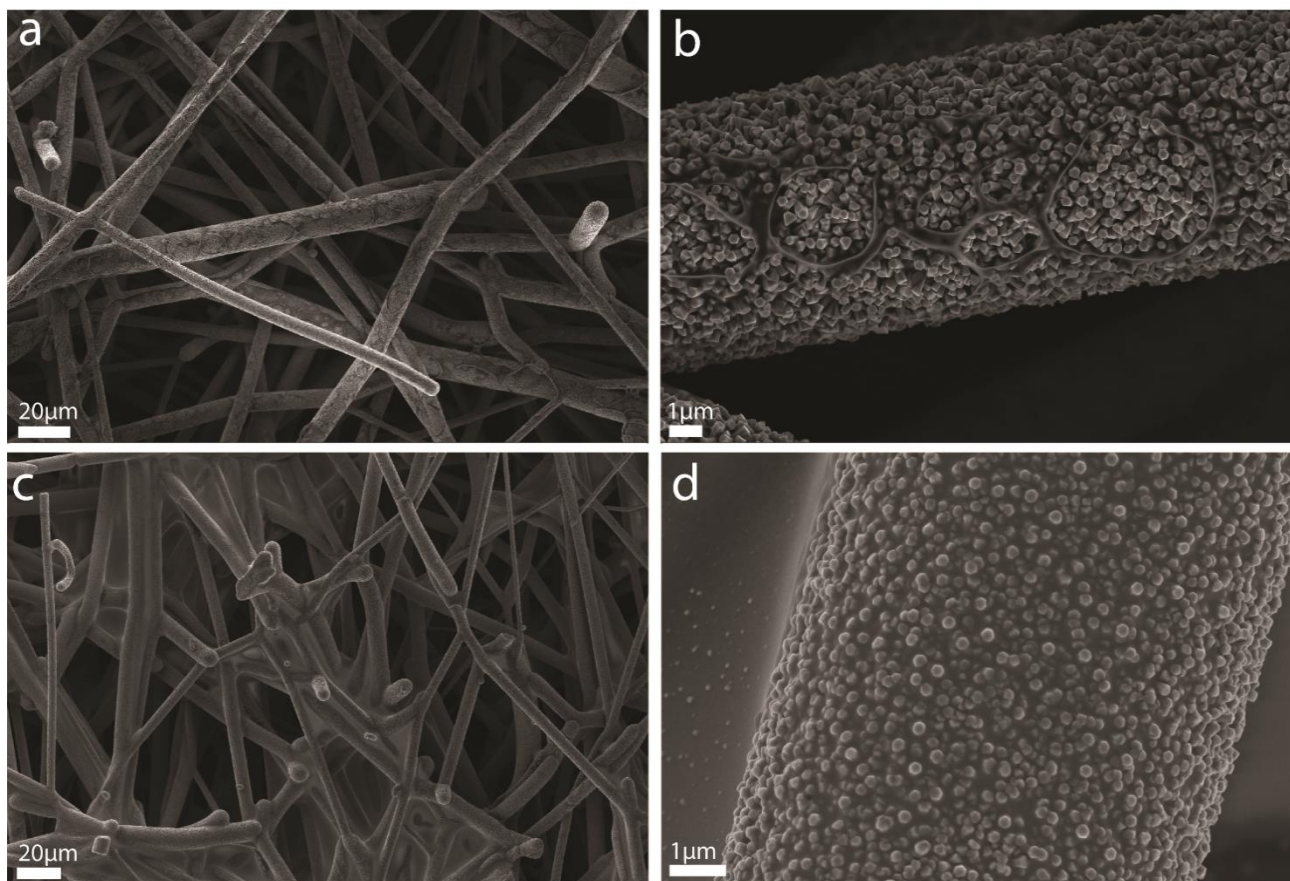


**Figure S5.6** Photograph of the automated dip-coating system

### Bulk heterojunction coating

A standard dip-coating system (see Appendix 5) is used to immerse vertically the electrode in the BHJ solution and to withdraw it at a constant rate. In the SEM images of the coated TPCSs (TPCS/CuSCN/BHJ) shown in Figure S5.7, we can see that we obtained a homogeneous BHJ coating with chlorobenzene, while with chloroform, we observed on some TPCS part, an inhomogeneous BHJ coverage with typical “coffee ring effect” due to the aggregation of the organic molecules near the contact line due to the evaporation-induced convective flow.<sup>183,195</sup>

The solvent plays an essential role, as it sets the evaporation rate and the film formation. Overall, dip-coating is a well-proven method with controllable setting such as withdrawal speed and relying on meniscus-guided theory.<sup>183</sup> The best homogeneity was obtained with a  $16 \text{ mg.mL}^{-1}$  BHJ solution in chlorobenzene and a withdrawal speed at  $60 \text{ mm min}^{-1}$ . Undoubtedly, further investigations could be done to determine the best conditions in terms of concentrations, withdrawal speed, temperature and solvent.



**Figure S5.7.** SEM pictures of TPCS-CuSCN-BHJ (a,b) dip-coated in chloroform (c,d) dip-coated in chlorobenzene.

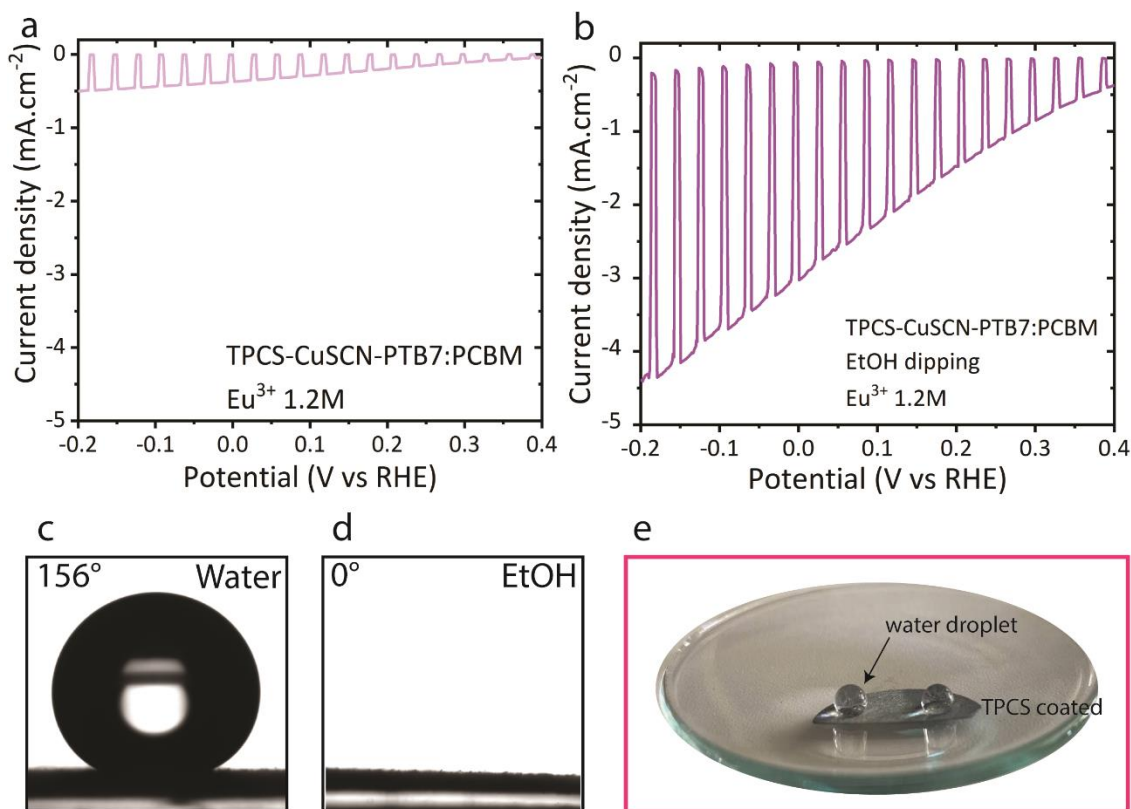
### Wettability impact

Despite the homogeneous BHJ coating demonstrated by the dip coating technique in chlorobenzene (Figure S5.8d), the photoelectrode performance in  $\text{Eu}^{3+}$  sacrificial electrolyte is low, exhibiting a photocurrent of  $-0.5 \text{ mA cm}^{-2}$  at 0V vs. RHE (Figure S5.8a).

However, one explanation for the poor performance was that the combination of the fibrous structure and the BHJ makes the electrode surface highly hydrophobic, as shown by the contact angle measurement (Figure S5.8c), which give a  $156^\circ$  as a contact angle with water. In the ideal case, the contact would be close to  $0^\circ$  representing the penetration of the electrolyte in the pores of the substrate. This indicates that it is difficult for the aqueous electrolyte to penetrate into the pores and to benefit from the entire substrate surface, as it can be seen in the photograph (Figure S5.8e) of the TPCS-CuSCN-BHJ in contact with water. By contrast, if the surface is fully wetted for example, when an alcohol such as ethanol or isopropanol is used (Figure S5.8d), the contact angle is  $0^\circ$ . Thus, we implemented an ethanol pre-wetting step enables the exposure of the entire fiber surface to the electrolyte, allowing us to increase the photocurrent to  $-3.5 \text{ mA.cm}^{-2}$  (Figure S5.8b).



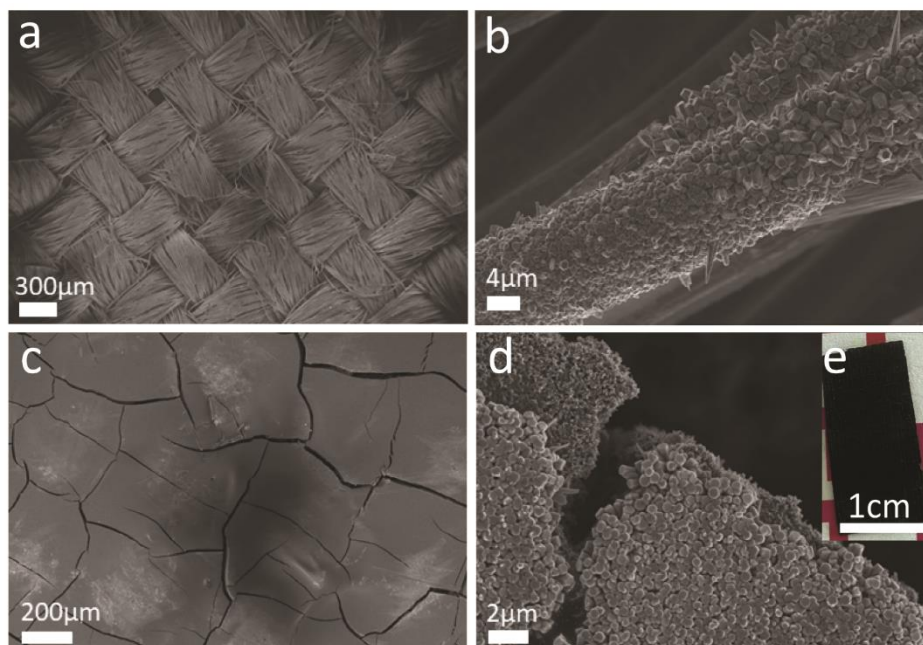
By increasing the surface of contact between the substrate and the liquid electrolyte, more material is available to reduce europium ions resulting in an increased photocurrent. On the other hand, to understand the behaviour of the electrode (surface and porosity) versus the liquid electrolyte, further investigation on the mass transport phenomenon and wettability impact would be required. In the view of the PEM-PEC operation of the electrode, the wettability could change and influence the final performance as it has been shown in the study of Iwata et al<sup>185</sup> where it was shown that the water splitting performance on porous electrodes is highly sensitive to the wettability.



**Figure S5.8.** Performance in sacrificial electrolyte (a) without pre-wetting (b) with EtOH pre-wetting (c,d) Contact angle measurement for TPCS-CuSCN-BHJ

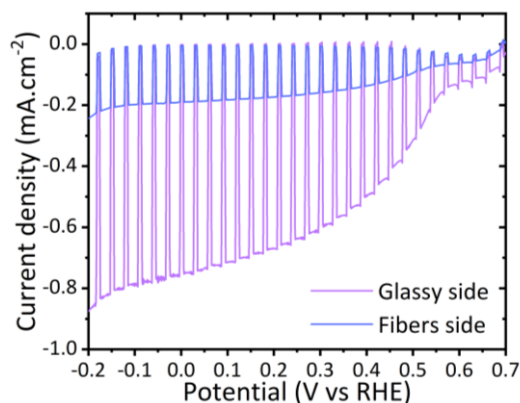
### Other types of porous substrates

CuSCN was coated on carbon cloth using the same parameters as TPCS. The carbon cloth exhibits two sides with diverse morphologies: fibrous and glassy. In Figure S5.9a,b, the carbon fibers are coated with CuSCN nanorods while in Figure S5.9c,d, the cracked structure (glassy side) is more homogenously coated. (e) photograph of the device Carbon cloth-CuSCN-BHJ.



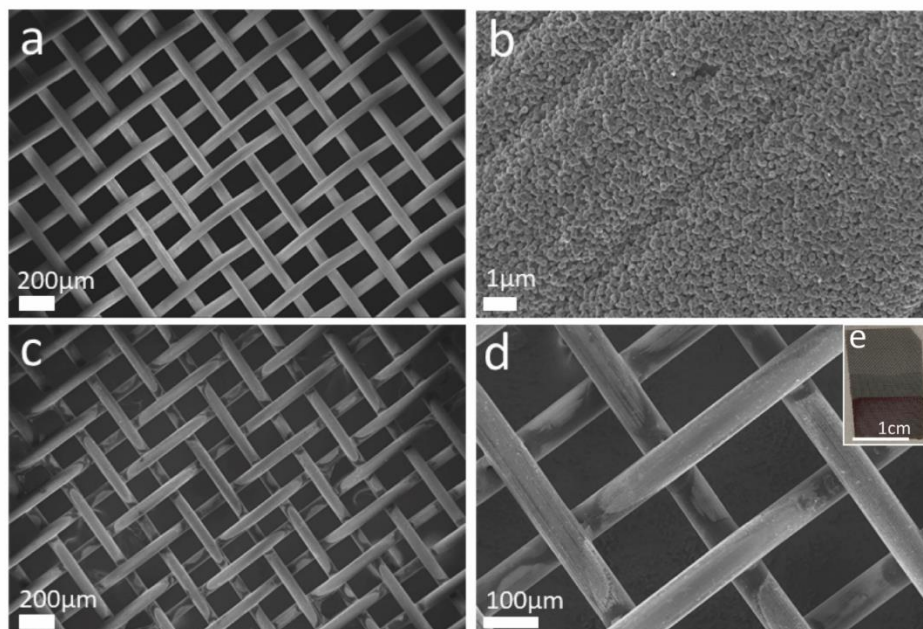
**Figure S5.9.** (a-d) SEM images and photograph of carbon cloth device, coated with CuSCN and BHJ (PBDTTTPD:PNDI(2HD)T) (e) photograph of the device Carbon cloth-CuSCN-BHJ.

The device with carbon cloth support exhibits photoactivity in sacrificial electrolyte ( $\text{Eu}^{3+}$ , 1.2M). The photocurrent is higher for the glassy side compared to the fibrous side (Figure S5.10). This difference could come from the CuSCN layer which seems more homogenously coated on the glassy side (Figure S5.9d) than on the fibrous side (Figure S5.9b). Overall, the device showed a photocurrent up to  $-0.75 \text{ mA.cm}^{-2}$  at 0 V vs. RHE.



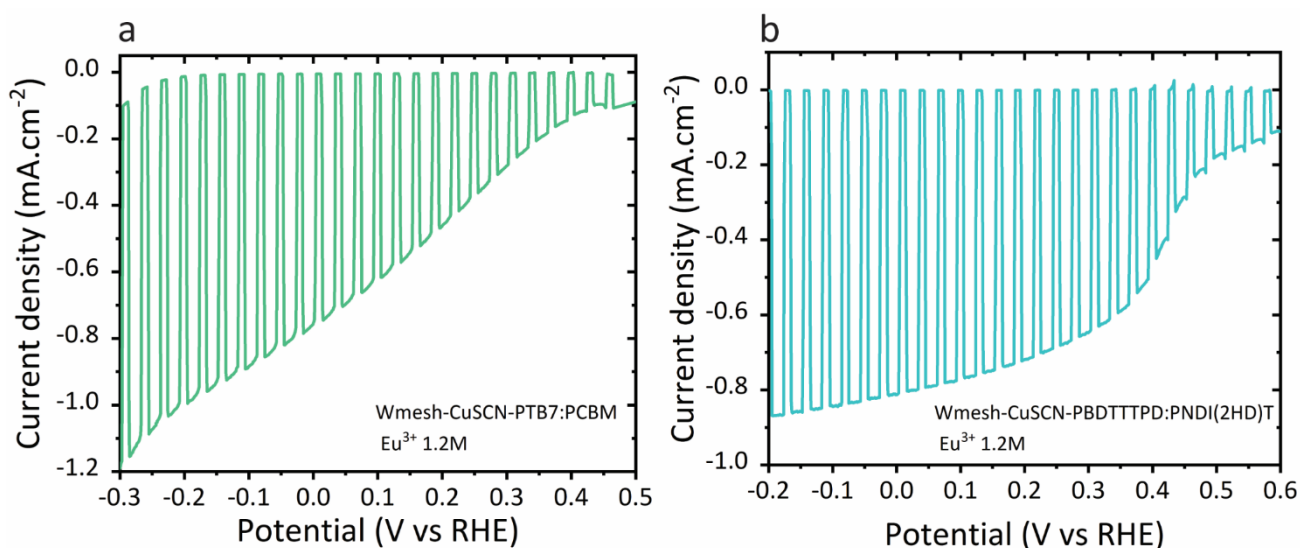
**Figure S5.10.** LSV curve under chopped (1 Sun) light illumination in  $\text{Eu}^{3+}$  1.2M of a device carbon cloth-CuSCN-(PBDTTTPD:PNDI(2HD)T).

The same device architecture was applied on W mesh substrates. In Figure S5.11a,b, we can see that the mesh is well coated with the CuSCN nanorods after electrodeposition. Following the same procedure than on TPCS, after dipping on the BHJ solution, the OS blend is clearly visible with dark spots on the mesh (Figure S5.11c-e) but does not seem uniformly coated.



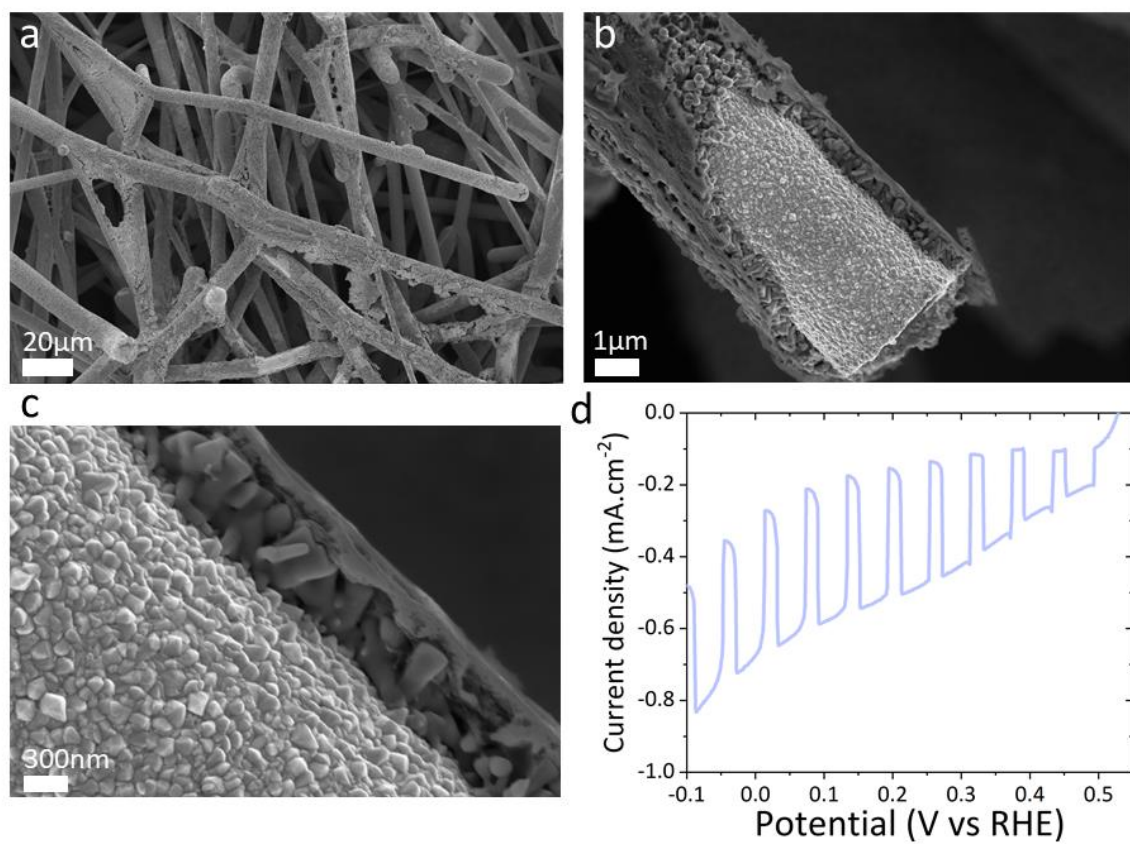
**Figure S5.11.** SEM images of CuSCN-coated W mesh (a-b) before BHJ coating (c-d) after BHJ coating (e) photograph of the device Wmesh-CuSCN-BHJ.

We fabricated the device with two BHJ blends, namely PTB7-Th:PCBM and PBDTTTPD:PNDI(2HD)T and tested the performance in sacrificial conditions. The devices exhibit a photocurrent of  $-0.8 \text{ mA} \cdot \text{cm}^{-2}$  at 0V vs. RHE for both PTB7-Th:PCBM and PBDTTTPD:PNDI(2HD)T (Figure S5.12).



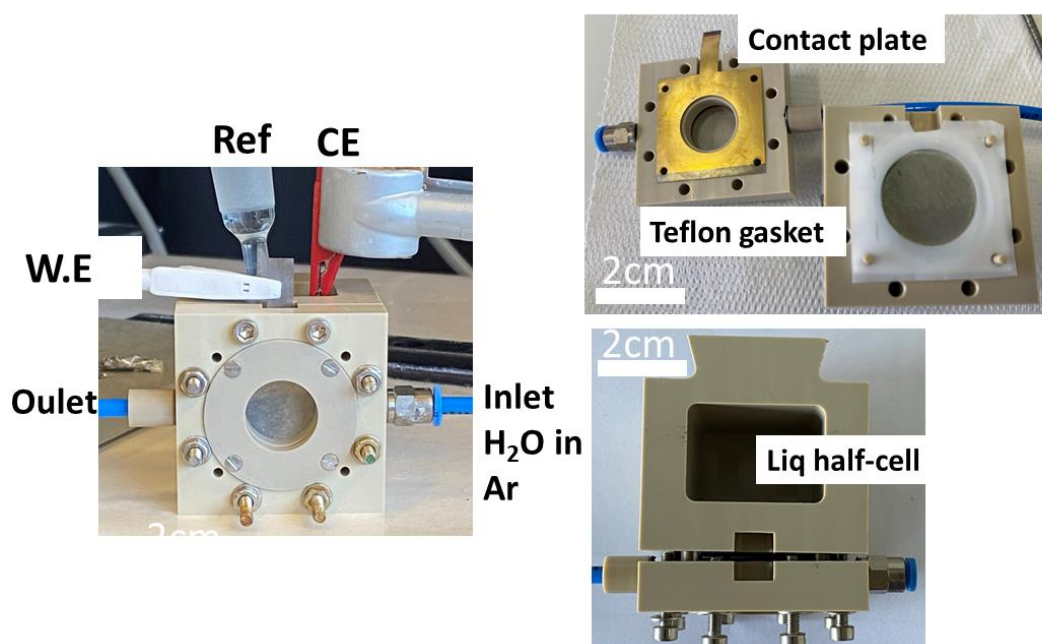
**Figure S5.12.** LSV curves under (1 Sun) chopped illumination, in  $\text{Eu}^{3+}$  (1.2M) for Wmesh-CuSCN-BHJ samples (a) BHJ is PTB7:PCBM (b) BHJ is PBDTTTPD:PNDI(2HD)T.

## Appendix 6

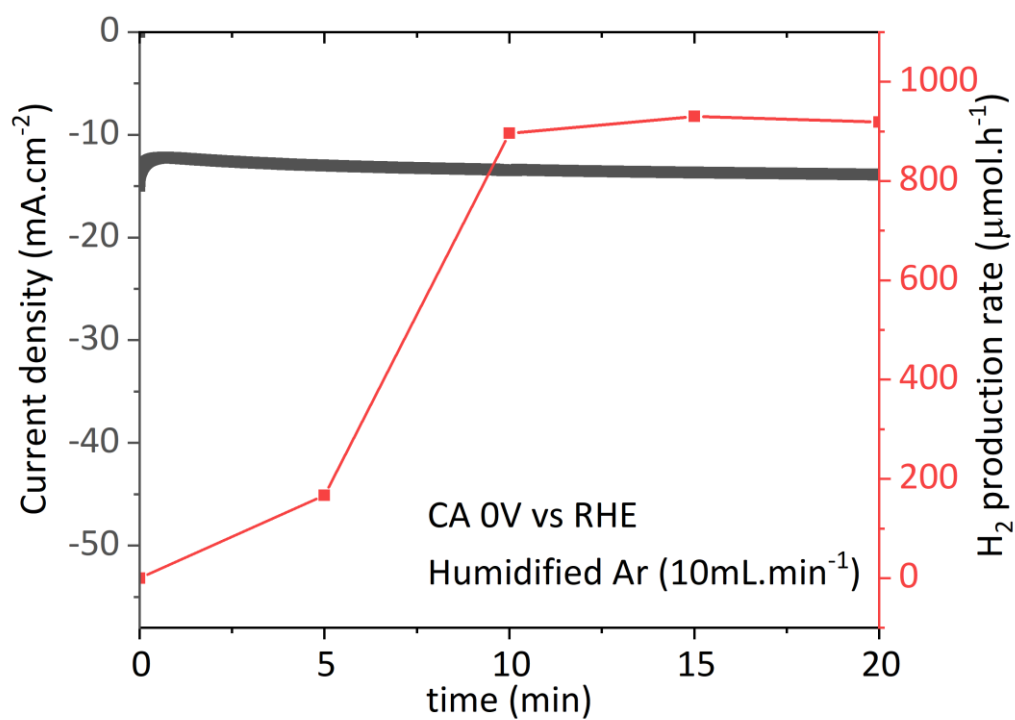


**Figure S6.1.** Characterization of the TPCS-CuSCN-BHJ-RuO<sub>2</sub> sample (a-c) SEM images (c) LSV curve in H<sub>2</sub>SO<sub>4</sub> pH 1 under intermittent (1 sun) light illumination.

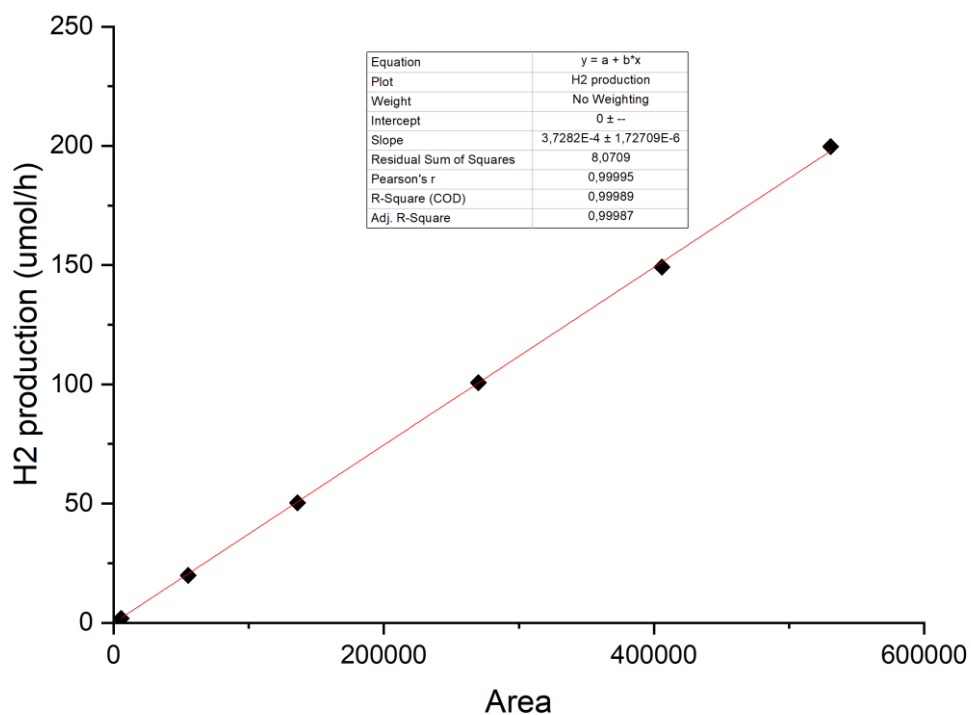




**Figure S6.2.** Half gas cell pictures



**Figure S6.3.** Half gas cell operation using a carbon cloth/Pt cathode, CA at 0V vs. RHE and H<sub>2</sub> production rate verified by GC (area tested 3.8cm<sup>2</sup>)



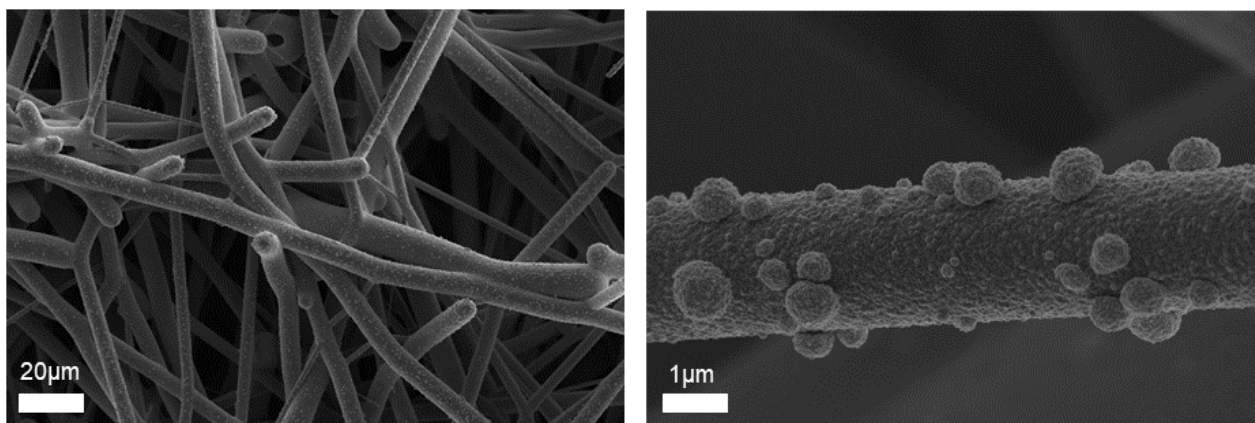
**Figure S6.4.** GC calibration curve for H<sub>2</sub> production

Calculation faradic efficiency:

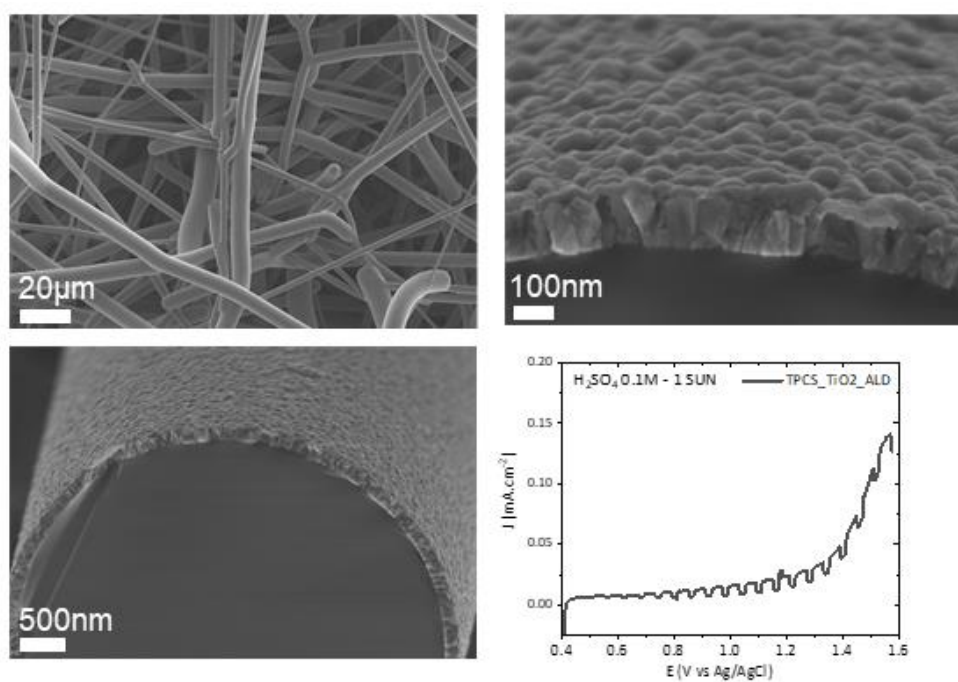
Using the calibration curve (Figure S6.4), for H<sub>2</sub> production on Pt, we assume a FE of 100%

18.66  $\mu\text{mol}$  of H<sub>2</sub>/h correspond to a current of 1mA

$\text{FE} = \mu\text{mol of H}_2 \text{ (measured by GC)} / (\text{Jph(measured)} \times 18.66)$



**Figure S6.5.** SEM images TPCS after Pt electrodeposition (60mC)



**Figure S6.6.** SEM images TPCS after TiO<sub>2</sub> deposition by ALD and LSV curve in H<sub>2</sub>SO<sub>4</sub> (0.1M) under intermittent (1 sun) light illumination.

# References

1. MIT News.
2. IPCC. *Sixth assesement report*. (2021).
3. The Global Carbon Project. *Report*. (2021).
4. BP Statistical Review of world Energy 2021. (2021).
5. J. K. Dawson. Prospects for hydrogen as an energy resource. *Nature* (1974).
6. <https://energies.airliquide.com/resources/planet-hydrogen-hydrogen>.
7. First there was hydrogen | Nature Chemistry. <https://www.nature.com/articles/nchem.2186>.
8. The Sun's Vital Statistics. <http://solar-center.stanford.edu/vitalstats.html>.
9. Spellman, F. R. & Stoudt, M. L. *Environmental Science: Principles and Practices*. (Scarecrow Press, 2013).
10. Agata Godula -Jopek. *Hydrogen Production by Electrolysis*. (2015).
11. Jiao, K. Designing the next generation of proton-exchange membrane fuel cells. *Nature* 9.
12. Lagadec, M. F. & Grimaud, A. Water electrolyzers with closed and open electrochemical systems. *Nat. Mater.* **19**, 1140–1150 (2020).
13. Formal, F. L., Bourée, W. S., Prévot, M. S. & Sivula, K. Challenges towards Economic Fuel Generation from Renewable Electricity: The Need for Efficient Electro-Catalysis. *Chim. Int. J. Chem.* **69**, 789–798 (2015).
14. Trattner, A., Höglinger, M., Macherhammer, M.-G. & Sartory, M. Renewable Hydrogen: Modular Concepts from Production over Storage to the Consumer. *Chem. Ing. Tech.* **93**, 706–716 (2021).
15. A. Hauch\*†, R. Küngas†, P. Blennow‡, A. B. Hansen‡, J. B. Hansen‡, B. V. Mathiesen‡, M. B. Mogensen. Recent advances in solid oxide cell technology for electrolysis. *Science*.
16. Miller, H. A. Green hydrogen from anion exchange membrane water electrolysis: a review of recent developments in critical materials and operating conditions. *Sustain. Energy* 20 (2020).

17. Carmo, M., Fritz, D. L., Mergel, J. & Stolten, D. A comprehensive review on PEM water electrolysis. *Int. J. Hydrog. Energy* **38**, 4901–4934 (2013).
18. Feng, Q. *et al.* A review of proton exchange membrane water electrolysis on degradation mechanisms and mitigation strategies. *J. Power Sources* **366**, 33–55 (2017).
19. Shiva Kumar, S. & Himabindu, V. Hydrogen production by PEM water electrolysis – A review. *Mater. Sci. Energy Technol.* **2**, 442–454 (2019).
20. A non-precious metal hydrogen catalyst in a commercial polymer electrolyte membrane electrolyser | Nature Nanotechnology. <https://www.nature.com/articles/s41565-019-0550-7>.
21. Stiber, S. *et al.* A high-performance, durable and low-cost proton exchange membrane electrolyser with stainless steel components. *Energy Environ. Sci.* **15**, 109–122 (2022).
22. Service, R. F. New electrolyzer splits water on the cheap. *Science* **367**, 1181–1181 (2020).
23. Lei, L., Tao, Z., Wang, X., Lemmon, J. P. & Chen, F. Intermediate-temperature solid oxide electrolysis cells with thin proton-conducting electrolyte and a robust air electrode. *J. Mater. Chem. A* **5**, 22945–22951 (2017).
24. Perez, M. & Perez, R. A fundamental look at supply side energy reserves for the planet. **62**, 4 (2015).
25. Kim, J. H., Hansora, D., Sharma, P., Jang, J.-W. & Lee, J. S. Toward practical solar hydrogen production – an artificial photosynthetic leaf-to-farm challenge. *Chem. Soc. Rev.* **48**, 1908–1971 (2019).
26. Polman, A., Knight, M., Garnett, E. C., Ehrler, B. & Sinke, W. C. Photovoltaic materials: Present efficiencies and future challenges. *Science* **352**, aad4424 (2016).
27. Giménez, B. *Photoelectrochemical Solar Fuel Production*.
28. Andreani, L. C., Bozzola, A., Kowalczewski, P., Liscidini, M. & Redorici, L. Silicon solar cells: toward the efficiency limits. *Adv. Phys. X* **4**, 1548305 (2019).
29. <https://www.nrel.gov/pv/cell-efficiency.html>.

30. Best Research-Cell Efficiency Chart. <https://www.nrel.gov/pv/cell-efficiency.html>.
31. Geisz, J. F. *et al.* Six-junction III–V solar cells with 47.1% conversion efficiency under 143 Suns concentration. *Nat. Energy* **5**, 326–335 (2020).
32. Wang, Q., Pornrungrroj, C., Linley, S. & Reisner, E. Strategies to improve light utilization in solar fuel synthesis. *Nat. Energy* (2021) doi:10.1038/s41560-021-00919-1.
33. Roger, I., Shipman, M. A. & Symes, M. D. Earth-abundant catalysts for electrochemical and photoelectrochemical water splitting. *Nat. Rev. Chem.* **1**, 0003 (2017).
34. Sivula, K. & van de Krol, R. Semiconducting materials for photoelectrochemical energy conversion. *Nat. Rev. Mater.* **1**, 15010 (2016).
35. Jiang, C., A. Moniz, S. J., Wang, A., Zhang, T. & Tang, J. Photoelectrochemical devices for solar water splitting – materials and challenges. *Chem. Soc. Rev.* **46**, 4645–4660 (2017).
36. Kudo, A. & Miseki, Y. Heterogeneous photocatalyst materials for water splitting. *Chem. Soc. Rev.* **38**, 253–278 (2008).
37. Hisatomi, T., Kubota, J. & Domen, K. Recent advances in semiconductors for photocatalytic and photoelectrochemical water splitting. *Chem. Soc. Rev.* **43**, 7520–7535 (2014).
38. Rongé, J. *et al.* Monolithic cells for solar fuels. *Chem. Soc. Rev.* **43**, 7963–7981 (2014).
39. Joost Manassen, David Cahen & Gary Hodes. Electrochemical, solid state, photochemical and technological aspects of photoelectrochemical energy converters. *Nature* (1976).
40. Rongé, J. *et al.* Solar Hydrogen Reaching Maturity. *Oil Gas Sci. Technol. – Rev. D’IFP Energ. Nouv.* **70**, 863–876 (2015).
41. Shaner, M. R., Atwater, H. A., Lewis, N. S. & McFarland, E. W. A comparative technoeconomic analysis of renewable hydrogen production using solar energy. *Energy Environ. Sci.* **9**, 2354–2371 (2016).

- 
42. Pinaud, B. A. *et al.* Technical and economic feasibility of centralized facilities for solar hydrogen production via photocatalysis and photoelectrochemistry. *Energy Environ. Sci.* **6**, 1983–2002 (2013).
  43. Jia, J. *et al.* Solar water splitting by photovoltaic-electrolysis with a solar-to-hydrogen efficiency over 30%. *Nat. Commun.* **7**, (2016).
  44. Cheng, W.-H. *et al.* Monolithic Photoelectrochemical Device for Direct Water Splitting with 19% Efficiency. *ACS Energy Lett.* **3**, 1795–1800 (2018).
  45. Liu, J. *et al.* Metal-free efficient photocatalyst for stable visible water splitting via a two-electron pathway. *Science* (2015) doi:10.1126/science.aaa3145.
  46. Nowotny, J. *et al.* Sustainable practices: Solar hydrogen fuel and education program on sustainable energy systems. *Int. J. Hydrog. Energy* **39**, 4151–4157 (2014).
  47. Fujishima, A. & Honda, K. Electrochemical Photolysis of Water at a Semiconductor Electrode. *Nature* **238**, 37–38 (1972).
  48. Pan, L. *et al.* Boosting the performance of Cu<sub>2</sub>O photocathodes for unassisted solar water splitting devices. *Nat. Catal.* **1**, 412–420 (2018).
  49. Wang, Q. & Domen, K. Particulate Photocatalysts for Light-Driven Water Splitting: Mechanisms, Challenges, and Design Strategies. *Chem. Rev.* **120**, 919–985 (2020).
  50. Schrauzer, G. N. & Guth, T. D. Photolysis of Water and Photoreduction of Nitrogen on Titanium Dioxide. *J. Am. Chem. Soc.* **99**, 7189–7193 (1977).
  51. Maeda, K. *et al.* Photocatalyst releasing hydrogen from water. *Nature* **440**, 295–295 (2006).
  52. Chen, S., Takata, T. & Domen, K. Particulate photocatalysts for overall water splitting. *Nat. Rev. Mater.* **2**, 17050 (2017).
  53. Nishiyama, H. *et al.* Photocatalytic solar hydrogen production from water on a 100-m<sup>2</sup> scale. *Nature* **598**, 304–307 (2021).



54. Kosco, J. *et al.* Enhanced photocatalytic hydrogen evolution from organic semiconductor heterojunction nanoparticles. *Nat. Mater.* **19**, 559–565 (2020).
55. Nocera, D. G. Solar Fuels and Solar Chemicals Industry. *Acc. Chem. Res.* **50**, 616–619 (2017).
56. Luan, P. & Zhang, J. Stepping towards Solar Water Splitting: Recent Progress in Bismuth Vanadate Photoanodes. *ChemElectroChem* **6**, 3227–3243 (2019).
57. Enhancing long-term photostability of BiVO<sub>4</sub> photoanodes for solar water splitting by tuning electrolyte composition | Nature Energy. <https://www.nature.com/articles/s41560-017-0057-0>.
58. Steier, L. *et al.* Understanding the Role of Underlayers and Overlayers in Thin Film Hematite Photoanodes. *Adv. Funct. Mater.* **24**, 7681–7688 (2014).
59. Steier, L. *et al.* Low-Temperature Atomic Layer Deposition of Crystalline and Photoactive Ultrathin Hematite Films for Solar Water Splitting. *ACS Nano* **9**, 11775–11783 (2015).
60. Le Formal, F., Grätzel, M. & Sivula, K. Controlling Photoactivity in Ultrathin Hematite Films for Solar Water-Splitting. *Adv. Funct. Mater.* **20**, 1099–1107 (2010).
61. Le Formal, F. *et al.* Passivating surface states on water splitting hematite photoanodes with alumina overlayers. *Chem. Sci.* **2**, 737–743 (2011).
62. Le Formal, F. *et al.* Rate Law Analysis of Water Oxidation on a Hematite Surface. *J. Am. Chem. Soc.* **137**, 6629–6637 (2015).
63. Yao, L., Rahmanudin, A., Guijarro, N. & Sivula, K. Organic Semiconductor Based Devices for Solar Water Splitting. *Adv. Energy Mater.* **8**, 1802585 (2018).
64. Kirner, J. T. & Finke, R. G. Water-oxidation photoanodes using organic light-harvesting materials: a review. *J. Mater. Chem. A* **5**, 19560–19592 (2017).
65. Sekar, A. & Sivula, K. Organic Semiconductors as Photoanodes for Solar-driven Photoelectrochemical Fuel Production. *Chim. Int. J. Chem.* **75**, 169–179 (2021).
66. Cho, H.-H. *et al.* A semiconducting polymer bulk heterojunction photoanode for solar water oxidation. *Nat. Catal.* **4**, 431–438 (2021).

- 
67. Yu, X. & Sivula, K. Layered 2D semiconducting transition metal dichalcogenides for solar energy conversion. *Curr. Opin. Electrochem.* **2**, 97–103 (2017).
  68. Bagal, I. V. *et al.* Cu<sub>2</sub>O as an emerging photocathode for solar water splitting - A status review. *Int. J. Hydrog. Energy* **44**, 21351–21378 (2019).
  69. Li, C., He, J., Xiao, Y., Li, Y. & Delaunay, J.-J. Earth-abundant Cu-based metal oxide photocathodes for photoelectrochemical water splitting. *Energy Environ. Sci.* **13**, 3269–3306 (2020).
  70. Bellani, S., Antognazza, M. R. & Bonaccorso, F. Carbon-Based Photocathode Materials for Solar Hydrogen Production. *Adv. Mater.* **31**, 1801446 (2019).
  71. Steier, L. & Holliday, S. A bright outlook on organic photoelectrochemical cells for water splitting. *J. Mater. Chem. A* **6**, 21809–21826 (2018).
  72. R.F. Frindt. The optical properties of single crystals of WSe<sub>2</sub> and MoTe<sub>2</sub>. *J. Phys. Chem.* **24**, 1107–1112 (1963).
  73. Mahalu, D., Jakubowicz, A., Wold, A. & Tenne, R. Passivation of recombination centers on the WSe<sub>2</sub> surface. *Phys. Rev. B* **38**, 1533–1536 (1988).
  74. Gobrecht, J., Gerischer, H. & Tributsch, H. Electrochemical Solar Cell Based on the d-Band Semiconductor Tungsten-Diselenide. *Berichte Bunsenges. Für Phys. Chem.* **82**, 1331–1335 (1978).
  75. McKone, J. R., Pieterick, A. P., Gray, H. B. & Lewis, N. S. Hydrogen Evolution from Pt/Ru-Coated p-Type WSe<sub>2</sub> Photocathodes. *J. Am. Chem. Soc.* **135**, 223–231 (2013).
  76. Yu, X., Prévot, M. S., Guijarro, N. & Sivula, K. Self-assembled 2D WSe<sub>2</sub> thin films for photoelectrochemical hydrogen production. *Nat. Commun.* **6**, 7596 (2015).
  77. Yu, X. & Sivula, K. Photogenerated Charge Harvesting and Recombination in Photocathodes of Solvent-Exfoliated WSe<sub>2</sub>. *Chem. Mater.* **29**, 6863–6875 (2017).

78. Yu, X., Guijarro, N., Johnson, M. & Sivula, K. Defect Mitigation of Solution-Processed 2D WSe<sub>2</sub> Nanoflakes for Solar-to-Hydrogen Conversion. *Nano Lett.* **18**, 215–222 (2018).
79. Paracchino, A., Laporte, V., Sivula, K., Grätzel, M. & Thimsen, E. Highly active oxide photocathode for photoelectrochemical water reduction. *Nat. Mater.* **10**, 456–461 (2011).
80. Paracchino, A. *et al.* Ultrathin films on copper(i) oxide water splitting photocathodes: a study on performance and stability. *Energy Environ. Sci.* **5**, 8673 (2012).
81. Tilley, S. D., Schreier, M., Azevedo, J., Stefik, M. & Graetzel, M. Ruthenium Oxide Hydrogen Evolution Catalysis on Composite Cuprous Oxide Water-Splitting Photocathodes. *Adv. Funct. Mater.* **24**, 303–311 (2014).
82. Steier, L. *et al.* Stabilizing organic photocathodes by low-temperature atomic layer deposition of TiO<sub>2</sub>. *Sustain. Energy Fuels* **1**, 1915–1920 (2017).
83. Shi, W. *et al.* PTB7:PC61BM Bulk Heterojunction-Based Photocathodes for Efficient Hydrogen Production in Aqueous Solution. *Chem. Mater.* **31**, 1928–1935 (2019).
84. Shi, W. *et al.* Nonfullerene Bulk Heterojunction-Based Photocathodes for Highly Efficient Solar Hydrogen Production in Acidic and Neutral Solutions. *Adv. Funct. Mater.* **30**, 2003399 (2020).
85. Bourgeteau, T. *et al.* Enhancing the Performances of P3HT:PCBM–MoS<sub>3</sub>-Based H<sub>2</sub>-Evolving Photocathodes with Interfacial Layers. *ACS Appl. Mater. Interfaces* **7**, 16395–16403 (2015).
86. Distler, A. *et al.* The Effect of PCBM Dimerization on the Performance of Bulk Heterojunction Solar Cells. *Adv. Energy Mater.* **4**, 1300693 (2014).
87. Yao, L. *et al.* Establishing Stability in Organic Semiconductor Photocathodes for Solar Hydrogen Production. *J. Am. Chem. Soc.* **142**, 7795–7802 (2020).
88. Seger, B. & Kamat, P. V. Fuel Cell Geared in Reverse: Photocatalytic Hydrogen Production Using a TiO<sub>2</sub>/Nafion/Pt Membrane Assembly with No Applied Bias. *J. Phys. Chem. C* **113**, 18946–18952 (2009).

- 
89. Ampelli, C., Centi, G., Passalacqua, R. & Perathoner, S. Electrolyte-less design of PEC cells for solar fuels: Prospects and open issues in the development of cells and related catalytic electrodes. *Catal. Sci. Technol. Sustain. Energy* **259**, 246–258 (2016).
90. Rongé, J., Nijs, D., Kerkhofs, S., Masschaele, K. & Martens, J. A. Chronoamperometric study of membrane electrode assembly operation in continuous flow photoelectrochemical water splitting. *Phys. Chem. Chem. Phys.* **15**, 9315–9325 (2013).
91. Iwu, K. O., Galeckas, A., Kuznetsov, A. Yu. & Norby, T. Solid-state photoelectrochemical H<sub>2</sub> generation with gaseous reactants. *Electrochimica Acta* **97**, 320–325 (2013).
92. Xu, K., Chatzidakis, A. & Norby, T. Solid-state photoelectrochemical cell with TiO<sub>2</sub> nanotubes for water splitting. *Photochem. Photobiol. Sci.* **16**, 10–16 (2017).
93. Verbruggen, S. W. *et al.* Harvesting Hydrogen Gas from Air Pollutants with an Unbiased Gas Phase Photoelectrochemical Cell. *ChemSusChem* **10**, 1413–1418 (2017).
94. Ampelli, C., Centi, G., Passalacqua, R. & Perathoner, S. Synthesis of solar fuels by a novel photoelectrocatalytic approach. *Energy Environ. Sci.* **3**, 292–301 (2010).
95. Amano, F., Shintani, A., Mukohara, H., Hwang, Y.-M. & Tsurui, K. Photoelectrochemical Gas–Electrolyte–Solid Phase Boundary for Hydrogen Production From Water Vapor. *Front. Chem.* **6**, 598 (2018).
96. Stoll, T., Zafeiropoulos, G. & Tsampas, M. N. Solar fuel production in a novel polymeric electrolyte membrane photoelectrochemical (PEM-PEC) cell with a web of titania nanotube arrays as photoanode and gaseous reactants. *Int. J. Hydrog. Energy* **41**, 17807–17817 (2016).
97. Xiang, C. *et al.* Modeling, Simulation, and Implementation of Solar-Driven Water-Splitting Devices. *Angew. Chem. Int. Ed.* **55**, 12974–12988 (2016).
98. Stoll, T. *et al.* Visible-light-promoted gas-phase water splitting using porous WO<sub>3</sub>/BiVO<sub>4</sub> photoanodes. *Electrochem. Commun.* **82**, 47–51 (2017).

- 
99. Ta, C. X. M., Akamoto, C., Furusho, Y. & Amano, F. A Macroporous-Structured  $\text{WO}_3/\text{Mo}$ -Doped  $\text{BiVO}_4$  Photoanode for Vapor-Fed Water Splitting under Visible Light Irradiation. *ACS Sustain. Chem. Eng.* **8**, 9456–9463 (2020).
100. Zafeiropoulos, G. *et al.* Rational Design of Photoelectrodes for the Fully Integrated Polymer Electrode Membrane–Photoelectrochemical Water-Splitting System: A Case Study of Bismuth Vanadate. *ACS Appl. Energy Mater.* **4**, 9600–9610 (2021).
101. Amano, F., Mukohara, H., Sato, H. & Ohno, T. Photoelectrochemical water vapor splitting using an ionomer-coated rutile  $\text{TiO}_2$  thin layer on titanium microfiber felt as an oxygen-evolving photoanode. *Sustain. Energy Fuels* **3**, 2048–2055 (2019).
102. Amano, F., Mukohara, H., Shintani, A. & Tsurui, K. Solid Polymer Electrolyte-Coated Macroporous Titania Nanotube Photoelectrode for Gas-Phase Water Splitting. *ChemSusChem* **12**, 1925–1930 (2019).
103. Zafeiropoulos, G., Johnson, H., Kinge, S., van de Sanden, M. C. M. & Tsampas, M. N. Solar Hydrogen Generation from Ambient Humidity Using Functionalized Porous Photoanodes. *ACS Appl. Mater. Interfaces* **11**, 41267–41280 (2019).
104. Amano, F. *et al.* Vapor-fed photoelectrolysis of water at 0.3 V using gas-diffusion photoanodes of  $\text{SrTiO}_3$  layers. *Sustain. Energy Fuels* **4**, 1443–1453 (2020).
105. Xu, K. *et al.* Hydrogen from wet air and sunlight in a tandem photoelectrochemical cell. *Int. J. Hydrog. Energy* **44**, 587–593 (2019).
106. Zafeiropoulos, G. *et al.* Rational Design of Photoelectrodes for the Fully Integrated Polymer Electrode Membrane–Photoelectrochemical Water-Splitting System: A Case Study of Bismuth Vanadate. *ACS Appl. Energy Mater.* **4**, 9600–9610 (2021).
107. Spurgeon, J. M. & Lewis, N. S. Proton exchange membrane electrolysis sustained by water vapor. *Energy Environ. Sci.* **4**, 2993–2998 (2011).

- 
108. Yu, X., Prévot, M. S., Guijarro, N. & Sivula, K. Self-assembled 2D WSe<sub>2</sub> thin films for photoelectrochemical hydrogen production. *Nat. Commun.* **6**, (2015).
109. Yu, X. & Sivula, K. Photogenerated Charge Harvesting and Recombination in Photocathodes of Solvent-Exfoliated WSe<sub>2</sub>. *Chem. Mater.* **29**, 6863–6875 (2017).
110. Pan, L. *et al.* Cu<sub>2</sub>O photocathodes with band-tail states assisted hole transport for standalone solar water splitting. *Nat. Commun.* **11**, 318 (2020).
111. Zafeiropoulos, G., Johnson, H., Kinge, S., van de Sanden, M. C. M. & Tsampas, M. N. Solar Hydrogen Generation from Ambient Humidity Using Functionalized Porous Photoanodes. *ACS Appl. Mater. Interfaces* **11**, 41267–41280 (2019).
112. Omrani, R. Chapter 5 - Gas diffusion layer for proton exchange membrane fuel cells. in *PEM Fuel Cells* (ed. Kaur, G.) 91–122 (Elsevier, 2022). doi:10.1016/B978-0-12-823708-3.00017-1.
113. Sivula, K. & van de Krol, R. Semiconducting materials for photoelectrochemical energy conversion. *Nat. Rev. Mater.* **1**, 15010 (2016).
114. Zafeiropoulos, G. *et al.* Porous titania photoelectrodes built on a Ti-web of microfibers for polymeric electrolyte membrane photoelectrochemical (PEM-PEC) cell applications. *Sol. Energy Mater. Sol. Cells* **180**, 184–195 (2018).
115. Amano, F., Mukohara, H., Sato, H. & Ohno, T. Photoelectrochemical water vapor splitting using an ionomer-coated rutile TiO<sub>2</sub> thin layer on titanium microfiber felt as an oxygen-evolving photoanode. *Sustain. Energy Fuels* **3**, 2048–2055 (2019).
116. Amano, F., Shintani, A., Mukohara, H., Hwang, Y.-M. & Tsurui, K. Photoelectrochemical Gas–Electrolyte–Solid Phase Boundary for Hydrogen Production From Water Vapor. *Front. Chem.* **6**, (2018).
117. Amano, F. *et al.* Vapor-fed photoelectrolysis of water at 0.3 V using gas-diffusion photoanodes of SrTiO<sub>3</sub> layers. *Sustain. Energy Fuels* **4**, 1443–1453 (2020).

- 
118. Stoll, T. *et al.* Visible-light-promoted gas-phase water splitting using porous WO<sub>3</sub>/BiVO<sub>4</sub> photoanodes. *Electrochem. Commun.* **82**, 47–51 (2017).
119. Grundmann, M. Transparent Conductive Oxide Semiconductors. in *The Physics of Semiconductors: An Introduction Including Nanophysics and Applications* (ed. Grundmann, M.) 511–514 (Springer International Publishing, 2021). doi:10.1007/978-3-030-51569-0\_20.
120. Sivula, K. *et al.* Photoelectrochemical Water Splitting with Mesoporous Hematite Prepared by a Solution-Based Colloidal Approach. *J. Am. Chem. Soc.* **132**, 7436–7444 (2010).
121. Sivula, K., Le Formal, F. & Grätzel, M. Solar Water Splitting: Progress Using Hematite ( $\alpha$ -Fe<sub>2</sub>O<sub>3</sub>) Photoelectrodes. *ChemSusChem* **4**, 432–449 (2011).
122. Cesar, I., Sivula, K., Kay, A., Zboril, R. & Grätzel, M. Influence of Feature Size, Film Thickness, and Silicon Doping on the Performance of Nanostructured Hematite Photoanodes for Solar Water Splitting. *J. Phys. Chem. C* **113**, 772–782 (2009).
123. Brillet, J., Grätzel, M. & Sivula, K. Decoupling Feature Size and Functionality in Solution-Processed, Porous Hematite Electrodes for Solar Water Splitting. *Nano Lett.* **10**, 4155–4160 (2010).
124. Steier, L. *et al.* Low-Temperature Atomic Layer Deposition of Crystalline and Photoactive Ultrathin Hematite Films for Solar Water Splitting. *ACS Nano* **9**, 11775–11783 (2015).
125. Mesa, C. A. *et al.* Impact of the Synthesis Route on the Water Oxidation Kinetics of Hematite Photoanodes. *J. Phys. Chem. Lett.* **11**, 7285–7290 (2020).
126. Ringdalen, E. & Tangstad, M. Softening and Melting of SiO<sub>2</sub>, an Important Parameter for Reactions with Quartz in Si Production. in *Advances in Molten Slags, Fluxes, and Salts: Proceedings of the 10th International Conference on Molten Slags, Fluxes and Salts 2016* (eds. Reddy, R. G., Chaubal, P., Pistorius, P. C. & Pal, U.) 43–51 (Springer International Publishing, 2016). doi:10.1007/978-3-319-48769-4\_4.

- 
127. Fracture and Size Effect on Strength of Plain Concrete Disks under Biaxial Flexure Analyzed by Microplane Model M7 | Journal of Engineering Mechanics | Vol 140, No 3. <https://ascelibrary.org/doi/10.1061/%28ASCE%29EM.1943-7889.0000683>.
128. Zi, G., Oh, H. & Park, S.-K. A novel indirect tensile test method to measure the biaxial tensile strength of concretes and other quasibrittle materials. *Cem. Concr. Res.* **38**, 751–756 (2008).
129. Moholkar, A. V., Pawar, S. M., Rajpure, K. Y., Bhosale, C. H. & Kim, J. H. Effect of fluorine doping on highly transparent conductive spray deposited nanocrystalline tin oxide thin films. *Appl. Surf. Sci.* **255**, 9358–9364 (2009).
130. Malik, O., Hidalgo-Wade, F. J. D. la & Amador, R. R. Fluorine-doped tin oxide films with a high figure of merit fabricated by spray pyrolysis. *J. Mater. Res.* **30**, 2040–2045 (2015).
131. Kim, K. H. & Chun, J. S. X-ray studies of SnO<sub>2</sub> prepared by chemical vapour deposition. *Thin Solid Films* **141**, 287–295 (1986).
132. Thibaut de Terris, Olivier Andreau, Patrice Peyre, Frédéric Adamski, Imade & Koutiri, Cyril Gorny, Corinne Dupuy. Optimization and comparison of porosity rate measurement methods of Selective Laser Melted metallic parts. in doi:Additive Manufacturing, Elsevier, 2019, 28, pp.802-813.
133. Respati, S. M. B. *et al.* The effect of palm fibers addition on density, porosity, water discharge and TDS of the natural zeolite ceramic. in 030007 (2018). doi:10.1063/1.5042927.
134. Majumdar, P., Singh, S. B. & Chakraborty, M. Elastic modulus of biomedical titanium alloys by nano-indentation and ultrasonic techniques—A comparative study. *Mater. Sci. Eng. A* **489**, 419–425 (2008).
135. Duret, A. Mesoscopic Thin Films of Hematite as Photoanode for Water Photoelectrolysis. (2005) doi:10.5075/epfl-thesis-3203.
136. Spray, R. L. & Choi, K.-S. Photoactivity of Transparent Nanocrystalline Fe<sub>2</sub>O<sub>3</sub> Electrodes Prepared via Anodic Electrodeposition. *Chem. Mater.* **21**, 3701–3709 (2009).



- 
137. Kleiman-Shwarscstein, A. *et al.* Electrodeposited Aluminum-Doped  $\alpha$ -Fe<sub>2</sub>O<sub>3</sub> Photoelectrodes: Experiment and Theory. *Chem. Mater.* **22**, 510–517 (2010).
138. Sivula, K., Formal, F. L. & Grätzel, M. WO<sub>3</sub>–Fe<sub>2</sub>O<sub>3</sub> Photoanodes for Water Splitting: A Host Scaffold, Guest Absorber Approach. *Chem. Mater.* **21**, 2862–2867 (2009).
139. Liu, Y., Le Formal, F., Boudoire, F. & Guijarro, N. Hematite Photoanodes for Solar Water Splitting: A Detailed Spectroelectrochemical Analysis on the pH-Dependent Performance. *ACS Appl Energy Mater* **2**, 6825–6833 (2019).
140. Yang, J. *et al.* Enhanced Performance of Photoelectrochemical Water Splitting with ITO@ $\alpha$ -Fe<sub>2</sub>O<sub>3</sub> Core–Shell Nanowire Array as Photoanode. *ACS Appl. Mater. Interfaces* **7**, 26482–26490 (2015).
141. Lin, Y., Zhou, S., Sheehan, S. W. & Wang, D. Nanonet-Based Hematite Heteronanostructures for Efficient Solar Water Splitting. *J. Am. Chem. Soc.* **133**, 2398–2401 (2011).
142. Bondarchuk, A. N., Corrales-Mendoza, I., Tomás, S. A. & Marken, F. A hematite photoelectrode grown on porous and conductive SnO<sub>2</sub> ceramics for solar-driven water splitting. *Int. J. Hydrog. Energy* **44**, 19667–19675 (2019).
143. Liu, Y. & Smith, R. D. L. Differentiating Defects and Their Influence on Hematite Photoanodes Using X-ray Absorption Spectroscopy and Raman Microscopy. *ACS Appl. Mater. Interfaces* **14**, 6615–6624 (2022).
144. Ling, Y. & Li, Y. Review of Sn-Doped Hematite Nanostructures for Photoelectrochemical Water Splitting. *Part. Part. Syst. Charact.* **31**, 1113–1121 (2014).
145. Van, M., AMB (Ton). Chemical vapour deposition of tin oxide thin films. (2003) doi:10.6100/IR569472.
146. Chae, Y., Houf, W. G., McDaniel, A. H., Troup, J. & Allendorf, M. D. Stagnation Flow Reactor Investigation of Tin Oxide CVD from Monobutyltin Trichloride. *J. Electrochem. Soc.* **151**, C527 (2004).

- 
147. McKone, J. R., Pieterick, A. P., Gray, H. B. & Lewis, N. S. Hydrogen Evolution from Pt/Ru-Coated p-Type WSe<sub>2</sub> Photocathodes. *J. Am. Chem. Soc.* **135**, 223–231 (2013).
148. Yu, X. & Sivula, K. Toward Large-Area Solar Energy Conversion with Semiconducting 2D Transition Metal Dichalcogenides. *ACS Energy Lett.* **1**, 315–322 (2016).
149. Manzeli, S., Ovchinnikov, D., Pasquier, D., Yazyev, O. V. & Kis, A. 2D transition metal dichalcogenides. *Nat. Rev. Mater.* **2**, (2017).
150. Mak, K. F., Lee, C., Hone, J., Shan, J. & Heinz, T. F. Atomically Thin MoS<sub>2</sub>: A New Direct-Gap Semiconductor. *Phys. Rev. Lett.* **105**, (2010).
151. Radisavljevic, B., Radenovic, A., Brivio, J., Giacometti, V. & Kis, A. Single-layer MoS<sub>2</sub> transistors. *Nat. Nanotechnol.* **6**, 147–150 (2011).
152. Samadi, M. *et al.* Group 6 transition metal dichalcogenide nanomaterials: synthesis, applications and future perspectives. *Nanoscale Horiz.* **3**, 90–204 (2018).
153. Velický, M. & Toth, P. S. From two-dimensional materials to their heterostructures: An electrochemist's perspective. *Appl. Mater. Today* **8**, 68–103 (2017).
154. Kang, J., Tongay, S., Zhou, J., Li, J. & Wu, J. Band offsets and heterostructures of two-dimensional semiconductors. *Appl. Phys. Lett.* **102**, 012111 (2013).
155. Cabrera, C. R. & Abrufia, H. D. Synthesis and Photoelectrochemistry of Polycrystalline Thin Films of p-WSe<sub>2</sub>, p-WS<sub>2</sub>, and p-MoSe<sub>2</sub>. **135**, 7 (1988).
156. Yu, X. & Sivula, K. Photogenerated Charge Harvesting and Recombination in Photocathodes of Solvent-Exfoliated WSe<sub>2</sub>. *Chem. Mater.* **29**, 6863–6875 (2017).
157. Jawaid, A. *et al.* Mechanism for Liquid Phase Exfoliation of MoS<sub>2</sub>. *Chem. Mater.* **28**, 337–348 (2016).
158. Jawaid, A. *et al.* Redox Exfoliation of Layered Transition Metal Dichalcogenides. *ACS Nano* **11**, 635–646 (2017).

159. Gupta, A., Arunachalam, V. & Vasudevan, S. Liquid-Phase Exfoliation of MoS<sub>2</sub> Nanosheets: The Critical Role of Trace Water. *J. Phys. Chem. Lett.* **7**, 4884–4890 (2016).
160. Manna, K., Huang, H.-N., Li, W.-T., Ho, Y.-H. & Chiang, W.-H. Toward Understanding the Efficient Exfoliation of Layered Materials by Water-Assisted Cosolvent Liquid-Phase Exfoliation. *Chem. Mater.* **28**, 7586–7593 (2016).
161. Backes, C. *et al.* Guidelines for Exfoliation, Characterization and Processing of Layered Materials Produced by Liquid Exfoliation. *Chem. Mater.* **29**, 243–255 (2017).
162. Yau, H. C., Bayazit, M. K., Steinke, J. H. G. & Shaffer, M. S. P. Sonochemical degradation of N-methylpyrrolidone and its influence on single walled carbon nanotube dispersion. *Chem. Commun.* **51**, 16621–16624 (2015).
163. Ogilvie, S. P. *et al.* Considerations for spectroscopy of liquid-exfoliated 2D materials: emerging photoluminescence of N-methyl-2-pyrrolidone. *Sci. Rep.* **7**, (2017).
164. Divigalpitiya, W. M. R., Frindt, R. F. & Morrison, S. R. Inclusion Systems of Organic Molecules in Restacked Single-Layer Molybdenum Disulfide. *Science* **246**, 369–371 (1989).
165. Salavagione, H. J. *et al.* Identification of high performance solvents for the sustainable processing of graphene. *Green Chem.* **19**, 2550–2560 (2017).
166. Yu, X., Guijarro, N., Johnson, M. & Sivula, K. Defect Mitigation of Solution-Processed 2D WSe<sub>2</sub> Nanoflakes for Solar-to-Hydrogen Conversion. *Nano Lett.* **18**, 215–222 (2018).
167. Yoon, M.-H., Yan, H., Facchetti, A. & Marks, T. J. Low-Voltage Organic Field-Effect Transistors and Inverters Enabled by Ultrathin Cross-Linked Polymers as Gate Dielectrics. *J. Am. Chem. Soc.* **127**, 10388–10395 (2005).
168. Liu, Y. *et al.* 3D Binder-free MoSe<sub>2</sub> Nanosheets/Carbon Cloth Electrodes for Efficient and Stable Hydrogen Evolution Prepared by Simple Electrophoresis Deposition Strategy. *Sci. Rep.* **6**, 22516 (2016).

169. Bhattacharjee, S. DLS and zeta potential – What they are and what they are not? *J. Controlled Release* **235**, 337–351 (2016).
170. Yu, X., Prévot, M. S., Guijarro, N. & Sivula, K. Self-assembled 2D WSe<sub>2</sub> thin films for photoelectrochemical hydrogen production. *Nat. Commun.* **6**, (2015).
171. Luo, J. *et al.* Cu<sub>2</sub>O Nanowire Photocathodes for Efficient and Durable Solar Water Splitting. *Nano Lett.* **16**, 1848–1857 (2016).
172. Polymer Photovoltaic Cells: Enhanced Efficiencies via a Network of Internal Donor-Acceptor Heterojunctions. <https://www.science.org/doi/abs/10.1126/science.270.5243.1789>.
173. Wang, G., Melkonyan, F. S., Facchetti, A. & Marks, T. J. All-Polymer Solar Cells: Recent Progress, Challenges, and Prospects. *Angew. Chem. Int. Ed.* **58**, 4129–4142 (2019).
174. Yao, L. *et al.* Establishing Stability in Organic Semiconductor Photocathodes for Solar Hydrogen Production. *J. Am. Chem. Soc.* **142**, 7795–7802 (2020).
175. Rojas, H. C. *et al.* All Solution-Processed, Hybrid Organic–Inorganic Photocathode for Hydrogen Evolution. *ACS Omega* **2**, 3424–3431 (2017).
176. Bronstein, H., Nielsen, C. B., Schroeder, B. C. & McCulloch, I. The role of chemical design in the performance of organic semiconductors. *Nat. Rev. Chem.* **4**, 66–77 (2020).
177. Fan, R. *et al.* Enhanced performance of polymer solar cells based on PTB7-Th:PC71BM by doping with 1-bromo-4-nitrobenzene. *J. Mater. Chem. C* **5**, 10985–10990 (2017).
178. Cheng, P. & Zhan, X. Stability of organic solar cells: challenges and strategies. *Chem. Soc. Rev.* **45**, 2544–2582 (2016).
179. Gasparini, N. *et al.* Burn-in Free Nonfullerene-Based Organic Solar Cells. *Adv. Energy Mater.* **7**, 1700770 (2017).
180. Bozheyev, F., Harbauer, K., Zahn, C., Friedrich, D. & Ellmer, K. Highly (001)-textured p-type WSe<sub>2</sub> Thin Films as Efficient Large-Area Photocathodes for Solar Hydrogen Evolution. *Sci. Rep.* **7**, (2017).

- 
181. Bourgeteau, T. *et al.* All solution-processed organic photocathodes with increased efficiency and stability via the tuning of the hole-extracting layer. *J. Mater. Chem. A* **4**, 4831–4839 (2016).
182. Cohen, E. & Lightfoot, E. J. Coating Processes. in *Kirk-Othmer Encyclopedia of Chemical Technology* 1–68 (John Wiley & Sons, Ltd, 2011).  
doi:10.1002/0471238961.1921182203150805.a01.pub3.
183. Gu, X., Shaw, L., Gu, K., Toney, M. F. & Bao, Z. The meniscus-guided deposition of semiconducting polymers. *Nat. Commun.* **9**, 534 (2018).
184. Performance of polymer solar cells fabricated by dip coating process | Elsevier Enhanced Reader.  
<https://reader.elsevier.com/reader/sd/pii/S0927024811006830?token=D18D1F96D2602F99E0E517AEFCDA2F1D14371DDB8DBB1DDCA0231CA90BD3076158AF19923D6877B05C156909D99527F3&originRegion=eu-west-1&originCreation=20211119145918>  
doi:10.1016/j.solmat.2011.12.002.
185. Iwata, R. *et al.* Bubble growth and departure modes on wettable/non-wettable porous foams in alkaline water splitting. *Joule* **5**, 887–900 (2021).
186. Smolinka, T. PEM Water Electrolysis - Present Status of Research and Development. 23.
187. Bernt, M. *et al.* Current Challenges in Catalyst Development for PEM Water Electrolyzers. *Chem. Ing. Tech.* **92**, 31–39 (2020).
188. Aqoma, H. *et al.* 11% Organic Photovoltaic Devices Based on PTB7-Th: PC71BM Photoactive Layers and Irradiation-Assisted ZnO Electron Transport Layers. *Adv. Sci.* **5**, 1700858 (2018).
189. Erten-Ela, S. Characterization and Performance Evaluation of Dye Sensitized Solar Cell Using Nanostructured TiO<sub>2</sub> Electrode. *Int. J. Photoenergy* **2014**, e941213 (2014).
190. Rojas, H. C. *et al.* Polymer-based photocathodes with a solution-processable cuprous iodide anode layer and a polyethyleneimine protective coating. *Energy Env. Sci* **9**, 3710–3723 (2016).

191. Chou, S. S. *et al.* Ligand Conjugation of Chemically Exfoliated MoS<sub>2</sub>. *J. Am. Chem. Soc.* **135**, 4584–4587 (2013).
192. Gupta, A., Arunachalam, V. & Vasudevan, S. Water Dispersible, Positively and Negatively Charged MoS<sub>2</sub> Nanosheets: Surface Chemistry and the Role of Surfactant Binding. *J. Phys. Chem. Lett.* **6**, 739–744 (2015).
193. Sherwood, J. *et al.* Dihydrolevoglucosenone (Cyrene) as a bio-based alternative for dipolar aprotic solvents. *Chem Commun* **50**, 9650–9652 (2014).
194. Pan, K. *et al.* Sustainable production of highly conductive multilayer graphene ink for wireless connectivity and IoT applications. *Nat. Commun.* **9**, (2018).
195. Wang, W. *et al.* Controlled 2D growth of organic semiconductor crystals by suppressing “coffee-ring” effect. *Nano Res.* **13**, 2478–2484 (2020).

# Curriculum vitae

Marina Caretti, born on the 12<sup>th</sup> January 1992 in Belley (France)

caretti.marina@outlook.fr

## Education

2018-2022: **PhD Chemistry and Chemical engineering**

Ecole Polytechnique Fédérale de Lausanne EPFL

2015-2018: **Chemical Engineer – Bachelor and Master in Chemistry**

Ecole Nationale Supérieure de Chimie de Montpellier ENSCM

2012-2014: **DUT, Technical degree in Chemistry**

University Lyon 1

## Career

**PhD assistant, EPFL (LIMNO), 2018-2022**

- Collaboration with project stakeholders: scientific communication, experiments management and planning
- Patent inventor for Toyota Motor Europe
- Contributed to multiple research and industrial projects on topics including gas diffusion layer, materials, semiconductors, cell engineering, proton-exchange membrane for hydrogen production (Toyota, Engie)
- Supervision and management of interns
- Laboratory safety management, organise safety meetings, maintained cleanliness of the laboratory and chemical inventory

**Master thesis, EPFL (LIMNO), 2018**

- Dimensionality control of solution processed hybrid perovskite semiconductors

**R&D engineer – Ferroglabe 2015-2018**

- Project management : pilot development for solar-electronic grade silicon industry
- Research new ways to improve the existing products to be cost-effective and at the same time retain the structural integrity.
- Present the results of my research to customers and management
- Design prototypes for small scale laboratory testing
- Coordinate and lead technology development between the co-development partners (Cottbus University and ILS, Germany).
- Performed regular audits of process, procedures, as well as 5S and Safety.

**Control Quality laboratory technician – Galderma 2014-2015**

- Analyse and perform tests on incoming raw material, utilizing GC, UV spectrometer, refractometer, HPLC, FTIR, potentiometric titrations, pH
- Adhere to Good Manufacturing Practice (GMP) as well as safety protocols, producing results that are accurate, safe, and compliant with regulatory standards
- Follow SOPs and maintain good documentation during work: data management and maintenance to ensure compliance for audit preparation.

**R&D technician intern –Baikowski 2014**

- Development and evaluation of new laboratory method for implementation: Sulfur impurity dosage in alumina powder by ICP.
- Development coloration range of alumina-reinforced powder
- Learn and perform tasks related to ceramic processing and analysis

**Teaching assistant**

- Chimie générale avancée I : Équilibres et réactivité chimiques (Pr. J.Moser)
- Chemical engineering practice (Pr K.Sivula)

**Languages**

- French : native
- English : fluent
- Italian : fluent

**List of publications**

1. Transparency and morphology control of Cu<sub>2</sub>O photocathodes via an in-situ electro-conversion. *M. Caretti, L. Lazouni, M. Xia, RA. Wells, S. Nussbaum, D. Ren, M. Grätzel, K. Sivula*. ACS Energy Letters, 2022.
2. High performance semiconducting nanosheets via a scalable powder-based electrochemical exfoliation technique. *RA. Wells, M. Zhang, TH. Chen, V. Boureau, M. Caretti, Y. Liu, JH. Yum, H. Johnson, S. Kinge, A. Radenovic, K. Sivula*. ACS Nano, 2022.
3. Scalable Method for the Production of Transparent Gas Diffusion Layers, *M. Caretti, H. Johnson, JH. Yum, E. Mensi, S. Kinge, K. Sivula*. Patent submitted (2021).
4. Robust Electron Transport Layers via In Situ Cross-Linking of Perylene Diimide and Fullerene for Perovskite Solar Cells. *Yum Jun-Ho, Moon Soo-Jin, Yao Liang, Caretti Marina, Nicolay Sylvain, Kim Do-Hyung, Sivula Kevin*. ACS Applied Energy Materials, 2019.